

# Metal–Organic Frameworks for Photo/Electrocatalysis

Junkuo Gao, Qing Huang, Yuhang Wu, Ya-Qian Lan,\* and Banglin Chen\*

Metal–organic frameworks (MOFs), constructed from metal clusters/ions and organic ligands, are ideal materials for photo/electrocatalysis, mainly due to the advantages of large surface areas, high porosity, and easily tunable optical and electronic structures. Herein, the recent and important advances on MOF-based photo/electrocatalysts including pristine MOFs, MOF composites, and MOF derivatives are summarized. The novel strategies to improve the photo/electrocatalytic performances are highlighted. Finally, the current challenges and future development of MOFs for photo/electrocatalysis are discussed and outlined.

## 1. Introduction

The depletion of fossil fuels and environmental pollution are the main challenges that the human society is facing. The demand for energy is highly dependent on fossil fuels, leading to air pollution and the increase of CO<sub>2</sub> concentration in the atmosphere which causes global warming. To solve these problems, scientists are seeking for sustainable and clean energy sources to replace fossil fuels.<sup>[1]</sup> Renewable energy-conversion and -storage systems, including solar energy, wind energy, hydropower, fuel

cells, and electrochemical systems, have received extensive attention due to their environment benignity and effectiveness to reduce pollution and the greenhouse gas emission. The capture and catalytic conversion of CO<sub>2</sub> into valuable chemicals is another promising approach to reduce the level of CO<sub>2</sub> in the atmosphere.<sup>[2]</sup> The catalytic conversion of various abundant energy into chemical energy via photo/electrocatalysis is recognized as a highly desirable approach to fulfil the requirement of sustainable development and therefore has attracted tremendous

research interest in the past several decades.<sup>[3]</sup>

Natural photosynthesis of green plants and certain other organisms transforms solar energy into chemical energy with high efficiency.<sup>[4]</sup> During photosynthesis of plants, light is harvested and utilized to convert water and CO<sub>2</sub> into O<sub>2</sub> and energy-rich carbohydrates.<sup>[5]</sup> In the photosynthesis reaction center, the chlorophyll pigment arrays in chloroplasts serve as light-harvesting antenna and the catalytic water-splitting reactions are conducted by the reaction center composed of Mn<sub>4</sub>O<sub>4</sub> cubane cluster in photosystem II.<sup>[6]</sup> Inspired by the photosynthesis process, photocatalysis, including photocatalytic water splitting, CO<sub>2</sub> reduction reaction (CO<sub>2</sub>RR), N<sub>2</sub> reduction reaction (NRR), pollution degradation, and organic transformation, is considered as the most promising technology for the utilization of abundant solar energy to resolve global energy crisis and pollution problems.<sup>[7]</sup> Numerous semiconductors with low cost, highly stability, and environment-friendly characteristics such as TiO<sub>2</sub>, graphitic carbon nitride (g-C<sub>3</sub>N<sub>4</sub>), metal sulfides, etc. have been reported to be promising photocatalysts for various photoredox reactions.<sup>[8]</sup>

Electrocatalysis, including electrocatalytic H<sub>2</sub> evolution reaction (HER), O<sub>2</sub> evolution reaction (OER), oxygen reduction reaction (ORR), CO<sub>2</sub>RR, NRR, electro-organic synthesis, etc., is another promising approach for the conversion of various energy into chemical energy via chemical bond formation, especially when the reaction is driven by electricity generated by solar, wind, and other renewable energy resources.<sup>[9]</sup> The particular attraction of electrocatalysis based on the high transformation efficiency (up to 100% Faradaic efficiencies [FEs]) compared with the low quantum yield of photocatalysis and the simple control of the reaction through modulating the applied electrical potential. The advanced electrochemical energy-conversion devices such as fuel cells, electrolytic cells, and metal–air batteries have the advantages of high efficiency, high energy density, and lack of harmful emission. These electrochemical systems are expected to produce green energy under operation conditions, in which HER, OER, and ORR reactions are involved. The high-activation barriers of these reactions lead to large overpotential, limiting both the efficiency and conversion rate. The electrocatalytic

Prof. J. Gao, Y. Wu  
School of Materials Science and Engineering  
Zhejiang Sci-Tech University  
Hangzhou 310018, China

Dr. Q. Huang, Prof. Y.-Q. Lan  
Department of Chemistry  
South China Normal University  
Guangzhou 510006, China  
E-mail: yqlan@nynu.edu.cn

Prof. Y.-Q. Lan  
Jiangsu Collaborative Innovation Centre of Biomedical Functional Materials  
Jiangsu Key Laboratory of New Power Batteries  
School of Chemistry and Materials Science  
Nanjing Normal University  
Nanjing 210023, China

Prof. B. Chen  
Department of Chemistry  
University of Texas at San Antonio  
One UTSA circle, San Antonio, TX 78249-0689, USA  
E-mail: banglin.chen@utsa.edu

The ORCID identification number(s) for the author(s) of this article can be found under <https://doi.org/10.1002/aesr.202100033>.

© 2021 The Authors. Advanced Energy and Sustainability Research published by Wiley-VCH GmbH. This is an open access article under the terms of the Creative Commons Attribution License, which permits use, distribution and reproduction in any medium, provided the original work is properly cited.

DOI: 10.1002/aesr.202100033

water-splitting process including HER and OER to produce clean hydrogen energy is hindered by the sluggish reaction kinetics of OER. Both the CO<sub>2</sub>RR and NRR reactions suffer low selectivity and FE. Till now, most of the benchmark catalysts for electrocatalysis are noble metal-based materials, such as Pt, IrO<sub>2</sub>, and RuO<sub>2</sub>, limiting the large-scale applications due to their high cost and scarcity. Thus, it is highly desirable to develop Earth-abundant materials as highly efficient electrocatalysts.

Metal–organic frameworks (MOFs), constructed from metal clusters/ions and organic ligands, are a new type of porous materials with high surface areas (up to 10 000 m<sup>2</sup> g<sup>−1</sup>), large pore volume, and tunable pore size distribution (from 3 to 100 Å).<sup>[10]</sup> MOFs have shown promising applications in gas storage and separation,<sup>[11]</sup> luminescence,<sup>[12]</sup> magnetism,<sup>[13]</sup> biology and medicine,<sup>[14]</sup> biomass conversion,<sup>[15]</sup> photovoltaic cells,<sup>[16]</sup> water purification,<sup>[17]</sup> and catalysis<sup>[18]</sup>. Also, metal ions/metal clusters and even some organic ligands in MOFs are photo/electro-redox active, making them ideal materials for photo/electrocatalysis. MOFs have some advantages compared with other photocatalysts and electrocatalysts. 1) MOFs possess both the merits of homogeneous catalysts and heterogeneous catalysts. The precise crystal structure at the molecular level makes MOFs ideal platforms for catalytic mechanism study, whereas the porous solid state makes MOFs have much higher catalytic activity, better chemical stability, and easier recyclability compared with their molecular counterparts. 2) The porous structure and large surface areas of MOFs are beneficial for increasing active sites and accelerating mass transport (such as reactant, product, and electrolyte), thus improving the photo/electrocatalytic performance. 3) The optical and electronic structure of MOFs can be easily modulated via metal ion doping or functionalization of organic ligands without changing the crystalline structure of MOFs. 4) More than one functional site can be integrated into one MOF, making MOFs act as bifunctional or multifunctional materials for catalysis, such as photocatalytic or electrocatalytic bifunctional overall water splitting. 5) The pore size and pore environment of MOFs are tunable, making the improvement of the selectivity of aimed products possible, especially for catalytic organic synthesis reactions. 6) The morphology of MOFs is controllable. Various nanostructures such as 1D nanorods, 2D ultrathin nanosheets, and hollow nanocrystals (NCs) can be facilely synthesized. Specific morphologies such as ultrathin nanosheets are critical for the improvement of photo/electrocatalytic activity, which will expose more active sites, boost charge transfer, and also benefit device fabrications. 7) Functional molecules or clusters with high photo/electroactivity can be easily introduced into the backbones or pores of MOFs, increasing the catalytic activity. 8) MOFs can be easily composed with other functional materials by either into the large pores or on the surface. Compared with each component, MOF nanocomposites have the advantages of increased intrinsic activity, enhanced conductivity and charge transfer process, minimized aggregation of the nanomaterials, and possible synergistic interfacial effect to improve the catalytic activity. To overcome the low conductivity and weak stability in the electrolyte, the pyrolysis of MOFs to their derivatives (such as carbon materials, oxides, sulfides, phosphides with unique structures, and single atom) has also been extensively studied.<sup>[19]</sup> Meanwhile, the stable MOF derivatives can not only enhance the ability to cope with complex

working environments (e.g., acidic, alkaline, and neutral), but also possess good recyclability to improve economic benefits.

In the past several years, significant growth of MOFs for photo/electrocatalysis (Figure 1) has been witnessed. Though some reviews focus on MOFs for photocatalysis or electrocatalysis, an overall summary that covers all these rapid developing fields is still lack, and a timely summary of these fast-growing fields is highly desirable for better understanding of the structure–property relationship and strategic guidelines to develop better MOF-based photo/electrocatalysts. In this comprehensive Review, we will focus on recent developments of MOF-based photo/electrocatalysts including pristine MOFs, MOF composites, and MOF derivatives. We summarized the latest advances in the design and architecture of MOFs for photo/electrocatalysis and highlighted novel strategies to improve the photo/electrocatalytic activities. Finally, the current challenges and future development of MOF-based materials for photo/electrocatalysis are briefly discussed and outlined.

## 2. MOFs and MOF Derivatives for Photocatalysis

Photocatalysis is an environmentally friendly way to convert solar energy into chemical energy, such as photocatalytic water splitting, photoreduction of CO<sub>2</sub>, photocatalysis of organic synthesis, and photodegradation of contaminants.<sup>[20]</sup> Efficient photocatalysts usually feature with 1) appropriate bandgap, 2) distribution of more active sites, and 3) efficient carrier separation and charge transfer. To develop such photocatalysts, numerous materials were investigated ranging from traditional semiconductor systems to organic compounds, including TiO<sub>2</sub>, CdS, MOFs, and their composites.<sup>[21]</sup> Traditional semiconductor catalysts suffer from limited bandgap, low charge separation efficiency, and low catalytic activity. Subsequently, a lot of research has been proposed to address these issues, such as doping with C/N materials to change bandgap and modifying with precious metal cocatalyst on the material surface to promote efficient charge separation.<sup>[22]</sup> However, the lack of definite structure of these materials leads to further research on the reaction mechanism being limited.

MOFs emerged as a kind of novel photocatalyst, due to the high specific surface area, clear active sites, and tunable structural components.<sup>[23]</sup> Intrinsic pores and ultrahigh specific surface area facilitate the adsorption of reactant molecules, which provides more opportunities for access to active sites; clear active sites are beneficial to further study the photocatalytic reaction mechanism; regulatable ligand and metal active centers are conducive to extending the light absorption region and investigating the effects of different metal activities to guide the development of highly efficient photocatalysts. In the section of MOF-based photocatalysis, we will introduce the charge transfer mechanism, the strategies of improving photocatalytic performance, and the application of photocatalysis (including photocatalytic water splitting, photoreduction of CO<sub>2</sub>, photocatalytic organic synthesis, photocatalytic degradation of pollutants, etc.).

### 2.1. MOFs as Photoresponsive Semiconductor

More than a decade ago, theoretical calculations demonstrated that the MOFs (such as IR-MOFs) can be regarded as

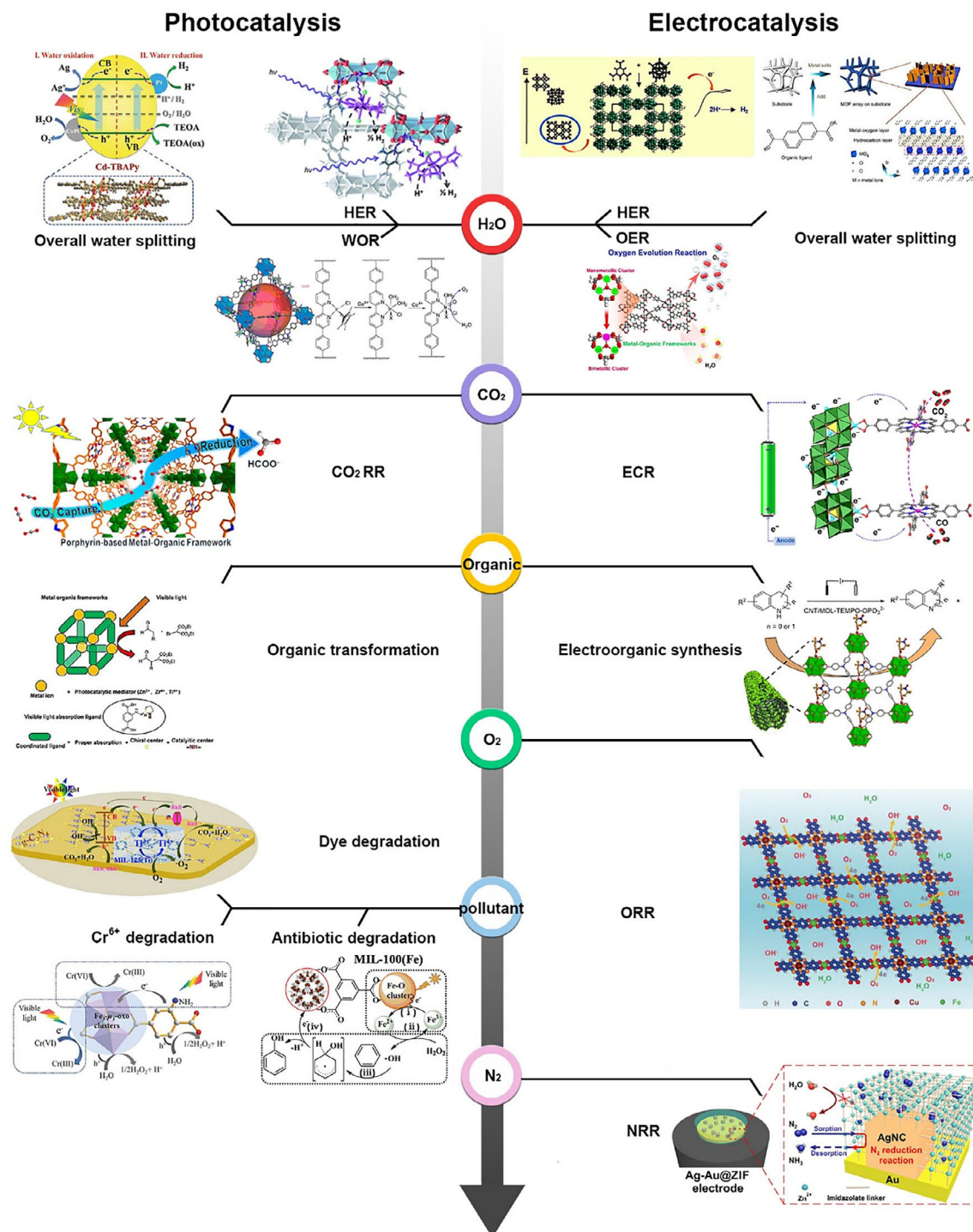


**Figure 1.** Schematic summary of MOFs for photo/electrocatalysis. MOFs for photocatalysis: HER. Reproduced with permission.<sup>[35]</sup> Copyright 2015, The Royal Society of Chemistry. OER. Reproduced with permission.<sup>[78]</sup> Copyright 2012, American Chemical Society. Overall water splitting. Reproduced with permission.<sup>[82]</sup> Copyright 2018, Wiley-VCH GmbH. CO<sub>2</sub>RR. Reproduced with permission.<sup>[39]</sup> Copyright 2015, American Chemical Society. Organic transformation. Reproduced with permission.<sup>[90]</sup> Copyright 2017, American Association for the Advancement of Science (AAAS). Dye degradation. Reproduced with permission.<sup>[286]</sup> Copyright 2015, Elsevier. Cr(VI) degradation. Reproduced with permission.<sup>[43]</sup> Copyright 2015, Wiley-VCH GmbH. Antibiotic degradation. Reproduced with permission.<sup>[40]</sup> Copyright 2015, American Chemical Society. MOFs for electrocatalysis: HER. Reproduced with permission.<sup>[135]</sup> Copyright 2011, American Chemical Society. OER. Reproduced with permission.<sup>[168]</sup> Copyright 2018, Wiley-VCH GmbH. Overall water splitting. Reproduced with permission.<sup>[143]</sup> Copyright 2017, Nature Publishing Group. CO<sub>2</sub>RR. Reproduced with permission.<sup>[204]</sup> Copyright 2018, Nature Publishing Group. Electro-organic synthesis. Reproduced with permission.<sup>[227]</sup> Copyright 2019, Wiley-VCH GmbH. ORR. Reproduced with permission.<sup>[184]</sup> Copyright 2019, Wiley-VCH GmbH. NRR. Reproduced with permission.<sup>[222]</sup> Copyright 2018, AAAS.



semiconductors with large bandgaps.<sup>[24]</sup> Generally, for MOFs, highest occupied molecular orbital (HOMO) and lowest unoccupied molecular orbital (LUMO) were utilized to describe the energy levels to distinguish from periodic semiconductors.<sup>[25]</sup> The HOMO–LUMO bands are mainly controlled by the C  $sp^2$  state of the linker molecules. Because the HOMO band is dominated by conjugation of organic ligands, the bandgaps of MOFs can be modulated by various ligands. Under illumination, the organic linkers of MOFs were generally assigned to harvest light and be photoexcited, further to activate the metal nodes or metal cluster through linker-to-metal charge transfer (LMCT).<sup>[25,26]</sup> Such a semiconductor-like behavior of MOFs provided a platform and new opportunity for photocatalytic reaction.

García and coworkers first utilized the UiO-66 and UiO-66-NH<sub>2</sub> as photocatalysts toward H<sub>2</sub> generation by water splitting due to the excellent water stability of the two MOFs.<sup>[27]</sup> It is

demonstrated that the absorption wavelength of MOF will be red shifted with the modification of ligand by amino group. The long-lived charge separation, about 300  $\mu$ s, was recorded by laser flash photolysis, illustrating the photoresponsive behaviors of MOF semiconductor. Furthermore, the semiconducting mechanism under illumination could be explicated by MIL-125(Ti) series. When MIL-125-NH<sub>2</sub> was used for CO<sub>2</sub> reduction, the electron spin resonance (ESR) experiments revealed that the transfer path of photogenerated electrons from the ligand to Ti<sup>4+</sup> is induced by O atom of 2-aminoterephthalate (ATA) group.<sup>[28]</sup> As a result, the Ti<sup>3+</sup> of Ti–O cluster was formed by transferring electron to Ti<sup>4+</sup> through LMCT (**Figure 2A**). In addition, compared with pristine MIL-125, MIL-125-NH<sub>2</sub> exhibited excellent performance attributed to –NH<sub>2</sub> functionalization, extending the light adsorption from ultraviolet (UV) to visible light. Inspired the development, organic ligands were rationally designed and synthesized toward photocatalytic reaction, considering the

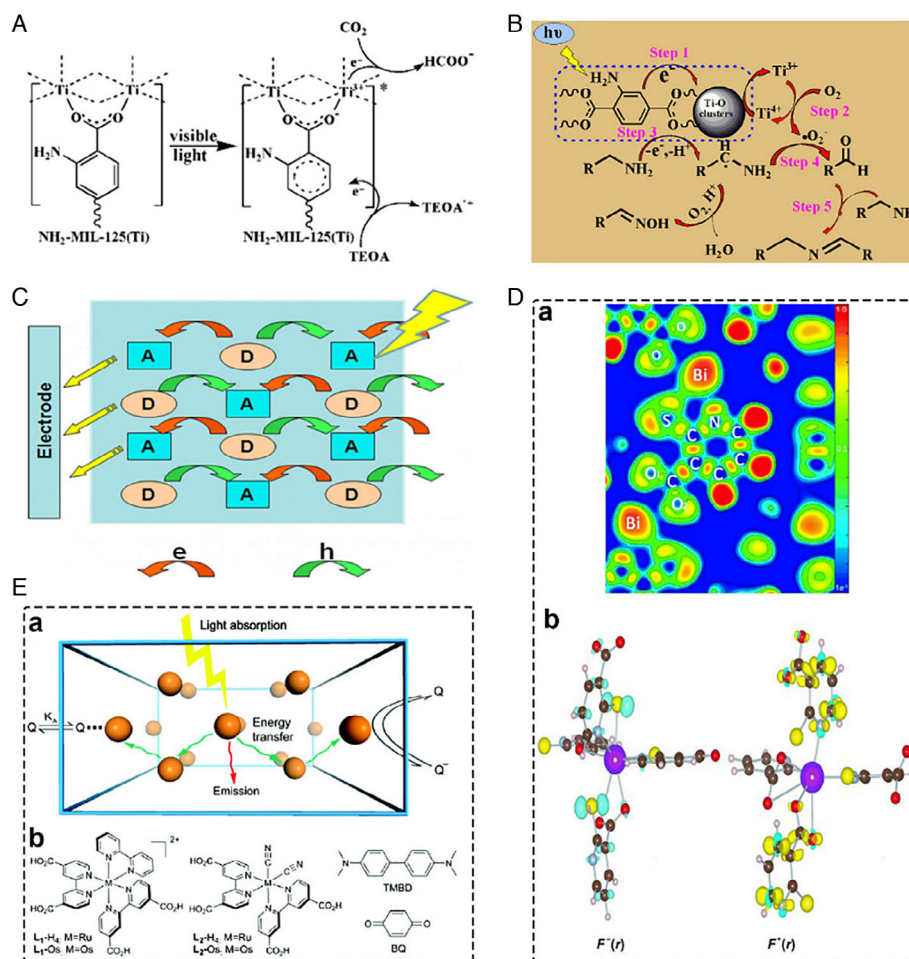


**Figure 2.** A) Proposed mechanism for the photocatalytic CO<sub>2</sub>RR over MIL-125-NH<sub>2</sub> under visible light irradiation. Reproduced with permission.<sup>[28]</sup> Copyright 2012, Wiley-VCH GmbH. B) Proposed mechanism of the photocatalytic amine oxidation over MIL-125-NH<sub>2</sub>. Reproduced with permission.<sup>[29]</sup> Copyright 2014, Elsevier. C) Sketch map of the possible electron transfer mechanism in the MOF with LLCT interaction. Reproduced with permission.<sup>[30]</sup> Copyright 2016, American Chemical Society. D) a) Calculated electron localization function (ELF) plots for Bi-mna. b) Fukui function  $F^-(r)$  and  $F^+(r)$  for Bi-mna. The isosurface value is 0.0015 eÅ<sup>-3</sup>. Bi, purple; C, brown; O, red; N, gray; H, pink. Reproduced with permission.<sup>[31]</sup> Copyright 2015, Wiley-VCH GmbH. E) a) Schematic representation of a light-harvesting MOF microcrystal. The <sup>3</sup>MLCT excited states undergo rapid intraframework energy migration to conduct electron transfer quenching at the MOF/solution interface. b) Chemical structures of the photoactive MOF building blocks and reductive (TMBD) and oxidative (BQ) quenchers. Reproduced with permission.<sup>[33]</sup> Copyright 2011, American Chemical Society.



importance of the integration of additional groups. The bandgaps will change due to the contribution of  $2p$  electrons, when functional groups ( $-\text{NH}_2$ ,  $-\text{CH}_3$ ,  $-\text{OH}$ , or  $-\text{Cl}$ ) are induced. Similar modification by the  $-\text{NH}_2$ , MIL-125- $\text{NH}_2$  can be utilized for photocatalytic oxidation of amines to imines in  $\text{O}_2$  atmosphere.<sup>[29]</sup> In this reaction, the  $\text{Ti}^{3+}$  ions were formed through LMCT, and the resulting  $\text{Ti}^{3+}$  further reacted with  $\text{O}_2$  molecules to form superoxide radical anion ( $\cdot\text{O}_2^-$ ), whereas the as-formed  $\text{Ti}^{3+}$  ions were oxidized back to  $\text{Ti}^{4+}$  ions (Figure 2B). Meanwhile, amine served as the electron donor to provide the electron and then formed the carbon-centered free radical through deprotonation. Next, aldehydes were generated by the reaction between  $\cdot\text{O}_2^-$  and carbon-centered free radical, followed by aldimine condensation on aldehydes via nuclear attack by unreacted amine.

The study of ligand-to-ligand charge transfer (LLCT) within MOFs is not extensive and in-depth enough, as it is difficult to control multiple factors at the same time. It demanded a mixed ligand coordination system, in which the coordination between metal ion and electron donor (D) as well as electron acceptor (A) must precede the M-A or M-D separation and D-A combination (Figure 2C).<sup>[30]</sup> Some LLCT within MOFs were presented, such as  $[\text{MnL}(\text{bpa})(\text{H}_2\text{O})]_n \cdot 2\text{nH}_2\text{O}$ ,  $[\text{MnL}(\text{bpe})_{0.5}(\text{DMF})]_n \cdot 2\text{nH}_2\text{O}$ , and  $[\text{MnL}(4,4'\text{-bpy})(\text{H}_2\text{O})]_n \cdot n\text{CH}_3\text{CN}$  ( $\text{L}$  = dimethylthio-tetrathiafulvalenebicarboxylate,  $\text{bpa}$  = 1,2-bis(4-pyridyl)ethane,  $\text{bpe}$  = 1,2-bis(4-pyridyl)-ethene and  $4,4'\text{-bpy}$  = 4,4'-bipyridine).<sup>[30]</sup> Theoretical calculations and ESR experiments revealed the charge transfers from L ligand to the other ligand. However, these LLCT light-responsive MOFs have not continued to be used for photocatalysis. Another LLCT light-responsive Bi-MOF (Bi-mna) was presented for decomposition of organic dyes rhodamine B and methylene blue.<sup>[31]</sup> LLCT occurred from Bi-S to Bi-S or Bi-O, in which Bi atom served as the bridge between two ligands. Compared with LMCT, LLCT within MOFs for photocatalytic reactions are not often observed and reported (Figure 2D).

Metal-to-ligand charge transfer (MLCT) is common in ligands with low-level  $\pi$  antibonding of empty orbitals, especially in complexes formed by aromatic ligands, such as photosensitive Ru-based and Ir-based complex compounds.<sup>[32]</sup> Integration of these photosensitive molecules to MOFs can improve the ability for sensitizing electron transfer, and the energy band structure can be facily regulated. Using photoactive Ru(II)-bpy as building blocks, Lin and coworkers presented microscale Ru-based MOFs which displayed "antenna"-like behaviors with efficient charge transfer efficiency ( $>98\%$ ).<sup>[33]</sup> MLCT excitations extended the light adsorption and underwent rapid energy migration in the crystal, which showed promising photochemical performance (Figure 2E). Such an integration strategy provided strong evidence that MOFs are viable platforms cooperating with photosensitive molecules to harvest light and realize energy conversion by electron transfer. MOFs can be the promising platform coupling with other catalytic components toward efficient artificial photosynthesis. Lin and coworkers successfully presented a series of novel MOFs, integrating Re-/Ru-/Ir-based complexes into UiO-MOF for various photocatalytic reactions.<sup>[34]</sup> A similar strategy or encapsulation method was also documented for photocatalytic  $\text{CO}_2$ RR, HER, and etc.<sup>[35,36]</sup>

## 2.2. Strategies to Improve Photocatalytic Activity of MOFs

### 2.2.1. Light Absorption

The main advantage of MOFs over other materials is that their assembled structure permits the combination of a variety of transition metals, organic linkers, and structural arrangements. Building blocks and predesigned organic ligands can be selected to make target MOFs have better photocatalytic performance. To obtain highly efficient photocatalytic MOF-based materials, the primary request is harvesting light to be photoexcited and further to transfer electrons. The proportion of visible light to total solar radiation energy is much higher than that of UV light. To utilize solar energy efficiently, photocatalytic reaction is preferred to perform under natural light or visible light. Therefore, a great deal of investigations focused on extending light absorption range and intensity of MOF materials.<sup>[28,37]</sup>

In particular, the use of  $-\text{NH}_2$  groups and macrocyclic conjugated ligands as linkers will extend the adsorption region from UV to visible light. To improve the catalytic activity of UiO-66 to produce  $\text{H}_2$ , García and coworkers presented an analogous MOF (UiO-66- $\text{NH}_2$ ) with  $-\text{NH}_2$  modification of 1,4-bicarboxybenzene (BDC) ligand.<sup>[27]</sup>  $-\text{NH}_2$  served as auxochrome group in BDC ligand that can make  $K$  band ( $\pi-\pi^*$ ) red shift, giving rise to an intense absorption region from 300 to 440 nm. Therefore, under visible light, compared with pristine UiO-66, UiO-66- $\text{NH}_2$  exhibited excellent performance due to the enhanced light harvesting. Similar functionalized MIL-125- $\text{NH}_2$  was reported for photoreduction of  $\text{CO}_2$  into  $\text{HCOOH}$ .<sup>[28]</sup> Light harvesting can be solved using porphyrin derivatives as organic linkers, as porphyrin rings have 26  $\pi$  electrons which are highly conjugated, leading to the highly photosensitive properties. Chen et al. presented a series of porphyrin-based Zr-MOFs, ZrPP- $n$ -M ( $\text{M} = \text{H}_2$ , Zn, Cu, Fe, Co,  $n = 1, 2$ ), toward photoreduction of  $\text{CO}_2$  under visible light irradiation (Figure 3).<sup>[38]</sup> Among these M-ZrPP- $n$  crystal materials, ZrPP-1-Co exhibited the best photocatalytic activity for  $\text{CO}_2$  conversion, splitting  $\text{CO}_2$  into CO with high selectivity of 96.4% without cocatalyst. Similarly, PCN-222 was used for photoreduction of  $\text{CO}_2$  into  $\text{HCOOH}$  under visible light region.<sup>[39]</sup>

Besides the design of ligands, metal ions or metal clusters can also be used as visible light collection centers. For example, Fe(III)-based MOFs consisting of  $\text{Fe}_3-\mu_3\text{-O}$  clusters can serve as photocatalysts for various photocatalytic reactions.<sup>[40,41]</sup> Under visible light irradiation, MIL-88B(Fe) and MIL-101(Fe) were used for degradation of Rhodamine 6 G in aqueous solution by Laurier et al.<sup>[42]</sup> Because the linker was insensitive to visible light, the  $\text{Fe}_3-\mu_3\text{-oxo}$  cluster was responsible for harvesting the visible light and acted as photocatalytic sites. Subsequently, Ye and coworkers combined  $\text{Fe}_3-\mu_3\text{-oxo}$  clusters and  $-\text{NH}_2$ -functionalized ligands to prepare  $\text{NH}_2\text{-MIL-88B(Fe)}$ ,  $\text{NH}_2\text{-MIL-53(Fe)}$ , and  $\text{NH}_2\text{-MIL-101(Fe)}$  toward photoreduction of Cr(VI) under visible light.<sup>[43]</sup> It was demonstrated that such a combination strategy contributed to photocatalytic activity for Cr(VI) degradation, which was due to the improved light absorption sites and efficient charge transfer via LMCT. MOFs are excellent photocatalytic platforms, as the light harvesting efficiency can be flexibly modulated by ligand and metal cluster.

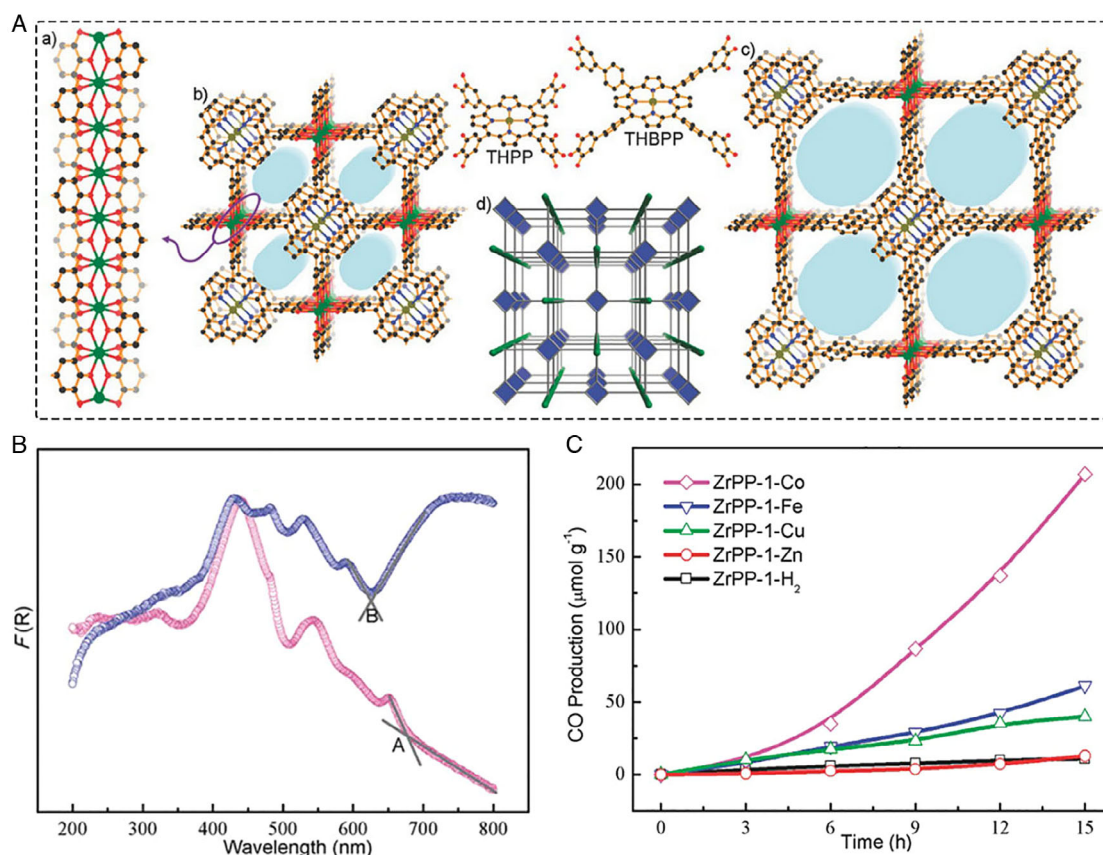


**Figure 3.** A) The structure of ZrPP-*n*. a) Zr<sup>IV</sup>-pyrogallate coordination chain. b) Structure of ZrPP-1. c) Structure of ZrPP-2. d) Augmented rod-like nbo topology of ZrPP-*n*, where the green rods and blue squares represent Zr<sup>IV</sup>-pyrogallate pillars and porphyrinic nodes. C, black, O, red, N, blue, Zr, Green, metal (in porphyrin core), yellow, all H atoms are not depicted for clarity. B) UV-vis-diffuse reflectance spectroscopy (DRS) of ZrPP-1-Co and mixture of Zr<sup>IV</sup>-pyrogallate chain and THPP-Co, with their absorption onsets tagged by A and B, respectively. C) Time courses of CO obtained from CO<sub>2</sub> photoreduction with catalysts of ZrPP-1-M under visible light irradiation. Reproduced with permission.<sup>[38]</sup> Copyright 2017, Wiley-VCH GmbH.

### 2.2.2. Active Sites

Ligands are mainly responsible for collecting light in photocatalysis, whereas metals or clusters usually act as active sites for photocatalysis. In addition to the traditional stable Zr-MOFs or Ti-MOFs,<sup>[44]</sup> novel MOF materials based on other metals and metal clusters were gradually used for photocatalysis and showed good performance. Recently, Wang et al. presented three stable MOFs, MOF-Ni, MOF-Co, and MOF-Cu, for photoreduction of CO<sub>2</sub>.<sup>[45]</sup> MOF-Ni showed a high selectivity of 97.7% for splitting CO<sub>2</sub> into CO, due to the strong binding between Ni and CO<sub>2</sub>, whereas a high energy barrier for H<sub>2</sub> evolution. It was demonstrated that Ni(II) ion was a good active site for CO<sub>2</sub> reduction. Introducing other highly active metals into MOFs is also a good way to increase the numbers of active sites and promote photocatalytic activity. Very recently, catalytic active Co(II) centers were anchored into the Zr-based MOF modified with thiol groups for metal insertion via postsynthetic exchange (PSE).<sup>[46]</sup> The resulting MOF material (denoted as Zr-DMBD@Co MOF) was modified by Co-thiolate units, which exhibited high photocatalytic activity (turnover number

[TON] = 97941) and high selectivity (98% for CO) toward CO<sub>2</sub> conversion under visible light irradiation. In addition, modification of different metals in porphyrin centers as active sites also promotes photocatalytic activity, due to adding new active centers and further greatly increasing separation efficiency of the photogenerated electrons and holes in porphyrin sections. Ye and coworkers realized modular optimization within MOFs through incorporating single atoms into porphyrin center (Figure 4A).<sup>[47]</sup> MOF-525, MOF-525-Zn, and MOF-525-Co were used for photocatalytic CO<sub>2</sub>RR under visible light irradiation, and MOF-525-Co exhibited highest activity toward CO generation (200.6 μmol g<sup>-1</sup> h<sup>-1</sup>) than that of MOF-525 and MOF-525-Zn (Figure 4B,C). The enhanced diversity in activity for two catalysts was attributed to the different charge separation efficiencies caused by different metal-locating porphyrin centers. Therefore, different active sites dispersion in MOF exhibited photocatalytic activity because of the energy transfer from the ligand to the lower energy center at Co or Zn “trap site” (Figure 4D,E). In fact, the electron-trapping effect promotes the charge separation efficiency. Apparent embodiment of the different catalytic active sites exhibited diversity.

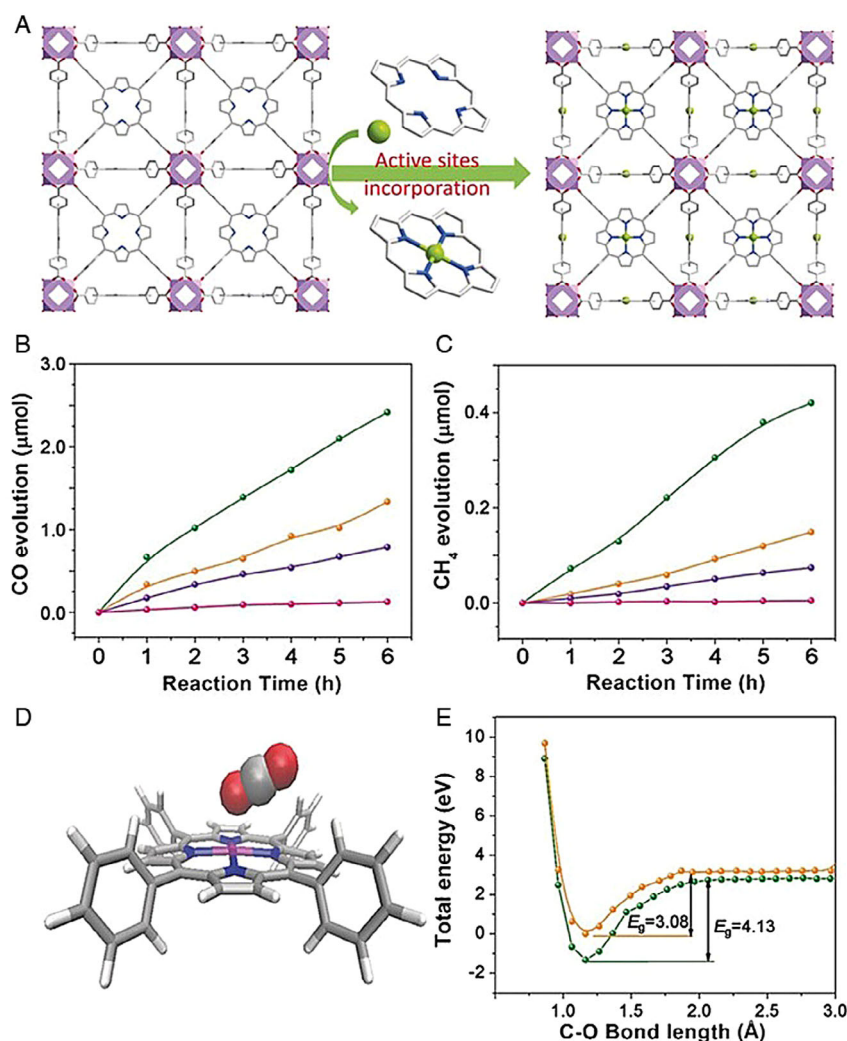


**Figure 4.** A) View of the 3D network of MOF-525-Co featuring a highly porous framework and incorporated active sites. B,C) Time-dependent CO and CH<sub>4</sub> evolution over MOF-525-Co (green), MOF-525-Zn (orange), MOF-525 (purple) photocatalysts, and H<sub>2</sub>TCP ligand (pink). D) The optimized structure for CO<sub>2</sub> adsorption on a porphyrin-Co unit. E) The C—O bond length-dependent CO<sub>2</sub> activation energy barrier. Key: charged with one electron (orange), neutral state (green). Reproduced with permission.<sup>[47]</sup> Copyright 2016, Wiley-VCH GmbH.

### 2.2.3. Charge Separation

Efficient charge separation and long lifetime of charge separation are critical for photocatalytic reaction, as the recombination of charges will hinder the smooth migration of charges and abate catalytic activity. A large number of studies on promoting electron-hole separation and extending charge separation lifetime were devoted to developing efficient MOF photocatalysts,<sup>[48]</sup> such as the introduction of other metals as intermediaries,<sup>[49]</sup> the integration of photosensitive dyes into MOF frameworks,<sup>[34]</sup> doping with metal nanoparticles (NPs),<sup>[50]</sup> and comprising other semiconductors.<sup>[51]</sup> Ti-substituted NH<sub>2</sub>-UiO-66(Zr/Ti) was synthesized by a PSE method, exhibiting a reinforced activity for both HER and CO<sub>2</sub>RR under irradiation.<sup>[49]</sup> Electron spin resonance (ESR) experiments and density functional theory (DFT) calculations showed that the enhanced photocatalytic activity was attributed to the efficient electron transfer from ligand to

Zr<sup>4+</sup> ion through the mediator at Ti section. The integration of photosensitive dyes into MOF frameworks also can greatly promote charge separation and lengthen charge separation time. Recently, Kong and coworkers designed and synthesized an Eu-Ru(phen)<sub>3</sub>-MOF (phen = phenanthroline) by combining Ru(phen)<sub>3</sub> with dinuclear Eu(III)<sub>2</sub>, and the developed MOF can convert CO<sub>2</sub> into HCOOH at the rate of 321.9 μmol h<sup>-1</sup> mmol<sub>MOF</sub><sup>-1</sup> (Figure 5).<sup>[52]</sup> The results of UV-vis absorption and time-resolved photoluminescence (PL) revealed that the electrons transfer from ligand to Eu<sub>2</sub> oxo-clusters due to quenching effect after Eu<sub>2</sub> coordination (Figure 5A,B).

Furthermore, ultrafast transient absorption and electron paramagnetic resonance (EPR) experiments coupling with fitting the kinetics detected the electron transfer time of 1.2 ns (Figure 5C,D). Ru(phen)<sub>3</sub> ligand effectively promoted charge separation and electron transfer to clusters, further improving charge separation lifetime (Figure 5F). In addition, Lin's group



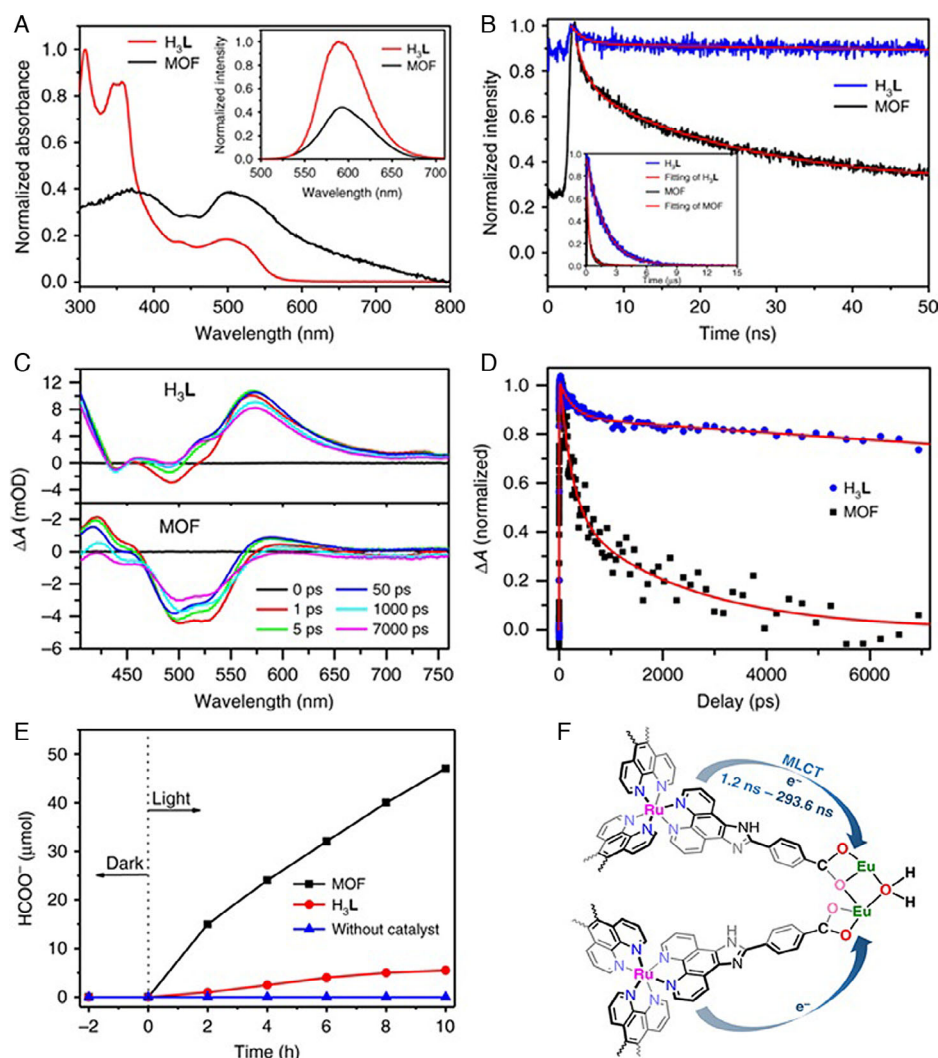


**Figure 5.** A) Normalized UV-vis spectra of Eu-Ru(phen)<sub>3</sub>-MOF and H<sub>3</sub>L in DMF. Inset: Emission spectra of Eu-Ru(phen)<sub>3</sub>-MOF and H<sub>3</sub>L ( $\lambda_{\text{ex}} = 465$  nm). B) Normalized luminescence decay traces of Eu-Ru(phen)<sub>3</sub>-MOF and H<sub>3</sub>L over the first 50 ns ( $\lambda_{\text{ex}} = 377$  nm). Inset: Decay transients measured at 630 nm ( $\lambda_{\text{ex}} = 465$  nm). C) Transient absorption spectra of Eu-Ru(phen)<sub>3</sub>-MOF and H<sub>3</sub>L at various time delays and (D) corresponding kinetic traces at 604 nm. E) Time profiles of HCOO<sup>-</sup>-produced catalyzed by Eu-Ru(phen)<sub>3</sub>-MOF or H<sub>3</sub>L or without catalyst under visible light. F) Schematic light-induced dynamics of Eu-Ru(phen)<sub>3</sub>-MOF based on the initial excitation of the Ru photocenter and the pathways of electron transfer from Ru to catalytic Eu<sub>2</sub> oxo-cluster center. Reproduced with permission.<sup>[52]</sup> Copyright 2018, Nature Publishing Group.

has been committed to photocatalytic reactions in photosensitive ligand-integrated MOFs. They have successfully integrated the Ir/Ru/Re complex into UiO-67 toward photocatalytic OER, CO<sub>2</sub>RR, and organic photocatalysis.<sup>[34]</sup> Similarly, Kitagawa's group integrated [Ru<sup>II</sup>(H<sub>2</sub>bpydc)(terpy)(CO)](PF<sub>6</sub>)<sub>2</sub> (H<sub>2</sub>bpydc = 2,2'-bipyridine-5,5'-dicarboxylic acid, terpy = 2,2',6',2''-terpyridine) into UiO-67 by the PSE method.<sup>[53]</sup> The developed MOF was used for photoreduction of CO<sub>2</sub>, and the HCOOH was the main product.

The earlier examples are all methods that directly change the building elements of MOFs to promote charge separation and increase separation lifetime. Compounds of other substances can achieve the same purpose. Noble-metal NPs were loaded on MOFs, which not only had the surface plasmonic effect, but also had the cocatalytic effect.<sup>[54]</sup> On the one hand, under

visible light illumination, the hot electrons can be injected into the MOF from the photoexcited noble-metal NPs; thus, the extra photogenerated electrons will enhance photocatalytic activity. On the other hand, the excited NPs can induce electrostatic field near NPs, which will increase charge distance and prolong carrier lifetime along with low recombination probability. Choi et al. covalently attached Re-based complex into UiO-67 and loaded Ag nanocubes into MOF (AgCRe<sub>3</sub>-MOF) (Figure 6).<sup>[54a]</sup> The enhancement of near-surface electric field of photoactive Re centers on Ag nanocubes results in a sevenfold increase for CO<sub>2</sub> to CO conversion along with long-term stability for about 48 h under visible light. In addition to loading with noble-metal NPs, other semiconductor materials have also been doped into MOFs, including metal oxide sulfide-based semiconductors, g-C<sub>3</sub>N<sub>4</sub>, etc. Most of the semiconductor materials combined with

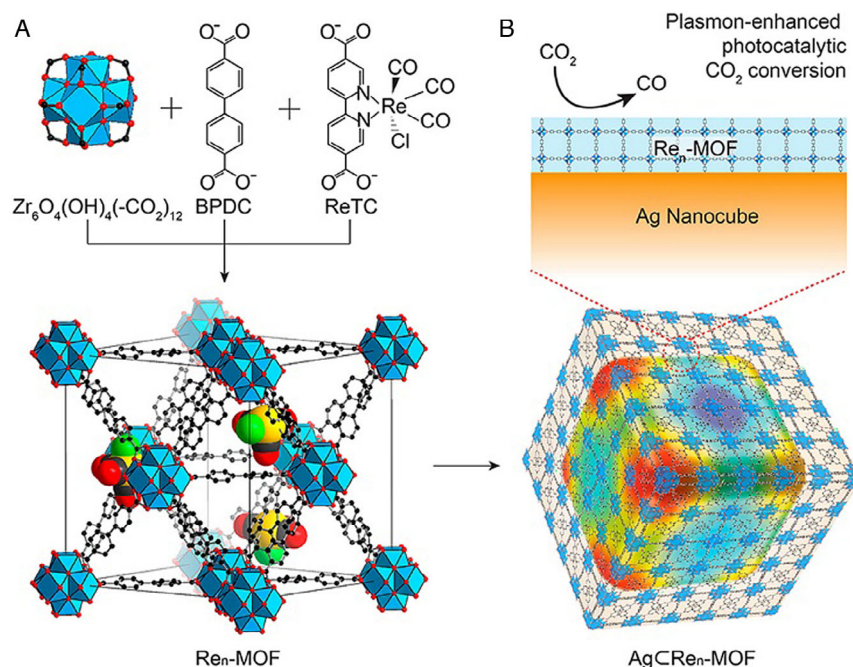


**Figure 6.** Structures of Re<sub>n</sub>-MOF and AgCRe<sub>n</sub>-MOF for plasmon-enhanced photocatalytic CO<sub>2</sub>RR. A) Zr<sub>6</sub>O<sub>4</sub>(OH)<sub>4</sub>(-CO<sub>2</sub>)<sub>12</sub> secondary building units are combined with biphenyl-3,4',5-tricarboxylic acid (BPDC) and ReTC linkers to form Re<sub>n</sub>-MOF. The structure of Re<sub>3</sub>-MOF identified from single-crystal X-ray diffraction is shown. The 12-coordinated Zr-based metal clusters are interconnected by 21 BPDC and 3 ReTC linkers in a face-centered cubic array. Atom-labeling scheme: C, black; O, red; Zr, blue polyhedra; Re, yellow; Cl, green; and H atoms are omitted for clarity. B) Re<sub>n</sub>-MOF coated on a Ag nanocube for enhanced photocatalytic conversion of CO<sub>2</sub>. Reproduced with permission.<sup>[54a]</sup> Copyright 2017, American Chemical Society.

MOFs, which can form Schottky junctions to prolong charge separation lifetime. Semiconductor TiO<sub>2</sub> was accurately positioned in the different pores of MIL-101 and its derivatives. The TiO<sub>2</sub> units were photoexcited to provide photogenerated electrons which efficiently transfer to the catalytic metal clusters in MOFs for photoreduction of CO<sub>2</sub>.<sup>[55]</sup> Cu<sub>2</sub>O was encapsulated in Cu<sub>3</sub>(BTC)<sub>2</sub> (BTC = 1,3,5-benzene tricarboxylate) used for photocatalytic CO<sub>2</sub> reduction.<sup>[56]</sup> The MOFs not only suppress the Cu<sub>2</sub>O corrosion, but also promote the charge separation and CO<sub>2</sub> uptake. CdS coupled with Co-ZIF-9 was applied for photocatalytic CO<sub>2</sub>RR,<sup>[57]</sup> and ZnIn<sub>2</sub>S<sub>4</sub> was dispersed on MIL-125-NH<sub>2</sub> toward photocatalytic HER.<sup>[58]</sup> g-C<sub>3</sub>N<sub>4</sub> is not only a visible light collector due to its conjugated polymeric characteristic, but also can promote efficiently charge separation. g-C<sub>3</sub>N<sub>4</sub> nanosheets were combined with UiO-66; such a hybrid showed enhanced photocatalytic performance on CO<sub>2</sub> to CO conversion due to prolonging of charge separation lifetime.<sup>[59]</sup>

## 2.3. MOFs for Photocatalytic Water Splitting

### 2.3.1. Photocatalytic HER

Porous MOFs can provide additional photoexcited possibility through integrating the light-harvesting moiety into organic ligands and the catalytic metal ions. Such advantages make MOFs good candidates for photocatalytic HER. The Zr-MOFs were widely developed for H<sub>2</sub> evolution by photocatalytic water splitting, due to their high chemical stability in different solvents and excellent mechanical stability. García and coworkers first

utilized UiO-66 and UiO-66-NH<sub>2</sub> for photocatalytic HER under UV or visible light, while methanol served as the sacrificial electron donor.<sup>[27]</sup> Compared with UiO-66, UiO-66-NH<sub>2</sub> showed better catalytic performance due to the integration of -NH<sub>2</sub> group, extending the region of absorption wavelength and promoting charge separation. When Pt NPs were added as cocatalyst into the photocatalytic reduction system, the total amount of H<sub>2</sub> generation accelerated evidently up to 2.4 mL (UiO-66/Pt) and 2.8 mL (UiO-66-NH<sub>2</sub>/Pt) after 3 h of illumination. In addition, a series of spectroscopic results revealed that the two Zr-MOFs have the veritable precondition of semiconductors due to long-lived charge separation time. This work opened up a new path for developing MOFs as semiconductors for photocatalytic HER.

**Doping with Precious Metal:** After that, a lot of excellent work based on MOFs as photocatalysts emerged. When mixing MOFs with precious metals and creating a Schottky barrier at the border, the photoexcited electrons can transfer from MOFs to the precious metals in the conduction band (CB).<sup>[60]</sup> As a result, loading precious metals (e.g., Pt, Au, and Pd) into MOFs, which efficiently promoted separation of photogenerated electron-hole pairs, suppressed the recombination of photogenerated electron-hole and prolonged the carrier lifetime.<sup>[61]</sup> Lin and coworkers utilized Pt-deposited Zr-MOF for HER. Pt NPs were loaded into the channels of UiO MOFs, which were assembled by photosensitive Ir-based molecular (L1 and L2) Zr<sub>6</sub>(O<sub>4</sub>(OH)<sub>4</sub>).<sup>[62]</sup> Higher Pt loading was observed in MOF 2 than MOF 1 as MOF 2 had a larger cavity structure and a higher Ir complex enrichment. Such two Pt@MOF assemblies showed outstanding performance for H<sub>2</sub> generation with triethylamine (TEA) as electron donor in

photocatalytic water splitting. After 48 h of illumination, the Ir-based TONs of 3400 and 7000 for  $H_2$  generation were recorded, which were assigned to Pt@1 and Pt@2, respectively. However, control groups of homogeneous  $K_2PtCl_4/[Ir(ppy)_2(bpy)]Cl$  exhibited lower TONs of 1500 and 2200, respectively. Such excellent photocatalytic activity gave the credit to efficient electron transfer from the photoexcited Ir complexes to Pt NPs. The Pt NPs accelerated  $H_2$  generation and slowed down the degradation of unstable Ir-based molecular compounds. Such a method can greatly enhance the photocatalytic performance of MOF-based materials.

To increase the photogenerated electron-hole separation efficiency, Pt NPs of  $\approx 3$  nm were encapsulated inside of UiO-66- $NH_2$  (Pt@UiO-66- $NH_2$ ) or attached on UiO-66- $NH_2$  surface (Pt/UiO-66- $NH_2$ ) by Xiao et al.<sup>[63]</sup> Both Pt-loading UiO-66- $NH_2$  catalysts exhibited excellent photocatalytic performance for HER compared with the pristine UiO-66- $NH_2$ , notably Pt@UiO-66- $NH_2$  (Figure 7A). In that case, the dramatic difference depends mainly on the position of Pt loading. Pt@UiO-66- $NH_2$  showed outstanding cyclic performance and stability due to the encapsulation of Pt NPs into UiO-66- $NH_2$ , whereas the activity for Pt/UiO-66- $NH_2$  gradually decreased due to the Pt NPs' attachments, which were easier to leach and aggregate. As a result of greatly shortening the electron-transfer distance to promote electron-hole separation by Pt@UiO-66- $NH_2$ , Pt@UiO-66- $NH_2$  catalyst exhibited excellent photocatalytic activity for HER. Jiang and coworkers also loaded Au into two types of MIL-125 surfaces, denoted as Pt/MIL-125/Au and Pt/MIL-125/Au (Figure 7B).<sup>[50]</sup> Plasmonic effect and Schottky junction electron trapping greatly extended the adsorption wavelength to visible light and accelerated electron-hole separation in Au-decorated Pt-MIL-125. Therefore, Pt@MOF/Au exhibited a better photocatalytic performance for HER by water splitting, far exceeding Pt/MIL-125/Au and MIL-125/Au.

**Decorating with Non-Noble Metal:** The high cost of precious metals makes it impossible to apply them on a large scale. Therefore, MOFs decorated with non-noble metals are also documented.<sup>[64]</sup> Nasalevich et al. proposed an ingenious strategy

(ship-in-a-bottle) to synthesize the Co@MOF photocatalyst toward HER.<sup>[35]</sup>  $L^{H2}$  was first encapsulated in MIL-125- $NH_2$ , and then  $CoBr_2$  was added to construct Co@MOF. Compared with the pristine Ti-MOF, a 20-fold improvement for  $H_2$  generation rate was achieved due to the encapsulation of the Co-based molecular active site into MIL-125- $NH_2$ . Co-based molecule complex  $[Co^{II}(TPA)Cl][Cl]$ , TPA = tris(2-pyridylmethyl)amine, was successfully encapsulated into MIL-125- $NH_2$  by the similar strategy.<sup>[65]</sup> ESR results revealed that the efficient photoelectrons directly transfer from  $NH_2$ -BDC to  $[Co^{II}(TPA)Cl][Cl]$  while hardly flowing to the Ti-O clusters. Compared with pristine MOF ( $17 \mu mol g^{-1} h^{-1}$ ), the host Co-based complex greatly increased  $H_2$  generation rate ( $553 \mu mol g^{-1} h^{-1}$ ).

**Loading with Metal Oxides:** Metal oxide loading on MOFs for photocatalytic HER also gradually attracted researchers' interest. Two main methods were commonly observed for photocatalytic HER by water splitting: 1) attaching metal oxide on the surface of the MOF and 2) forming core-shell structures between metal oxide and MOFs. Shen et al. prepared a series of UiO-66- $NH_2$ -based complexes decorated with NiO NPs, which were denoted by U6N-NiO.<sup>[66]</sup> When the complex was embedded with 10 wt% NiO, the  $H_2$  generation rate greatly increased to  $2561.32 \mu mol h^{-1} g^{-1}$  with eosin Y as the photosensitizer and triethanolamine (TEOA) as the electron donor, driven by visible light. The rate has been enhanced fivefold than that of pristine MOF and 23-folds than that of U6N-NiO (10 wt% NiO) without the photosensitizer. It is demonstrated that high efficiency comes from both photoexcited eosin Y and organic ligand. The efficient photogenerated electron-hole pair separation stems from the cascaded band structure where electrons transfer to a more negative CB of NiO with a high concentration of electrons along with the excellent dispersion of NiO NPs on the MOF surface. Zhang et al. prepared the core-shell material (MIL-125- $NH_2$ @TiO<sub>2</sub>) by corroding MOF from outer to inner.<sup>[67]</sup> A great deal of linker defects and oxygen vacancies was created to accelerate mass/charge transfer and offer more active sites by the pyrolysis method. As a result, compared with pristine MOF,

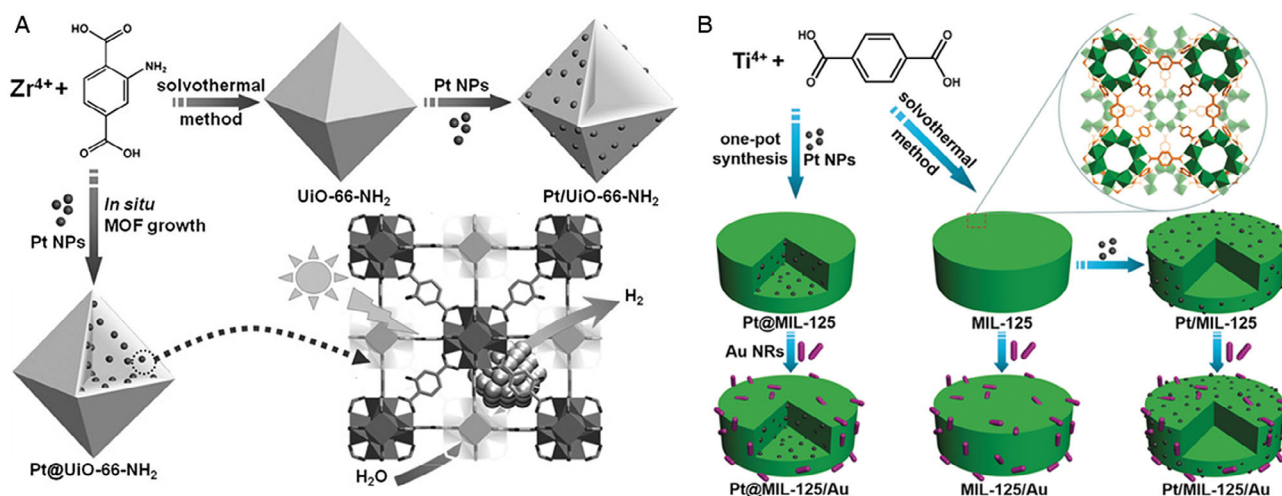


**Figure 7.** A) Schematic illustration for the synthesis of Pt@UiO-66- $NH_2$  and Pt/UiO-66- $NH_2$ , with the photocatalytic HER process over Pt@UiO-66- $NH_2$  being highlighted. Reproduced with permission.<sup>[63]</sup> Copyright 2016, Wiley-VCH GmbH. B) Schematic illustration showing the synthesis of Pt@MIL-125/Au and the corresponding Pt/MIL-125/Au and MIL-125/Au analogues. Reproduced with permission.<sup>[50]</sup> Copyright 2018, Wiley-VCH GmbH.



70-fold enhancement was caused by MIL-125-NH<sub>2</sub>@TiO<sub>2</sub> core-shell material for HER.

**Combining with Metal Sulfides:** CdS is a common semiconductor photocatalyst and is widely used for photocatalytic water splitting for H<sub>2</sub> generation due to more negative flat-band potential than reduction potential of H<sup>+</sup>. However, the fast recombination of photogenerated electrons and holes leads to low quantum efficiency of solar light absorption. Also, the photocatalytic stability of CdS semiconductor is poor. Therefore, it is necessary to combine or deposit with other materials to give full play to their good properties. CdS NPs were first embedded on MOFs by Wang and coworkers with greatly enhanced photocatalytic efficiency. Due to the large specific surface area of MIL-101(Cr) and good dispersion of CdS NPs, the more active sites and photoexcited locations were caused.<sup>[68]</sup> After that, CdS NPs also could be grown on UiO-66<sup>[69]</sup> and MIL-125<sup>[70]</sup> using hydrothermal method in situ. In addition, other sulfides loading MOFs also showed excellent photocatalytic performance for HER, such as Cd<sub>0.2</sub>Zn<sub>0.8</sub>S@UiO-66-NH<sub>2</sub><sup>[71]</sup> and ZnIn<sub>2</sub>S<sub>4</sub>@MIL-125-NH<sub>2</sub>.<sup>[72]</sup>

**Doping with Metal Phosphides:** Given the unique structural and electronic properties of transition-metal phosphides (TMPs) (e.g. Co<sub>2</sub>P, Ni<sub>2</sub>P, etc.), they have been considered as promising noble-metal-alternative cocatalysts for photocatalytic HER. However, the large size, small interface contact with semiconductors, and easy agglomeration are still challenging issues. In recent years, Sun and coworkers first time reported the fabrication of the MOF (UiO-66-NH<sub>2</sub>) doped with monodispersed, small-sized, and noble metal-free TMPs for photocatalytic H<sub>2</sub> production.<sup>[73]</sup> TMPs@MOF composites exhibited significantly enhanced H<sub>2</sub> production rates. Thermodynamic and kinetic studies demonstrate that the doping of TMPs can greatly accelerate the linker-to-cluster charge transfer, which promotes charge separation and reduces the activation energy of H<sub>2</sub> production.

**Introducing with Carbon-Containing Materials:** In recent years, carbon-containing materials, such as g-C<sub>3</sub>N<sub>4</sub> and reduced graphene oxide (RGO), are gradually introduced into MOFs due to their good photoelectrochemical properties.<sup>[74]</sup> g-C<sub>3</sub>N<sub>4</sub> is a planar pi-conjugated nonmetallic semiconductor with medium bandgap. Introducing g-C<sub>3</sub>N<sub>4</sub> into MOFs can effectively promote the separation and transmission of photogenerated electrons and holes, prolong the lifetime of electrons and holes, and improve the photocatalytic performance. Recently, Zhou et al. synthesized the composite catalyst of CFB/MIL-125-NH<sub>2</sub> (CFBM) by covalent bonds, utilizing g-C<sub>3</sub>N<sub>4</sub> functionalized by benzoic acid (CFB) and MIL-125-NH<sub>2</sub>.<sup>[70]</sup> As a result, CFBM exhibited a high H<sub>2</sub> generation rate of 1.123 mmol h<sup>-1</sup> g<sup>-1</sup>, which caused an enhancement of about 6-fold than that of the pristine MOF. Graphene is composed of a 2D carbon atom layer, which has flexible structure and good optical and electrical properties. Cao and coworkers introduced the RGO into CdS@NU-1000 to prepare the composite of CdS@NU-1000/RGO toward photocatalytic water splitting for HER.<sup>[75]</sup>

**Hybridizing with Covalent Organic Frameworks (COFs):** Porous COFs have attracted attention in photocatalytic water splitting for H<sub>2</sub> generation attributed to the high stability, large surface areas, and porosity.<sup>[76]</sup> Integrating the COF into MOFs can combine the advantages of both and design highly stable and porous hybrid materials with light absorption locations and active sites.

Recently, Lan and coworkers designed and prepared the MOF/COF complex for HER under visible light.<sup>[77]</sup> UiO-66-NH<sub>2</sub> was anchored onto TpPa-1-COF by covalent bonds. UiO-66-NH<sub>2</sub>/TpPa-1-COF (4:6) exhibited outstanding photocatalytic activity of HER (23.41 mmol g<sup>-1</sup> h<sup>-1</sup>), which is 20-folds higher than that of pristine COF (Figure 8).

### 2.3.2. Photocatalytic OER

Both OER and HER are half reactions in water splitting. In general, it is sluggish for OER in kinetic, due to the high overpotential, high energy barrier, and the rate-determining step involving multiple-electron participation.<sup>[54b]</sup> Therefore, compared with HER in photocatalytic water splitting, the development of OER is relatively limited, which is also more restricted than hydrogen production in the field of MOFs.<sup>[21d]</sup>

Three iridium-based MOF photocatalysts were prepared via incorporating three iridium-based complexes into UiO-67, respectively, and were used for photocatalytic OER by Lin and coworkers.<sup>[34]</sup> Compared with pristine MOF and homogeneous catalyst, the three modified MOF photocatalysts have high stability and catalytic activity, wherein cerium ammonium nitrate served as an oxidant. Subsequently, in 2012, they synthesized two stable UiO-MOFs with elongated dicarboxylate ligands based on the Ir complexes.<sup>[78]</sup> The detailed kinetic investigations of Ce<sup>4+</sup>-driven and MOF-catalyzed OER were conducted by diffuse-reflectance UV-vis absorption, luminescence, X-ray photoelectron, and IR spectra. Moreover, they established the diffusion reaction model for MOF-catalyzed OER.

In addition to the incorporation of noble metal complexes into MOF, non-noble metal complexes have also been introduced into MOF for OER. Das and coworkers successfully encapsulated ([Mn(tpy)]<sub>2</sub>(μ-O)<sub>2</sub>)<sup>3+</sup> (tpy = 2,2':6',2''-terpyridine), denoted by MnTD, into the MIL-101(Cr) cage for OER.<sup>[79]</sup> Such a simple method greatly improved the sustainability of catalysis with minimized degradation of side reactions. In MIL-101(Cr), the cage is too small to migrate to the adjacent cage for the catalyst, whereas the cavity itself is enough to provide catalytic environment for active sites. Therefore, the catalyst molecule can be detained in the cage. In the cage, its function is similar to that of a homogeneous system, but it can be separated from the accumulation of catalysts. Compared with homogeneous catalyst, this cage encapsulation catalyst caused 20 times enhancement of TON in OER with good sustainability.

Su and coworkers used three Fe-based MOFs, MIL-101(Fe), MIL-88B(Fe), and MIL-53(Fe), as photocatalysts for OER.<sup>[80]</sup> Among them, MIL-101(Fe) showed high photocatalytic activity for OER when Na<sub>2</sub>S<sub>2</sub>O<sub>8</sub> served as the electron acceptor and [Ru(bpy)<sub>3</sub>]<sup>2+</sup> acted as the sensitizer under visible light. [Ru(bpy)<sub>3</sub>]<sup>2+</sup> was transformed to [Ru(bpy)<sub>3</sub>]<sup>2+\*</sup> under photoexcitation and the photogenerated electrons transferred to S<sub>2</sub>O<sub>8</sub><sup>2-</sup>, generating SO<sub>4</sub><sup>2-</sup> and SO<sub>4</sub><sup>•-</sup>. As the oxidation potential of SO<sub>4</sub><sup>•-</sup> is higher than that of [Ru(bpy)<sub>3</sub>]<sup>2+</sup> ([E<sup>0</sup>(SO<sub>4</sub><sup>•-</sup>/SO<sub>4</sub><sup>2-</sup>) = +2.40 V vs Ag/AgCl], [E<sup>0</sup>([Ru(bpy)<sub>3</sub>]<sup>2+</sup>/[Ru(bpy)<sub>3</sub>]<sup>3+</sup>) = +1.12 V vs Ag/AgCl]), which is a strong oxidant and can convert [Ru(bpy)<sub>3</sub>]<sup>2+</sup> into [Ru(bpy)<sub>3</sub>]<sup>3+</sup>. The catalyst provided the electrons for accumulated [Ru(bpy)<sub>3</sub>]<sup>3+</sup>. Finally, the generated holes of the catalyst were consumed by water, which was oxidized to generate O<sub>2</sub>.

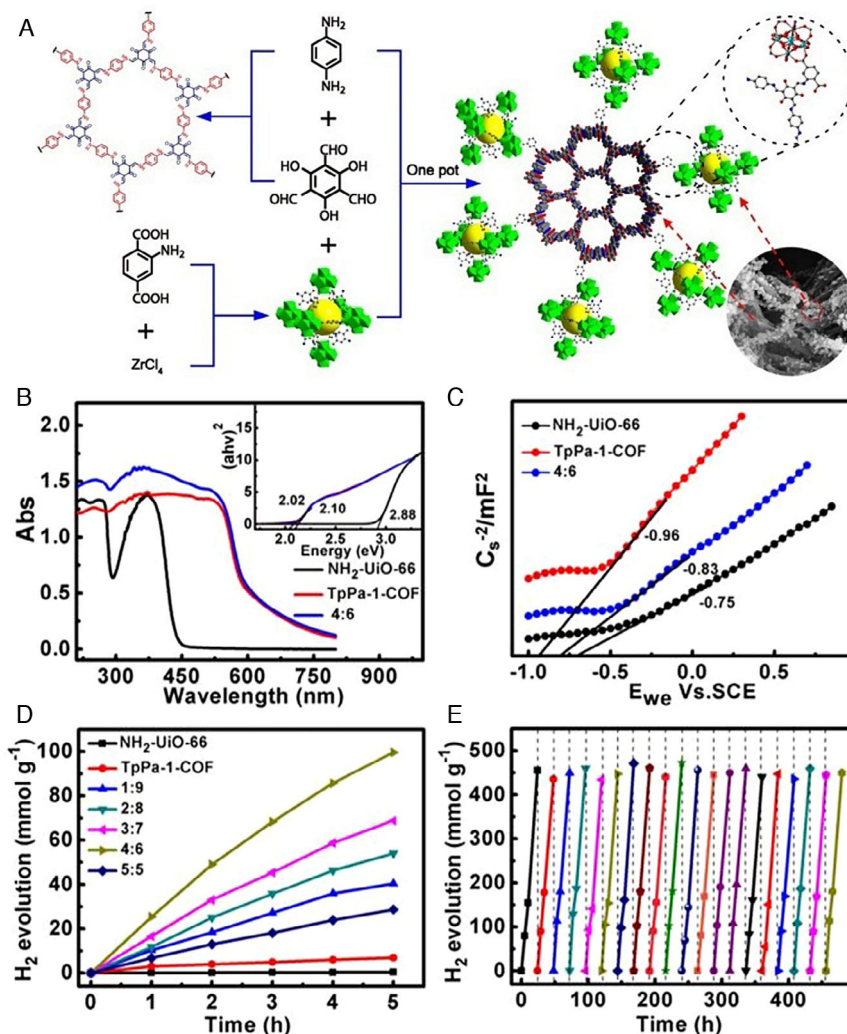


**Figure 8.** A) Schematic illustration of the synthesis of UiO-66-NH<sub>2</sub>/TpPa-1-COF hybrid material. B) DRS and bandgap energies (inset) and C) Mott-Schottky plots for UiO-66-NH<sub>2</sub>, TpPa-1-COF, and UiO-66-NH<sub>2</sub>/TpPa-1-COF (4:6). D) The photocatalytic HER activities. E) The photocatalytic stability of UiO-66-NH<sub>2</sub>/TpPa-1-COF (4:6). Reproduced with permission.<sup>[77]</sup> Copyright (2018) Wiley-VCH GmbH.

### 2.3.3. Photocatalytic Overall Water Splitting

Photocatalytic water splitting is a carbon-free and sustainable alternative to fossil fuels. Through the combination of HER and OER, overall water splitting aims to light fuel conversion. An et al. developed Al-based MOF (Al-ATA-Ni) for photocatalytic overall water splitting.<sup>[81]</sup> They selected amino-modified ligand to construct the MOF and aimed to incorporate Ni<sup>2+</sup> into the pore via the coordination of amino groups and Ni<sup>2+</sup> ions (Figure 9A,B). Compared with the O<sub>2</sub> evolution rate of 16.5 mmol h<sup>-1</sup> for Al-ATA MOF without Ni<sup>2+</sup> incorporation, the Al-ATA-Ni MOF exhibited a much higher O<sub>2</sub> evolution rate of 155 mmol h<sup>-1</sup>. The Al-ATA-Ni MOF also showed excellent performance for HER at a rate of 36.0 mmol h<sup>-1</sup>, whereas the Al-ATA MOF was silent for HER. The attenuation of light absorption intensity between 450 and 650 nm of the resulting MOF may be due to the *d-d* transition of the Ni<sup>2+</sup> ions in an octahedral environment (Figure 9B). However, it is demonstrated that

Al-ATA-Ni MOF is more conducive to enhancing electron-hole separation via the PL and UV-vis diffuse reflectance spectra.

Li and coworkers used the Cd-TBAPy MOF as the bifunctional catalyst for photoreduction and oxidation of water (Figure 9C).<sup>[82]</sup> Cd-TBAPy MOF showed a wide adsorption region from UV to visible light attributed to the organic ligand. It is demonstrated that the Cd-TBAPy is an n-type semiconductor via the analysis of Mott-Schottky measurement. The combination of Mott-Schottky measurement and UV-vis analysis, the bandgap, CB, and VB were recorded at 2.15, -0.05, and 2.10 eV. After loading Pt cocatalyst, the H<sub>2</sub> generation rate is about 4.3 μmol h<sup>-1</sup> by Cd-TBAPy catalyst. After loading CoPi cocatalyst, Cd-TBAPy exhibited high oxygen evolution rate of 81.7 μmol h<sup>-1</sup> and high apparent quantum efficiency of 5.6% at 420 nm (Figure 9D,E). Such performance is attributed to three main respects: 1) the  $\pi$ -conjugated 2D layered structure for transportation of photoinduced carriers; 2) the appropriate band edge positions for redox reaction; and 3) the loading of suitable cocatalysts.

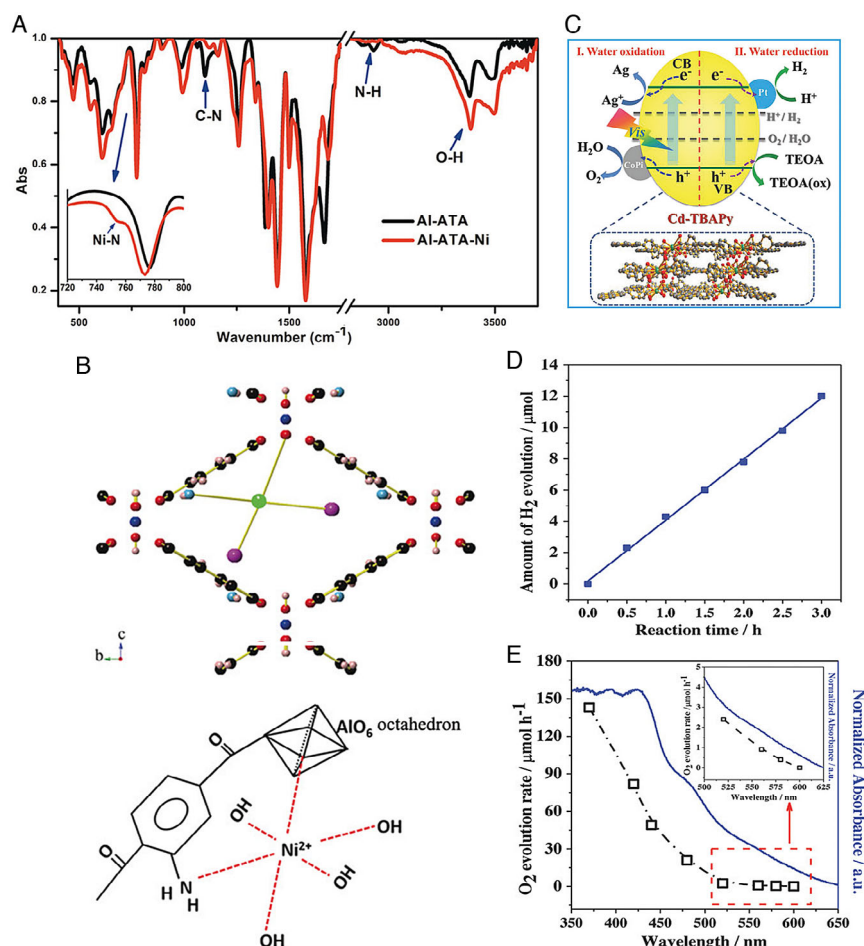


**Figure 9.** A) FTIR spectra of the as-prepared Al-ATA and Al-ATA-Ni MOFs. B) Possible coordination of Ni with Al-ATA MOF; blue: Al, green: Ni, red: O, light-blue: N, black: C, purple: OH. Reproduced with permission.<sup>[81]</sup> Copyright 2017, Wiley-VCH GmbH. C) Photoreduction and oxidation of water. D) The time course of photocatalytic H<sub>2</sub> evolution on 3.5 wt% Pt/Cd-TBAPy. E) Dependence of the O<sub>2</sub> evolution rate on the cutoff wavelength of incident light (black line) and the UV-vis DRS of 0.4 wt% CoPi-loaded Cd-TBAPy (blue line). Reproduced with permission.<sup>[82]</sup> Copyright 2018, Wiley-VCH GmbH.

Recently, Zhang et al. designed a Pt@NH<sub>2</sub>-UiO-66@MnO<sub>x</sub> (PUM) heterostructured photocatalyst for water splitting.<sup>[83]</sup> Pt and MnO<sub>x</sub> serve as cocatalysts, which promote the trap of electrons and collect holes. The electrons and holes flow inward and outward of the MOF, accumulating on the corresponding cocatalysts, and conduct redox reactions separately. The spatially separated cocatalysts also accelerate the kinetics of surface oxidation and reduction reactions simultaneously, which improve water-splitting efficiency.

## 2.4. MOFs for Photocatalytic CO<sub>2</sub>RR

### 2.4.1. Ligand Candidate

MOFs have exhibited great potential for photoreduction of CO<sub>2</sub> due to its modifiable ligands, high CO<sub>2</sub> adsorption, and clear metal active sites.<sup>[21d,41b]</sup> By modifying the ligand with -NH<sub>2</sub>, -NHX, or directly using photosensitive molecules as ligands to construct MOF, the absorbance range of MOF can be extended and the absorbance performance can be improved. The porous

structure of MOF is usually tunable, which has a certain adsorption capacity for CO<sub>2</sub>. MOFs with well-defined structures are more conducive to clarifying the catalytic active sites and further studying the catalytic mechanism. The summary of MOF catalysts for photocatalytic CO<sub>2</sub>RR is shown in Table 1.

In view of the facile availability, unique connection angle mode, and a wide range of functional groups of isophthalic acid (IPA), Wang and coworkers first reported Ti-IPA MOF (MIP-208) that combines the as-prepared Ti<sub>8</sub> oxoclusters and in situ acetylation of the 5-NH<sub>2</sub>-IPA linker.<sup>[84]</sup> MIP-208 was utilized as a cocatalyst to participate in photoreduction of CO<sub>2</sub> cooperating with ruthenium oxide, resulting in easily capturing and reducing of CO<sub>2</sub>. It will open up a new path in photoreduction of CO<sub>2</sub> by emerging functionalized ligands, different active metals, and photosensitive compounds into MOFs. Cheng and coworkers focused on the facet regulation based on NH<sub>2</sub>-MIL-125(Ti) for improving the photocatalytic activity.<sup>[85]</sup> The different exposed facets of NH<sub>2</sub>-MIL-125(Ti) ({001}, {111}, and coexposed {001} and {111} facets) were successfully prepared with various morphologies. The {111} facets exhibit a large specific surface area,



**Table 1.** MOF catalysts for photocatalytic CO<sub>2</sub>RR.

MOF photocatalyst	Main product	Illumination range	Catalytic activity	References
UiO-66-NH <sub>2</sub>	HCOO <sup>-</sup>	Visible	13.2 μmol	[287]
NH <sub>2</sub> -UiO-66(Zr/Ti)-120-16	HCOO <sup>-</sup>	Visible	3.4 mmol mol <sup>-1</sup>	[43]
NH <sub>2</sub> -UiO-66(Zr)	HCOO <sup>-</sup>	Visible	5.8 mmol mol <sup>-1</sup>	[43]
MIL-125	HCOO <sup>-</sup>	UV	4.28 μmol g <sup>-1</sup> h <sup>-1</sup>	[28]
MIL-125-NH <sub>2</sub>	HCOO <sup>-</sup>	Visible	16.28 μmol g <sup>-1</sup> h <sup>-1</sup>	[28]
MIL-101(Fe)	HCOO <sup>-</sup>	Visible	147.5 μmol g <sup>-1</sup> h <sup>-1</sup>	[41c]
NH <sub>2</sub> -MIL-101(Fe)	HCOO <sup>-</sup>	Visible	445 μmol g <sup>-1</sup> h <sup>-1</sup>	[41c]
MIL-53(Fe)	HCOO <sup>-</sup>	Visible	74.25 μmol g <sup>-1</sup> h <sup>-1</sup>	[41c]
NH <sub>2</sub> -MIL-53(Fe)	HCOO <sup>-</sup>	Visible	116.25 μmol g <sup>-1</sup> h <sup>-1</sup>	[41c]
MIL-88(Fe)	HCOO <sup>-</sup>	Visible	22.5 μmol g <sup>-1</sup> h <sup>-1</sup>	[41c]
NH <sub>2</sub> -MIL-88(Fe)	HCOO <sup>-</sup>	Visible	75 μmol g <sup>-1</sup> h <sup>-1</sup>	[41c]
PCN-222	HCOO <sup>-</sup>	Visible	60 μmol g <sup>-1</sup> h <sup>-1</sup>	[39]
MOF-525	CO	Visible	64.02 μmol g <sup>-1</sup> h <sup>-1</sup>	[47]
	CH <sub>4</sub>	Visible	6.2 μmol g <sup>-1</sup> h <sup>-1</sup>	[47]
MOF-525-Zn	CO	Visible	111.7 μmol g <sup>-1</sup> h <sup>-1</sup>	[47]
	CH <sub>4</sub>	Visible	11.63 μmol g <sup>-1</sup> h <sup>-1</sup>	[47]
MOF-525-Co	CO	Visible	200.6 μmol g <sup>-1</sup> h <sup>-1</sup>	[47]
	CH <sub>4</sub>	Visible	36.76 μmol g <sup>-1</sup> h <sup>-1</sup>	[47]
ZrPP-1-Co	CO	Visible	210 μmol g <sup>-1</sup>	[38]
	CH <sub>4</sub>	Visible	7.5 μmol g <sup>-1</sup>	[38]
ZrPP-1-Fe	CO	Visible	61.8 μmol g <sup>-1</sup>	[38]
	CH <sub>4</sub>	Visible	-	[38]
ZrPP-1-Cu	CO	Visible	40.4 μmol g <sup>-1</sup>	[38]
	CH <sub>4</sub>	Visible	-	[38]
NNU-13	CH <sub>4</sub>	Visible	704 μmol g <sup>-1</sup>	[87]
	CO	Visible	25 μmol g <sup>-1</sup>	[87]
NNU-14	CH <sub>4</sub>	Visible	311 μmol g <sup>-1</sup>	[87]
	CO	Visible	12 μmol g <sup>-1</sup>	[87]
NNU-28	HCOO <sup>-</sup>	Visible	52.8 12 μmol g <sup>-1</sup> h <sup>-1</sup>	[288]
Co-ZIF-9	CO	Visible	41.8 μmol	[289]
Al-PMOF	CH <sub>3</sub> OH	Visible	37.5 μmol g <sup>-1</sup> h <sup>-1</sup>	[290]
Al PMOF embedded Cu <sup>2+</sup>	CH <sub>3</sub> OH	Visible	262.6 μmol g <sup>-1</sup> h <sup>-1</sup>	[290]
Eu-Ru(phen) <sub>3</sub> -MOF	HCOO <sup>-</sup>	Visible	321.9 μmol mmol <sup>-1</sup> h <sup>-1</sup>	[52]
UiO-66-Cr <sup>III</sup> CAT	HCOO <sup>-</sup>	Visible	1724.3 ± 88 μmol g <sup>-1</sup> h <sup>-1</sup>	[291]
UiO-66-Ga <sup>III</sup> CAT	HCOO <sup>-</sup>	Visible	959.3 ± 84 μmol g <sup>-1</sup> h <sup>-1</sup>	[291]
UiO-67-Re(5,5'-dcbpy)(CO) <sub>3</sub> Cl	CO	Visible	TON = 5	[34]
Y[Ir(ppy) <sub>2</sub> (4,4'-dcbpy)] <sub>2</sub> [OH]	HCOO <sup>-</sup>	Visible	118.8 μmol g <sup>-1</sup> h <sup>-1</sup>	[292]
(Cd <sub>3</sub> [Ru(5,5'-dcbpy) <sub>3</sub> ] <sub>2</sub> (Me <sub>2</sub> NH <sub>2</sub> )) <sub>n</sub>	HCOO <sup>-</sup>	Visible	67.5 μmol g <sup>-1</sup> h <sup>-1</sup>	[293]
(Cd[Ru(bpy)(4,4'-dcbpy) <sub>2</sub> ] <sub>3</sub> H <sub>2</sub> O) <sub>n</sub>	HCOO <sup>-</sup>	Visible	67.5 μmol g <sup>-1</sup> h <sup>-1</sup>	[293]
UiO-67-Cp*Rh(5,5'-dcbpy)Cl <sub>2</sub> (10%)	HCOO <sup>-</sup>	Visible	464 μmol g <sup>-1</sup> h <sup>-1</sup>	[294]
MOF-253-Ru(5,5'-dcbpy)(CO) <sub>2</sub> Cl <sub>2</sub>	CO	Visible	46.5 μmol g <sup>-1</sup> h <sup>-1</sup>	[295]
	HCOO <sup>-</sup>	Visible	16.8 μmol g <sup>-1</sup> h <sup>-1</sup>	[295]
Ag C Re <sub>3</sub> -MOF-16 nm	CO	Visible	TON = 2.8	[54a]
Pt/MIL-125-NH <sub>2</sub>	HCOO <sup>-</sup>	Visible	32.4 μmol g <sup>-1</sup> h <sup>-1</sup>	[296]
Au/MIL-125-NH <sub>2</sub>	HCOO <sup>-</sup>	Visible	16.3 μmol g <sup>-1</sup> h <sup>-1</sup>	[296]
Cu <sub>3</sub> (BTC) <sub>2</sub> @TiO <sub>2</sub>	CH <sub>4</sub>	UV	2.64 μmol g <sup>-1</sup> h <sup>-1</sup>	[297]

**Table 1.** Continued.

MOF photocatalyst	Main product	Illumination range	Catalytic activity	References
TiO <sub>2</sub> -Co-ZIF-9	CO	UV-visible	8.8 $\mu\text{mol g}^{-1} \text{h}^{-1}$	[298]
	CH <sub>4</sub>	UV-visible	2.0 $\mu\text{mol g}^{-1} \text{h}^{-1}$	
CdS- Co-ZIF-9	CO	Visible	TON = 12.6	[57]
CdS- Co-MOF-74	CO	Visible	TON = 9.9	[57]
CdS- Mn-MOF-74	CO	Visible	TON = 0.3	
CdS-Zn-ZIF-8	CO	Visible	TON = 0.2	[57]
CdS-UiO-66-NH <sub>2</sub>	CO	Visible	TON = 0.1	[57]
Zn <sub>2</sub> GeO <sub>4</sub> -Zn-ZIF-8	CH <sub>3</sub> OH	-	0.22 $\mu\text{mol g}^{-1} \text{h}^{-1}$	[299]
Cd <sub>0.2</sub> Zn <sub>0.8</sub> S-UiO-66-NH <sub>2</sub> (20%)	CH <sub>3</sub> OH	Visible	6.8 $\mu\text{mol g}^{-1} \text{h}^{-1}$	[300]
g-C <sub>3</sub> N <sub>4</sub> -Co-ZIF-9	CO	Visible	495 $\mu\text{mol g}^{-1} \text{h}^{-1}$	[301]
CNNS-UiO-66(Zr)	CO	Visible	2.9 $\mu\text{mol g}^{-1} \text{h}^{-1}$	[59]

which provide a superior CO<sub>2</sub> uptake and more active sites for CO<sub>2</sub> reduction.

Introducing photosensitive molecules into MOFs for photocatalytic CO<sub>2</sub>RR can also improve the light absorption range and intensity and promote charge separation.<sup>[52]</sup> As we all know, Re<sup>I</sup>(CO)<sub>3</sub>(bpy)X complexes were good photosensitizers and were widely used in photoreduction of CO<sub>2</sub>. Instead of bpy ligand, fac-ReBr(CO)<sub>3</sub>(4,4'-dcbpy) (dcbpy = 2-phenylpyridine-5,40-dicarboxylic acid) was successfully entrapped into the cages of MIL-101-NH<sub>2</sub>(Al) for CO<sub>2</sub> conversion under visible light, which is a sensible strategy designed by Stanley's group for the integration of molecular photosensitizers into MOF.<sup>[86]</sup> Some of the works have focused on photosensitized ligands such as porphyrins and their derivatives to construct MOF toward photoreduction of CO<sub>2</sub>.<sup>[38,39,47]</sup> Jiang and coworkers utilized PCN-222 as a photocatalyst for converting CO<sub>2</sub> into HCOOH (60  $\mu\text{mol g}^{-1} \text{h}^{-1}$ ) with 100% selectivity under visible light.<sup>[39]</sup> Compared with porphyrin ligand, detrimental electron-hole recombination was greatly inhibited in PCN-222 due to the deep electron trap state, which demonstrated the relationship between the electron-hole separation efficiency and the photocatalytic activity. In addition, ZrPP-*n*-M (*n* = 1, 2, M = H<sub>2</sub>, Zn, Cu, Fe, Co) was successfully synthesized and further utilized in CO<sub>2</sub> photoreduction, and ZrPP-1-Co exhibited a much higher CO generation rate of 14  $\mu\text{mol g}^{-1} \text{h}^{-1}$  than other ZrPP-*n*-M MOFs.<sup>[38]</sup> Similarly, atomic dispersion of active sites (Co or Zn) in MOF-525 and the Co-MOF-525 exhibited relatively good performance for CO<sub>2</sub> photoreduction.<sup>[47]</sup>

#### 2.4.2. Metal/Metal Oxygen Clusters

As the secondary building unit, metal/metal oxygen clusters are not only important components of MOFs, but also play an indispensable role in the elaboration of the photocatalysis mechanism. Ti-O, Zr-O, Fe-O, and polyoxometalates (POMs) are common metal oxygen cluster-based MOFs for the photoreduction of CO<sub>2</sub>. MIL-125(Ti) series are the main representatives of the Ti-O clusters. The Zr-O clusters mainly contain UiO-66 series and porphyrin-based Zr-MOF. The Fe-O clusters include MIL-101(Fe), MIL-88(Fe), and MIL-53(Fe) series. POMs mainly

concern the reductive Zn-*e*-Keggin-based MOFs. In addition, other non-noble metals also exhibited relatively effective photocatalysts, such as Co-based MOFs. In the MIL-125-NH<sub>2</sub> photoreduction system, it was important to detect the valence changes in the reaction process by EPR experiments and propose a reasonable photocatalytic mechanism.<sup>[28]</sup> Under the irradiation of visible light, the excited photoelectrons were transferred from the organic ligand to the Ti-O cluster, whereas the electron holes were consumed by sacrificial agents (TEOA). Ti<sup>4+</sup> was reduced to Ti<sup>3+</sup>, and CO<sub>2</sub> was reduced to HCOOH on Ti<sup>3+</sup>. Li and coworkers utilized the post-PSE method to synthesize Ti-substituted NH<sub>2</sub>-UiO-66(Zr/Ti) for enhancing photocatalytic performance in CO<sub>2</sub> reduction (CO<sub>2</sub> to HCOOH).<sup>[49]</sup> DFT calculations and ESR results showed that electrons tend to transfer to Ti<sup>4+</sup> than that to Zr<sup>4+</sup> when the part of Zr<sup>4+</sup> was replaced by Ti<sup>4+</sup>. Ti<sup>4+</sup> was reduced to Ti<sup>3+</sup> in the excited (Ti<sup>3+</sup>/Zr<sup>4+</sup>)-O cluster; thus, Ti<sup>3+</sup> can further provide electrons to Zr<sup>4+</sup> to form Ti<sup>4+</sup>-O-Zr<sup>3+</sup>. The electron transfer mechanism is similar to previously reported Fe-doped SrTiO<sub>3</sub> and zeolite-anchored bimetallic assemblies. Such incorporation of the second metal is conducive to promoting the interfacial charge transfer from organic ligand to clusters, which contributes to photocatalytic activity. Most of the excitation and transfer of electrons in MOFs correspond to the LMCT mechanism, but the mechanism of synergistic light response between ligands and metal clusters is observed in the MOFs constructed by Fe-O clusters, such as NH<sub>2</sub>-MIL-53(Fe), NH<sub>2</sub>-MIL-88B(Fe), and NH<sub>2</sub>-MIL-101(Fe). Fe-O clusters can be directly excited by visible light, leading to the electron being induced from O<sup>2-</sup> to Fe<sup>3+</sup>. Besides the direct excitation, Fe center accepted the electron from the excited ligand modified by -NH<sub>2</sub>. Thus, these Fe-based MOFs with amine modification can significantly enhance their catalytic performance for CO<sub>2</sub> photoreduction (CO<sub>2</sub> to HCOOH) due to the synergistic effect of dual excitation routes.

MOFs constructed by these high-valent metal oxygen clusters were widely used for the photoreduction of CO<sub>2</sub>. The main products are two-electron products, such as HCOOH or CO. Recently, Lan and coworkers found that incorporating reductive POM (Zn-*e*-Keggin) into porphyrin-based MOF can boost eight-electron products (CH<sub>4</sub>) in photoreduction of CO<sub>2</sub> (Figure 10).<sup>[87]</sup> Given that

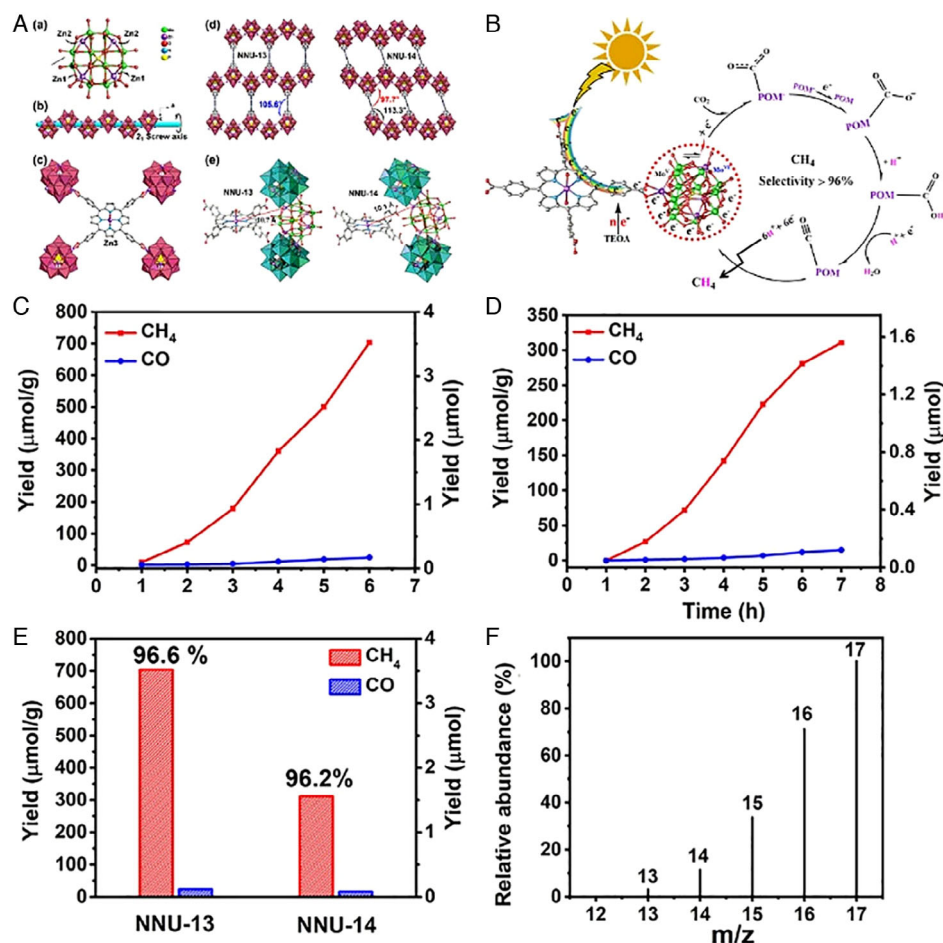


**Figure 10.** A) Ball-and-stick view of NNU-13 and NNU-14 crystal structures. (a) Four Zn atoms tetrahedron-capped Zn- $\epsilon$ -Keggin cluster; (b) a wavy POM chain was formed by Zn- $\epsilon$ -Keggin units, under the symmetry operation of  $2_1$  screw axis; (c) four carboxyl groups of every Zn-TCPP ligand concurrently in contact with four different Zn- $\epsilon$ -Keggin clusters from four POM chains; the dihedral angles between POM chain and Zn-TCPP metalloligand in d) NNU-13 and NNU-14 (coordinated H<sub>2</sub>O molecules have been eliminated for clarity); the shortest Zn-Zn distances in e) NNU-13 and NNU-14. Color code: Mo, green; Zn, purple; O, red; N, blue; P, yellow; and C, grey. Hydrogen atoms have been eliminated for clarity. B) Proposed mechanism for photocatalytic CO<sub>2</sub>RR over POMCFs under visible light irradiation. Performance for photoreduction CO<sub>2</sub> into CH<sub>4</sub>. Amounts of CH<sub>4</sub> and CO produced as a function of the visible illumination time over C) NNU-13 and D) NNU-14. E) Total product yield and selectivity of gas products in photoreduction of CO<sub>2</sub>. F) The mass spectra of <sup>13</sup>CH<sub>4</sub> recorded under a <sup>13</sup>CO<sub>2</sub> atmosphere. Reproduced with permission.<sup>[87]</sup> Copyright 2019, Oxford University Press.

eight Mo<sup>V</sup> atoms can theoretically provide eight electrons to accomplish the multielectron transformation process of CO<sub>2</sub> into CH<sub>4</sub>. NNU-13 and NNU-14 were synthesized and used for CO<sub>2</sub> photoreduction with the high selectivity of CH<sub>4</sub> over 96%. DFT calculations revealed that the photoexcited electrons more easily transfer from 4,4',4'',4'''-(porphyrin-5,10,15,20-tetrayl)tetrabenzoate (TCPP) linker to Zn- $\epsilon$ -Keggin unit. Such a sensible approach, assembling strong reductive clusters into photosensitive architecture, could inspire to develop more reductive MOF or other materials for selective photoreduction of CO<sub>2</sub> into CH<sub>4</sub> or other high-valued hydrocarbons.

Wang et al. demonstrated that the active metal center can cooperate with  $\mu$ -OH<sup>-</sup> of ligand to promote the CO<sub>2</sub> photoreduction.<sup>[88]</sup> At 1.0 atm, the MOFs with  $\mu$ -OH<sup>-</sup> ligands neighboring the open Co catalytic centers exhibited high CO selectivity (98.2%) and turnover frequency (TOF) (0.059 s<sup>-1</sup>). A combination of isotope tracing experiments and periodic DFT

calculations revealed that the  $\mu$ -OH<sup>-</sup> ligands act as the strong hydrogen-bonding donors to stabilize the initial Co-CO<sub>2</sub> adduct and serve as local proton sources to accelerate the C–O bond breaking.

## 2.5. MOFs for Photocatalytic Organic Transformation

Under light irradiation, photocatalysts can be photoexcited to generate electron–holes, which provide the platform for reduction (reacting with electrons) and oxidation (reacting with holes) of organic molecules, offering a new methodology for the synthesis of fine chemicals. Lin and coworkers developed two modified UiO-67 (MOF 5 and MOF 6) by incorporation of [Ir<sup>III</sup>(ppy)<sub>2</sub>(dcbpy)]Cl (H<sub>2</sub>L<sub>5</sub>) and [Ru<sup>II</sup>(bpy)<sub>2</sub>(dcbpy)]Cl<sub>2</sub> (H<sub>2</sub>L<sub>6</sub>).<sup>[34]</sup> The two MOFs served as photocatalysts toward Aza–Henry reactions with tetrahydroisquinoline as the amine substrate in CH<sub>3</sub>NO<sub>2</sub> solvent under visible light. The catalytic



conversion efficiency of the two MOF catalysts can reach up to 97% after 12 h, which is comparable with that of homogeneous catalysts. Moreover, the catalysts also exhibited excellent cyclic stability compared with homogenous catalysts. Then, they also found that MOF 6 exhibited excellent performance for photocatalytic aerobic amine coupling reactions and photocatalytic aerobic oxidation of thioanisole. The cyclic experiments revealed that there was no loss of activity and no deterioration of the MOF frameworks.

Chiral MOFs showed promise as heterogeneous asymmetric catalysts, as the chiral active sites can be immobilized into the porous MOF framework. The strategy was adopted by Wu et al.<sup>[89]</sup> The organocatalyst L- or D-pyrrolidin-2-ylimidazole (PYI) was incorporated into the frameworks as well as contains the triphenylamine photoredox group, denoted as Zn-PYI1 and Zn-PYI2, respectively. Catalytic activities of Zn-PYI1 and Zn-PYI2 toward light-driven asymmetric  $\alpha$ -alkylation of aliphatic aldehydes were evaluated. In these MOFs, triphenylamine was excited and induced the photogenerated electron transport, acting as an active intermediate for  $\alpha$ -alkylation (Figure 11A). Meanwhile, the chiral PYI served as the cooperative active sites of  $\alpha$ -alkylation, driving asymmetric catalysis with excellent stereoselectivity (Figure 11B). Such a collaborative strategy, integration of chiral active sites and photosensitive ligands into MOF frameworks, is essential for enantioselective photocatalysis. Another similar strategy was developed for heterogeneous asymmetric

photocatalysis by Tang and coworkers, establishing the tunable MOF frameworks by chiral photoredox ligands and various metal ions.<sup>[90]</sup> The resulting MOFs, S(R)-Ti-MOF, S(R)-Zn-MOF, and S(R)-Zr-MOF, exhibited efficient photocatalytic activity for  $\alpha$ -alkylation of aldehydes due to the synergistic effect of photoredox chiral ligand and metal ions (Figure 11C). Compared with pristine S(R)-HL, these MOFs showed enhancement for catalytic activity at 25 W illumination under visible light (Figure 11D). For Ti-MOF, LUMO and HOMO were located at Ti  $d$  orbital and organic linker, respectively, leading to an effective overlap. When the ligand was excited under visible light, the photogenerated electrons transferred from ligand to Ti<sup>4+</sup> species, giving rise to Ti<sup>3+</sup> as active site. Therefore, the Ti-MOF exhibited a superior photocatalytic active for  $\alpha$ -alkylation of aldehydes. For Zn-MOF, the weak adsorption of visible light led to much lower conversion than Ti-MOF. Binding energy of  $d$  orbital in Zr is too low to overlap with  $\pi^*$  orbital of ligand efficiently, resulting in relatively low transformation for the organic reaction.

MOFs were also applied for organic oxidation reaction. The photocatalytic activity of UiO-66-NH<sub>2</sub> was evaluated by oxidation of hexyl alcohol, cyclohexanol, cyclohexane, and benzyl alcohol.<sup>[91]</sup> Recently, Xiao et al. developed Cu@UiO-66 and Cu/Cu@UiO-66 for oxidation of aromatic alcohols under visible light.<sup>[92]</sup> Cu@UiO-66 was prepared by the encapsulation of Cu quantum dots (QDs) into UiO-66 cages via double-solvent

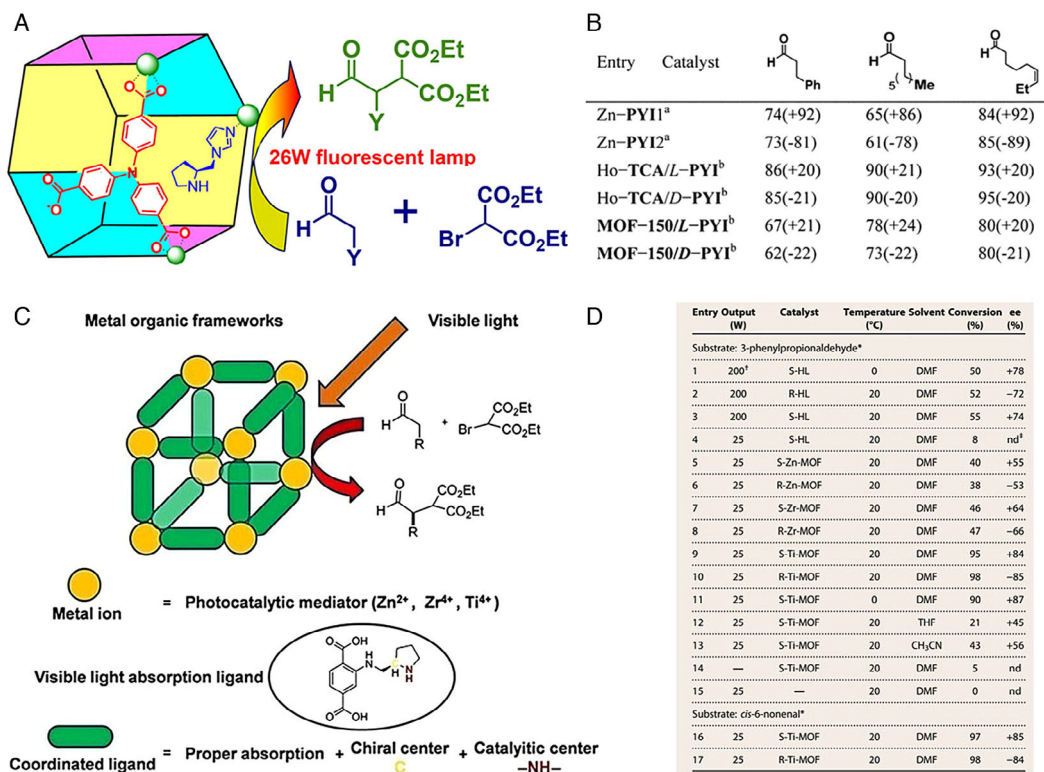


**Figure 11.** A) Chiral MOF to prompt the asymmetric  $\alpha$ -alkylation of aliphatic aldehydes in a heterogeneous manner. B) Conversions and ee values (in parentheses) of the photocatalytic  $\alpha$ -alkylation of aliphatic aldehydes. Reproduced with permission.<sup>[89]</sup> Copyright 2012, American Chemical Society. C) Basic illustration, ligand design, and synthesis of photocatalytic asymmetric  $\alpha$ -alkylation of aldehyde by MOFs that are constructed with chiral photoredox ligands and metal ions. D) Catalytic performance under different conditions. Reproduced with permission.<sup>[90]</sup> Copyright 2017 AAAS.

approach (DSA). The advanced double-solvent approach (ADSA) was adopted to synthesize Cu@UiO-66 by encapsulating the QDs and simultaneously load Cu NPs. 0.1%Cu/Cu@UiO-66 exhibited high photocatalytic activity for conversion of aromatic alcohols into aldehydes due to the cooperation of plasmonic effect and Schottky junction. The work on the oxidation of aromatic alcohols to aldehydes has also been reported by Jiang's group. They prepared Pt/PCN-224(M) (M = Zn, Ni, Co, Mn, 2H) composites by loading the Pt NCs to porphyrin-based MOFs, PCN-224(M).<sup>[93]</sup> Pt/PCN-224(M) exhibited excellent photocatalytic activity for oxidation of aromatic alcohols under O<sub>2</sub> atmosphere, thanks to the combination of singlet-oxygen production and photothermal effect. In addition, the hot electrons transferred from plasmonic Pt into MOF, reducing the electron density of Pt surface. The oxidation reaction can be modulated via competition between the plasmonic and Schottky junction. They also developed Pt/PCN-777 and Pt/MOF-808 as photocatalysts for selective benzylamine oxidation along with the generation of H<sub>2</sub> fuel.<sup>[94]</sup> Such coupled reactions showed great potential of combining H<sub>2</sub> evolution with organic transformation to produce high-valued chemicals. The similar work about oxidation of benzylamine was documented by Zhang and coworkers.<sup>[95]</sup> The bipyridyl-containing Cd-MOFs were used as photocatalysts toward oxidation of benzylamine and exhibited high selectivity for converting benzylamine into N-benzylbenzaldimine.

## 2.6. MOFs for Photocatalytic Contaminant Degradation

Photocatalysis is an efficient and alternative method for the degradation of contaminants by solar energy. MOFs have high porosity, tunable scale, and modulated semiconducting functions, which are good platforms for photocatalytic contaminant degradation. MOFs have been used for degradation of organic dyes, aromatic molecules, Cr(VI), and other contaminants. In photocatalytic degradation of organic dyes, the performance of photocatalysis is usually evaluated by the time of color change, because light-induced active substances attack weak organic bonds of dyes, making dyes colorless in this process.<sup>[96]</sup> Three common organic dyes were frequently reported to evaluate the MOF photocatalytic performance, including rhodamine family, methyl orange, and methyl blue. Roeyfaers' group utilized Fe(III)-based MOF toward the degradation of Rhodamine 6 G. It is demonstrated that Fe<sub>3</sub>-μ<sub>3</sub>-oxo clusters of MOFs are crucial for photocatalytic degradation of Rhodamine 6 G, which unveiled the prelude in the study of photocatalysis of Fe-based MOF.<sup>[42]</sup> Subsequently, MIL-53(Fe) served as a photocatalyst for photocatalytic degradation of Rhodamine B cooperating with H<sub>2</sub>O<sub>2</sub> under visible light.<sup>[97]</sup> In such a synergistic system, the degradation rate enhanced 4.3-folds than that of the system without H<sub>2</sub>O<sub>2</sub> due to the activation of H<sub>2</sub>O<sub>2</sub> by MIL-53(Fe). The results of transient photocurrent responses and hydroxyl radicals (·OH) detection revealed that H<sub>2</sub>O<sub>2</sub> can be activated by MIL-53(Fe) to generate ·OH undergoing two pathways. Under visible light irradiation, photogenerated electrons transferred from the excited state of MIL-53(Fe) to H<sub>2</sub>O<sub>2</sub>, giving rise to ·OH. Further, ·OH was used to degrade organic dyes.

Aromatic compounds are relatively stable, not easy to decompose, and have strong toxicity, which will cause serious environmental pollution and great harm to human body. In the participation of H<sub>2</sub>O<sub>2</sub>, benzene was oxidized to phenol under visible light irradiation using MIL-100(Fe) and MIL-68(Fe) as catalysts.<sup>[40]</sup> Fe–O clusters were photoexcited to generate photoelectrons that were captured by H<sub>2</sub>O<sub>2</sub> to form ·OH radicals via a Fenton-like reaction. The ·OH radicals attacked the benzene ring to generate the corresponding radicals and then formed phenol with the electron transfer and the proton release. Phenol has to be further degraded into less toxic products. In 2007, MOF-5 was used to photodegrade phenol and N,N,N',N'-tetramethyl-p-phenylenediamine to a less toxic compound under visible light.<sup>[98]</sup> Under photoexcitation, MOF-5 served as a semiconductor with a bandgap of 3.4 eV, and the charge separation lifetime is up to 30 μs. Interestingly, it was demonstrated that the bulky phenol substrate showed enhanced degradation rate compared with phenol. In addition, a dicarboxyl-functionalized Fe<sup>III</sup>–salen complex was incorporated into two heterometallic organic frameworks, denoted as [Zn<sub>2</sub>(Fe–L)<sub>2</sub>(μ<sub>2</sub>-O)(H<sub>2</sub>O)<sub>2</sub>·4DMF·4 H<sub>2</sub>O and [Cd<sub>2</sub>(Fe–L)<sub>2</sub>(μ<sub>2</sub>-O)(H<sub>2</sub>O)<sub>2</sub>·2DMF·H<sub>2</sub>O] (H<sub>4</sub>L = 1,2-cyclohexanediamino-N,N'-bis(3-methyl-5-carboxysalicylidene)), which was used for photocatalytic degradation of 2-chlorophenol under visible light.<sup>[99]</sup> When *tert*-butyl alcohol (TBA) as ·OH radical scavenger was added into the photocatalytic system, the degradation activities dramatically decreased about 44% for [Zn<sub>2</sub>(Fe–L)<sub>2</sub>(μ<sub>2</sub>-O)(H<sub>2</sub>O)<sub>2</sub>·4DMF·4 H<sub>2</sub>O and 19% for [Cd<sub>2</sub>(Fe–L)<sub>2</sub>(μ<sub>2</sub>-O)(H<sub>2</sub>O)<sub>2</sub>·2DMF·H<sub>2</sub>O]. The ·OH quenching results revealed that the degradation process of 2-chlorophenol predominantly involved the attacking by ·OH radicals when the aforementioned-resulting MOFs served as photocatalysts. The central [salen-Fe<sup>III</sup>] was coordinated by H<sub>2</sub>O to form [salen-Fe<sup>III</sup>·OH] species, which was attacked by hydrogen peroxide from the axial site of the Fe<sup>III</sup> center, giving rise to [salen-Fe<sup>III</sup>OOH] species. The [salen-Fe<sup>III</sup>OOH] was photoexcited, forming [salen-Fe<sup>III</sup>·OOH] \* under visible light irradiation. Subsequently, ·OH radical species and [salen-Fe(V)=O] emerged by breaking O–O bond. Finally, 2-chlorophenol was degraded by the generated ·OH radicals immediately.

Cr(VI) has strong migration ability and toxicity; thus, reducing it to Cr(III) is an environmentally friendly strategy to remove Cr(VI) pollutants from wastewater.<sup>[100]</sup> MIL-88B(Fe) served as photocatalyst toward the degradation of Cr(VI) into Cr(III) under visible light irradiation, which was recorded by monitoring the decolorization of diphenylcarbazide (DPC)-Cr(VI) complex solution through UV–vis absorption spectroscopy. UV–vis spectra revealed that Cr(VI) almost completely degraded by MIL-88B(Fe) after 45 min of irradiation.<sup>[43]</sup> It was demonstrated that the lower pH solution led to the better degradation activity. In addition, compared with MIL-88B(Fe), UiO-66-NH<sub>2</sub>, and MIL-125-NH<sub>2</sub>, NH<sub>2</sub>-MIL-88B(Fe) exhibited the best photocatalytic performance on the degradation of Cr(VI), which was attributed to two light-harvesting sections including both amino ligands and Fe–O clusters. Other MOFs also can be used for the photocatalytic reduction of Cr(VI) under visible light, such as MIL-68(In) and MIL-68(In)-NH<sub>2</sub>.<sup>[101]</sup> Mott–Schottky results and degradation results suggested that MIL-68(In)-NH<sub>2</sub> is a promising photocatalyst toward the reduction of Cr(VI) due to the relatively high CB.

## 2.7. MOF Derivatives for Photocatalysis

Although MOFs possess huge potential in photocatalysis due to their unique properties, the moisture sensitivity and instable coordination bond between metal clusters and organic ligands hinder the development of MOFs for photocatalysis. For example, the reaction environment (wide pH solution) significantly affects the stability of MOFs and the low electrical conductivity of MOFs limits the application in catalytic reactions.<sup>[102]</sup> It is worth noting that MOF derivatives inherit the superior properties of pristine MOFs with outstanding stability. In recent years, MOF derivatives have been widely developed for various photocatalytic reactions such as photocatalytic water splitting, CO<sub>2</sub>RR, and contaminant degradation.<sup>[103]</sup> As promising photocatalysts, MOF derivatives possess unique advantages, for example, the high porosity can promote charge carriers with the substrates access to active sites and inhibit the volume recombination of electrons and holes. Here, we summarize the remarkable application of MOF derivatives in photocatalysis in the past several years (Table 2).

### 2.7.1. Photocatalytic HER

Semiconductor nanostructures as photocatalysts for HER have drawn considerable attention. The semiconductor structure derived from MOFs effectively improves the activity and stability of the catalyst in photocatalytic hydrogen production.<sup>[102a,104,105]</sup> Zhao et al. developed a MOF-templated strategy to fabricate heterostructured ZnO/ZnS with excellent photocatalytic HER activity.<sup>[106]</sup> The heterostructured ZnO/ZnS can be adjusted to enhance photocatalytic activity and visible light absorption through controlled calcination of host-guest MOF-5 and

thioacetamide. The nanoscale ZnS@C exhibited an excellent light absorption capability and charge separation efficiency with enhanced photocatalytic HER activity (435  $\mu\text{mol g}^{-1} \text{h}^{-1}$ ) and recoverability. Recently, Chen et al. designed a novel MOF-derived photocatalyst decorated with CdS NPs via annealing the N-containing MOF.<sup>[104]</sup> The economic CdS/Zn<sub>x</sub>Co<sub>3-x</sub>O<sub>4</sub> (CdS/ZCO) nanohybrid showed outstanding catalytic activity and excellent stability for hydrogen production. When the optimized loading of CdS NPs reached 30%, the hydrogen evolution rate reached 3978.6  $\mu\text{mol g}^{-1} \text{h}^{-1}$  with sacrificial agent, and the hydrogen evolution efficiency of CdS/ZCO is four times higher than that of CdS/Co<sub>3</sub>O<sub>4</sub> or CdS nanospheres.

### 2.7.2. Photocatalytic CO<sub>2</sub>RR

Due to the high thermodynamic stability of the linear CO<sub>2</sub> molecule, MOF derivatives have been considered as functional photocatalysts to improve the energy conversion efficiency of CO<sub>2</sub> photoreduction.<sup>[107,108]</sup> Wang et al. reported a sequential templating approach (STA) to prepare the Co<sub>3</sub>O<sub>4</sub> dodecahedron with hollow multishelled structures (HoMSs).<sup>[109]</sup> The Co<sub>3</sub>O<sub>4</sub> NC well inherited the topologic arrangement of Co atom in ZIF-67, increasing the exposure of (111) facets, which possesses high activity for CO<sub>2</sub> photoreduction. In addition, quadruple-shelled (QS) Co<sub>3</sub>O<sub>4</sub> HoMSs exhibited three and five times higher catalytic activity than Co<sub>3</sub>O<sub>4</sub> HoMSs without facet control and Co<sub>3</sub>O<sub>4</sub> NPs, respectively. Recently, Su et al. fabricated hollow nickel hydroxide nanocages (Ni(OH)<sub>2</sub>-NCs) derived from ZIF-8 via ion-assisted etching protocol.<sup>[110]</sup> The optimal cavernous structure with thin walls significantly improved light harvest, which promoted multiple light reflection and scattering, static charge transfer, and facilitated the coherent energy flow. The optimized

**Table 2.** Recent remarkable summary of the MOF derivatives for photocatalysis.

Catalyst	MOF precursor	Reaction	References
ZnO/ZnS	MOF-5	HER	[106]
CdS/ZCO	Zn/Co ZIFs	HER	[104]
Cu-TiO <sub>2</sub> /C	HKUST-1	HER	[302]
Ni/g-C <sub>3</sub> N <sub>4</sub>	Ni-based MOF	HER	[303]
MOC-16@CZIF	ZIF-8	HER	[304]
TiO <sub>2</sub>	MIL-125-NH <sub>2</sub>	HER	[305]
g-C <sub>3</sub> N <sub>4</sub> /α-Fe <sub>2</sub> O <sub>3</sub>	g-C <sub>3</sub> N <sub>4</sub> /MIL-100	HER	[306]
Cu <sub>0.9</sub> Co <sub>2.1</sub> S <sub>4</sub> @MoS <sub>2</sub>	Cu/Co MOF	HER	[307]
Cu/TiO <sub>2</sub>	Cu-MOF	HER	[308]
Co <sub>1.11</sub> Te <sub>2</sub> CC	ZIF-67	CO <sub>2</sub> RR	[309]
PMMCoCC-1200	Co-MOF74	CO <sub>2</sub> RR	[310]
Co <sub>3</sub> O <sub>4</sub> HoMSs	ZIF-67	CO <sub>2</sub> RR	[109]
Co <sub>3</sub> O <sub>4</sub> -NS	ZIF-67	CO <sub>2</sub> RR	[107]
MWCNT@MOF-derived In <sub>2</sub> S <sub>3</sub>	MIL-68(In)	Photodegradation of tetracycline (TC)	[112]
magnetic carbon-α-Fe/Fe <sub>3</sub> C	Zn-doped MIL-53(Fe)	Photodegradation of TC	[311]
ZnO/C	MOF-5	Photodegradation of dyes	[113]
M <sub>x</sub> S <sub>y</sub> @C	M-MOF (M = Co, Zn, Cu, Ni)	Photodegradation of dyes	[312]
HKUST-1-P-300	HKUST-1	Photodegradation of phenol	[313]



structure of  $\text{Ni}(\text{OH})_2\text{-NC-2}$  achieved a remarkable CO evolution rate of  $1.44 \times 105 \mu\text{mol g}^{-1} \text{co-cat}^{-1} \text{h}^{-1}$  and a desirable CO selectivity of 96.1%.

### 2.7.3. Photocatalytic Degradation of Dyes

MOF derivatives have led to extensive researches as promising photocatalysts due to their advantages of cost efficiency, cycle stability and outstanding optical absorption/mass transfer.<sup>[111]</sup> Semiconducting metal oxides have been demonstrated to be effective photocatalysts for the degradation of dyes. As shown

in Figure 12A, Pi et al. presented a fabrication of MWCNT@MOF-derived  $\text{In}_2\text{S}_3$  hollow-tube heterostructure by general MOF sulfidation.<sup>[112]</sup> The obtained 0.3%-MWCNT@MOF-derived  $\text{In}_2\text{S}_3$  exhibited an outstanding photocatalytic activity for TC degradation under visible light, which achieved almost 100% degradation efficiency and high apparent reaction rate constants (3–5 times higher than traditional  $\text{In}_2\text{S}_3$  bulk and pure MOF-derived hollow  $\text{In}_2\text{S}_3$ ) (Figure 12B–D). Later, Hussain et al. reported a porous carbon matrix photocatalyst embedded with crystalline ZnO NPs via carbonizing MOF-5 at different temperatures and atmospheres (Figure 12E).<sup>[113]</sup> The obtained

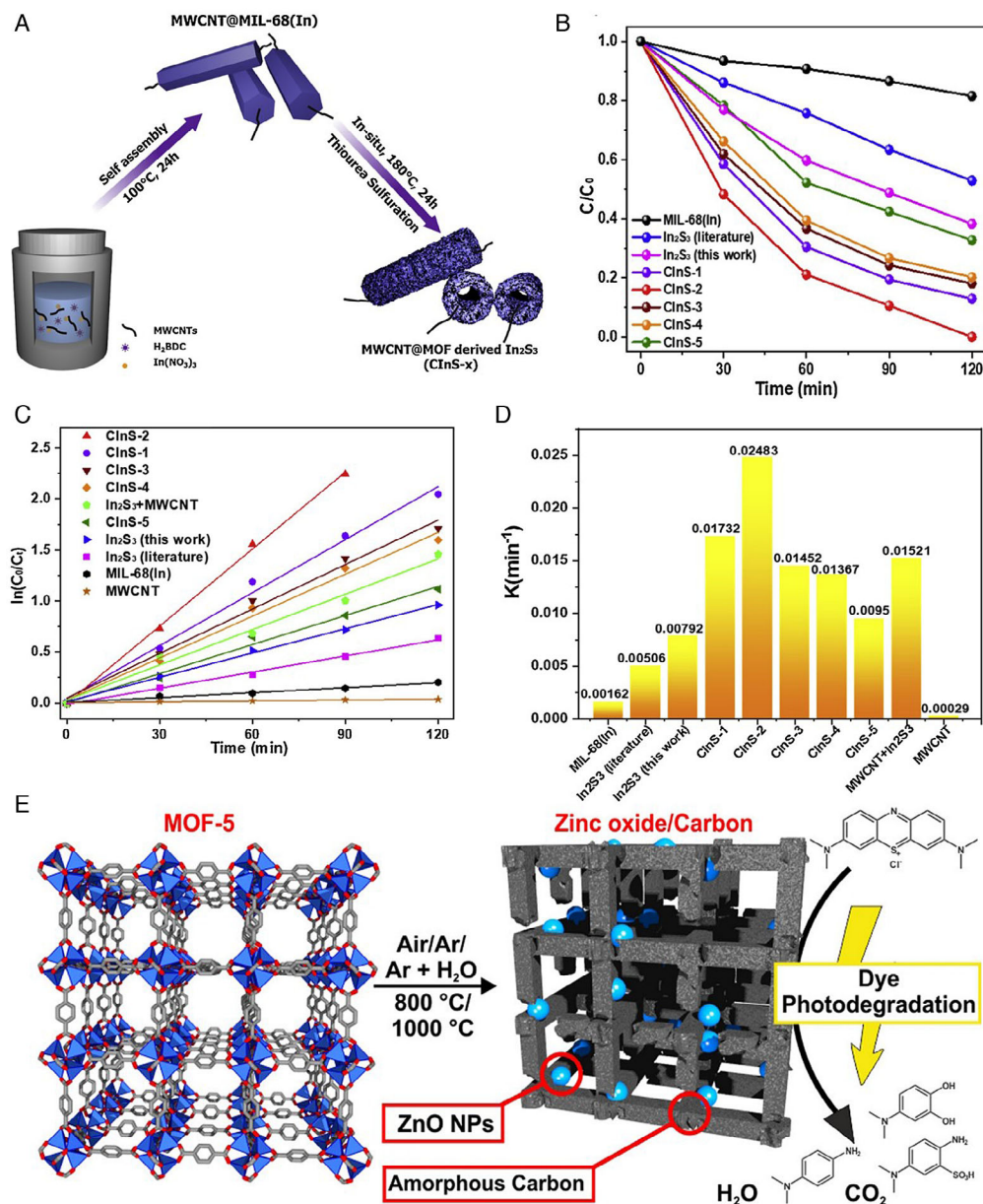


**Figure 12.** A) Schematic representation for the preparation process of MWCNT@MOF-derived  $\text{In}_2\text{S}_3$  core-shell nanocomposites. B) Photodegradation efficiency plots over the various samples and C) pseudo-first-order kinetics curves under different conditions of the degradation of TC. D) The comparison of the apparent reaction rate constants for TC degradations with various photocatalysts. Reproduced with permission.<sup>[112]</sup> Copyright 2019, Elsevier. E) Illustration of ZnO/C nanocomposites. Reproduced with permission.<sup>[113]</sup> Copyright 2018, American Chemical Society.

ZnO/C nanocomposites inherit the cubic particle and high porosity of MOF-5, and ZnO is uniformly dispersed in the porous carbon, which is beneficial to the adsorption of methylene blue and the photodegradation performance under visible light irradiation. In addition, ZnO/C-Ar + W(S)1000 showed excellent stability and reusability after five consecutive methylene blue degradation cycles.

### 3. MOFs and MOF Derivatives for Electrocatalysis

Electrocatalysis is an efficient method for converting electrical energy into chemical energy, such as electrocatalytic water splitting, ORR, CO<sub>2</sub>RR, NRR, and electro-organic synthesis. Efficient electrocatalysts possess the advantages of 1) favorable electrical conductivity, 2) more active sites, and 3) excellent charge transfer and carrier separation. Currently, traditional commercial precious metal electrocatalysts suffer from expensive price, rare reserves, and poor stability. Thus, a large number of materials have been developed to avoid these issues, such as transition metal composites, semiconductive composites, and carbon composites. As a new generation of electrocatalyst, MOFs possess features with ultrahigh surface areas, definite structure, and clear active sites, which are beneficial to investigate the electrocatalytic reaction mechanism (the adsorption and separation of carrier, mass transfer and active sites access, etc.). In following section, we will introduce the mechanism for energy-related MOF-based electrocatalysts, the strategies of improving electrocatalytic performance, and the applications of electrocatalysis of MOF-based materials (including electrocatalytic water splitting, ORR, CO<sub>2</sub>RR, NRR, etc.).

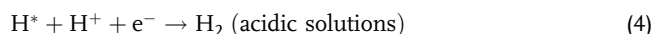
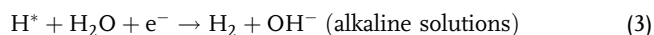
#### 3.1. Mechanism and Criteria for Energy-Related Electrocatalysts

The cathodic HER is the simplest electrocatalytic reaction, which involves a central intermediate and a two-electron transfer. The basic step can be depicted by Volmer–Heyrovsky’s mechanism or Vomer–Tafel’s mechanism, as shown in the following reactions (Equation (1)–(5)).

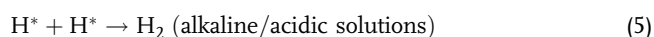
Volmer step (120 mV dec<sup>−1</sup>):



Heyrovsky step (40 mV dec<sup>−1</sup>):



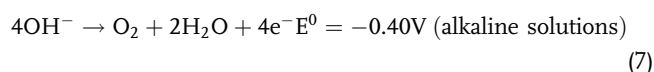
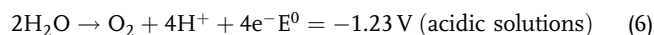
Tafel step (30 mV dec<sup>−1</sup>):



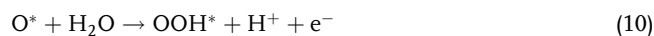
The rate of the reaction is highly related to Gibbs’ free energy for hydrogen evolution ( $\Delta G_{\text{H}^*}$ ). A volcano relationship (Figure 13A)<sup>[114]</sup> revealed the Sabatier principle: If the binding between H\* and catalysts is too strong, the Volmer step (adsorption) will be limited. On the contrary, if the binding is

too weak, Heyrovsky/Tafel (desorption) will limit the overall reaction.<sup>[115]</sup> Controlling the binding energy of catalytic reaction intermediates is the key to improving activity. Theoretical research has shown that the activity trend is based on hydrogen adsorption ( $H_{\text{ad}}$ ) of active sites in acidic environment, whereas the trend is controlled by three crucial descriptors in alkaline environment: 1)  $H_{\text{ad}}$  on the electrocatalyst surface, 2) prevention from the adsorption of hydroxyl ( $\text{OH}_{\text{ad}}$ ), and 3) the energy for H<sub>2</sub>O dissociation. As shown in the HER volcano plot, platinum (Pt) possesses optimal binding energy ( $\Delta G_{\text{H}^*} \approx 0$ ) with only negligible overpotential in acidic environment.<sup>[116]</sup>

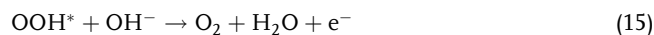
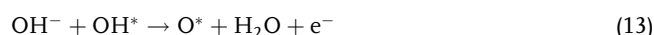
OER in acidic or alkaline environment is a complex four-electron process and involves several intermediates ( $\text{OH}^*$ ,  $\text{O}^*$ , and  $\text{OOH}^*$ ) on the catalyst surface (Equations (6)–(15),  $E_0$  represents thermodynamic potential). Many different reaction mechanisms have been proposed for heterogeneous OER electrocatalysis, such as oxide path, electrochemical metal peroxide path, electrochemical oxide path, and lattice O participated mechanism.<sup>[117]</sup> The most difficult step in OER is to form  $\text{OOH}^*$  on the metal surface by decomposing water on the adsorbed  $\text{O}^*$  and this formation is uphill at the equilibrium potential (1.23 V vs. reversible hydrogen electrode [RHE]) for OER. The voltage above 1.23 V to motivate OER is defined as overpotential.<sup>[118]</sup>



Proposed mechanisms based on DFT calculations in acidic solutions.



Proposed mechanisms based on DFT calculations in alkaline solutions.



For metal-based catalysts, the oxygen adsorption energy can be a good descriptor.<sup>[119]</sup> However, for metal oxides,  $\Delta G_{\text{O}^*} - \Delta G_{\text{OH}^*}$  is often used as a single descriptor to draw a volcano plot (Figure 13B).<sup>[120]</sup> It can be observed that the state-of-art IrO<sub>2</sub> is an active OER catalyst while IrO<sub>2</sub> still binds oxygen too strong. Therefore, achieving stabilization of  $\text{OOH}^*$  and  $\text{OH}^*$  is crucial for designing catalysts. In addition, except for adsorption energy, some other descriptors such as *d*-band center and  $e_g$  filling degree can also be utilized to evaluate the OER catalytic activities.<sup>[121]</sup>

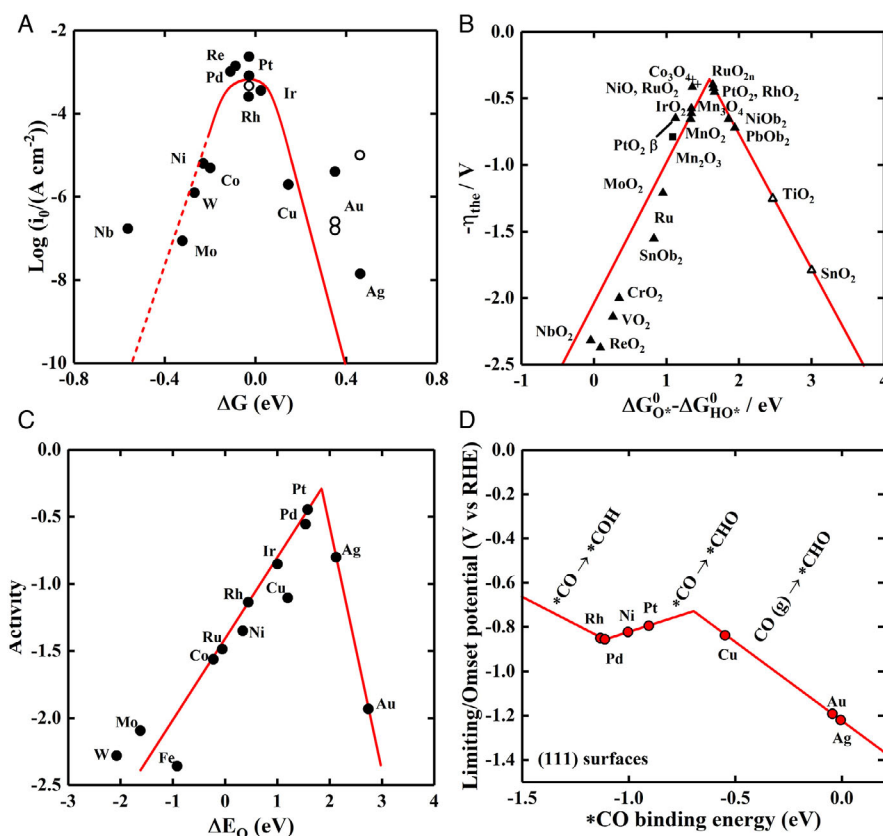
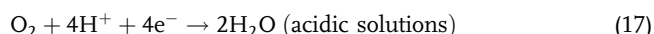


**Figure 13.** A) HER volcano plot for metals. Reproduced with permission.<sup>[114]</sup> Copyright 2010, American Chemical Society. B) OER volcano plot for metal oxides. Reproduced with permission.<sup>[120]</sup> Copyright 2019, Oxford University Press. C) ORR volcano plot for metals. Reproduced with permission.<sup>[125]</sup> Copyright 2004, American Chemical Society. D) CO<sub>2</sub>RR volcano plot for metals. Reproduced with permission.<sup>[130]</sup> Copyright 2014, The Royal Society of Chemistry.

ORR is a core half reaction in electrochemical energy devices such as electrolyte membrane fuel cells (PEMFCs) and metal–air batteries. Various intermediates including O\*, OH\*, and OOH\* species can be generated during ORR. Oxygen is generally reduced by two ways during ORR process, including a direct four-proton–electron pathway (Equation (16) and (17)) to generate O<sub>2</sub>-species (H<sub>2</sub>O or OH<sup>−</sup>) and indirect two-proton–electron two pathways (Equation (18) and (19)) to generate hydrogen peroxide.<sup>[122]</sup> The direct reduction route is highly efficient for application as H<sub>2</sub>O<sub>2</sub> reduces the energy conversion efficiency and accelerates the electrolyte degradation in PEMFCs.<sup>[123]</sup>

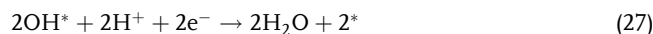
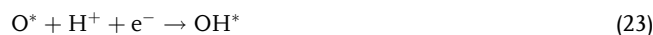
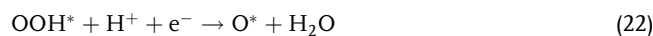
Direct four-proton–electron pathway:



Indirect two-proton–electron pathway:



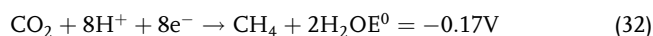
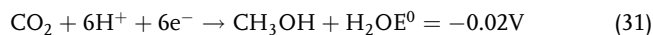
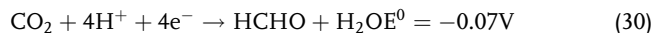
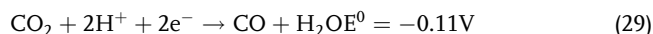
Two possible mechanisms including associative mechanism and dissociation mechanism are proposed in the following steps (in acidic solutions).<sup>[124]</sup>



In most instances, the rate of overall ORR is determined by the following steps: 1) the first electron transfer to the adsorbed O<sub>2</sub> molecules at the surface of electrocatalysts, 2) O<sub>2</sub> hydration, and 3) the desorption of H<sub>2</sub>O. A theoretical ORR activity volcano plot was established using  $\Delta E_0$  as a descriptor, where Pt is near the top (Figure 13C).<sup>[125]</sup> As illustrated in the ORR volcano plot, when the metal binds oxygen too strong, the property will be limited by the proton–electron transfer between intimate O\* and OH\*. On the contrary, the activity is hampered by an associative/dissociate mechanism when the metal binds oxygen too weak.<sup>[126]</sup>



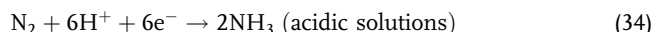
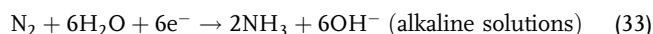
CO<sub>2</sub>RR can be considered as a reversed reaction of fuel cells. The reduction process involves different pathways, leading to different value-added products (Equation (28)–(32)).<sup>[127]</sup>



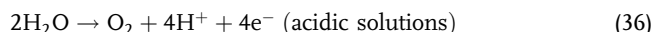
These various products require the transfer of large amounts of protons and electrons that may also be conducted through different intermediates.<sup>[128]</sup> Therefore, electrocatalysts with excellent activity and selectivity are highly required for CO<sub>2</sub>RR. CO<sub>2</sub>RR begins with the formation of ·COO<sup>−</sup> and the adsorption of a proton leads to the formation of ·COOH, which is further reduced to ·CO. Finally, ·CO will be desorbed or subsequently reduced to additional products.<sup>[129]</sup> DFT calculation was carried out to provide theoretical guidance and a volcano plot is drawn, as shown in Figure 13D.<sup>[130]</sup> The DFT calculations suggested that if the metal binds CO\* too strong, the overpotential of CO<sub>2</sub>RR will be limited by the protonation of CO\* to CHO\*. On the other hand, the protonation of CO to CHO\* will be the determined reaction.<sup>[130]</sup>

Electrocatalytic NRR (2N<sub>2</sub> + 6H<sub>2</sub>O → 4NH<sub>3</sub> + 3O<sub>2</sub>) possesses high efficiency and has the ability to occur under moderate conditions. The detailed reactions at both cathode and anode are presented (Equation (33), (36)).

Cathodic reaction:



Anodic reaction:



When the metal binds N too strong, the catalytic activity is limited by the protonation of NH\* to NH<sub>2</sub>\* or the evolution of NH<sub>2</sub>\* as NH<sub>3</sub>. In contrast, when metal binds N too weak, the reductive adsorption of N<sub>2</sub> to N<sub>2</sub>H\* is limited in the first step.<sup>[131]</sup> Furthermore, the HER can be a major competing reaction during NRR for the electrocatalysts near the top of the volcano. It is worth highlighting that limiting the supply of proton and electron can suppress HER and therefore motivates NRR.<sup>[132]</sup> It is noted that most of the electrocatalytic reactions are conducted in a standard three-electrode system.

## 3.2. Electrocatalytic Water Splitting

### 3.2.1. Electrocatalytic HER

Electrocatalytic water splitting is a clean and efficient method to generate H<sub>2</sub>. Pt is the most efficient electrocatalyst in both acidic and alkaline conditions. Yet, the high cost and scarcity of noble

metals limit its practical applications. So, it is highly desirable to develop non-noble metals-based catalysts for HER. Enzymes such as hydrogenases and nitrogenases which can produce hydrogen contain Ni–Fe and Fe–Mo active sites for catalysis. Inspired by nature and DFT calculations (volcano plots in Figure 13A), Co-, Fe-, Ni-, and Mo-based homogenous and heterogeneous electrocatalysts were developed for efficient HER. Yet, the drawbacks such as large overpotentials and low stability hindered their electrocatalytic applications. Most of the MOFs are constructed from transition metals which are Earth abundant. The pore environments and electronic structures of MOFs can be systematically modulated. Also, MOFs can be easily functionalized with HER active components such as inorganic NPs or molecules. All these merits as well as their intrinsic activity make MOFs promising electrocatalysts for HER. However, there are only limited reports of MOFs for HER reaction (Table 3) and the development of MOFs for HER application is still at its early stage.

POMs, a rich family of soluble metal–oxygen anion clusters of early transition metals in high oxidation states (Mo<sup>V,VI</sup>, W<sup>VI</sup>, V<sup>IV,V</sup>), have reversible multivalence reduction/oxidation states, and are active HER molecular catalyst.<sup>[133]</sup> POM could be used as building blocks to form porous POM-based MOFs (POMOFs).<sup>[134]</sup> The first report of MOFs for electrocatalytic HER was reported by Nohra et al. by introducing POMs into MOFs to construct POMOFs.<sup>[135]</sup> The 3D electroactive POMOF (TBA)<sub>3</sub>[PMo<sup>V</sup><sub>8</sub>Mo<sup>VI</sup><sub>4</sub>O<sub>36</sub>(OH)<sub>4</sub>Zn<sub>4</sub>][C<sub>6</sub>H<sub>3</sub>(COO)<sub>3</sub>]<sub>4/3</sub>·36H<sub>2</sub>O (ε(trim)<sub>4/3</sub>) was fabricated using Zn-modified ε-Keggin POM as the building block and connecting with trimesic acid linkers. The HER activity of ε(trim)<sub>4/3</sub> was studied in pH = 1 electrolyte that contains 1 M of alkali cations (Li<sup>+</sup>, Na<sup>+</sup>, K<sup>+</sup>). ε(trim)<sub>4/3</sub>-based electrode demonstrated higher HER activity than Pt, and a TON as high as 1.2 × 10<sup>5</sup> after 5 h was achieved. The excellent activity of this POMOF for HER was mainly attributed to the unique 3D open framework structures and the confinement effect of electroactive POMs into the pores of MOFs. Since then, a series of POM-based MOFs were developed for efficient HER catalysis.<sup>[136–138]</sup> Later, Qin et al. synthesized two novel 3D POMOFs (TBA)<sub>3</sub>[PMo<sup>V</sup><sub>8</sub>Mo<sup>VI</sup><sub>4</sub>O<sub>36</sub>(OH)<sub>4</sub>Zn<sub>4</sub>][BTB]<sub>4/3</sub>·xGuest (NENU-500) and (TBA)<sub>3</sub>[PMo<sup>V</sup><sub>8</sub>Mo<sup>VI</sup><sub>4</sub>O<sub>37</sub>(OH)<sub>3</sub>Zn<sub>4</sub>][BPT] (NENU-501) using the connections of Zn-modified ε-Keggin POM and tricarboxylate acids benzene tribenzoate (BTB) and [1,1'-biphenyl]-3,4,5-tricarboxylate (BPT).<sup>[136]</sup> In both NENU-500 and NENU-501, the electroactive ε-Keggin POM moiety is connected with organic ligands as the node directly, which will expose more accessible active sites. The HER activities of NENU-500 and NENU-501, as well as ε(trim)<sub>4/3</sub>, NENU-5, and HKUST-1 for comparison, were investigated in 0.5 M H<sub>2</sub>SO<sub>4</sub> solution. In all the MOFs studied, NENU-500 demonstrated the best HER activity, with an overpotential of 237 mV at 10 mA cm<sup>−2</sup> and a Tafel slope of 96 mV dec<sup>−1</sup>. Both NENU-500 and NENU-501 displayed excellent stability, maintaining their activities after 2000 cycles. The much higher activity of NENU-500 results from its unique framework and pore structures that showed more accessible active sites and faster diffusion of electrolyte.

Zhang et al. reported two novel POM-encapsulated MOFs with 1D nanotube-like channels (metal-organic nanotube frameworks, MONT).<sup>[137]</sup> Using Dawson-type POMs as templates,

**Table 3.** Summary of benchmark MOF electrocatalysts for HER.

Catalysts	Electrolyte	Substrate	Onset potential [mV]	$\eta_{10}$ [mV]	Tafel slope [mV dec <sup>-1</sup> ]	References
$\epsilon(\text{trim})_{4/3}$	0.5 M H <sub>2</sub> SO <sub>4</sub>	Glassy carbon (GC)	420	515	142	[135]
NENU-500	0.5 M H <sub>2</sub> SO <sub>4</sub>	Rotating glassy carbon disk electrode (GC-RDE)	180	237	96	[136]
NENU-501	0.5 M H <sub>2</sub> SO <sub>4</sub>	GC-RDE	304	392	137	[136]
HUST-200	0.5 M H <sub>2</sub> SO <sub>4</sub>	GC	76	131	51	[137]
HUST-201	0.5 M H <sub>2</sub> SO <sub>4</sub>	GC	101	192	79	[137]
MOS-1	pH = 1.3	GC	280	340	–	[140]
MOS-2	pH = 1.3	GC	480	530	–	[140]
THT-Ni	0.5 M H <sub>2</sub> SO <sub>4</sub>	GC	110	333	80.5	[141]
H <sub>3</sub> [Co <sub>3</sub> (THT) (THA)](CoS <sub>2</sub> N <sub>2</sub> )	0.5 M H <sub>2</sub> SO <sub>4</sub>	GC-RDE	93	283	71	[142]
Graphene-CoS <sub>2</sub> N <sub>2</sub>	0.5 M H <sub>2</sub> SO <sub>4</sub>	GC	66	230	70	[142]
UU-100(Co)	Acetate buffer at pH 4	GC	150	–	210	[314]
GO/Cu-MOF	0.5 M H <sub>2</sub> SO <sub>4</sub>	GC	87	209@30 mA cm <sup>-2</sup>	84	[144]
AB/CTGU-5	0.5 M H <sub>2</sub> SO <sub>4</sub>	GC	18	44	45	[145]
Hf <sub>12</sub> -CoDBP/CNTs	0.1 M HClO <sub>4</sub>	GC-RDE	315	650	178	[146]
NiFe-NPC	0.1 M KOH	NF	–	134	–	[143]
Ni-S@NU-1000	0.1 M HCl	FTO	–	238	120	[147]
MoS <sub>x</sub> /UiO-66-NH <sub>2</sub>	0.5 M H <sub>2</sub> SO <sub>4</sub>	GC	–	200	59	[148]
Mo <sub>2</sub> S@HKUST-1	0.5 M H <sub>2</sub> SO <sub>4</sub>	GC	99	300	69	[149]
Mo <sub>2</sub> S@Co-BDC	1.0 M KOH	GC-RDE	155	248	86	[150]
CoP/Co-MOF	0.5 M H <sub>2</sub> SO <sub>4</sub>	CF	–	27	43	[151]
	PBS (pH = 7)	CF	–	49	63	
	1.0 M KOH	CF	–	34	56	
Au/CoFe MOFNs (dark condition)	0.1 M KOH	GC	228	≈435	[59]	[154]
Au/CoFe-MOFNs (808 nm irradiation)	0.1 M KOH	GC	135	≈292	94	
Fe <sub>3</sub> S <sub>4</sub> /MIL-53(Fe)	0.5 M H <sub>2</sub> SO <sub>4</sub>	GC	48	92	60	[315]
MIL-53	0.5 M H <sub>2</sub> SO <sub>4</sub>	GC	–	172	99	[315]

the coordination assembly of Cu<sup>2+</sup> with multidentate ligand 5-(2-pyrazinyl)tetrazole (pzta) and 4,4'-bpy forms two POMOFs [Cu<sup>II</sup><sub>6</sub>(pzta)<sub>6</sub>(4,4'-bpy)<sub>3</sub>(P<sub>2</sub>W<sub>18</sub>O<sub>62</sub>)]·2H<sub>2</sub>O (HUST-200) and [Cu<sup>II</sup><sub>6</sub>(pzta)<sub>6</sub>(4,4'-bpy)<sub>3</sub>(As<sub>2</sub>W<sub>18</sub>O<sub>62</sub>)]·2H<sub>2</sub>O (HUST-201). Both HUST-200 and HUST-201 exhibited exceptional chemical stability due to the encapsulation of POMs in the 1D channels of MONT and high activity for HER in acidic solutions. Remarkably, HUST-200 displayed an overpotential of 131 mV at 10 mA cm<sup>-2</sup>, with a Tafel slope of 96 mV dec<sup>-1</sup>, which showed the lowest overpotential in all reported POMOFs.

The main drawbacks for MOFs as HER electrocatalysts are their poor conductivity. Metal dithiolene (M–S) or metal-diamine (M–N) coordination bonds-based planar 2D MOFs demonstrate good electroconductivity, which have potential applications for electrocatalysis.<sup>[139]</sup> Clough et al. synthesized two isorecticular 2D MOFs H<sub>3</sub>[Co<sub>3</sub>(BHT)<sub>2</sub>] (MOS 1) and H<sub>3</sub>[Co<sub>3</sub>(THT)<sub>2</sub>] (MOS 2) with high HER activity.<sup>[140]</sup> Isostructural MOS 1 displayed an overpotential of 340 mV at 10 mA cm<sup>-2</sup> and a TOF (at 550 mV) of 0.113 s<sup>-1</sup> in 0.05 M H<sub>2</sub>SO<sub>4</sub> solution (pH = 1.3). However, MOS 2

displayed poorer electroactivity with an overpotential of 530 mV at 10 mA cm<sup>-2</sup>, which is 190 mV larger than that of MOS 1. MOS 1 also demonstrated high stability and good durability in electrocatalysis under acid conditions. The results indicated that metal dithiolene-based 2D MOFs are promising HER electrocatalysts. Yet, the different performances between BHT and THT ligands-based MOS 1 and MOS 2 were not elucidated.

Later, Feng's group reported the synthesis of the nanosheet layer of 2D MOF H<sub>3</sub>[Ni<sub>3</sub>(THT)<sub>2</sub>] (THT-Ni) using Langmuir–Blodgett's method, as shown in Figure 14A.<sup>[141]</sup> THT-Ni is isostructural with MOS 2 and the lateral dimensions of the fabricated nanosheet are several millimeters with thickness of about 0.7–0.9 nm. Due to the sufficient exposure of Ni-dithiolene moieties in 2D MOF, THT-Ni demonstrated high HER activity, with an overpotential of 333 mV at 10 mA cm<sup>-2</sup> and a Tafel slope of 80.5 mV dec<sup>-1</sup> in 0.5 M H<sub>2</sub>SO<sub>4</sub> solution (Figure 14B). The overpotential (413 mV) of THT-Ni at pH = 1.3 is 117 mV lower than that of MOS 2 at the same conditions, indicating that different metal–dithiolene complexes lead to different electrocatalytic activity. Also,

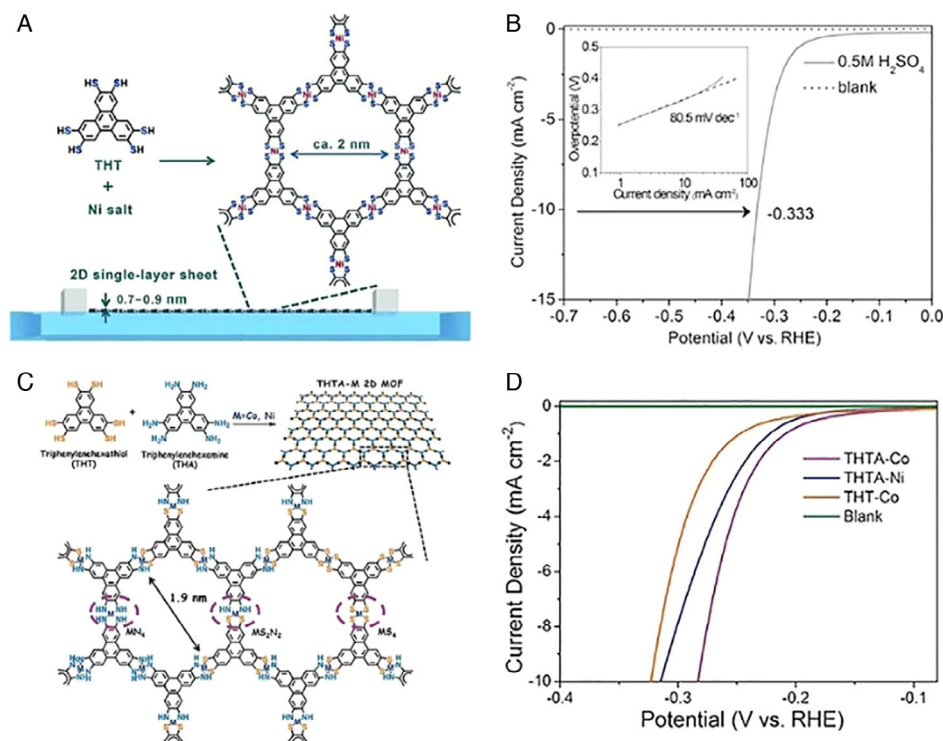


**Figure 14.** A) Synthesis of a 2D MOF THT-Ni single-layer sheet using the Langmuir–Blodgett method at an air/water interface. B) HER polarization plots of the THT-Ni electrode in 0.5 M H<sub>2</sub>SO<sub>4</sub>. The inset shows the corresponding Tafel plot of aqueous solution. Reproduced with permission.<sup>[141]</sup> Copyright 2015, Wiley-VCH GmbH. C) Schematic synthesis of single-layer 2D MOFs THTA-Co and THAT-Ni. D) HER polarization plots of THTA-Co, THAT-Ni, and THA-Co in 0.5 M H<sub>2</sub>SO<sub>4</sub>. Reproduced with permission.<sup>[142]</sup> Copyright 2017, Wiley-VCH GmbH.

THT-Ni showed an overpotential of 574 mV at 10 mA cm<sup>-2</sup> at alkaline conditions (pH = 15.4), indicating its good HER activity over a wide pH range. The same group also synthesized 2D MOFs H<sub>3</sub>[M<sub>3</sub>(THT)(THA)] (MS<sub>2</sub>N<sub>2</sub> or THAT-M, M = Co, Ni) with mixed dithiolene and diamine ligands and compared their HER performance with single ligand-based 2D MOFs H<sub>3</sub>[M<sub>3</sub>(THT)<sub>2</sub>] (MS<sub>4</sub>) and H<sub>3</sub>[M<sub>3</sub>(THA)<sub>2</sub>] (MS<sub>4</sub>) (Figure 14C).<sup>[142]</sup> The CoS<sub>2</sub>N<sub>2</sub> nanosheet electrode showed an overpotential ( $\eta_{10}$ ) of 283 mV with a Tafel slope of 71 mV dec<sup>-1</sup> in a 0.5 M H<sub>2</sub>SO<sub>4</sub> solution, which is much lower than the nanosheet electrode of single ligand-based 2D MOFs (328 mV for CoS<sub>4</sub> and 315 mV for NiS<sub>2</sub>N<sub>2</sub>) (Figure 14D). Also, the HER activity bulk powders-based electrode of 2D MOFs follow the order of CoS<sub>2</sub>N<sub>2</sub> > CoN<sub>4</sub> > CoS<sub>4</sub>, with overpotentials ( $\eta_{10}$ ) of 332, 382, and 495 mV, respectively. DFT calculations showed that the  $\Delta G_{H^*}$  of CoS<sub>2</sub>N<sub>2</sub> is -0.12 eV, which is closest to the  $\Delta G_{H^*}$  of Pt (-0.09 eV). The combination of experimental results and DFT calculations indicated that the main active sites in CoS<sub>2</sub>N<sub>2</sub> are the Co–N units, whereas S atom improves the H<sub>2</sub> adsorption ability of Co atoms, leading to synergistic improvement of HER activity. Further composition of CoS<sub>2</sub>N<sub>2</sub> with graphene would further improve the electron transfer process and show much better HER activity ( $\eta_{10}$  = 230 mV).

The integration of MOFs with materials of high conductivity such as graphene (oxide), carbon nanotubes (CNTs), and acetylene black (AB) is another efficient approach to improve the electroconductivity and electron transfer capability, thus enhancing the electrocatalytic activity.<sup>[143–146]</sup> Jahan et al. reported a

composite made from the assembly of Cu-based MOF and GO (GO/Cu-MOF), which showed good electrocatalytic performance.<sup>[144]</sup> The synthesized pure Cu-MOF showed an overpotential (at 30 mA cm<sup>-2</sup>) of 369 mV with a Tafel slope of 135 mV dec<sup>-1</sup> in 0.5 M H<sub>2</sub>SO<sub>4</sub> solution. When this MOF is assembled with graphene oxide (with 8 wt% GO), the HER performance was obviously improved, with an overpotential (at 30 mA cm<sup>-2</sup>) of 209 mV with a low Tafel slope of 84 mV dec<sup>-1</sup>. The unique porous scaffold structure, synergistic interactions between the GO and MOF, and improved electron transfer lead to the enhanced HER activity and good stability.

Wu et al. reported the combination of Co-MOF (CTGU-5) with conductive AB to get a new MOF composite (AB/CTGU-5) with superior HER activity.<sup>[145]</sup> CTGU-5 is a 2D structure with one H<sub>2</sub>O molecule coordinated to Co atom. The onset potential, overpotential ( $\eta_{10}$ ), and Tafel slope of pure CTGU-5 electrocatalyst are 298, 388, and 125 mV dec<sup>-1</sup> respectively. When the stoichiometric ratio between CTGU-5 and AB is 1:4 [AB/CTGU-5(1:4)], the composite exhibited superior HER properties, with an onset potential of 18 mV, an overpotential ( $\eta_{10}$ ) of 44 mV, and a low Tafel slope of 45 mV dec<sup>-1</sup> in 0.5 M H<sub>2</sub>SO<sub>4</sub> solution. The composites of CTGU-5 with graphene/CTGU-5 (with 6 wt% graphene) also showed good HER activity with an overpotential ( $\eta_{10}$ ) of 91 mV and a Tafel slope of 88 mV dec<sup>-1</sup>. The unique 2D structure of CTGU-5 and the interactions between MOFs and conductive materials to improve the electron transfer of the electrode contribute the high HER activities.



The large porosity and easy functionalization of MOFs make them ideal platforms to host or join with various HER active catalysts, such as metal sulfides, metal phosphides, and precious metals, to generate synergistic enhancement for HER activity. MOF scaffolds can improve the catalytic active sites and facilitate the electron transfer and mass transport, thereby boosting the electrocatalytic activities of electrodes. Hod et al. reported a high HER active composite utilizing a mesoporous and highly stable Zr-based MOF NU-1000 film as scaffold for the deposition of  $\text{NiS}_x$  electrocatalyst (Figure 15A).<sup>[147]</sup> As shown in Figure 15B,C, the fabricated Ni-S/NU-1000 electrode showed an overpotential ( $\eta_{10}$ ) of 238 mV in 0.1 M HCl solution, which is 402 and 322 mV lower than that of NU-1000 film and Ni-S film, respectively. The Tafel slope of Ni-S/NU-1000 electrode is 120 mV dec<sup>-1</sup>, indicating a Volmer–Tafel reaction mechanism. Though NU-1000 has mesopores and large surface areas, the scaffold does not improve the electroactive surface areas of Ni–S. Instead, this MOF scaffold changes the environment of Ni–S, making the electrocatalytic electrode more favorable for proton transport. Later, Dai et al. anchored molybdenum polysulfide ( $\text{MoS}_x$ ) on Zr-MOF UiO-66- $\text{NH}_2$  via the one-pot solvothermal method to get a new MOF/metal sulfide composite  $\text{MoS}_x/\text{UiO-66-NH}_2$ .<sup>[148]</sup> The optimized component of  $\text{MoS}_x/\text{UiO-66-NH}_2$  nanocomposites showed high HER activity and excellent durability in 0.5 M  $\text{H}_2\text{SO}_4$  solution, with an overpotential ( $\eta_{10}$ ) of 200 mV and a low Tafel slope of 59 mV dec<sup>-1</sup>. The electrode had a TOF of 1.28 s<sup>-1</sup> at  $\eta = 200$  mV. Wang et al. fabricated  $\text{MoS}_2$ -based nanohybrid for HER by combining Cu-MOF HKUST-1 with  $\text{MoS}_2$  nanosheets (Figure 21C).<sup>[149]</sup> Compared with pure  $\text{MoS}_2$ , the  $\text{MoS}_2/\text{HKUST-1}$  nanocomposite exhibited enhanced HER activity and stability in acidic condition (0.5 M  $\text{H}_2\text{SO}_4$  solution)

with an overpotential ( $\eta_{10}$ ) of 300 mV and Tafel slope of 69 mV dec<sup>-1</sup> (Figure 15D).

While most MOFs and composites are reported to show good HER performance in acidic solutions, the applications of MOFs for HER in basic solutions were not well studied, which is mainly because the HER kinetics in alkaline conditions are more sluggish and complex. Recently, Qiao's group synthesized new 2D hybrid nanosheets combining MOF Co-BDC and  $\text{MoS}_2$  nanosheet via a facile sonication-assisted method, as shown in Figure 16A.<sup>[150]</sup> The Co-BDC/ $\text{MoS}_2$  electrocatalyst showed excellent HER activity in 1 M KOH solution, with an overpotential ( $\eta_{10}$ ) of 248 mV and Tafel slope of 86 mV dec<sup>-1</sup>. However, the overpotentials ( $\eta_{10}$ ) of Co-BDC and  $\text{MoS}_2$  are 529 mV and 349 mV, respectively (Figure 16B,C). Also, the hybrid nanosheet showed quite high stability for 15 h at a constant current density of 10 mA cm<sup>-2</sup>. The decoration of Co-BDC on the semiconducting 2 H- $\text{MoS}_2$  phase leads to the partial phase transfer to metallic 1 T- $\text{MoS}_2$ , which is more active for HER. The interfacial interactions between Co-BDC and  $\text{MoS}_2$  not only improved the intrinsic activity, but also has a synergistic effect by reducing the sluggish water dissociation step in alkaline HER, paving the way for interface engineering of MOF composites for improved electrocatalytic performance.

TMPs are new types of advantageous HER electrocatalysts. The incorporation of TMPs and MOFs represents promising MOF composites for highly active HER catalysts. Liu et al. reported the doping of CoP into Co-based MOFs to generate CoP/Co-MOF composites with superior pH-universal HER activity and high stability.<sup>[151]</sup> CoP/Co-MOF exhibited an overpotential ( $\eta_{10}$ ) of 27, 49, and 34 mV in 0.5 M  $\text{H}_2\text{SO}_4$ , 1.0 M PBS (pH = 7), and 1.0 M KOH solutions, respectively.

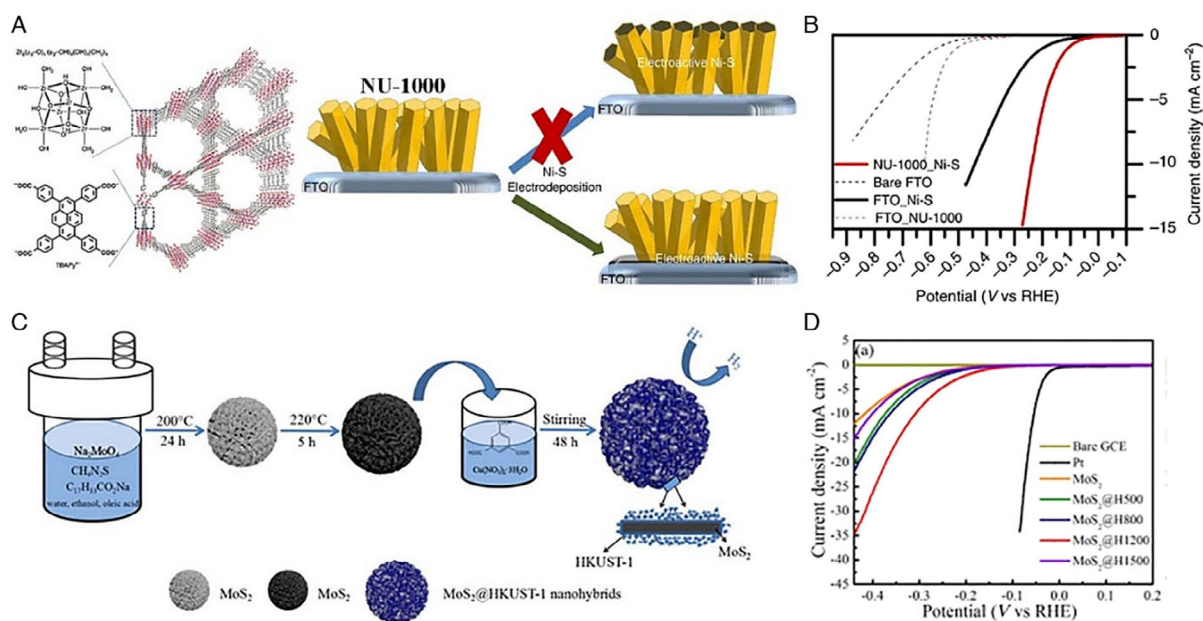


**Figure 15.** A) Schematic representation of the crystal structures of NU-1000 and the synthesis of Ni-S/NU-1000 electrode. B) HER polarization plots of the Ni-S/NU-1000 electrode and related catalysts. Reproduced with permission.<sup>[147]</sup> Copyright 2015, Nature Publishing Group. C) Schematic representation of the preparation of  $\text{MoS}_2/\text{HKUST-1}$  flower-like nanohybrid materials. D) HER polarization plots of  $\text{MoS}_2$ ,  $\text{MoS}_2/\text{H500}$ ,  $\text{MoS}_2/\text{H800}$ ,  $\text{MoS}_2/\text{H1200}$ , and  $\text{MoS}_2/\text{H1500}$ . Reproduced with permission.<sup>[149]</sup> Copyright 2018, Wiley-VCH GmbH.

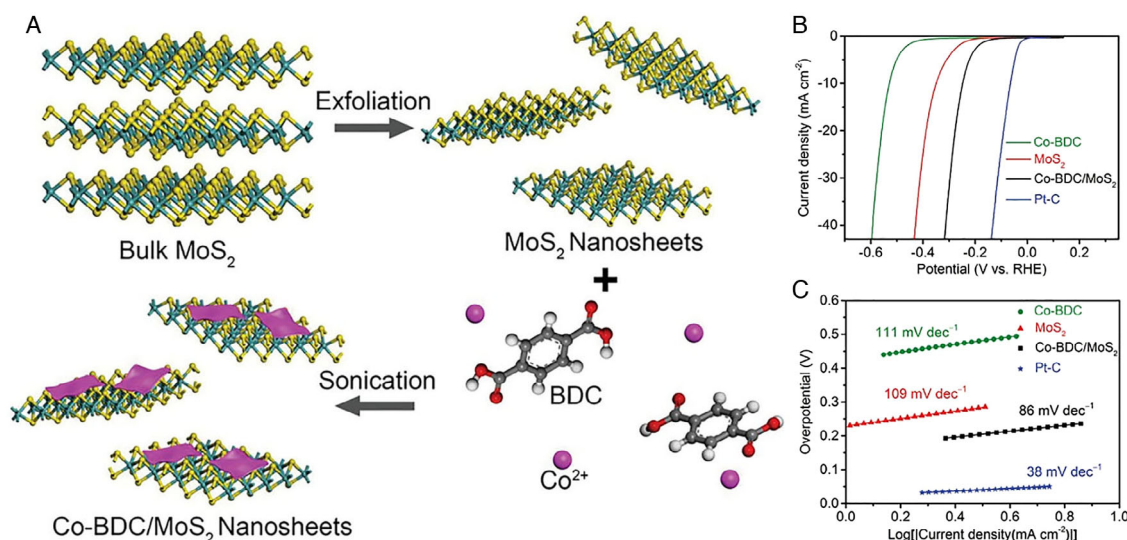


**Figure 16.** A) Schematic representation of synthesis for Co-BDC/MoS<sub>2</sub> hybrid nanosheets. B) HER polarization plots of the Co-BDC/MoS<sub>2</sub> electrode and related catalysts. C) Tafel plots of the corresponding polarization curves. Reproduced with permission.<sup>[150]</sup> Copyright 2019, Wiley-VCH GmbH.

Experimental and DFT calculations revealed that the electron transfer from CoP to MOFs results in the optimized adsorption energy of hydrogen ( $\Delta G_{H^*}$ ) and water molecules ( $\Delta G_{H_2O^*}$ ). Also, the unique porous structure of Co-MOFs contributes significantly to the remarkable HER activity of CoP/Co-MOF in different pH conditions.

Plasmonic noble metal NPs can generate localized surface plasmon resonance (LSPR) driven by incident light and can provide metal NPs several unique benefits, such as enhanced local electromagnetic fields and efficient charge carrier separation.<sup>[152]</sup> The resulting hot electron injection can reduce the activation barrier of a chemical reaction by electronically or vibrationally exciting the adsorbed atoms or molecules, and it was found recently that it can accelerate the electrochemical reactions.<sup>[153]</sup> It is expected that the LSPR effect can be applied in MOFs to improve the electrocatalytic activity. Wang et al. reported that the composites of bimetallic MOF nanosheets (CoFe-MOFNs) and Au nanorods (Au/CoFe-MOFNs) can dramatically improve the HER activity under light illumination, as shown in Figure 17.<sup>[154]</sup> The Au/CoFe-MOFN composite showed an onset potential of 228 mV, an overpotential ( $\eta_{10}$ ) of about 435 mV, and a Tafel slope of 115 mV dec<sup>-1</sup> in the dark at 0.1 M KOH. When irradiated with light at wavelength of 808 nm, the Au/CoFe-MOFNs composite demonstrated improved HER activity, with an onset potential of 135 mV, an overpotential ( $\eta_{10}$ ) of about 292 mV, and a Tafel slope of 94 mV dec<sup>-1</sup> (Figure 17B,C). Mechanism studies revealed that the enhancement of HER performance was mainly contributed from the LSPR effect that injects hot electrons from Au nanorods to CoFe-MOFNs, affording decreased activation energy for HER. This work provides a new approach to utilize solar energy to boost the electrocatalytic activity.

### 3.2.2. Electrocatalytic OER

OER is the key process for fuel cells, water-splitting electrolyzers, and metal-air batteries.<sup>[155]</sup> Most of the OER activity catalysts

such as metal oxides are not stable in acids, so OER performances are usually investigated in strong alkaline solutions.<sup>[156]</sup> Currently, the most efficient OER catalysts are precious metal-based IrO<sub>2</sub>/RuO<sub>2</sub>, which seriously suffers from the high cost and poor operation stability. Hence, it is highly desirable to develop Earth-abundant OER catalysts with low overpotential, high mass activity, and high durability.<sup>[118]</sup> MOFs especially metal-oxo nodes-based MOFs have been demonstrated to display promising OER activity. At the early stage, MOFs for OER are mainly based on a trial-and-error approach without a rational guidance and a clear relationship of structure activity. Some MOFs, such as Prussian Blue-type MOFs,<sup>[157]</sup> UTSA-76<sup>[158]</sup>, Co-ZIF-9,<sup>[159]</sup> ZIF-67,<sup>[160]</sup> etc.,<sup>[161]</sup> were reported to show OER activity. Yet, their performances are not satisfactory. In the last several years, MOFs for OER catalysis are the most fantastic and fast-growing field in MOF electrocatalysts based on rational design strategies. There are three distinctive approaches to efficiently improve OER activity of catalysts:<sup>[117b,162]</sup> 1) improving the intrinsic activity of catalysts; 2) increasing the number of active sites via porosity or morphology control; and 3) enhancing electron conductivity/charge transfer by composing. In this section, we mainly focus on summarizing the strategies to improve the OER activity of MOFs (Table 4).

**Improving the Intrinsic Activity:** The coordination environments of MOFs can be modulated, thus changing the electronic structures of metal nodes and intrinsic activity of MOFs. Lu et al. prepared OER-active MOF [Co<sub>2</sub>(μ-OH)<sub>2</sub>(BBTA)] (MAF-X27-OH) with both open metal sites and hydroxide ligands via a postsynthetic ion-exchange approach of [Co<sub>2</sub>(μ-Cl)<sub>2</sub>(BBTA)] (MAF-X27-Cl) (Figure 18A,B).<sup>[163]</sup> The bridge Cl<sup>-</sup> ligand of MAF-X27-Cl can be successfully replaced by OH<sup>-</sup> ligand to get MAF-X27-OH by immersing MAF-X27-Cl into 1.0 M KOH solution for 24 h at room temperature (RT). MAF-X27-OH coated on Cu foil exhibited an outstanding OER activity, with an overpotential ( $\eta_{10}$ ) of 292 mV and a Tafel slope of 88 mV dec<sup>-1</sup> in 1.0 M KOH solution (Figure 18C). The TOF is up to 0.25 s<sup>-1</sup> at an overpotential of

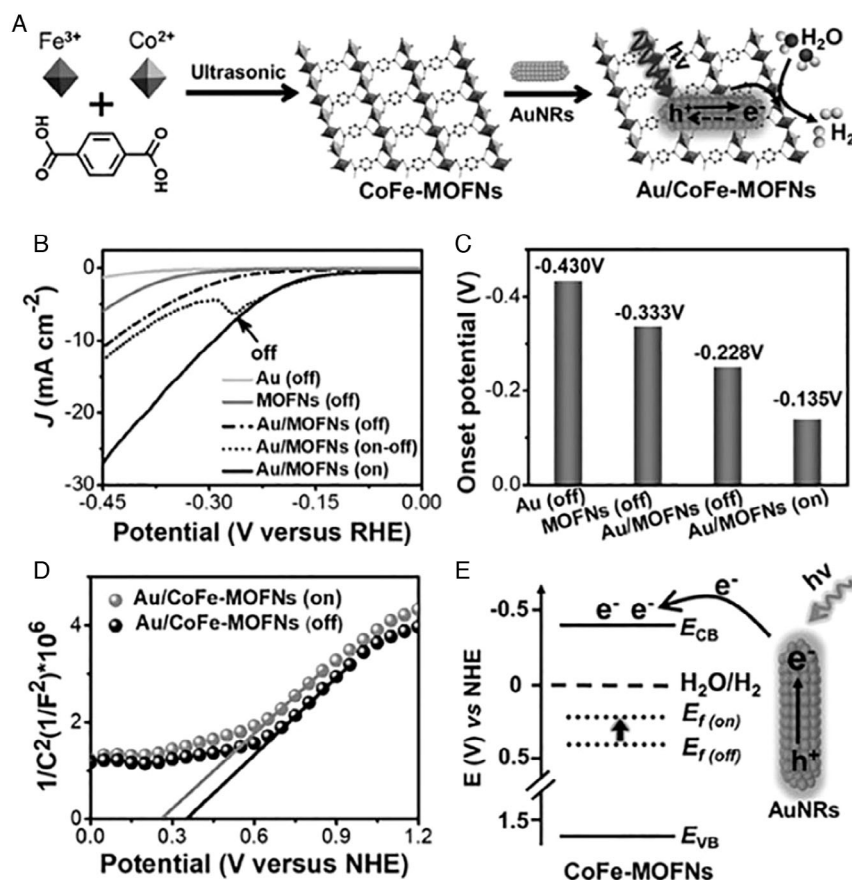


**Figure 17.** A) Synthesis of Au/CoFe-MOFNs. B) HER polarization plots of AuNRs, CoFe-MOFNs, and Au/CoFe-MOFNs in the absence or presence of light irradiation. C) Tafel plots of the corresponding polarization curves. D) Mott-Schottky plots of Au/CoFe-MOFNs with light off and on. E) Schematic and energy-level diagram illustrating hot electron injection from AuNRs to CoFe-MOFNs. Reproduced with permission.<sup>[154]</sup> Copyright 2019, Wiley-VCH GmbH.

400 mV and the FE is almost 100%. Controlled experiments at pH = 7 and isotope tracing experiments demonstrated that the OH<sup>-</sup> ligands were involved in the OER process and it played a critical role in improved activity.

Using a modular and step-wise synthesis strategy, Shen et al. successfully introduced the paddle-wheel-type cluster Co<sub>2</sub>(RCOO)<sub>4</sub> with open metal sites and high catalytic activity into MOFs (Figure 18D).<sup>[164]</sup> After two-step postsynthetic modifications, an outstanding OER catalyst [(Fe<sub>3</sub>(μ<sub>3</sub>-O)(BDC)<sub>3</sub>)<sub>4</sub> (Co<sub>2</sub>(NA)<sub>4</sub>(L<sup>T</sup>)<sub>2</sub>)<sub>3</sub>] (Fe<sub>3</sub>-Co<sub>2</sub> or MCF-49) was fabricated, which otherwise cannot be synthesized directly. MCF-49 coated on GC electrode showed high OER activity, with an overpotential ( $\eta_{10}$ ) of 283 mV, a low Tafel slope of 43 mV dec<sup>-1</sup>, and a TOF of 0.27 s<sup>-1</sup> at an overpotential of 300 mV in 0.1 M KOH solution (Figure 18E,F). However, for the pure Fe-based MOF precursors Fe<sub>3</sub>-Fe and Fe<sub>3</sub>, they showed very poor OER performance at the same condition. The OER performance of MCF-49 can be further improved when utilizing nickel foams (NFs) as substrates, with an outstanding overpotential ( $\eta_{10}$ ) of 225 mV, a Tafel slope of 48 mV dec<sup>-1</sup>, and a high TOF of 1.82 s<sup>-1</sup> at overpotential of 300 mV. The results confirmed that the introduced paddle-wheel type Co<sub>2</sub> cluster with special coordination environment of Co atoms contributed to the high OER performance.

However, MOF catalysts for OER mainly perform at strong alkaline conditions, in which most MOFs are not stable. The development of OER catalysts in benign neutral media is ecofriendly and practically useful.<sup>[165]</sup> Xu et al. reported a cobalt imidazolate framework-based catalyst by introduction of a high-valence non-3d metal Mo (Figure 19A).<sup>[166]</sup> The [Co<sub>4</sub>(MoO<sub>4</sub>)<sub>6</sub>] (Co<sub>4</sub>Mo) catalyst showed a much better OER activity than RuO<sub>2</sub> and Co(EIM)<sub>2</sub> in neutral PBS solution (pH = 7), with an onset potential of 1.50 V, an overpotential ( $\eta_{10}$ ) of 490 mV, and a Tafel slope of 144 mV dec<sup>-1</sup> (Figure 19B–D). The combination of experimental results and theoretical calculations revealed that introducing non-3d metals can modulate the oxidation state and electronic structure of Co. Correspondingly, the energy of the OER rate-determining step and the reactant/product adsorption energy were optimized, resulting in greatly improved OER performances.

The introduction of coordinatively unsaturated metal sites (CUMSs) has been proved to be an efficient approach to enhance the OER activity of MOFs. Plasma treatment can partially destroy the coordination geometry of metal nodes in MOFs to generate unsaturated metal sites, which can act as active sites for improving the OER performance.<sup>[160,167]</sup> Tao et al. reported the treatment of MOFs with dielectric barrier discharge (DBD) plasma



**Table 4.** Summary of benchmark MOF electrocatalysts for OER.

MOFs	Electrolyte	Substrate	$E_{\text{onset}}$ [V vs RHE]	$\eta_{10}$ [mV]	Tafel slope [mV dec <sup>-1</sup> ]	Ref
UTSA-16	1.0 M KOH	GC	1.60	408	77	[158]
Co-ZIF-9	0.1 M KOH	FTO	–	510@1 mA cm <sup>-2</sup>	93	[159]
FeTPyP-Co	0.1 M KOH	GC	1.47	351@1 mA cm <sup>-2</sup>	–	[161a]
Co-WOC-1	0.1 M KOH	GC	–	390@1 mA cm <sup>-2</sup>	128	[161b]
MAF-X27-OH	1.0 M KOH	GC	1.55	387	66	[163]
	1.0 M KOH	Cu foil	1.47	292	88	
MCF-49	0.1 M KOH	GC	1.46	283	43	[164]
	0.1 M KOH	NF	1.43	225	48	
	0.1 M PBS	GC	1.53	431@2 mA cm <sup>-2</sup>	134	
ZIF-67	1.0 M KOH	GC	–	400	74.9	[160]
CUMS-ZIF-67	1.0 M KOH	GC	–	320	53.7	[160]
Co-PBA	1.0 M KOH	NF	–	334	67	[167b]
Co-PBA-plasma-2 h	1.0 M KOH	NF	–	274	53	[167b]
P-Phy-CoFe	0.5 M KBi	–	–	265	36.1	[167a]
MAF-48	1.0 M PBS	GC	1.54	352	71	[165]
MAF-69-Mo	CO <sub>2</sub> -0.5 M KHCO <sub>3</sub>	GC	–	456	219	[166]
	0.1 M PBS	GC	1.67	490	144	
Ni/Fe-BTC	0.1 M KOH	NF	–	270	43	[169a]
Fe <sub>2</sub> Ni-BPTC (NNU-23)	0.1 M KOH	Carbon cloth	–	365	72.2	[168]
CGTU-10c2	0.1 M KOH	GC	1.37	240	58	[169b]
CoFe-2D-MOF	1.0 M KOH	GC	–	351	44	[169c]
Co <sub>0.6</sub> Fe <sub>0.4</sub> -MOF-74	1.0 M KOH	RRDE	–	280	56	[169g]
CoFe-PYZ	0.1 M KOH	GC	–	300	44	[169d]
FeNi <sub>2.4</sub> Co <sub>0.4</sub> -MIL-53	1.0 M KOH	GC	–	219	53.5	[169e]
FeNiMn <sub>0.4</sub> -MIL-53	1.0 M KOH	NF	–	238@100 mA cm <sup>-2</sup>	71.3	[169e]
Fe <sub>0.2</sub> Ni <sub>0.3</sub> Co <sub>0.5</sub> -MIL-53	1.0 M KOH	NF	–	236	39.2	[169f]
A <sub>2.7</sub> B-MOF-FeCo <sub>1.6</sub>	1.0 M KOH	GC	–	288	39	[169h]
NiPc-MOF	1.0 M KOH	FTO	1.48	350	74	[316]
NiFe-HHTP	1.0 M KOH	Carbon cloth	–	213	96	[317]
NiCo-UMOFN	1.0 M KOH	GC	1.42	250	42	[172a]
	1.0 M KOH	NF	1.39	189	–	
FeNi-MIL-53	1.0 M KOH	NF	–	233@50 mA cm <sup>-2</sup>	31.3	[318]
Fe <sub>2</sub> Ni-MIL-88-NH <sub>2</sub>	1.0 M KOH	NF	–	240	58.8	[319]
NiFe-NPC	0.1 M KOH	NF	–	240	34	[143]
NiFe-NPC-4.3%	0.1 M KOH	NF	–	210@200 mA cm <sup>-2</sup>	68	[173]
CoFe-MOF-OH	1.0 M KOH	GC	–	310	48	[169c]
		NF	–	265	44	
ZIF-9(III) nanosheet	1.0 M KOH	–	–	380	55	[320]
NiFe-BDC-NS	1.0 M KOH	GC	–	221	56	[172b]
MCF-12-NS (2D-Co-NS)	0.1 M KOH	NF	–	211	46	[172c]
(Ni <sub>2</sub> Co <sub>1</sub> ) <sub>1-x</sub>	1.0 M KOH	GC	–	257	41.3	[172d]
Fe <sub>x</sub> -MOF-NF						
LDH-FeNi-MOF	1.0 M KOH	NF	–	318@50 mA cm <sup>-2</sup>	47	[172e]
Fe(II)-MOF-74	1.0 M KOH	NF	–	207	41.1	[172f]
Fe@BIF-89	1.0 M KOH	NF	1.49	310	56	[174a]
Fe@BIF-91	1.0 M KOH	GC-RDE	1.50	350	71	[174b]

**Table 4.** Continued.

MOFs	Electrolyte	Substrate	$E_{\text{onset}}$ [V vs RHE]	$\eta_{10}$ [mV]	Tafel slope [mV dec <sup>-1</sup> ]	Ref
ZIF-67 /NPC-2(2:1)	0.1 M KOH	GC-RDE	1.55	410	117	[174c]
Ti <sub>3</sub> C <sub>2</sub> T <sub>x</sub> /CoBDC	0.1 M KOH	GC	1.51	410	48.2	[174d]
Co-MOF /CNTs	1.0 M KOH	GC	1.51	340	69	[174e]
Ni(OH) <sub>2</sub> /Ni-BDC	1.0 M KOH	GC	–	320	41	[174f]
Ni <sub>3</sub> S <sub>2</sub> /NiS @Ni-BDC	1.0 M KOH	GC-RDE	–	298	58.6	[174g]

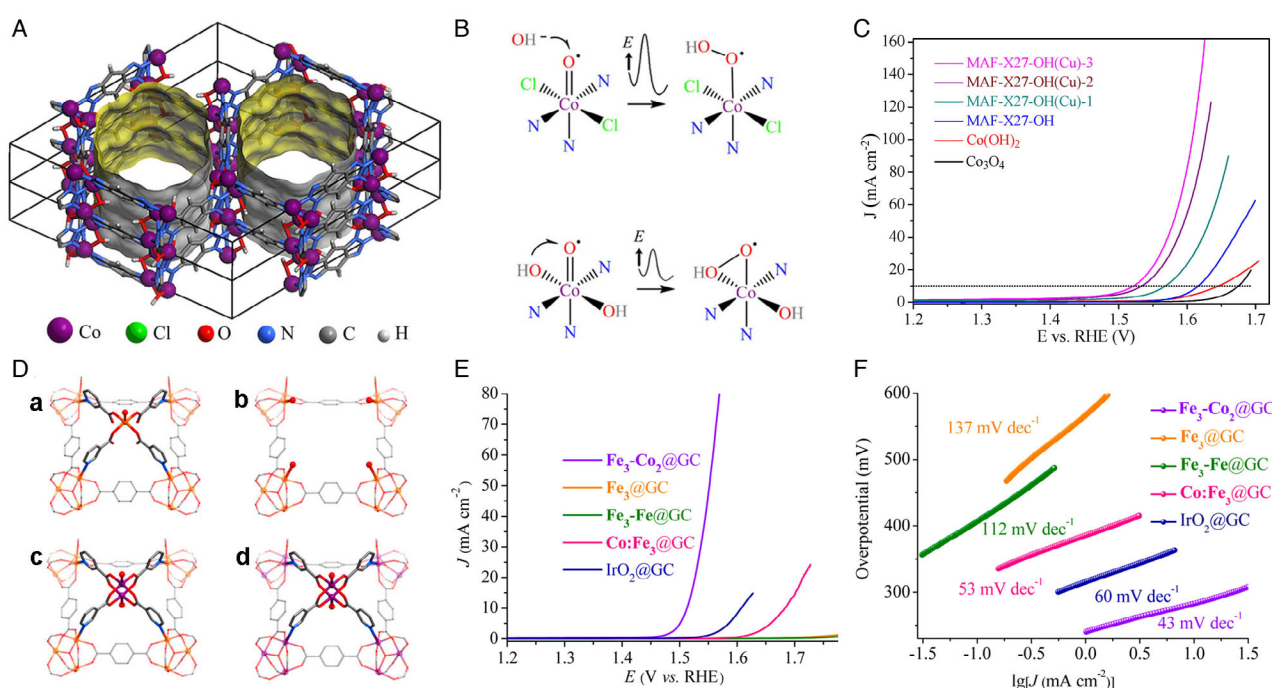


**Figure 18.** A) 3D coordination network and pore structures of MAF-X27-OH. B) Solid-liquid coupling pathway for MAF-X27-Cl and intraframework coupling pathway for MAF-X27-OH. C) Linear sweep voltammetry (LSV) plots of MAF-X27-OH(Cu)-(1-3), MAF-X27-OH, Co(OH)<sub>2</sub>, and Co<sub>3</sub>O<sub>4</sub> at pH = 14. Reproduced with permission.<sup>[163]</sup> Copyright 2016, American Chemical Society. D) The structures of a) Fe<sub>3</sub>-Fe, b) Fe<sub>3</sub>, c) Fe<sub>3</sub>-Co<sub>2</sub>, and d) Co<sub>3</sub>-Co<sub>2</sub>. E) LSV plots of Fe<sub>3</sub>-Co<sub>2</sub>@GC, Fe<sub>3</sub>@GC, Fe-Fe@GC, Co:Fe<sub>3</sub>@GC, and IrO<sub>2</sub>@GC and F) corresponding Tafel slope in water at pH = 13. Reproduced with permission.<sup>[164]</sup> Copyright 2017, American Chemical Society.

to create CUMSSs with enhanced OER performance for the first time.<sup>[160]</sup> Some ligands of ZIF-67 are removed via plasma treatment for several minutes to generate abundant coordinatively unsaturated Co atoms in ZIF-67 (CUMSSs-ZIF-67). CUMSSs-ZIF-67 showed significantly enhanced OER activity compared with pristine ZIF-67 in 1.0 M KOH solution, with an overpotential ( $\eta_{10}$ ) of 320 mV, a Tafel slope of 53.7 mV dec<sup>-1</sup>, and a TOF of 0.462 s<sup>-1</sup> at an overpotential of 300 mV. The overpotential ( $\eta_{10}$ ), Tafel slope, and TOF of pristine ZIF-67 are 400 mV, 74.9 mV dec<sup>-1</sup>, and 0.043 s<sup>-1</sup>, respectively. The specific activity of CUMSSs-ZIF-67 at potential of 1.55 V demonstrated a current of 37.35 mA m<sup>-2</sup><sub>BET</sub> (normalized by the Brunauer–Emmett–

Teller (BET) surface) compared with that of pristine ZIF-67 (3.34 mA m<sup>-2</sup><sub>BET</sub>), indicating the good intrinsic activity of the CUMSSs. DFT calculations indicated that the plasma-induced CUMSSs in ZIF-67 with excellent adsorption of reactant are the active sites for improved OER performances. This work provided a new route to generate unsaturated metal sites for modification of MOFs as superior OER electrocatalysts. Later, Guo et al. treated Co-/Fe-based Prussian blue analogues with air plasma (Co-PBA-plasma-2h).<sup>[167b]</sup> The low-temperature air plasma contains highly reactive oxygen species, which can mildly etch the ligands in Co-PBA and react with the coordinatively unsaturated Co sites while keeping the framework structure (Figure 20A).

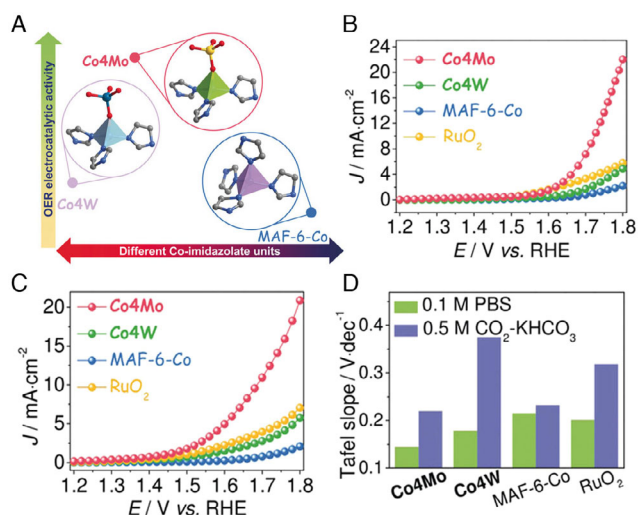


**Figure 19.** A) The crystal structures and OER activities of Co4W, Co4Mo, and MAF-6-Co without ethyl groups and hydrogen atoms. LSV plots of Co4Mo in B) 0.1 M PBS and C) CO<sub>2</sub>-saturated 0.5 M KHCO<sub>3</sub>. D) The corresponding Tafel slopes. Reproduced with permission.<sup>[166]</sup> Copyright 2019, Wiley-VCH GmbH.

X-ray photoelectron spectroscopy (XPS) and Fourier transform infrared spectroscopy (FTIR) spectra confirmed the introduction of oxygen binding to metal cations and the valence states of Co ions are increased via air plasma treatment. The plasma-treated

catalyst Co-PBA-plasma-2h demonstrated improved OER activity compared with pristine Co-PBA. The overpotential ( $\eta_{10}$ ) and Tafel slope of Co-PBA-plasma-2 h are 274 mV and 53 mV dec<sup>-1</sup> respectively, compared with that of Co-PBA ( $\eta_{10}$  of 334 mV and Tafel slope of 74.9 mV dec<sup>-1</sup>) (Figure 20B,C). Remarkably, Co-PBA-plasma-2 h showed only a low overpotential of 330 mV at high current density of 100 mA cm<sup>-2</sup> and an FE of near 100%.

In electrocatalysis, doping is an efficient approach to improve the electrocatalytic performance, because the dopant can alter the electron distribution and also improve the electrical conductivity. One of the most advantage for MOFs is that part of the metal clusters can be replaced without changing the crystal structure, making MOFs ideal platforms to study the doping strategies to improve the OER activity. Based on this strategy, a series of bimetal-/multimetal-based MOFs have been reported to show superior OER activities, resulting in the synergistic effect between different metals that can modulate the electronic structures of active sites to optimize the free energy of adsorbed intermediates.<sup>[168,169]</sup> Wang et al. synthesized a series of bimetal MOFs based on Fe<sub>2</sub>M( $\mu_3$ -O)(CH<sub>3</sub>COO)<sub>6</sub>(H<sub>2</sub>O)<sub>3</sub> (M = Fe, Co, Ni, Zn) clusters.<sup>[168]</sup> The trinuclear clusters were bridged by biphenyl-3,4',5-tricarboxylic acid (BPTC) to get four stable isostructural MOFs, Fe<sub>3</sub>-BPTC (NNU-21), Fe<sub>2</sub>Co-BPTC (NNU-22), Fe<sub>2</sub>Ni-BPTC (NNU-23), and Fe<sub>2</sub>Zn-BPTC (NNU-24) (Figure 21A). All the heterometallic MOFs realized better OER performance than the monometallic Fe<sub>3</sub>-BPTC (NNU-21), and Fe<sub>2</sub>Ni-BPTC (NNU-23) showed the best OER performance, with an overpotential ( $\eta_{10}$ ) of 365 mV, a Tafel slope of 72.2 mV dec<sup>-1</sup>, and a TOF of

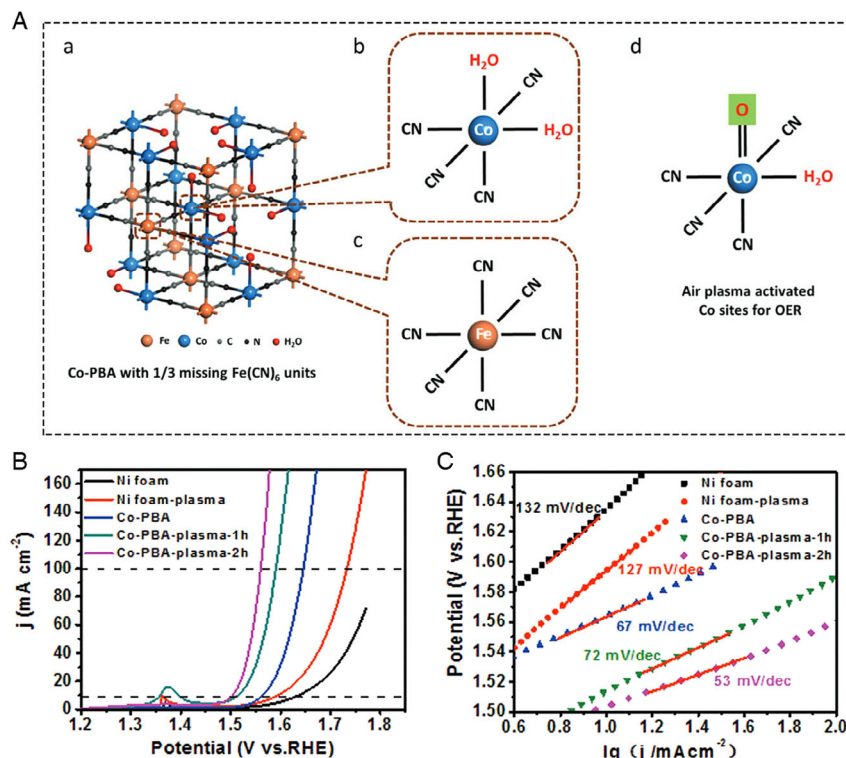


**Figure 20.** A) Structure of plasma treatment of Co-PBA. a) The coordination structures of the Co and Fe sites are illustrated in (b) and (c) and the structure of the air plasma-activated Co sites (d). B) LSV plots and C) Tafel slope of pristine and plasma-treated Co-PBA samples. Reproduced with permission.<sup>[167b]</sup> Copyright 2018, Wiley-VCH GmbH.

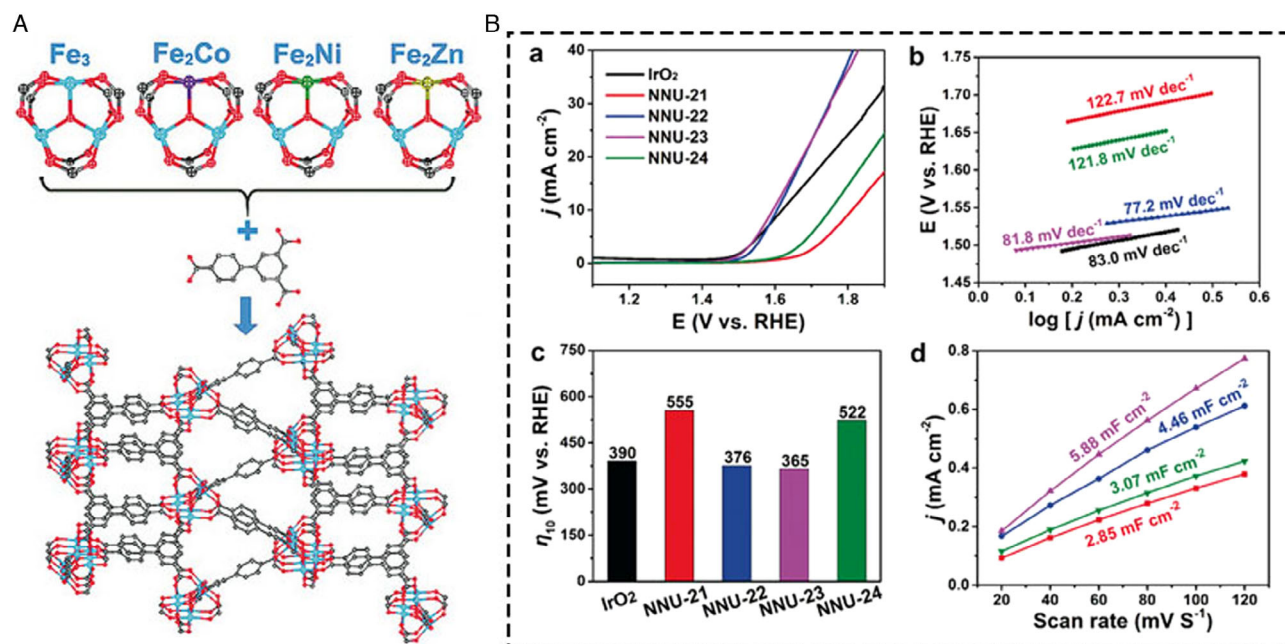


**Figure 21.** A) 3D framework of NNU-21-24 connected by trinuclear metal clusters and tridentate carboxylate ligand. B) OER performance of IrO<sub>2</sub> and NNU-21-24 in 0.1 M KOH. a) LSV plots, b) Tafel slopes, c) a comparison of overpotentials ( $\eta_{10}$ ) and d) plots for  $C_{dl}$ . Reproduced with permission.<sup>[168]</sup> Copyright 2018, Wiley-VCH GmbH.

0.03 s<sup>-1</sup> at an overpotential of 400 mV in 0.1 M KOH solution (Figure 21B). Also, NNU-23 had the largest electrochemical double-layer capacitance ( $C_{dl}$ ) (5.10 mF cm<sup>-2</sup>), which is much larger than that of NNU-21 (2.48 mF cm<sup>-2</sup>), indicating the large electrochemical active surface area (ECSA) of bimetallic MOFs. DFT calculations revealed that the introduction of heteroatoms into Fe<sub>3</sub> cluster can efficiently strengthen the adsorption of O\* intermediate species, thus improving the OER activity. Further investigation of the partial density of states (DOS) of metal atoms in Fe<sub>2</sub>M clusters demonstrated that the *d*-band centers of Fe<sub>2</sub>Co, Fe<sub>2</sub>Ni, and Fe<sub>2</sub>Zn cluster are much closer to the Fermi level than that of Fe<sub>3</sub> cluster, which leads to stronger binding interactions between the adsorbates and catalysts and essentially contributes to the improvement of OER performance of heterometallic clusters. Later, Li et al. prepared a series of trimetallic MOFs (Fe/Ni/Co(Mn)-MIL-53) with high OER activity and stability, in which the molar ratios of different metals can be precisely modulated.<sup>[169e]</sup> The Fe/Ni-based bimetallic MIL-53 exhibited better OER activity than monometallic Fe-MIL-53 with an overpotential ( $\eta_{10}$ ) of 255 mV and a Tafel slope of 37.8 mV dec<sup>-1</sup> for Fe/Ni<sub>1.6</sub>MIL-53 in 1.0 M KOH, in which Ni was recognized as the active center for OER, whereas Fe can tune the intrinsic activity of catalysts. Further introducing a small amount of third metal Co or Mn into Fe/Ni-MIL-53, the resulting trimetallic MOFs Fe/Ni/Co(Mn)-MIL-53 showed improved OER activity as compared with the bimetallic Fe/Ni-MIL-53. The optimized trimetallic MOF Fe/Ni<sub>2.4</sub>/Co<sub>0.4</sub>-MIL-53 can reach a low overpotential ( $\eta_{10}$ ) of 219 mV and a Tafel slope of 53.5 mV dec<sup>-1</sup>. The synergistic effect in different metal ions was confirmed via XPS spectra. Compared with bimetallic MOFs, the Ni 2p<sub>3/2</sub> in trimetallic MOFs is shifted to a higher binding energy (≈0.4 eV), indicating

that the third metal doping can efficiently modify the coordination environment of the Ni active centers. Because of the synergistic effects of mixed metals, the modulation of electronic properties of the active centers is crucial for promoting the OER activity.

Not only the metal ions, the organic ligands also can be easily replaced in MOFs without changing the framework structure, in which their conductivity, pore size, and active centers can be simultaneously modulated. Xue et al. prepared a heterogeneity MOF A<sub>x</sub>B<sub>y</sub>-MOF-FeCo<sub>1.6</sub> (A = terephthalic, B = 2-aminoterephthalic) by modulating the molar ratio of A/B (Figure 22A).<sup>[169h]</sup> The optimized A<sub>2.7</sub>B-MOF-FeCo<sub>1.6</sub> MOF showed a low overpotential ( $\eta_{10}$ ) of 288 mV, a small Tafel slope of 39 mV dec<sup>-1</sup>, and a TOF of 0.46 s<sup>-1</sup> at an overpotential of 300 mV in 1.0 M KOH solution, exceeding the OER performance of A-MOF-FeCo<sub>1.6</sub> and B-MOF-FeCo<sub>1.6</sub> (Figure 22B,C). Experimental and DFT calculations revealed that not only the synergistic effects of bimetal, but also the synergistic effects of mixed linkers can efficiently modulate the electronic structure of the intrinsic catalytic center, improving the OER activity.

**Increasing the Active Sites Via Morphology Control:** The morphology of electrocatalysts plays an important role in electrochemical performance. The ideal morphological structures can increase the number of active sites, allow superior electron transfer, and provide channels for the diffusion of reactants and products, efficiently improving the electrocatalytic activities. Ultrathin 2D nanomaterials, including graphene, MoS<sub>2</sub>, layered double hydroxides (LDHs), etc., have exhibited outstanding electrocatalytic activities due to their unique shape, high surface-to-volume ratios, and exposure of more active sites on the surface.<sup>[170]</sup> Compared with the 3D counterparts, 2D MOF



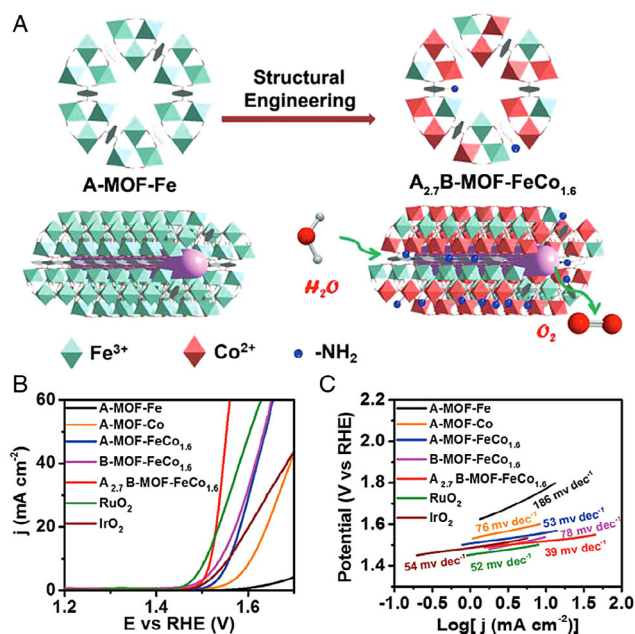


**Figure 22.** A) Illustration of preparation of heterogeneity MOF for OER. B) LSV plots and C) Tafel slopes of a series of heterogeneity MOFs. Reproduced with permission.<sup>[169h]</sup> Copyright 2018, Wiley-VCH GmbH.

ultrathin nanosheets demonstrate considerable advantages for efficient electrocatalysis.<sup>[171]</sup> For example, the nanometer thicknesses allow the superior electron transfer, rapid mass transport, and fast permeation of gas/liquid molecules, rendering enhanced performance in electrocatalysis. Moreover, the high density of exposed catalytic active surfaces, with CUMSSs, improves the catalytic activity. Also, the 2D morphology is preferred to form films and increase the contact area between MOF nanosheets and the substrate. Till now, most of the superior active OER MOF catalysts are 2D nanosheet structures, especially MOF nanosheets coated on porous conductive substrates.<sup>[172]</sup>

In the pioneering work, Zhao et al. prepared ultrathin NiCo bimetal-organic framework nanosheets (NiCo-UMOFNs) with BDC ligands as promising electrocatalysts for OER (Figure 23A).<sup>[172a]</sup> NiCo-UMOFNs on glassy-carbon electrodes demonstrated an overpotential ( $\eta_{10}$ ) of 250 mV, a small Tafel slope of 42 mV dec<sup>-1</sup>, and a TOF of 0.86 s<sup>-1</sup> at an overpotential of 300 mV in 1.0 M KOH solution (Figure 23B,C). The overpotential ( $\eta_{10}$ ) of NiCo-UMOFNs was much smaller than that of bulk NiCo-MOFs (317 mV), Ni-UMOFNs (321 mV), Co-UMOFNs (371 mV), and commercial RuO<sub>2</sub> (279 mV) at the same conditions. When NiCo-UMOFNs were loaded on conductive Cu foam, the electrode showed further enhanced OER activity with an ultralow overpotential ( $\eta_{10}$ ) of 189 mV. XAS analysis and DFT calculations revealed that the high OER activity of NiCo-UMOFNs compared with bulk NiCo-MOFs mainly result from the CUMSSs on the exposed surface of ultrathin nanosheets.

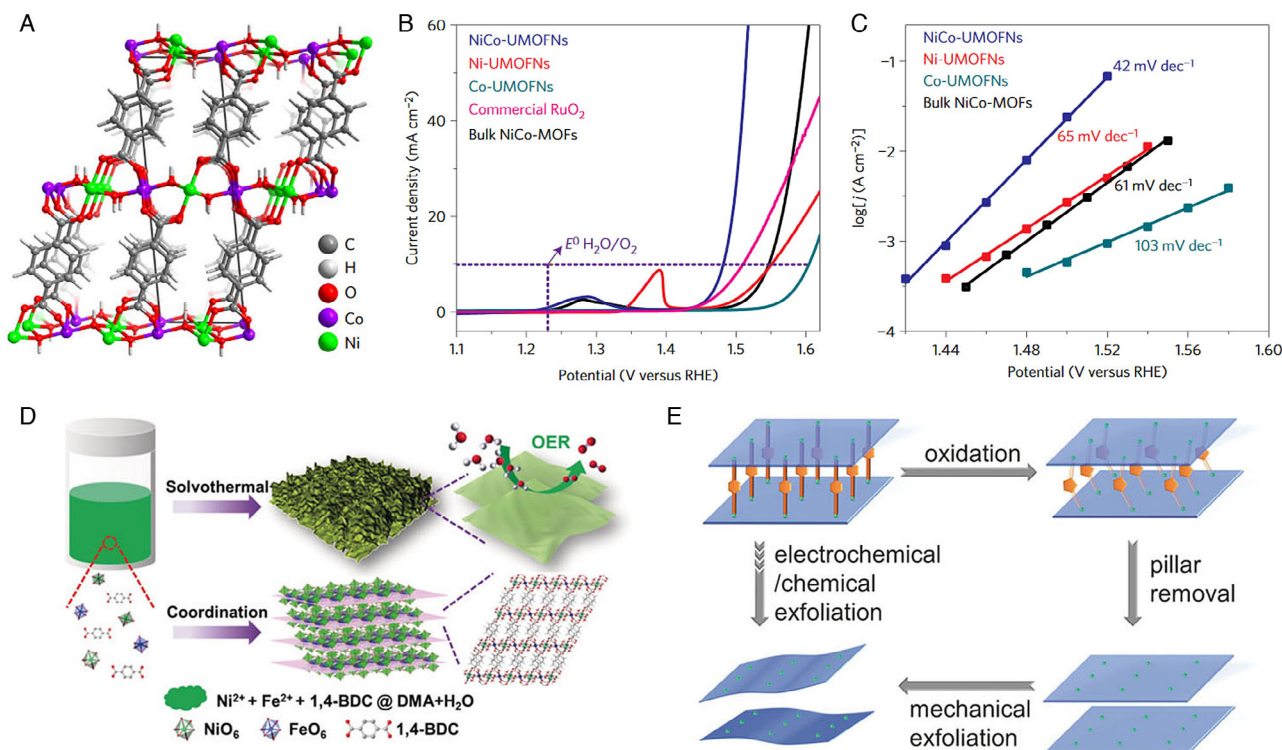


**Figure 23.** A) Crystal structure of NiCo-UMOFNs. B) LSV plots and C) Tafel slopes of NiCo-UMOFNs, Ni-UMOFNs, Co-UMOFNs, RuO<sub>2</sub>, and bulk NiCo-MOFs in O<sub>2</sub>-saturated 1.0 M KOH solution. Reproduced with permission.<sup>[206a]</sup> Copyright 2016, Nature Publishing Group. D) Illustration of the synthesis of ultrathin MOF nanosheets and their utilization for OER. Reproduced with permission.<sup>[206b]</sup> Copyright 2019, Wiley-VCH GmbH. E) Schematic illustration of the exfoliation of a pillared-layer MOF and selective pillar removal. Reproduced with permission.<sup>[206c]</sup> Copyright 2018, Wiley-VCH GmbH.

Also, the electronic coupling effect between unsaturated Co and Ni benefits the improvement of OER activity. This work demonstrated a new ultrathinning MOF strategy for improving OER activity.

The large-scale synthesis of MOF ultrathin nanosheets is still a challenging task. Li et al. developed a method for large-scale and bottom-up synthesis of bimetallic MOF nanosheets for efficient OER (Figure 23D).<sup>[172b]</sup> The bimetallic MOF nanosheet NiM-BDC-NS ( $M = \text{Fe, Al, Co, Mn, Zn and Cd}$ ) with a thickness of only several layers at large scale was prepared by a simple solvothermal method. All the MOF nanosheets were OER active, in which NiFe-BDC-NS demonstrated the best OER performance, with an overpotential ( $\eta_{10}$ ) of 221 mV and a Tafel slope of  $56 \text{ mV dec}^{-1}$  in  $1.0 \text{ M KOH}$  solution. The increased active sites of the ultrathin nanosheets and the synergistic effects in mixed metals contributed to the outstanding OER activity of MOF nanosheets. Huang et al. reported a new electrochemical/chemical exfoliation strategy for synthesizing MOF ultrathin nanosheet with outstanding OER activity and stability (Figure 23E).<sup>[172c]</sup> A redox-active pillar ligand 2,3-dihydroxy-1,4-benzenedicarboxylic acid ( $\text{H}_4\text{DHBDC}$ ) was utilized to construct a pillared-layer Co-based MOF (MCF-13 or 3D-Co). When MCF-13 was applied as OER catalysts in  $0.1 \text{ M KOH}$ , an in situ oxidation of the pillar ligands occurred, and a new 2D MOF ultrathin nanosheet was obtained (named as MCF-12 or 2D-Co-NS). 2D-Co-NS showed a low overpotential ( $\eta_{10}$ ) of 211 mV, a small Tafel slope of  $46 \text{ mV dec}^{-1}$ , and a high TOF of  $30 \text{ s}^{-1}$  at an overpotential of 300 mV in  $0.1 \text{ M KOH}$  solution.

Recently, Liu's group grew NiFe-NPC nanosheet arrays on porous NFs via simple solvothermal method and then treated the sample with UV light to get lattice-strained MOF arrays for outstanding OER activity (Figure 24A).<sup>[173]</sup> The interlayer spacing distance of lattice-strained NiFe-MOF is enlarged by

about  $0.2\text{--}0.5 \text{ \AA}$  based on the UV light treatment time as confirmed via high resolution transmission electron microscope (HRTEM). The enlargement of  $0.5 \text{ \AA}$  corresponds to the lattice expansion ratio of 4.3%, and the MOF is denoted as NiFe-NPC-4.3%. XPS spectroscopy indicated that the valence state of Ni is between +2 and +3, which is higher than the valence state in pristine NiFe-NPC (+2), indicating THAT the lattice strain modulation can redistribute the atomic and electronic configurations of Ni sites in NiFe-NPC. NiFe-NPC-4.3% exhibited the best OER activity with an overpotential of 210 mV at a high current density of  $200 \text{ mA cm}^{-2}$  and a Tafel slope of  $68 \text{ mV dec}^{-1}$  in  $0.1 \text{ M KOH}$ . The mass activity ( $2000 \text{ A g}_{\text{metal}}^{-1}$ ) at an overpotential of 300 mV of NiFe-NPC-4.3%, is about two orders of magnitude higher than those of pristine NiFe-NPC MOF and  $\text{RuO}_2$ , which are 116 and  $17 \text{ A g}_{\text{metal}}^{-1}$  at an overpotential of 300 mV, respectively (Figure 24B,C). After continuous OER for 200 h, the initial current density remains 97%, indicating the excellent stability (Figure 24D). Via operando synchrotron radiation Fourier-transform infrared spectroscopy (SR-FTIR), a key superoxide  $^*\text{OOH}$  intermediate emerging on  $\text{Ni}^{4+}$  sites was observed, confirming that the high valence  $\text{Ni}^{4+}$  species are the active sites and the OER was conducted via an efficient four-electron mechanistic pathway.

**MOF Composites:** Hetero-nanostructures have shown to be a promising strategy to improve the electrocatalytic activities due to the synergetic effects existing in the interfaces, which can enhance the charge transfer process and increase the intrinsic activity.<sup>[162b]</sup> MOFs can be easily composed of conductive materials or OER active catalysts to significantly enhance the OER performance.<sup>[174]</sup> Zhao et al. combined 2D MOF nanosheets (CoBDC) with electrically conductive  $\text{Ti}_3\text{C}_2\text{T}_x$  (the MXene phase) nanosheets to obtain an MOF composite ( $\text{Ti}_3\text{C}_2\text{T}_x/\text{CoBDC}$ ) with outstanding OER activity (Figure 25A).<sup>[174d]</sup>

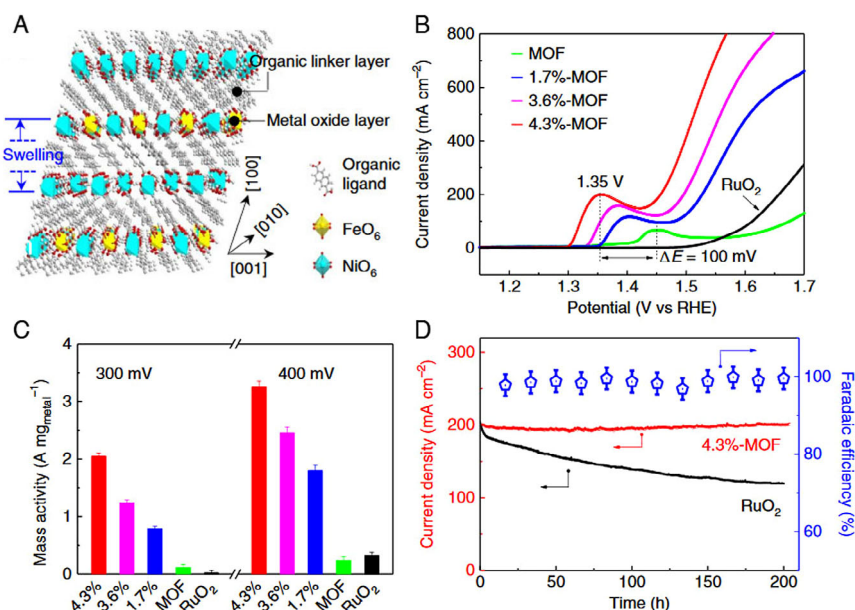


**Figure 24.** A) Schematic illustration of the crystal structure variation of NiFe MOFs under UV irradiation. B) LSV plots and C) mass activity of OER for the MOFs (pristine, 1.7%, 3.6% and 4.3%) and commercial  $\text{RuO}_2$  in  $\text{N}_2$ -saturated  $0.1 \text{ M KOH}$ . D) The stability of 4.3%-MOF and  $\text{RuO}_2$  and FE for 4.3%-MOF. Reproduced with permission.<sup>[173]</sup> Copyright 2019, Nature Publishing Group.

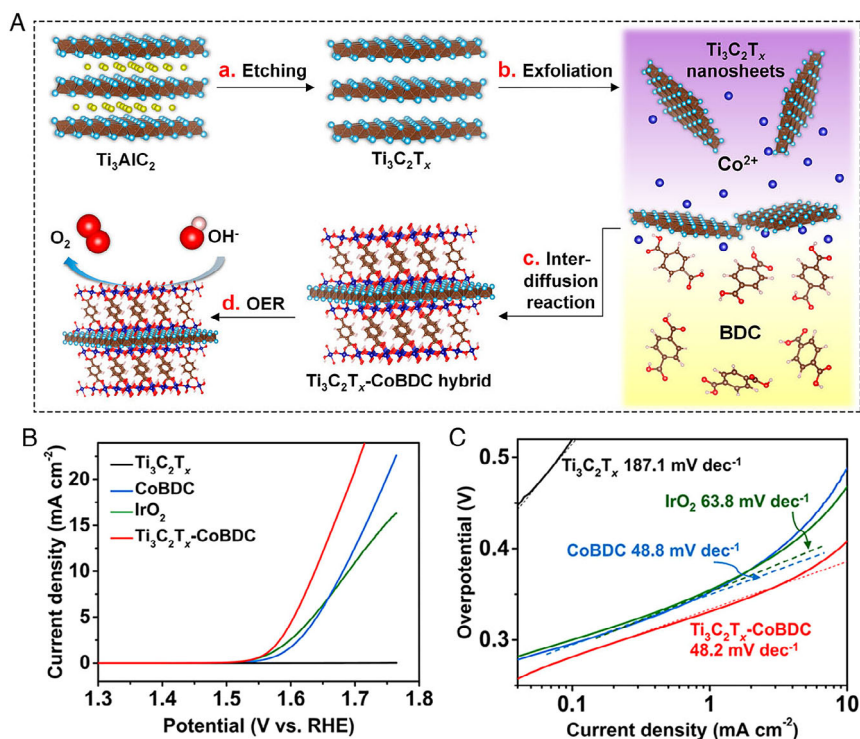


**Figure 25.** A) Illustration of fabrication of  $\text{Ti}_3\text{C}_2\text{T}_x/\text{CoBDC}$  hybrid for OER. B) LSV plots and C) Tafel slopes of  $\text{Ti}_3\text{C}_2\text{T}_x$ , CoBDC,  $\text{IrO}_2$ , and  $\text{Ti}_3\text{C}_2\text{T}_x\text{-CoBDC}$  hybrid in  $\text{N}_2$ -saturated 0.1 M KOH. Reproduced with permission.<sup>[208d]</sup> Copyright 2017, American Chemical Society.

The  $\text{Ti}_3\text{C}_2\text{T}_x/\text{CoBDC}$  nanocomposite was fabricated via an inter-diffusion reaction-assisted process.  $\text{Ti}_3\text{C}_2\text{T}_x/\text{CoBDC}$  exhibited improved OER performance compared with CoBDC nanosheets and  $\text{Ti}_3\text{C}_2\text{T}_x$  nanosheets, with an overpotential ( $\eta_{10}$ ) of 410 mV and a small Tafel slope of  $48.2 \text{ mV dec}^{-1}$  in 0.1 M KOH solution (Figure 25B,C). In the nanocomposite, CoBDC provided a large active surface area, whereas the electrically conductive  $\text{Ti}_3\text{C}_2\text{T}_x$  increased the charge transfer process across the heterointerface, making a synergistic effect to improve the OER activity.

### 3.2.3. Bifunctional Electrocatalysts for Water Splitting

Water-splitting process ( $2\text{H}_2\text{O} \rightarrow 2\text{H}_2 + \text{O}_2$ ) involves two half reactions: HER at the cathode and OER at the anode which require multiple-electron transfer, leading to large overpotentials. A cell voltage of 1.8–2.0 V is needed for commercial electrolyzers, which is much higher than the theoretical minimum value of 1.23 V for water splitting. The benchmark catalysts are Pt and its alloys for the HER and Ir/Ru oxides for the OER, which are all precious metal-based materials. However, the cost and scarcity of these catalysts limited their large-scale applications. For practical overall water splitting, both the HER and OER catalysts are conducted in the same electrolyte (usually strong acidic or basic solutions). Low-cost bifunctional electrocatalysts that can conduct both HER and OER in the same electrolyte are highly imperative, which can reduce the overpotential, cut the cost, and simplify the operating system. A great number of transition metal-based catalysts have been investigated as outstanding bifunctional electrocatalysts for overall

water splitting. Though MOFs are well studied for HER and OER catalysis, the applications of MOFs for overall water splitting are still rare (Table 5). The cell voltage at  $10 \text{ mA cm}^{-2}$  of the water electrolyzer cell and the electrocatalytic stability are the main parameters to evaluate the overall water-splitting performance of catalysts.

One exciting example was reported by Duan et al. by assembling an ultrathin bimetal MOF (NiFe-MOF) nanosheet array on porous NFs with superior electrocatalytic water-splitting performances (Figure 26).<sup>[143]</sup> The bimetal MOF electrodes demonstrated a HER overpotential ( $\eta_{10}$ ) of 134 mV, with a high TOF of  $2.8 \text{ s}^{-1}$  at 400 mV in 0.1 M KOH solution. For OER performance, an overpotential ( $\eta_{10}$ ) of 240 mV with a low Tafel slope of  $34 \text{ mV dec}^{-1}$  and a TOF of  $3.8 \text{ s}^{-1}$  at 400 mV was observed. To investigate the overall water-splitting performance, a two-electrode cell was built using NiFe-NPC nanosheet-loaded NFs as both the cathode and the anode, where  $\text{H}_2$  and  $\text{O}_2$  were generated, respectively. The electrolytic cell reached a voltage of 1.55 V at the current density of  $10 \text{ mA cm}^{-2}$ , which is smaller than that of cells using the benchmark precious metal-based  $\text{IrO}_2$  anodes and Pt/C cathodes (1.62 V at  $10 \text{ mA cm}^{-2}$ ). The in situ growth of NiFe-NPC nanosheet on NFs avoided the use of binders that usually have to adhere the electrocatalysts on the electrode, leading to enhanced catalyst-substrate contact and efficient electron transport. Also, the unique hierarchical architecture of MOF nanosheet arrays on NFs contributed to highly exposed active molecular metal sites, thus improving electrical conductivity and effective mass transport of gas products and electrolyte, resulting in the unexpected high electrocatalytic activity.



**Table 5.** Summary of MOF electrocatalysts for bifunctional overall water splitting.

MOFs	Electrolyte	Substrate	$\eta_{10}$ for HER [mV]	Tafel slope [mV dec <sup>-1</sup> ]	$\eta_{10}$ for OER [mV]	Tafel slope [mV dec <sup>-1</sup> ]	Electrolytic cell voltage at 10 mA cm <sup>-1</sup> [V]	Ref
NiFe-MOF	0.1 M KOH	NF	134	–	240	34	1.55	[143]
FeNi-BDC DMF	1.0 M KOH	NF	160	96.2	227@60 mA cm <sup>-2</sup>	37.4	1.58	[176]
Fe <sub>2</sub> Ni-MIL -88-NH <sub>2</sub>	1.0 M KOH	NF	87	35.2	240	58.8	1.56	[319]
MFN-MOFs	1.0 M KOH	NF	79	30.1	235@50 mA cm <sup>-2</sup>	55.4	1.495	[321]

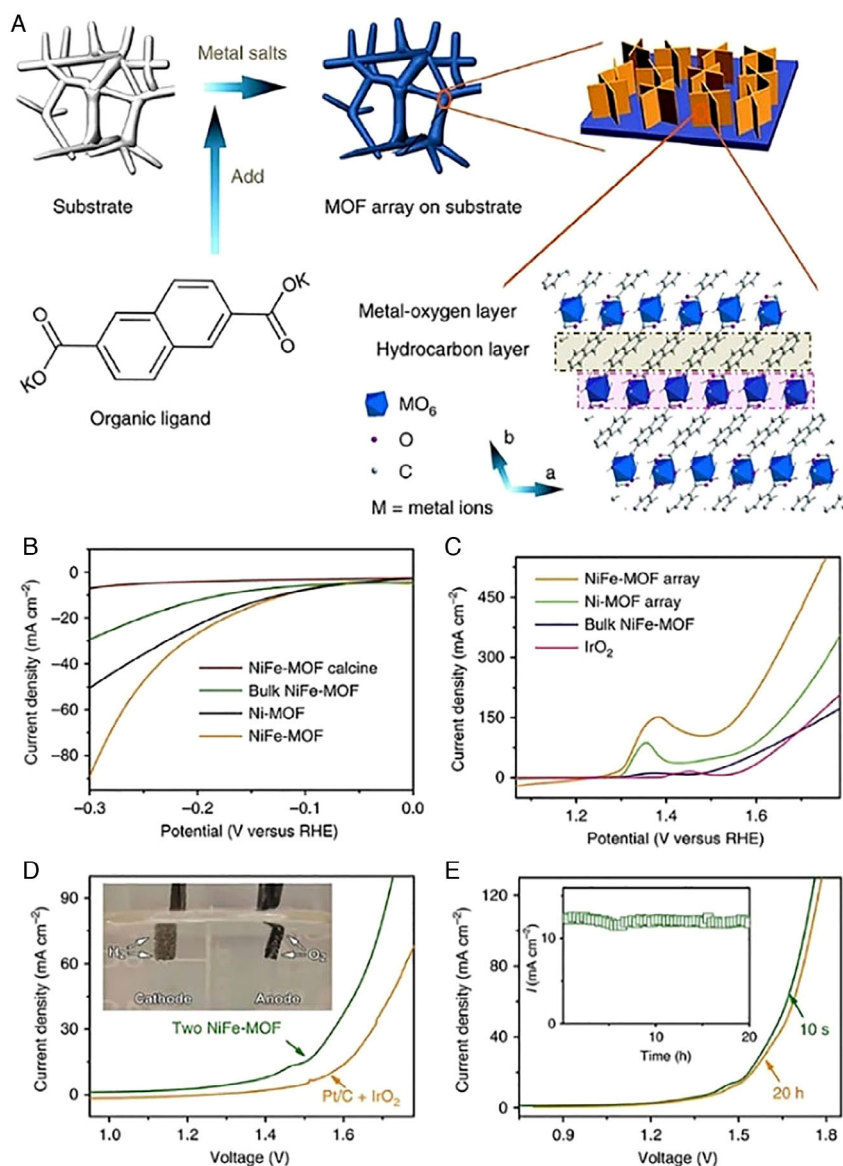


**Figure 26.** A) Synthetic approach of bimetallic NiFe-MOF nanosheet array. B) LSV plots obtained with NiFe-MOF, bulk NiFe-MOF, Ni-MOF, and calcined NiFe-MOF for HER. C) LSV plots obtained with NiFe-MOF, Ni-MOF, bulk NiFe-MOF, and IrO<sub>2</sub> for OER. D) LSV plots of a full electrolytic cell using two NiFe-MOF electrodes; the inset photograph shows the evolution of hydrogen and oxygen gas bubbles at the NiFe-MOF electrodes at an applied cell voltage of 1.6 V. E) LSV plots of the two-electrode electrolytic cell obtained before and after 20 h of chronoamperometric tests at a cell voltage of 1.5 V; the inset shows corresponding chronoamperometric plot. Reproduced with permission.<sup>[143]</sup> Copyright 2017, Nature Publishing Group.



Most of the MOF catalysts for HER and OER are investigated at low current densities (smaller than  $100 \text{ mA cm}^{-2}$ ), which are not practical for large-scale and industrial applications.<sup>[175]</sup> So, it is quite desirable to develop electrocatalysts that can perform good activity and stability at high current densities such as  $500 \text{ mA cm}^{-2}$  for practical water electrolyzers. Lin et al. deposited bimetal-based MOFs with BDC ligands (FeNi-BDC-DMF) on porous NFs substrate directly without binders.<sup>[176]</sup> The obtained FeNi-BDC-DMF/NF electrode demonstrated outstanding electrocatalytic activity for overall water splitting due to the hierarchical synergistic effects between MOFs and conductive NF substrates. The electrode exhibited an overpotential ( $\eta_{10}$ ) of 160 mV and a Tafel slope of  $96.2 \text{ mV dec}^{-1}$  for HER and a low overpotential (at  $60 \text{ mA cm}^{-2}$ ) of 227 mV and a Tafel slope of  $37.4 \text{ mV dec}^{-1}$  for OER in 1.0 M KOH solution. Low cell voltages of 1.58 and 1.90 V at a current density of 10 and  $400 \text{ mA cm}^{-2}$  were obtained using FeNi-BDC-DMF/NF as both the anode and the cathode.

Raja et al. grew bimetallic Fe and Ni-based MOFs (MFN-MOFs) onto conductive NFs as highly efficient bifunctional catalysts for overall water splitting at high current densities. The MFN-MOFs/NF electrode showed overpotentials of 235 mV and 294 mV at 50 and  $500 \text{ mA cm}^{-2}$  for OER and overpotentials of 79 and 234 mV at 10 and  $500 \text{ mA cm}^{-2}$  for HER in 1 M KOH solution, respectively. The electrolytic cell reached a voltage of 1.495 and 1.80 V at the current density of  $10 \text{ mA cm}^{-2}$  and  $500 \text{ mA cm}^{-2}$  respectively.

### 3.3. Electrocatalytic ORR

Oxygen electrocatalysis plays an important role in the fields of electrochemistry and catalysis in view of its significance in various electrochemical energy-conversion and -storage devices.<sup>[177]</sup> As the cathode reaction of fuel cell, the ORR suffers sluggish kinetics, which limits the overall device performance kinetically. Therefore, it is extremely urgent to investigate effective and

efficient ORR electrocatalysts for fuel cell technology development. To date, a wide range of non-noble materials, including nanocarbons, carbides/nitrides, their composites, metal alloys, etc., have been found electroactive toward the oxygen electrochemical processes.<sup>[178]</sup>

Based on the previous report, the local electronic structure and physical properties of catalysts are deemed as decisive factors for ORR activity. Some moieties, such as the heteroatom dopants and M–N sites, have been demonstrated as active sites in ORR. Incorporation of heteroatom dopants or metal atoms dopants is an efficient way to increase the active sites by tuning the electronic structure of catalysts.<sup>[179]</sup> However, the porosity and specific surface area are key factors in determining the density of the exposed aforementioned active sites on the surface of the catalyst. Thus, increasing porosity and surface area of the catalysts is beneficial for their ORR activity. Other than the earlier two points, several aspects should be considered such as the interface compatibility, the mass, and electron transfer ability, which are all related to the electrocatalytic performance of an ORR catalyst.<sup>[180]</sup>

With the mentioned theory-guided strategy, to some extent, it is accessible to design non-noble ORR catalysts rationally. MOFs hold great expectations as non-noble catalysts due to their tunable composition/structures. The large surface area and high porosity that are the typical features of MOFs are beneficial for the sufficient exposure of active sites and good transport properties of ORR-relevant species. Therefore, here we set our sights on MOF ORR electrocatalysts and present some relevant research progress nowadays (Table 6).

#### 3.3.1. Metalloporphyrin Catalysts

In nature, metalloporphyrin plays a key role in various proteins and enzymes for  $\text{O}_2$  binding, transport, and storage, electron transfer,  $\text{O}_2$  activation and utilization, and peroxide management and degradation.<sup>[181]</sup> It has been proved that the structural

**Table 6.** Summary of benchmark MOF electrocatalysts for ORR reactions.

Catalysts	$E_{\text{onset}}$ [V vs RHE]	$E_{1/2}$ [V vs RHE]	TS [mV $\text{dec}^{-1}$ ]	The transfer number	Electrolyte	Substrate	References
$[\text{Cu}_2(\text{OH})(\text{bpy})_2(\text{BTC})_3]$	0.5	–	–	3.8	0.1 M PB	GC-RDE	[322]
PcCu–O <sub>8</sub> –Co	–	0.83	61	3.93	0.1 M KOH	GC-RDE	[184]
Co–Al–PMOF	0.75	0.55 cal	–	2.9	0.1 M $\text{H}_2\text{SO}_4$	GC-RDE	[183]
Ni–CAT	–	0.236	–	3.7	0.1 M $\text{KClO}_4$ and 0.02 M PBS	GC-RDE	[323]
$\text{Ni}_3(\text{tha})_2$	0.82	0.67 cal	128	2.25	0.1 M KOH	GC-RDE	[188]
$\text{Co}_{0.27}\text{Ni}_{0.73}$ –CAT	0.47	0.34	104	3.94	0.1 M $\text{NaClO}_4$ and 0.02 M PBS	GC-RDE	[190]
PolyCuDAB–CB	0.862	0.76	–	3.57	0.1 M KOH	GC-RDE	[185]
$(\text{Fe–P})_n$ MOF	0.70	0.57 cal	–	1.93	0.1 M KOH	GC-RDE	[193]
Cu–BTC	0.71	0.56 cal	–	1.74	0.1 M KOH	GC-RDE	[191]
$\epsilon$ – $\text{MnO}_2$ /MOF(Fe)	0.84	0.64	117	3.8	0.1 M KOH	GC-RDE	[324]
$\text{CuS}(28 \text{ wt}\%)@$ Cu–BTC	0.91	0.73 cal	–	3.82	0.1 M KOH	GC-RDE	[325]
$(\text{G–dye–FeP})_n$	0.93	0.78 cal	–	3.82	0.1 M KOH	GC-RDE	[193]
NiFe–NPC–4.3%	0.92	0.83	70	3.8	0.1 M KOH	GC-RDE	[173]

arrangement of the porphyrins can greatly influence the ORR performance.<sup>[182]</sup> By adjusting the pore shape and polarity as well as the relative arrangement of porphyrins, Lions et al. reported  $[\text{Al}_2(\text{OH})_2(\text{Co}(\text{TCPP}))]$  (Co-Al-PMOF) catalyst which is the porphyrin metalated analog of  $[\text{Al}_2(\text{OH})_2(\text{H}_2\text{TCPP})]$  ( $\text{H}_2$ -Al-PMOF), as shown in Figure 27A.<sup>[183]</sup> The obtained samples possess microporous characters and a large BET surface area of  $1150 \text{ m}^2 \text{ g}^{-1}$ . In addition, Co-Al-PMOF displayed a further enhanced ORR activity. In an  $\text{O}_2$ -saturated  $0.1 \text{ M H}_2\text{SO}_4$ , Co-Al-PMOF exhibited an  $E_{\text{onset}}$  of  $0.75 \text{ V}$  whereas the  $E_{\text{onset}}$  of  $\text{H}_2$ -Al-PMOF and the discrete complex  $[\text{Co}(\text{TCPP})]$  (CoTCPP, insoluble and used as a heterogeneous catalyst) are  $0.72$  and  $0.75 \text{ V}$ , respectively. These results clarified that the use of ORR-active complexes as building blocks is available to develop higher electroactive ORR catalysts. The enhanced ORR activity can be attributed to the increased porosity of the extended framework.

Zhong et al. constructed a copper phthalocyanine-based 2D-conjugated MOF with cobalt bis(dihydroxy) complexes ( $\text{Co}-\text{O}_4$ ) as linkages ( $\text{PcCu}-\text{O}_8-\text{Co}$ ) through a solvothermal method, as shown in Figure 27B.<sup>[184]</sup> Thanks to the high coverage of electrochemically active Co centers, high conductivity, and highly ordered porous structure,  $\text{PcCu}-\text{O}_8-\text{Co}$  2D MOF mixed with CNTs exhibited a superior ORR activity (Figure 27C). It exhibited a half-wave potential ( $E_{1/2}$ ) of  $0.83 \text{ V}$  in an  $\text{O}_2$ -saturated  $0.1 \text{ M KOH}$ , and the electronic transfer number ( $n$  value) was calculated to be  $3.93$ , which is the record value among the reported intrinsic MOF electrocatalysts. Their work elucidated that optimizing the architecture and electronic structure of 2D MOFs is an effective way to enhance the ORR electroactivity.

### 3.3.2. Conductive MOF Catalysts

Although MOFs have been considered as the promising materials for electrocatalytic applications, the majority of MOFs cannot

be used directly in electrocatalytic applications because they are typically electrical insulators. Recently, some conductive MOFs have been developed as oxygen reduction catalysts.<sup>[185,186]</sup> Among them, conductive 2D-conjugated MOFs with unique 2D structure, enhanced electron transport capability, high utilization of exposed active sites, and the inherent merits of traditional MOFs attracted a lot of attention.<sup>[187]</sup> For example, Miner et al. reported  $\text{Ni}_3(\text{hexaiminotriphenylene})_2$  ( $\text{Ni}_3(\text{HITP})_2$ ) 2D MOF as an ORR electrocatalyst (Figure 28A).<sup>[188]</sup>  $\text{Ni}_3(\text{HITP})_2$  exhibited outstanding oxygen reduction activity and was comparable with most of the nonplatinum group metal electrocatalysts. In Figure 28B, the catalyst reduced oxygen with an onset potential of  $0.82 \text{ V}$  in  $\text{O}_2$ -saturated  $0.1 \text{ M KOH}$  aqueous solution. Notably,  $\text{Ni}_3(\text{HITP})_2$  also possessed excellent stability that it retained 88% of its initial current density over  $8 \text{ h}$  at  $0.77 \text{ V}$  and underwent no visible morphological degradation during prolonged electrochemical cycling. The notable ORR activity may result from the defined active sites ( $\text{Ni}-\text{N}_4$ ) as well as the 2D porous structure of  $\text{Ni}_3(\text{HITP})_2$ , which is able to increase the density and facilitate easy access to the catalytic active sites. Thus Miner et al. drew the conclusion that a well-defined, intrinsically conductive MOF is available to be a powerful platform for the development of tunable ORR electrocatalysts.

Recently, conductive 2D hexagonal MOF layers (called M-CAT;  $\text{M}=\text{Co}, \text{Ni}$  or  $\text{Cu}$ ) have been widely used in the electrocatalysis, which were constructed by the hydrothermal reaction between 2,3,6,7,10,11-hexahydroxytriphenylene (HHTP) and a divalent metal ion, such as  $\text{Co}^{2+}$ ,  $\text{Ni}^{2+}$ , or  $\text{Cu}^{2+}$ .<sup>[189]</sup> However, most research has been regarded on the material preparation related to monometallic M-CATs and their electrochemical utilization. Yoon et al. put forward a strategy for property enhancement via mixing the metal components (Figure 28C).<sup>[190]</sup> Importantly, compared with their monometallic counterparts, Co-CAT and Ni-CAT, the  $\text{Co}_{0.27}\text{Ni}_{0.33}$ -CATs catalyst displayed

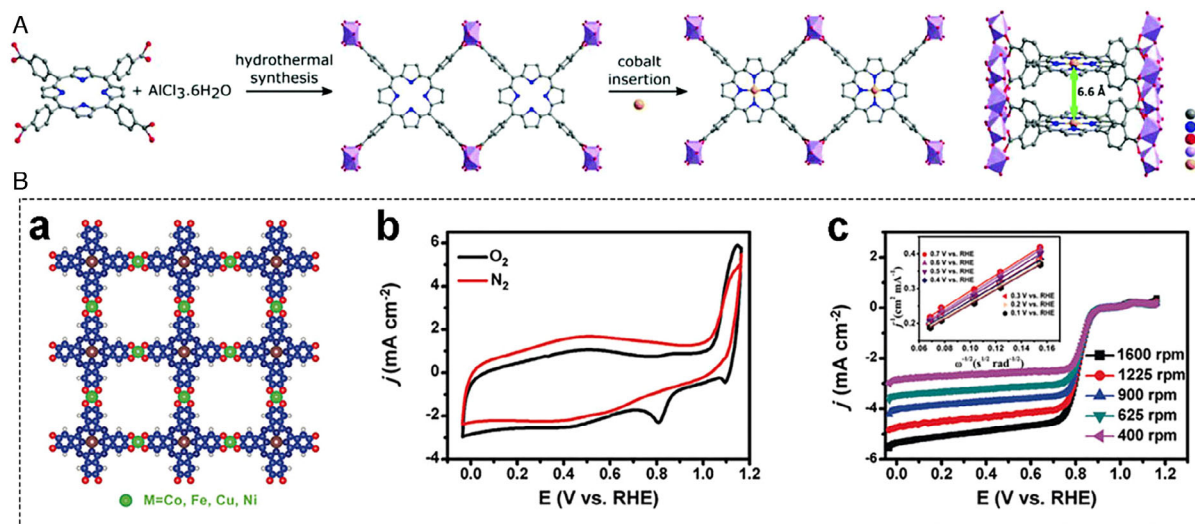


**Figure 27.** A) Illustration of the fabrication process and structure of Co-Al-PMOF. Reproduced with permission.<sup>[183]</sup> Copyright 2017, The Royal Society of Chemistry. B) a) The structure of  $\text{PcCu}-\text{O}_8-\text{Co}$ . b) CV curves of  $\text{PcCu}-\text{O}_8-\text{Co}/\text{CNT}$  in  $\text{N}_2$ - and  $\text{O}_2$ -saturated  $0.1 \text{ M KOH}$ . c) ORR polarization curves of  $\text{PcCu}-\text{O}_8-\text{Co}/\text{CNT}$  at different rotating speeds (inset: corresponding K-L plots of  $\text{PcCu}-\text{O}_8-\text{Co}/\text{CNT}$ ). Reproduced with permission.<sup>[184]</sup> Copyright 2019, Wiley-VCH GmbH.

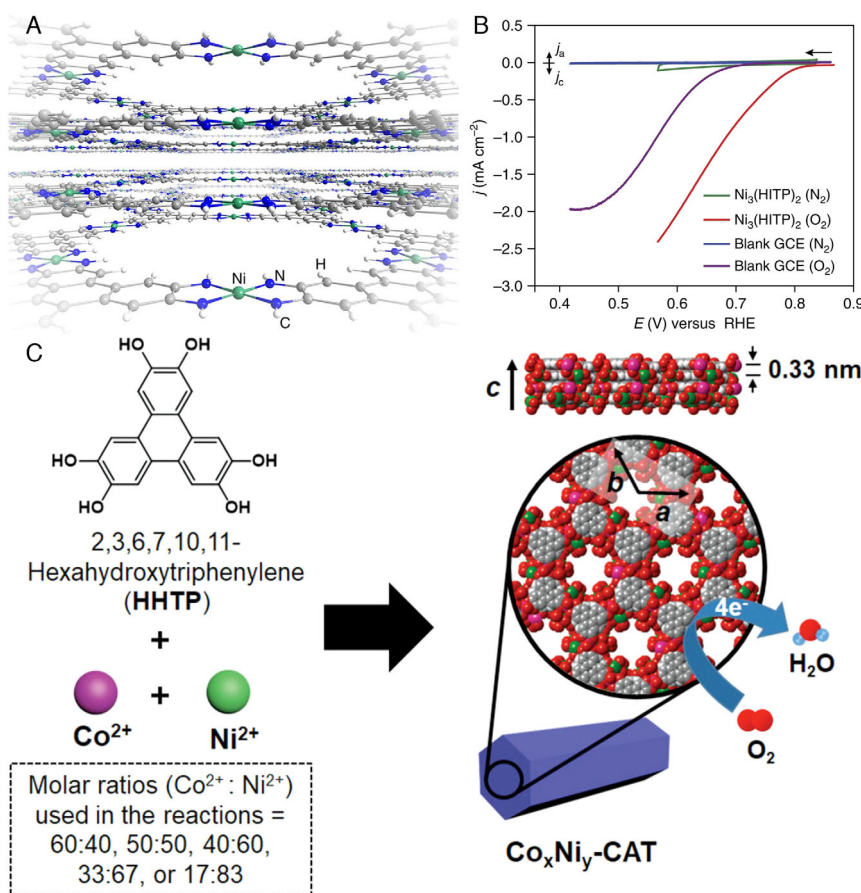


**Figure 28.** A) Scheme of 2D-layered structure of  $\text{Ni}_3(\text{HITP})_2$ . B) Polarization curves of  $\text{Ni}_3(\text{HITP})_2$  in  $\text{N}_2$ - and  $\text{O}_2$ -saturated 0.1 M KOH. Reproduced with permission.<sup>[188]</sup> Copyright 2016, Nature Publishing Group. C) Schematic illustration of the construction of bimetallic 2D  $\text{Co}_x\text{Ni}_y\text{-CAT}$ s. Reproduced with permission.<sup>[190]</sup> Copyright 2019, Wiley-VCH GmbH.

obviously enhanced ORR activity. In the  $\text{O}_2$ -saturated 0.1 M  $\text{NaClO}_4$  and 0.02 M PBS electrolyte solutions, the acquired bimetallic  $\text{Co}_{0.27}\text{Ni}_{0.33}\text{-CAT}$ s exhibited an onset potential and half-wave potential of 0.46 and 0.34 V, respectively. The electron transfer number of  $\text{Co}_{0.27}\text{Ni}_{0.73}\text{-CAT}$  was found to be 3.95. The enhanced ORR activity may be attributed to the abundant active sites of  $\text{Co}_{0.27}\text{Ni}_{0.33}\text{-CAT}$ s and the high conductivity of two monometallic M-CATs.

### 3.3.3. MOF Composite Catalysts

It has been reported that modifying the interface properties of the ORR catalysts is able to exert synergistic functions to the ORR.<sup>[180]</sup> Especially, constructing graphene, metal sulfide composites, and other hierarchical structures is deemed as an efficient way. In the consideration of improving the ORR activity, Cho et al. reported a new method for fabricating various amounts of CuS NPs (nano-CuS) in/on a 3D Cu-MOF,  $[\text{Cu}_3(\text{BTC})_2 \cdot (\text{H}_2\text{O})_3]$ .<sup>[191]</sup> The electrical conductivity and the porosity of the composites can be tuned by the amount of nano-CuS. As the content of nano-CuS increases, the electrical conductivity of the modified Cu-MOF increases exponentially by up to  $10^9$ -fold, whereas its

porosity decreases. In the present composite materials,  $\text{CuS}(28 \text{ wt}\%)\text{@Cu-BTC}$  exhibits the best ORR activity with an onset potential of 0.91 V, a quasi-four-electron transfer pathway ( $n = 3.82$ ), and a kinetic current density of  $11.3 \text{ mA cm}^{-2}$  at 0.55 V. The enhanced ORR activity is due to the synergistic effect of the two different materials that plays a key role in terms of conductivity and porosity, respectively.

Among 2D materials, graphene which possesses unique structure and brilliant electron conductivity has drawn a great deal of attention.<sup>[192]</sup> Not only can it be modified to be a metal-free catalyst, but it also can be a support for developing graphene-based composite catalysts. Jahan et al. prepared electrocatalytically active graphene-porphyrin MOF composites as ORR catalysts by the combination of  $(\text{Fe-P})_n$  MOF and RGO sheets that are functionalized with donor- $\pi$ -acceptor dye (G-dye).<sup>[193]</sup> The obtained catalyst (G-dye- $\text{FeP}$ ) $_n$  MOF exhibited a higher ORR activity and stability. In 0.1 M KOH solution saturated with  $\text{O}_2$ , (G-dye 50%- $\text{FeP}$ ) $_n$  MOF displayed the best ORR activity as well as high  $4e^-$  selectivity. Apart from the activity, the durability of (G-dye 50%- $\text{FeP}$ ) $_n$  is also superior; it exhibits a very slow attenuation after a 39% loss in its initial current density at a constant voltage of  $-0.23 \text{ V}$  in alkaline media. These superiorities can be explained by the unique structure of the hybrid in which G-dye

interconnects with Fe-MOF in a 3D manner and the synergistic effect between them afforded better ORR activity.

### 3.3.4. Other MOF Catalysts

In addition to the three types described earlier, inducing lattice strain in the structure also can enhance the electroactivity of the catalysts toward ORR. Cheng et al. developed lattice-strained transition metal MOF materials by an additional UV light treatment for both the enhancement of OER and ORR.<sup>[173]</sup> The sample that was treated with 12 h of UV irradiation (NiFe-NPC-4.3%) exhibited the best ORR activity with an onset potential of 0.92 V, a half-wave potential of 0.83 V, as well as a Tafel slope of 70 mV dec<sup>-1</sup>, which are superior to those of commercial Pt/C (a half-wave potential of 0.81 V and a Tafel slope of 76 mV dec<sup>-1</sup>). The electron transfer number of the 4.3%-MOF was estimated to be 3.8, indicating an efficient 4e<sup>-</sup>-dominated ORR pathway. The ORR improvement was attributed to the redistribution of atomic and electronic configurations of Ni sites in NiFe-NPC via lattice strain modulation. Their work shed light to a new avenue to construct efficient and low-cost materials for oxygen catalysis. Meanwhile, it can deepen our understanding of the operating mechanism.

## 3.4. Electrocatalytic CO<sub>2</sub>RR

CO<sub>2</sub>RR is one of the most promising approaches to reduce the greenhouse gas CO<sub>2</sub> into valuable chemicals, such as CO, CH<sub>4</sub>, C<sub>2</sub>H<sub>4</sub>, HCOOH, oxalic acid, and alcohols.<sup>[2,194]</sup> Yet, the essential chemical inertness of CO<sub>2</sub> and the participation of multiple electrons lead to high thermodynamic and kinetic energy barriers for CO<sub>2</sub>RR and often low conversion efficiency and poor selectivity toward aimed chemicals. MOFs can be designed to have open metal sites, embedded electroactive molecules, functionalized ligands, specific heteroatoms, and tunable porosity. Also, the large BET surface area of MOFs enables strong adsorption ability of CO<sub>2</sub> molecules and fast mass transport, which are quite essential for CO<sub>2</sub>RR. In the past several years, MOFs have been investigated to be promising CO<sub>2</sub>RR electrocatalysts with high FE and selectivity (Table 7).<sup>[3,195]</sup>

Cu is one of the most promising metallic CO<sub>2</sub>RR catalysts to convert CO<sub>2</sub> to valuable hydrocarbons such as CH<sub>4</sub>, C<sub>2</sub>H<sub>4</sub>, and ethanol.<sup>[196]</sup> Yet, Cu showed poor selectivity for specific carbon products.<sup>[197]</sup> The molecular size refinement effect in MOF pores may be beneficial to improve the catalytic selectivity of CO<sub>2</sub>RR. Cu-MOFs, especially Cu<sub>2</sub>(COO)<sub>4</sub> paddle-wheel cluster-based MOFs that possess open metal sites, are promising

**Table 7.** The summary of MOFs for CO<sub>2</sub>RR.

Electrocatalysts	Main product	Peak FE [%]	Potential [V]	TOF [s <sup>-1</sup> ]	Electrolyte	Substrate	References
CR-MOF	HCOOH	30	-1.20 standard hydrogen electrode (SHE)	—	0.5 M KHCO <sub>3</sub>	CP	[198]
Cu-BTC	Oxalic acid	51	-2.2 SHE	—	0.01 M TBATFB/DMF	GC	[199]
Cu-BTC	ethanol	10.3	-0.70 SHE	0.02	0.5 M KHCO <sub>3</sub>	CP	[200]
CuAdeAce	MeOH	1.2	-1.55 SHE	0.002	0.5 M KHCO <sub>3</sub>	CP	[200]
HKUST-1	CH <sub>4</sub>	27	-1.16 RHE	—	0.5 M KHCO <sub>3</sub>	GC	[202]
Al <sub>2</sub> (OH) <sub>2</sub> TCPP-Co	CO	76	-0.7 RHE	0.056	0.5 M K <sub>2</sub> CO <sub>3</sub>	Carbon disk	[205]
Fe-MOF-525	CO	50	-1.30 normal hydrogen electrode (NHE)	0.018	1.0 M TBATF <sub>6</sub> / CH <sub>3</sub> CN	FTO	[206]
PCN-222(Fe)	CO	91	-0.60 RHE	0.014	0.5 M KHCO <sub>3</sub>	CP	[207]
Cu <sub>2</sub> (Cu-TCPP)	HCOO <sup>-</sup>	68.4	-1.55 Ag/AgCl	0.566	0.5 M EminBF <sub>4</sub> / CH <sub>3</sub> CN	FTO	[208]
NNU-15	CO	99.2	-0.6 V RHE	0.011	0.5 M KHCO <sub>3</sub>	CP	[326]
Co-PMOF	CO	98.7	-0.8 RHE	0.46	0.5 M KHCO <sub>3</sub>	Carbon cloth	[204]
Zn-BTC	CH <sub>4</sub>	80	-2.0 SHE	—	BmimBF <sub>4</sub>	CP	[209]
ZIF-7	CO	23.8	-1.10 RHE	—	0.25 M K <sub>2</sub> SO <sub>4</sub>	CP	[210]
ZIF-8	CO	81	-1.10 RHE	—	0.25 M K <sub>2</sub> SO <sub>4</sub>	CP	[210]
ZIF-108	CO	63.5	-1.10 RHE	—	0.25 M K <sub>2</sub> SO <sub>4</sub>	CP	[210]
SIM-1	CO	66.6	-1.10 RHE	—	0.25 M K <sub>2</sub> SO <sub>4</sub>	CP	[210]
ZIF-A-LD	CO	90.57	-1.10 RHE	—	0.1 M KHCO <sub>3</sub>	CP	[211]
Cu@NU-1000	HCOO <sup>-</sup>	28	-0.82 RHE	—	0.1 M NaClO <sub>4</sub>	FTO	[214]
Cu <sub>2</sub> O/Cu-MOF	CH <sub>4</sub>	63.2	-1.71 RHE	—	0.1 M KHCO <sub>3</sub>	GC	[215]
Ag <sub>2</sub> O/ZIF-L	CO	80.5	-1.2 RHE	—	0.25 M K <sub>2</sub> SO <sub>4</sub>	CP	[216]
Ag@Al-PMOF	CO	55.8	-1.1 RHE	0.014	0.1 M KHCO <sub>3</sub>	GC	[217]
Enzyme FDH@NU-1006	HCOOH	—	-1.1 Ag/AgCl	—	0.5 M Tris-buffered solution	FTO	[327]
Zn-ReSURMOF	CO	93	-1.60 NHE	0.192	0.1 M TBAH/CH <sub>3</sub> CN	FTO	[328]
2D Ni-ZIF	CO	78.8	-0.85 RHE	0.214	0.5 M KHCO <sub>3</sub>	CP	[329]



electrocatalysts for CO<sub>2</sub>RR.<sup>[198,199]</sup> In 2012, Cu-MOFs CR-MOF<sup>[198]</sup> and Cu-BTC (HKUST-1)<sup>[199]</sup> were reported to convert CO<sub>2</sub> into HCOOH (FE = 30%) and oxalic acid (FE = 51%) via electrocatalysis respectively, which represent the first examples of MOFs for CO<sub>2</sub>RR applications. Later, Albo et al. systematically studied the CO<sub>2</sub>RR activity of two Cu-MOFs (HKUST-1 and CuAdeAce) and two Cu-based metal organic aerogels (MOAs) supported on gas diffusion electrodes.<sup>[200]</sup> HKUST-1 contains Cu paddle-wheel clusters with open metal sites which act as adsorption sites for CO<sub>2</sub>. However, Cu CuAdeAce is based on dicopper paddle-wheel units similar to HKUST-1 but without uncoordinated metal sites. Both HKUST-1 and CuAdeAce are active for CO<sub>2</sub>RR in CO<sub>2</sub>-saturated 0.5 M KHCO<sub>3</sub> aqueous solutions. Recently, Yi et al. proposed the in situ synthesis of Cu<sub>2</sub>O(111) QDs on porous conductive Cu-based MOFs (CuHHTP) to stable key reaction intermediates, which enhance the sluggish kinetics and achieve the high selectivity of CH<sub>4</sub> in CO<sub>2</sub>RR.<sup>[201]</sup> The Cu<sub>2</sub>O QDs transformed by partial Cu<sup>2+</sup> centers in CuHHTP exposed sole (111) crystalline planes and liberated hydroxyl groups from the uncoordinated HHTP ligand. Thus, the obtained Cu<sub>2</sub>O@CuHHTP exhibited a high FE of 73 % and a partial current density of 10.8 mA cm<sup>-2</sup>.

Stability is still one issue that has to be addressed for Cu-MOFs, as most Cu-MOFs are not stable in water. In situ and operando characterization techniques are advanced powerful tools to examine the local coordination environment changes of catalysts during reaction conditions, identify the real active sites, and illustrate the catalytic mechanism. Recently, Weng et al. investigated the CO<sub>2</sub>RR performance of Cu-MOF HKUST-1 and identified the active sites via in situ and operando X-ray absorption spectroscopy (XAS), as shown in Figure 29A.<sup>[202]</sup> HKUST-1 can transform CO<sub>2</sub> into methanol with a high FE of 27% at a reduction potential of -1.16 V vs RHE in CO<sub>2</sub>-saturated 0.5 M KHCO<sub>3</sub> aqueous solution (Figure 29B). After

CO<sub>2</sub>RR, the scanning electron microscopy (SEM) characterization demonstrated that the submicron-sized morphology of HKUST-1 changed to dendritic nanostructures. Powder X-ray diffraction (PXRD) patterns showed the coexistence of Cu<sub>2</sub>O and Cu. In situ and operando extended X-ray absorption fine structure (EXAFS) characterization revealed that at the reduction potential of -1.06 V, the EXAFS spectra of HKUST-1 were similar to that of the Cu metal, indicating the formation of Cu metal. When the electrode potential was back to 0.64 V, the EXAFS spectra confirmed the existence of Cu<sub>2</sub>O, suggesting that the metallic Cu that originated from HKUST-1 was oxidized to form Cu<sub>2</sub>O. Thus, the in situ-generated Cu nanomaterials were the real catalytic active sites for CO<sub>2</sub>RR in HKUST-1.

Metal (Co, Fe, Ni etc.) porphyrin molecular compounds with M-N<sub>4</sub> coordination environment were proven to demonstrate high activity for CO<sub>2</sub>RR.<sup>[203]</sup> Inspired by the M-porphyrin molecules, M-porphyrin-based MOFs were investigated as potential catalysts for CO<sub>2</sub>RR.<sup>[204–208]</sup> Kornienko et al. reported a Coporphyrin-based MOF Al<sub>2</sub>(OH)<sub>2</sub>TCPP-Co that demonstrated high CO<sub>2</sub>RR activity for reduction of CO<sub>2</sub> to CO.<sup>[205]</sup> The MOF thin film was deposited onto conductive carbon disk electrodes via the atomic layer deposition (ALD) method. Al<sub>2</sub>(OH)<sub>2</sub>TCPP-Co electrode with optimized thickness showed excellent CO<sub>2</sub>RR activity, with a high FE of 76% for CO at a reduction potential of -0.70 V vs. RHE and a high TOF of 0.056 s<sup>-1</sup> in CO<sub>2</sub>-saturated 0.5 M K<sub>2</sub>CO<sub>3</sub> aqueous solution. In situ spectroelectrochemical measurements revealed that the reduced Co(I) from Co(II) is the active site for CO<sub>2</sub>RR. Later, Hod et al. synthesized Fe-porphyrin based MOF (Fe-MOF-525) thin films on FTO substrates via the electrochemical deposition method for CO<sub>2</sub>RR.<sup>[206]</sup> Fe-MOF-525 film electrode showed CO<sub>2</sub>RR activity for converting CO<sub>2</sub> to CO, with an FE of 50% at a reduction potential of -0.70 V vs RHE and a TOF of 0.018 s<sup>-1</sup> in CO<sub>2</sub>-saturated 0.1 M TBAPF<sub>6</sub> acetonitrile electrolyte. However, the electrocatalytic

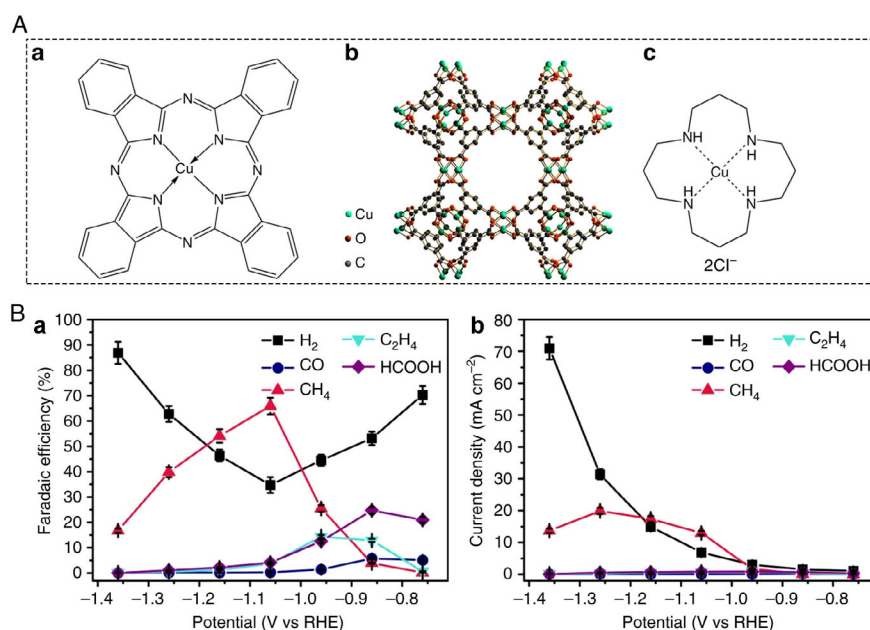


**Figure 29.** A) Molecular structures of three Cu complex materials: a) CuPc, b) HKUST-1, and c) [Cu(cyclam)]Cl<sub>2</sub>. B) a) FE and b) partial current densities of CuPc for CO<sub>2</sub> electroreduction reaction. Reproduced with permission.<sup>[202]</sup> Copyright 2018, Nature Publishing Group.

stability of Fe-MOF-525 film electrode was not good, as after electrocatalysis for 5 h, the MOF was found to degrade. Dong et al. synthesized Fe-porphyrin MOF PCN-222(Fe) as CO<sub>2</sub>RR catalyst.<sup>[207]</sup> The PCN-222(Fe)/carbon black electrode exhibited high CO<sub>2</sub>RR activity for the conversion of CO<sub>2</sub> to CO, with a high FE of 91% at a reduction potential of −0.60 V versus RHE and a TOF of 0.014 s<sup>−1</sup> in CO<sub>2</sub>-saturated 0.5 M KHCO<sub>3</sub> aqueous solution. PCN-222(Fe) also demonstrated high catalytic stability, as confirmed via PXRD without loss of crystallinity after 10 h of electrolysis. Recently, Wu et al. designed a Cu paddle-wheel cluster-based Cu-porphyrin MOF nanosheet [Cu<sub>2</sub>(Cu-TCPP)] deposited on conductive fluorine-doped tin oxide (FTO) substrate for CO<sub>2</sub>RR.<sup>[208]</sup> The Cu<sub>2</sub>(Cu-TCPP) electrode showed outstanding activity for formate production with an FE of 68.4% and a superior TOF of 0.566 s<sup>−1</sup> at a reduction potential of −1.55 V versus Ag/AgCl in CO<sub>2</sub>-saturated 0.5 M EmimBF<sub>4</sub> acetonitrile electrolyte. Due to the instability of Cu paddle-wheel clusters, Cu<sub>2</sub>(Cu-TCPP) was decomposed into Cu and Cu<sub>x</sub>O as confirmed via PXRD and XPS analysis after catalysis. The Cu<sub>x</sub>O/Cu-porphyrin complex composite was believed to mainly contribute to the CO<sub>2</sub>RR performance.

Lan and colleagues combined reductive Zn-ε-Keggin POM and M-porphyrin to form POM-metalloporphyrin MOFs (M-PMOF, M = Co, Fe, Ni, Zn) for highly selective CO<sub>2</sub>RR.<sup>[204]</sup> The introduction of POMs benefited the electron collecting and donating, and the electron mobility in MOFs. All the M-PMOFs were CO<sub>2</sub>RR active for converting CO<sub>2</sub> to CO, among which Co-PMOF demonstrated the best catalytic activity. Co-PMOF electrode showed an ultrahigh FE of 98.7% for CO at a reduction potential of −0.80 V vs RHE and a high TOF of 0.46 s<sup>−1</sup> in CO<sub>2</sub>-saturated 0.5 M KHCO<sub>3</sub> aqueous solution. Also, Co-PMOF showed high catalytic stability with negligible decay in activity after 36 h. DFT calculations revealed that the excellent CO<sub>2</sub>RR performance was attributed from synergistic effects of reductive POMs and Co-porphyrin, whereas the Co centers in the porphyrin species were the active sites for CO<sub>2</sub>RR. This work demonstrated that POM-based MOFs could be promising catalysts for CO<sub>2</sub>RR. It should be noted that POM-based MOFs exhibited outstanding HER activity, which acts a competing reaction for CO<sub>2</sub>RR. The HER process should be avoided via rational design in the synthesis of POM-MOFs for CO<sub>2</sub>RR applications.

Except the metal active sites in MOFs, the organic ligands may also act as catalytic centers. Zn(II) has a fully occupied 3d orbital; thus, Zn-MOFs are ideal platforms to study the role of ligands in electrocatalysis. Recently, Zn-based MOFs have also been investigated for CO<sub>2</sub>RR.<sup>[209–212]</sup> Jiang et al. systematically investigated the CO<sub>2</sub>RR performances of Zn-ZIFs (ZIF-8, ZIF-108, ZIF-7, and SIM-1) with the same SOD (sodalite) topology but different organic ligands (Figure 30A).<sup>[210]</sup> All the four ZIFs are CO<sub>2</sub>RR active for converting CO<sub>2</sub> to CO in CO<sub>2</sub>-saturated 0.25 M K<sub>2</sub>SO<sub>4</sub> aqueous solution, among which ZIF-8 showed the highest CO<sub>2</sub>RR performance, with a high FE of 81% for CO at a reduction potential of −1.10 V vs RHE. However, the FEs for ZIF-7, ZIF-108, and SIM-1 are 23.8%, 63.5%, and 66.6%, respectively (Figure 30B). The morphology and the Zn/N ratio in ZIF-8 after CO<sub>2</sub>RR showed no change, indicating the strong stability of ZIF-8 in CO<sub>2</sub>RR. In Figure 30C,D, in situ XAS characterization and DFT calculations revealed that the sp<sup>2</sup> C atoms of the imidazolate ligands in ZIFs are the real active sites for CO<sub>2</sub>RR. This work presented the first report of ligands as active sites for CO<sub>2</sub>RR

in MOFs, pointing out a new strategy to improve the CO<sub>2</sub>RR activity of MOFs by tuning the organic ligands. Followed this work, Dou et al. proposed a new strategy of ligand doping to boost the CO<sub>2</sub>RR performances of MOFs (Figure 30E,F).<sup>[211]</sup> 1,10-phenanthroline, a strong electron-donating ligand, was introduced to the vacant Zn sites of thermal-activated ZIF-8 (ZIF-8-A-LD) as an efficient CO<sub>2</sub>RR electrocatalyst, as shown in Figure 30E. Raman, EPR, and XANES spectra confirmed the charge transfer from phenanthroline to Zn centers and imidazole ligands. ZIF-8-A-LD with 20 wt% of carbon black to improve the conductivity was deposited on carbon paper (CP) electrode and CO<sub>2</sub>-saturated 0.1 M KHCO<sub>3</sub> aqueous solution was used as the electrolyte. Constant potential electrolysis (CPE) showed that ZIF-8-A-LD with an optimized doping amount of phenanthroline exhibited quite a high FE (90.57%) for CO at a reduction potential of −1.10 V vs RHE. However, the pristine ZIF-8 demonstrated poor activity, with an FE for CO lower than 50%. DFT calculations in Figure 30F revealed that the sp<sup>2</sup> C atoms in the imidazole ligand are still the main active sites for CO<sub>2</sub>RR, whereas the charge transfer from phenanthroline increases the charge density of the adjacent active sites in ZIF-8 and facilitates the generation of \*COOH intermediate. As a result, the CO<sub>2</sub>RR performance of ZIF-8-A-LD was efficiently improved compared with the pristine ZIF-8.

2D conductive MOFs have shown outstanding electrocatalytic activities in water splitting and ORR, yet there are still no reports of their applications in CO<sub>2</sub>RR, which may result from their poor stability under high overpotentials. Tian et al. investigated potential applications of several metal bis(dithiolene) MOF nanosheets (M<sub>3</sub>C<sub>12</sub>S<sub>12</sub>, M: Fe, Co, Ni, Ru, Rh, and Pd) for CO<sub>2</sub>RR via comprehensive DFT calculations.<sup>[213]</sup> The results indicated that Rh<sub>3</sub>C<sub>12</sub>S<sub>12</sub> nanosheets exhibited the highest CO<sub>2</sub>RR catalytic activity among all the studied MOFs with CH<sub>4</sub> as the main product, resulting from the low limiting potential (−0.43 V) and a low activation barrier of 1.60 eV. This work suggests that 2D conductive MOFs could be promising CO<sub>2</sub>RR catalysts with high activity via metal atom modulations.

Composing MOFs with other electrocatalytic active catalysts is an efficient approach to boost the catalytic performance. Several NPs such as Ag, Ag<sub>2</sub>O, Cu, and Cu<sub>2</sub>O have been combined with MOFs to form MOF composites with improved CO<sub>2</sub>RR activity.<sup>[214–218]</sup> Kung et al. embedded Cu NPs into a Zr-MOF (NU-1000) thin film via solvothermal deposition of single-site Cu(II) into MOFs followed by electrochemical reduction to metallic Cu NPs in the channels of NU-1000.<sup>[214]</sup> The obtained Cu@NU-1000 composite electrode demonstrated high CO<sub>2</sub>RR activity, with an FE of 28% for HCOOH at a reduction potential of −0.82 V vs RHE in CO<sub>2</sub>-saturated 0.1 M NaClO<sub>4</sub> aqueous solution. Both the morphology and crystallinity of the composites remained unchanged after CO<sub>2</sub>RR, indicating its high electrocatalytic stability.

Recently, Guntern et al. developed a new approach to synthesize metal NCs (NCs)/MOF hybrids as efficient CO<sub>2</sub>RR catalysts.<sup>[217]</sup> Ag NCs were first coated with Al<sub>2</sub>O<sub>3</sub> via ALD method on glassy carbon substrate and then treated with TCPP ligands by converting the Al<sub>2</sub>O<sub>3</sub> into Al-based MOF (Al-PMOF), and the final Ag@Al-PMOF hybrid thin films were formed. The Ag@Al-PMOF electrode showed excellent CO<sub>2</sub>RR performance, with an FE of 55.8% for CO at a reduction potential

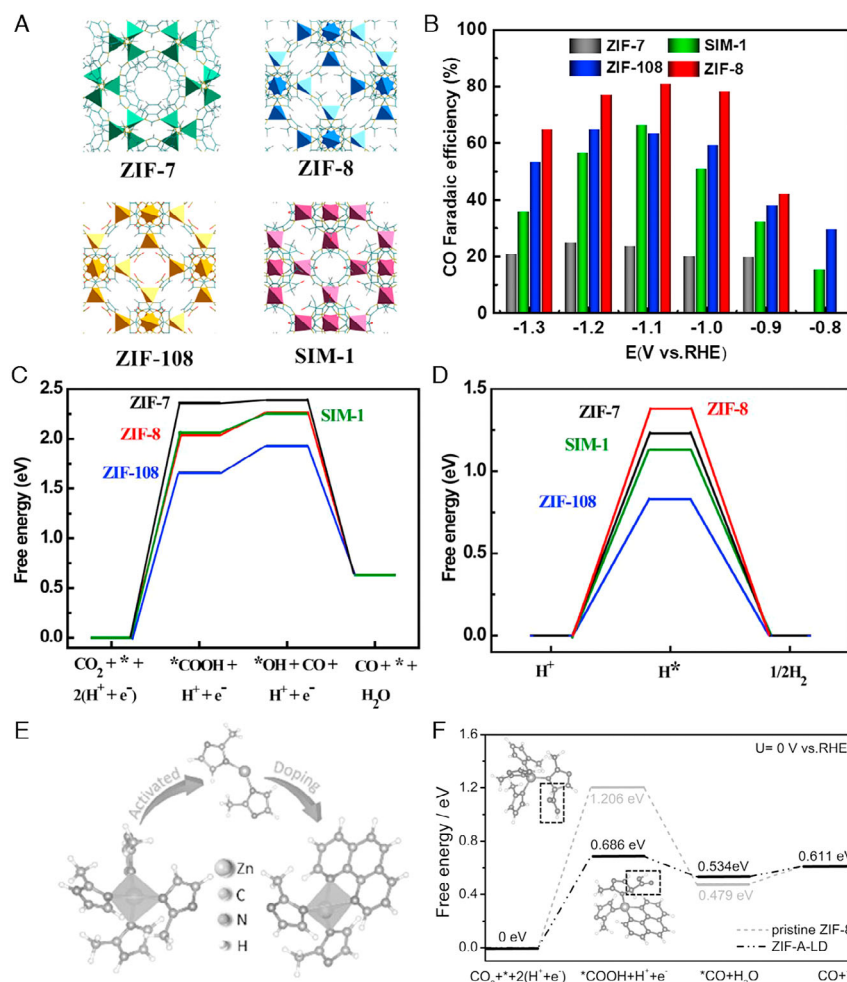


**Figure 30.** A) Molecular structures of various ZIF catalysts. B) FEs of various ZIF catalysts. C) Calculated free energy diagrams of various ZIF catalysts for CO<sub>2</sub>RR. D) Calculated free energy diagrams of various ZIF catalysts for HER. Reproduced with permission.<sup>[210]</sup> Copyright 2018, Elsevier. E) The fabrication of phenanthroline-doped ZIF-8. F) Free energy diagrams for CO<sub>2</sub>RR on the sp<sup>2</sup>C atom sites. Reproduced with permission.<sup>[211]</sup> Copyright 2019, Wiley-VCH GmbH.

of  $-1.1$  V vs RHE and a TOF of  $0.14 \text{ s}^{-1}$  in CO<sub>2</sub>-saturated  $0.1 \text{ M}$  KHCO<sub>3</sub> aqueous solutions, which is much larger than that of Ag NCs (FE of 25% for CO). The synergistic electronic coupling effects in the interface of Ag and Al-PMOF contributed to the enhanced CO<sub>2</sub>RR performance. As confirmed via XPS and UV spectra, the charge transfer from Al-PMOF to Ag NCs led to the electron enrichment of Ag within the hybrids. Not only the catalytic activity, but also the catalytic stability was improved by composing Ag NCs and MOFs. The bare Ag NCs suffered serious sintering after CO<sub>2</sub>RR, whereas for Ag@Al-PMOF, sintering was strongly inhibited during CO<sub>2</sub>RR. This approach was also applied to fabricate other electrochemically active NC/MOF composites. Cu nanocubes@Al-PMOF, Au nanorods@Al-PMOF, and Au nanospheres@Al-PMOF were facilely prepared and demonstrated CO<sub>2</sub>RR activity.

### 3.5. Electrocatalytic NRR

NH<sub>3</sub>, one of the most important industrial chemicals, is produced by the reduction of N<sub>2</sub> via the century-old Haber–Bosch

process, consuming half of the global H<sub>2</sub> production and 1–2% of global energy.<sup>[219]</sup> The electrocatalytic reduction of N<sub>2</sub> to NH<sub>3</sub> at mild conditions is a promising alternative for the Haber–Bosch process and has attracted tremendous attention in the past few years.<sup>[220]</sup> Yet, the inertness of N<sub>2</sub> with strong N≡N bond ( $941 \text{ kJ mol}^{-1}$ ) and low solubility of N<sub>2</sub> in water significantly limit the NRR performance. Also, the potential window between HER and NRR is quite narrow, making HER more preferred for most electrocatalysts and seriously reducing the NRR selectivity. The ambient ammonia contamination during experiments is another issue that should be addressed, which would affect the reproducibility and even result in misleading conclusions.<sup>[221]</sup> Though numerous catalysts have been investigated to exhibit NRR activity, the low catalytic activity and ultralow selectivity do not allow them for practical applications.<sup>[132]</sup> Till now, there are only three reports of MOFs and MOF composites for NRR.<sup>[222,223]</sup>

Zhao et al. reported the first application of MOFs for NRR using MIL-100(Fe), ZIF-67, and HKUST-1 as catalysts.<sup>[223a]</sup> All the three MOFs showed excellent NRR activity for the electrochemical synthesis of NH<sub>3</sub> using pure N<sub>2</sub> and water as raw



materials at a potential of 1.2 V, ambient pressure, and at 90 °C in 2 M KOH solution. Among the MOFs, MIL-100(Fe) exhibited the best NRR activity, with a high  $\text{NH}_3$  formation rate of  $2.12 \times 10^{-9} \text{ mol s}^{-1} \text{ cm}^{-2}$  and an FE of 1.43%. The stability of the MOFs at these conditions was not studied in this work and no control experiments were conducted to avoid the ambient ammonia contamination during experiments.

One promising strategy to improve NRR efficiency and selectivity is to suppress the competitive HER reaction at the catalyst surface.<sup>[224]</sup> Lee et al. coated Ag–Au alloy NRR catalyst surface with a superhydrophobic MOF layer (ZIF-71) to inhibit HER and improve NRR activity, as shown in **Figure 31A**.<sup>[222]</sup> The obtained Ag–Au@ZIF composite exhibited both excellent NRR selectivity and improved FE. The NRR investigation was conducted at 298 K and 1 bar at an applied potential of  $-2.9 \text{ V vs Ag/AgCl}$  for 6 h. The electrolyte is a dry tetrahydrofuran (THF) solution containing 0.2 M  $\text{LiCF}_3\text{SO}_3$  and 1 volume % ethanol. The Ag–Au@ZIF electrode showed a  $\text{NH}_3$  formation rate of about  $1 \times 10^{-11} \text{ mol s}^{-1} \text{ cm}^{-2}$  and a high FE of  $18 \pm 4\%$ , which are fourfold and twofold superior to Ag–Au electrode without ZIF encapsulation, respectively (Figure 31B,C). The hydrophobic interior of ZIF can block the entrance of water for impeding HER and also accumulate  $\text{N}_2$  and other reactant molecules at catalytic active sites, leading to efficiently improved NRR performance. Recently, Yang et al. coated nanoporous gold (NPG) with hydrophobic ZIF-8 layer to fabricate NPG@ZIF-8 nanocomposite with high NRR performance, as shown in Figure 31D.<sup>[223b]</sup> In the nanocomposite, NPG was the catalytic active site for NRR, and ZIF-8 shell can suppress HER and accelerate the reactant diffusion. The NRR investigation was conducted at 298 K and

1 bar at an applied potential of  $-6 \text{ V vs RHE}$  for 2 h. The NPG@ZIF-8 electrode displayed a high FE of 44% and selectivity of 98% for  $\text{NH}_3$ , and a  $\text{NH}_3$  formation rate of about  $0.36 \times 10^{-9} \text{ mol s}^{-1} \text{ cm}^{-2}$ , which are superior to NPG and traditional Au NPs (Figure 31E). Also, the nanocomposite electrode showed high electrochemical stability, without an obvious drop of electrocatalytic activity after a 20 h test (Figure 31F). In the nanocomposite, ZIF-8 showed no NRR activity and performed to inhibit HER due to its hydrophobic interior. Both the works earlier indicated that the strategy by coating NRR catalysts with hydrophobic MOFs to suppress HER can construct promising NRR electrocatalysts for practical applications.

### 3.6. Electro-Organic Synthesis

Electro-organic synthesis has risen as a new mild, environmentally friendly, and large-scale transformation method that uses electricity for redox transformations.<sup>[225]</sup> With proper potential bias, organic starting materials can generate highly reactive intermediates at the electrode surface by gaining or losing electrons. The reactivity and chemoselectivity of electrochemical reactions can be precisely controlled by regulating the applied potential, making electro-organic synthesis one of the most promising approaches to synthesize some complex organic molecules.<sup>[226]</sup>

There are some advantages of MOFs for electro-organic synthesis, for example, the large porosity is beneficial for mass transfer, and the tunable pore structures make the improvement of chemoselectivity or even chiral selectivity possible. Yet, the main drawback of MOFs for electro-organic synthesis is the low conductivity of most MOFs. Compared with vast reports of MOFs for

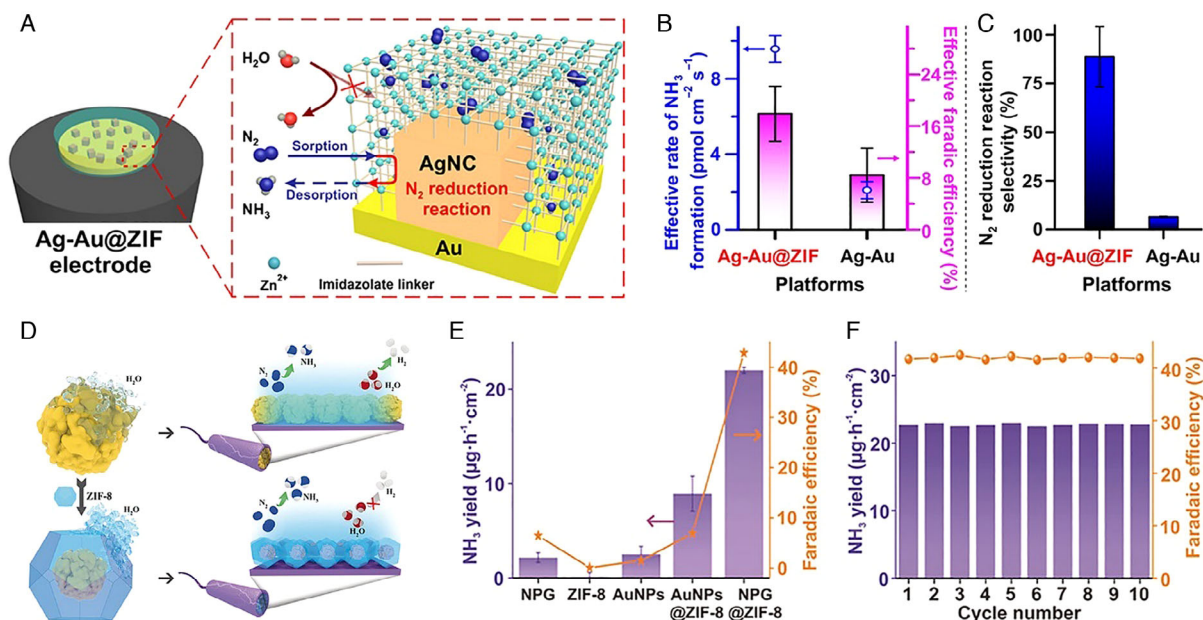


**Figure 31.** A) Schematic depicting the importance of Ag–Au@ZIF as a water repellent and  $\text{N}_2$  molecular concentrator for subsequent application in electrochemical NRR into ammonia (inset). HCl-treated Ag nanocube is denoted as AgNC. B) Effective rate of ammonia formation and FE for various electrode platforms. C) Comparison of NRR selectivity in the presence and absence of ZIF encapsulation. Reproduced with permission.<sup>[222]</sup> Copyright 2018, AAAS. D) Schematic depicting the NRR enhancement by NPG@ZIF-8 electrocatalyst. E) Comparison of catalytic performances of various electrocatalysts at  $-0.6 \text{ V vs RHE}$ . F) Cycling tests of NPG@ZIF-8 catalyst at  $-0.6 \text{ V vs RHE}$ . Reproduced with permission.<sup>[223b]</sup> Copyright 2019, Wiley-VCH GmbH.



electrocatalytic water splitting, ORR, and CO<sub>2</sub>RR applications, there are only several reports of MOFs in electro-organic synthesis applications.<sup>[227,228]</sup> Much more studies are needed in this promising field.

Yang et al. fabricated a nanocomposite by decorating 2D ultrathin MOF nanosheets of Hf<sub>6</sub>(μ<sub>3</sub>-O)<sub>4</sub>(μ<sub>3</sub>-OH)<sub>4</sub>(μ<sub>1</sub>-OH)<sub>2</sub>(μ<sub>1</sub>-OH)<sub>2</sub>(HCO<sub>2</sub>)<sub>4</sub>(NTB)<sub>2</sub>, also called metal-organic layers (MOL), onto conductive multiwalled CNTs (CNT/MOL) to improve the conductivity of MOFs in electrocatalysis (Figure 32A).<sup>[227]</sup> Then CNT/MOL was modified with TEMPO-OPO<sub>3</sub>H<sub>2</sub> (CNT/MOL-TEMPO-OPO<sub>3</sub><sup>2-</sup>) and loaded on a macroporous reticulated vitreous carbon (RVC, 100 PPI) electrode to act as an efficient electrocatalyst for electrochemical acceptorless dehydrogenation of *N*-heterocycles to obtain quinoline or indole derivatives. The monolayer structure of MOL can accelerate the diffusivity of organic substrates and afford high densities of active sites, and CNTs can efficiently improve the conductivity of catalyst. CNT/MOL-TEMPO-OPO<sub>3</sub><sup>2-</sup> electrode exhibited excellent electrocatalytic performance for the acceptor-less dehydrogenation of *N*-heterocycles in a mixed solvent of CH<sub>3</sub>CN/H<sub>2</sub>O (9/1) containing 0.5 M *n*Bu<sub>4</sub>NBF<sub>4</sub> at room temperature. When we used 1,2,3,4-tetrahydroquinoline as the organic substrate, the desired quinoline product was synthesized with a high yield of 79% at a constant current of 7 mA. The electrode could be used three times without loss of activity, indicating the strong stability of CNT/MOL-TEMPO-OPO<sub>3</sub><sup>2-</sup> catalyst. Control experiments confirmed that the TEMPO moiety anchored on CNT/MOL was the active site for electro-organic synthesis.

Guo et al. reported a new approach to improve the conductivity and selectivity for electro-organic synthesis by incorporating ion electrocatalyst (TEMPO-SO<sub>3</sub><sup>-</sup>) in charged MOFs [MIL-101(Cr)-HIMBr] (Figure 32B).<sup>[228]</sup> The ionic MIL-101(Cr)-HIMBr was obtained by introducing ionic liquid group (HIMBr) into porous MIL-101(Cr) via postfunctionalization method, leading to markedly improved electrical conductivity and accelerating electron transfer compared with pristine MIL-101(Cr). Then, the catalytic-active TEMPO-SO<sub>3</sub><sup>-</sup> ions were trapped in the charged pores by ion exchange with Br<sup>-</sup> ions in MIL-101(Cr)-HIMBr to obtain the hybrid electrocatalyst TEMPO-SO<sub>3</sub>@MIL-101(Cr)-HIM.

TEMPO-SO<sub>3</sub>@MIL-101(Cr)-HIM was coated onto a carbon plate as the working electrode, and the electrocatalytic oxidative self-coupling of the benzylamine reaction was conducted at a constant potential of 1.0 V versus Ag/AgCl in 0.1 M Bu<sub>4</sub>NBF<sub>4</sub> acetonitrile solution. After catalytic reaction for 3 h, benzylamine was fully converted to imine with >99.9% conversion and a high selectivity of 94.9%. However, the homogenous catalyst TEMPO-SO<sub>3</sub>H using the carbon plate as a working electrode only showed a low selectivity (61.3%) of self-coupling imine product with the formation of a large amount byproducts under identical conditions. TEMPO-SO<sub>3</sub>@MIL-101(Cr)-HIM electrode also demonstrated high catalytic stability, with almost no performance drop after six recycling runs. The cationic pores of MIL-101(Cr)-HIM prevented the leaching of TEMPO-SO<sub>3</sub><sup>-</sup> active sites, and the unique pore structure can prevent the degradation of the oxidative intermediates, thus resulting in the improvement of catalytic selectivity and stability.

### 3.7. Other Electrocatalytic Applications

Except for the aforementioned OER, HER, ORR, CO<sub>2</sub>RR, and NRR, some other electrocatalytic reactions motivated by MOFs have also been reported, including the synthesis of chemical substances, energy conversion, degradation of organic pollutants, and sensing (Table 8).

For example, direct alcohol fuel cells have recently attracted great interest for electronic devices. Wu and coworkers achieved a novel 3D MOF [Ni<sub>4</sub>(OH)<sub>4</sub>(tatb)<sub>4/3</sub>-(bpe)<sub>2</sub>] (CTGU-15) based on the cubane [M<sub>4</sub>(OH)<sub>4</sub>] (M = Ni, Co) clusters via facile solvothermal method.<sup>[229]</sup> The obtained CTGU-15 was studied as an electrocatalyst for methanol oxidation reaction (MOR). The CTGU-15 possessed a large BET surface area (3537 m<sup>2</sup> g<sup>-1</sup>) and showed well-defined bimicropores features at 0.86 nm and 1.51 nm. Moreover, CTGU-15 exhibited an excellent stability in alkaline media (0.1 M KOH), which was suitable for alkaline MOR. Compared with the pure Ni-MOF electrocatalyst, the optimized KB/CTGU-15 (1:2) presented an outstanding electrocatalytic MOR activity with a large mass specific current density

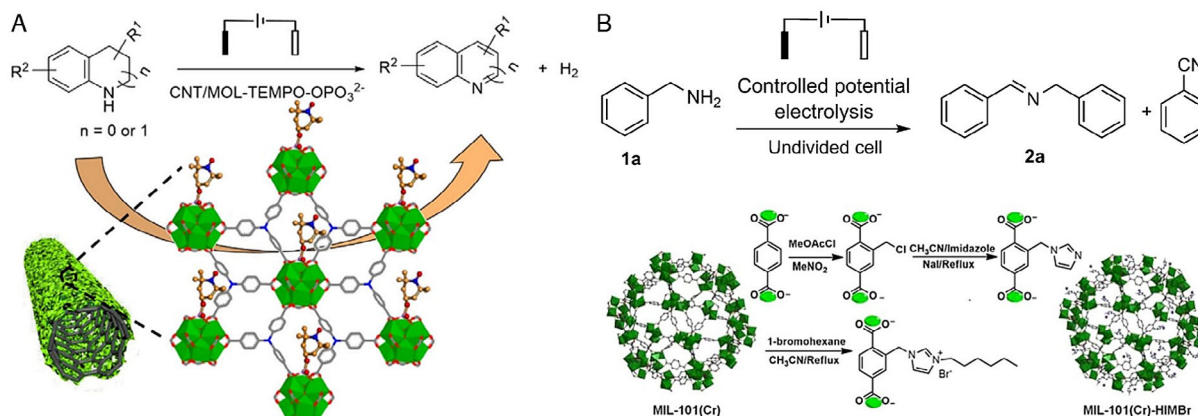


**Figure 32.** A) CNT/MOL-TEMPO-OPO<sub>3</sub><sup>2-</sup> for electrochemical acceptorless dehydrogenation of *N*-heterocycles. Reproduced with permission.<sup>[227]</sup> Copyright 2019, Wiley-VCH GmbH. B) Schematic representation of the synthetic procedures for MIL-101(Cr)-HIMBr for electrocatalytic oxidative self-coupling of benzylamine. Reproduced with permission.<sup>[228]</sup> Copyright 2019, Wiley-VCH GmbH.

**Table 8.** Summary of MOFs for other electrocatalytic applications.

Type of catalysis	Catalysts	Substrate	Electrolyte	References
Alcohol oxidation	[Ni <sub>4</sub> (OH) <sub>4</sub> (tatb) <sub>4/3</sub> -(bpe) <sub>2</sub> ]	GCE	0.1 M KOH	[229]
	Pt/NPC-900	GCE	0.5 M H <sub>2</sub> SO <sub>4</sub>	[330]
	Co-MOF-71@GO	GCE	1.0 M KOH	[331]
	Au/HKUST-1	GCE	0.5 M H <sub>2</sub> SO <sub>4</sub>	[332]
	Cu(II)-bpy-BTC	Carbon rod	0.1 M KOH	[333]
	CNT/MOL	RVC	0.02 M H <sub>3</sub> PO <sub>4</sub>	[230]
Glucose oxidation	[(HOC <sub>2</sub> H <sub>4</sub> ) <sub>2</sub> dtoaCu]	GCE	0.5 M H <sub>2</sub> SO <sub>4</sub>	[334]
	Co <sub>2</sub> (OH) <sub>2</sub> pta	GCE	0.1 M NaOH	[232]
	[Cu <sub>3</sub> (BTC) <sub>2</sub> ]	GCE	0.1 M NaOH	[335]
Nitrite oxidation	MOF-525/GNR	ITO	0.1 M KCl	[231]
	Au/Cu-MOF/CPE	Carbon paste	0.1 M phosphate buffer solution	[336]
Phenixin reduction	Co(TCPP)	FTO	0.1 M LiClO <sub>4</sub> /DMF	[337]
Hydrazine oxidation	Co-MOF-MPC-2	GCE	0.1 M NaOH	[338]
	Cu-MOFs/OMC	GCE	0.1 M KCl	[339]
Nitrophenols oxidation	Ag@MOF-5(Zn)	GCE	0.1 M KCl	[340]
Acetaminophen oxidation	Au/ZIF-L	GCE	0.1 M phosphate buffer solution	[341]
Cysteine oxidation	Au-SH-SiO <sub>2</sub> @Cu-MOF	GCE	0.1 M phosphate buffer solution	[342]
Peroxide oxidation	Cu-bpy-BTC	GCE	0.1 M phosphate buffer solution	[343]
	[Cu(adp)(bib)(H <sub>2</sub> O)] <sub>n</sub>	GCE	0.1 M NaOH	[344]

(527 mA mg<sup>-1</sup>) and superior peak current density of 29.8 mA cm<sup>-2</sup> at a potential of 0.6 V.

Yang et al. constructed a 2D MOL with multiwalled CNT as an electrocatalyst for selective alcohol oxidation reaction.<sup>[230]</sup> The MOLs were assembled by 4,4',4''-nitrotribenzoate and Hf<sub>6</sub>(μ<sub>3</sub>-O)<sub>4</sub>(μ<sub>3</sub>-OH)<sub>4</sub>(HCO<sub>2</sub>)<sub>6</sub> to form a 2D network, which existed in the form of a wrinkled ultrathin film (0.3 × 0.3 μm<sup>2</sup>). The composite structure of CNT/MOL dramatically enhanced the conductivity of MOLs from 1.6 × 10<sup>-7</sup> to 3.65 S m<sup>-1</sup>. After further modification with 4-carboxy-2,2,6,6-tetramethylpiperidine (TEMPO), the catalyst was loaded on a microporous RVC electrode. An electrocatalytic oxidation current could be observed at 0.34 V with high selectivity (100%) and FE (97%). The only products for benzyl alcohol are benzaldehyde and H<sub>2</sub>. Further research revealed that the kinetic measurements of catalysis exhibited a Langmuir-type dependence of density on the concentration of the substrate.

Nitrite is an important class of food additives and its concentration is vital for controlling food quality. Kung et al. grew MOF-525 on graphene nanoribbons (GNRs) and the thin film MOF-525/GNR can not only catalyze nitrite oxidation reaction, but also be utilized as a nitrite sensor.<sup>[231]</sup> Nitrogen adsorption-desorption curves revealed the porous characteristic of the composite (1535 m<sup>2</sup> g<sup>-1</sup>). Cyclic voltammograms (CV) curves demonstrated that the existence of MOF-525 was required to achieve better catalytic performance than the GNR. Furthermore, MOF-525/GNR thin film was assembled as an amperometric nitrite sensor with a high sensitivity of 93.8 μA mM<sup>-1</sup> cm<sup>-2</sup>, a low limit of detection (LOD) of 0.75 mM, and a wide linear range of 100–2500 μM.

Glucose is the most widely distributed and most important monosaccharide in nature. Electrocatalytic glucose oxidation has a wide range of applications, such as sensors and biofuel cells. Co<sub>2</sub>(OH)<sub>2</sub>pta is a 2D ultrathin network, where the coordination mode of central cobalt ion has both six- and five-coordinated positions.<sup>[232]</sup> The 2D Co-MOF (2.041 nm of thickness) had a large specific surface area and good catalytic activity for glucose oxidation reaction. The CV curves showed a couple of redox peaks in the range from 0.2 to 0.5 V, corresponding to the Co(III)/Co(II) couple. The ultrathin 2D structure provided abundant active sites, shorter particle transport path, and high electron conductivity. Based on the earlier results, Co<sub>2</sub>(OH)<sub>2</sub>pta was used to develop an amperometric glucose sensor and superior selectivity (219.67 μA mM<sup>-1</sup> cm<sup>-2</sup>) was obtained, together with an LOD of 0.25 μM and a linear range of 0.5–8065.5 μM.

### 3.8. MOF Derivatives for Electrocatalysis

In view of the highly adjustable structure and compositional characteristics of MOFs, their derivatives have been considered to be the most promising alternatives to electrocatalytic materials.<sup>[233]</sup> Through rigorous control of the experimental process, as well as rational modification/post-treatment, the pristine MOFs present as promising templates/precursors to fabricate outstanding catalysts with compositional properties and desirable structures after controlled thermal/chemical treatment.<sup>[234]</sup> MOF derivatives not only inherit the dominant features of MOF precursors (large specific surface, high porosity, and compositional diversity), but also transform MOFs to carbon-/metal-based nanomaterials with more stable structures and richer active sites.

Since the first acquisition of MOF derivatives from pyrolysis MOFs reported by Xu et al., subsequently, the exploration of MOF-derived materials presented explosive growth, especially as catalysts for electrocatalysis.<sup>[233a]</sup> However, few earlier reviews reported the applications of MOFs derivatives. For example, Jiang's group reviewed MOF-derived porous materials for catalysis.<sup>[18a,102a]</sup> Moreover, Xu's group paid attention to the development of MOF derivatives in the field of energy applications.<sup>[234b,235]</sup> Here, we summarize the recent remarkable applications of MOF derivatives in electrocatalysis (Table 9).

### 3.8.1. MOF Derivatives

Up to now, a large number of MOF derivatives with different morphologies and structures have been widely prepared, such as polyhedral and core-shell structures of NPs, nanorods, nanotubes, nanosheets, arrays, and so on. In addition, the investigations of MOF derivatives with various composition features (e.g., porous carbon, metal compounds, and composites) were

**Table 9.** Recent remarkable applications of the MOF derivatives for electrocatalysis.

Catalyst	MOF precursor	Reaction	References
Co-Fe-P	MIL-88B	HER	[260]
CoPS-N/C	ZIF-67	HER	[261]
Cu <sub>3</sub> P@NPPC	Cu-NPMOF	HER	[345]
CoP/NCNWs	Co-MOF	HER	[346]
CS@CNC NAs/CC	Co-MOF NAs	HER	[347]
Co <sub>3</sub> O <sub>4</sub> /Co-Fe	ZIF-67	OER	[348]
FeNiP/C	BMM-10	OER	[349]
ZnCo-Fe	ZnCo MOF	OER	[350]
CoN/C	ZIF-67	OER	[351]
NiCoOOH-NiCoS	ZIF-67	OER	[352]
Ni <sub>2</sub> P/CoN-PCP	ZnCo-BMOF	HER/OER	[353]
Co <sub>3</sub> S <sub>4</sub> /EC-MOF	Co-based MOF	HER/OER	[266]
Co/NBC	BIF-82-Co	HER/OER	[354]
N-CNTs	ZIF-67 with N-Cdot	ORR	[268]
H-M <sub>mix</sub> -N <sub>x</sub> -C	ZIF-8	ORR	[270]
Co-Zn-N-C	Zn-Co-MOF	ORR	[271]
Fe-N-C	Fe-ZIF-8	ORR	[273]
Fe SAs-N/C-x	FePc-x@ZIF-8	ORR	[274]
Co-Fe alloy NPs	CoFe-BMOF	ORR	[244]
Co-N <sub>2</sub>	Co/Zn ZIFs	CO <sub>2</sub> RR	[277]
M-N-C	Fe or Co doped ZIF-8	CO <sub>2</sub> RR	[355]
Ni/Fe-N-C	Zn/Ni/Fe ZIF	CO <sub>2</sub> RR	[278]
Fe <sup>3+</sup> -N-C	Fe-doped ZIF-8	CO <sub>2</sub> RR	[279]
NP-C-MOF-5	MOF-5	CO <sub>2</sub> RR	[356]
NPC	ZIF-8	CO <sub>2</sub> RR	[281]
Ru SAs/N-C	ZIF-8	CO <sub>2</sub> RR	[282]
NiCo/NiO-CoO/NPCC	Co-Ni-MOF	MOR	[285]
Cu@Pt/C	Cu-MOF	MOR	[357]

also under way, to explore the complex transformation mechanism and influencing conditions like annealing temperature and atmospheres for MOF derivative fabrication.

**The Strategies of MOF Derivatives:** In recent years, tremendous efforts have been devoted to studying various strategies for the preparation of MOF derivatives due to the diversity of composition and structural tunability of pristine MOFs.<sup>[236]</sup> Apart from a large number of direct carbonization strategies, other strategies (such as direct oxidation and direct sulfidation) have also been used to develop MOF derivatives. For example, Castillo-Blas et al. developed a series of new MOFs with different arrangements (up to four different metal elements) and programmed the composition of multimetal oxides via direct oxidation in air.<sup>[237]</sup> Due to the distribution of multiple metal cations at specific locations when constructing MOFs, it is possible to prepare a multimetal oxide with a novel composition by facile oxidation of the code-selected metal ratio MOFs. The adjustable new oxides presented an enhancement of ORR activity, and the activity approached to commercial Pt/C. Meanwhile, Yilmaz et al. developed a feasible strategy to reconstruct Zn-Co-coordinated Co-Mo disulfide, which was derived from bimetallic (Co, Zn) MOFs by doping heteroatoms and functionalizing ligands.<sup>[238]</sup> The Zn-N-coordinated cobalt-molybdenum disulfide (MoS-CoS-Zn) was fabricated through successively sulfidation of Co<sub>8</sub>Zn<sub>1</sub>-MOF to CoS-Zn followed by two steps of solvothermal transformation. The MoS-CoS-Zn achieved distinct HER activity compared with MoS and MoS-CoS hybrid.

Recently, single-atom catalysts (SACs) have caused widespread concern, thanks to their special catalytic properties. Due to the advantages of highly ordered arrangements of metal sites, ordered pore structure, and chemical stability, MOFs represent ideal templates to fabricate carbon-supported SACs.<sup>[239]</sup> For example, Deng et al. reported a novel metal-organic gaseous doping strategy to prepare embedding single Fe atoms N-doped carbon polyhedron catalysts.<sup>[240]</sup> The single Fe atom catalyst was obtained by the pyrolysis of as-optimized ZIF-8 precursor. The Fe-N<sub>x</sub> sites were successfully doped in the porous structure of ZIF-8, resulting in an outstanding ORR activity and stability in both acidic and alkaline media. Jiao et al. proposed a novel dual protection strategy to fabricate high-contented single-atom Fe-implanted N-doped porous carbon (Fe<sub>SA</sub>-N-C) by nanocasting SiO<sub>2</sub> in porphyrinic MOFs.<sup>[234e]</sup> SiO<sub>2</sub> in MOFs created the thermally stable FeN<sub>4</sub>/SiO<sub>2</sub> interfaces to provide addition protection. The Fe<sub>SA</sub>-N-C exhibited excellent catalytic activity and durability for ORR in both alkaline and acidic media because of high-density single-atom Fe sites. Recently, Hou et al. reported an overhang-eave structure decorated with iron single-atom sites (Fe/OES) by silica-mediated MOF-templated (SMMT) strategy.<sup>[241]</sup> The overhang-eave design provided three-phase exchange spots, which are favorable to the transport of ORR-relevant species and to maximize the exposure of single-atom active sites.

**Structural Design of MOF Derivatives:** In view of the key role of nanostructure structure/morphology in catalytic applications, MOF derivatives possess the stable structures that facilitate the transportation of mass/electron, and the unique morphology is desirable for high exposure of active sites.<sup>[233b,d,242]</sup> Various synthetic strategies have been proposed to synthesize MOFs with different structures/morphologies, and the MOFs were further

converted to various types of MOF derivatives (0D, 1D, 2D, and 3D) through controlled self-templating and external-templating methods.

Through reasonable controlling of the synthesis conditions, the morphology of the MOF precursors can be well inherited after chemical/thermal conversion. Therefore, MOF NCs with high thermal stability can be used to fabricate MOF-derived polyhedral/hollow NPs. For example, Chen et al. proposed a simple and straight method to synthesize yolk-shell Co@C-N nanoreactor with highly efficient, controllable and recyclable properties.<sup>[243]</sup> As shown in **Figure 33A**, the multiyolk@shell nanostructures were obtained through direct pyrolysis of hollow Zn/Co-ZIF precursors. Compared with the single metal MOF derivatives, bimetal MOF-derived polyhedral structures owned more active sites and better facile mass dispersion. Xiong et al. designed a series of bimetallic MOF-derived carbon nanocomposites embedded with Co-Fe alloys via a facile host-guest method.<sup>[244]</sup> The nanocomposite possessed a high specific surface and uniformly distributed bimetallic NPs, which are favorable toward ORR.

Given the high exposure of active sites, stable structure, and abundant channels/space for electron/mass transport, controlled synthesis of 1D MOF derivatives has made rapid development in catalytic applications.<sup>[245]</sup> Xie et al. reported Co@CoN<sub>x</sub>/N-doped carbon tubes hybrid (Co@CoN<sub>x</sub>/NCT hybrid) derived from ZIF-67 via the facile and economical one-step pyrolysis with urea.<sup>[246]</sup> Urea not only served as nitrogen and carbon sources, but also promoted the growth of carbon tubes. Recently, Xu et al. proposed nitrogen-doped CNTs encapsulated with Co NPs through direct pyrolysis of GO-wrapped ZIF-67.<sup>[247]</sup> The fabrication is shown in **Figure 33B**. The addition of triethylamine (TEA) can accelerate the crystallization of ZIF-67, and due to the pinning effect of RGO sheet, the N-CNTs are bonded with both sides of the RGO sheet seamlessly.

In recent years, in view of the favorable electron transport, abundant active sites, and short ion-diffusion pathway, 2D materials are widely applied in various catalysts.<sup>[248]</sup> The self-templating

and external-templating methods are usually used to fabricate 2D MOF derivatives. Recently, Zheng et al. presented a rational strategy to fabricate the N-doped carbon nanosheets with high loading of single/paired Fe atoms via carbonization of 2D bimetal MOF precursor (**Figure 34A**).<sup>[249]</sup> g-C<sub>3</sub>N<sub>4</sub> provides a nitrogen source for the catalyst and promotes the formation of Fe single atoms. The 2D carbon structure and the single/paired Fe atoms are favorable for OER catalysis. Compared with self-templating, external templating is the process of growing the MOF in situ on the external template and then maintaining the morphology. Zhong et al. presented 2D sandwich-like N-doped porous carbon nanosheets through the growing of ZIF on the surface of GO.<sup>[250]</sup> The N-doped porous carbon nanosheets were obtained through annealing the MOF/GO nanosheets and exhibited excellent catalytic performance for ORR.

The 3D structure of the MOF derivatives possesses the advantages of easy mass transfer/dispersion, high electrolyte permeability, and high electron transfer rate. The 3D MOF derivatives with different morphologies can be controllably synthesized by rational design of the structure and composition of MOF precursors.<sup>[234b,251]</sup> For example, Sun et al. reported a series of urchin-like nanotube structure catalysts anchored with hierarchical single cobalt atoms (UNT Co SAs/N-C) derived from well-aligned 3D hollow urchin-like ZIF-superstructures (UNT ZIF-67) (**Figure 34B**).<sup>[252]</sup> The as-prepared UNT Co SAs/N-C catalysts manifests superior functionality for both ORR/OER. Zhou et al. developed a facile strategy to synthesize a series of nanoarrays constructed with metal oxide/carbon (MO<sub>x</sub>/C, M = Co, Ni, and Cu).<sup>[253]</sup> Among them, the array of nanosheets can expose more active sites with high conductivity, high catalytic activity, and long-term durability.

**Compositional Design of MOF Derivatives:** Apart from the effects of structure/morphology, the components of MOF derivatives also play an important role in various catalytic applications. Through chemical treatment and pyrolysis in different atmospheres, active sites or active materials can be introduced during

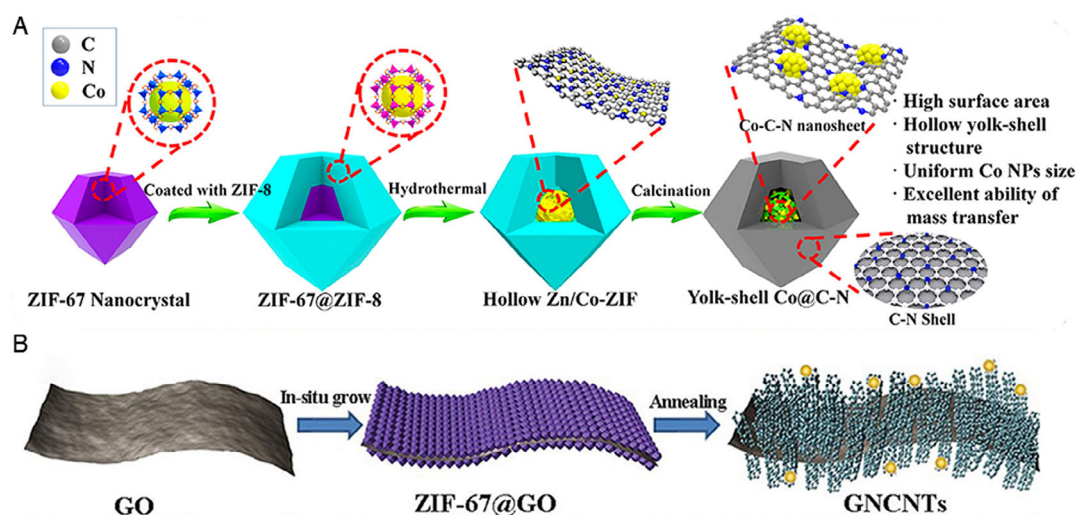


**Figure 33.** A) Illustration of the synthesis process for yolk-shell Co@C-N nanoreactor. Reproduced with permission.<sup>[243]</sup> Copyright 2018, American Chemical Society. B) Schematic illustration of the fabrication of the graphene nitrogen-doped carbon nanotubes (GNCNTs). Reproduced with permission.<sup>[247]</sup> Copyright 2020, Wiley-VCH GmbH.



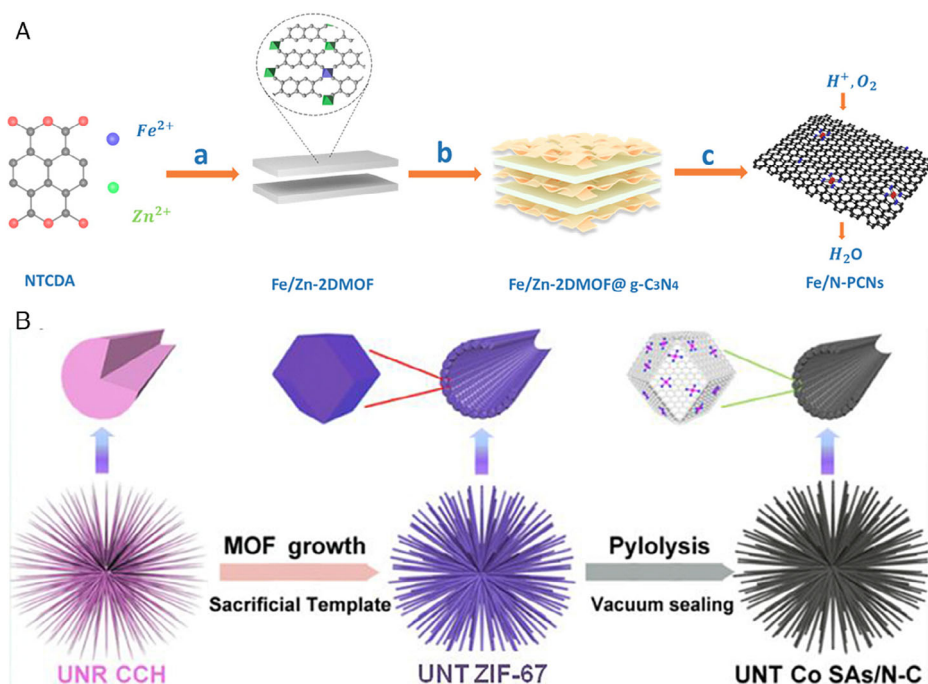


**Figure 34.** A) The synthesis of Fe/N-PCNs: (a) self-assembly, b) mixing the MOF precursor and g-C<sub>3</sub>N<sub>4</sub>, and c) pyrolysis. Reproduced with permission.<sup>[249]</sup> Copyright 2020, American Chemical Society. B) Illustration of the fabrication process for UNT Co SAs/N-C. Reproduced with permission.<sup>[252]</sup> Copyright 2019, Elsevier.

the conversion of the original MOF to MOF-derived materials, such as heteroatom doping (N, P, S and B), metal compounds doping (sulfides, phosphides selenides, etc.), and SACs.

Metal-free carbon catalysts with defect structure and the introduced heteroatoms are widely investigated in catalytic applications, as the doping of heteroatoms can tune the optoelectronic properties and provide active sites.<sup>[254]</sup> MOF derivatives can limit the active sites to permeable carbon and effectively improve the catalytic performance.<sup>[255]</sup> Recently, Zhang et al. reported N-, P-, S-codoped carbon hollow polyhedron derived from ZIF-8.<sup>[256]</sup> The ZIF-8 precursor was coated

with poly(cyclotriphosphazene-co-4,4'-sulfonyldiphenol), which provided N, P, S atoms, and Zn evaporated at a high temperature, thus causing the porous structure.

Metal compounds have shown great potential in electrocatalytic applications and MOF-derived functional metal compounds have been extensively studied as MOF is a promising template/precursor. Deng et al. developed MOF-derived carbon nanorods-encapsulated bismuth oxides by a facile in situ oxide method for the efficient CO<sub>2</sub> electroconversion.<sup>[257]</sup> The preparation process of MOF-derived oxide encapsulated in in situ carbon is shown in Figure 35A. The strategy also can be extended to prepare MOF

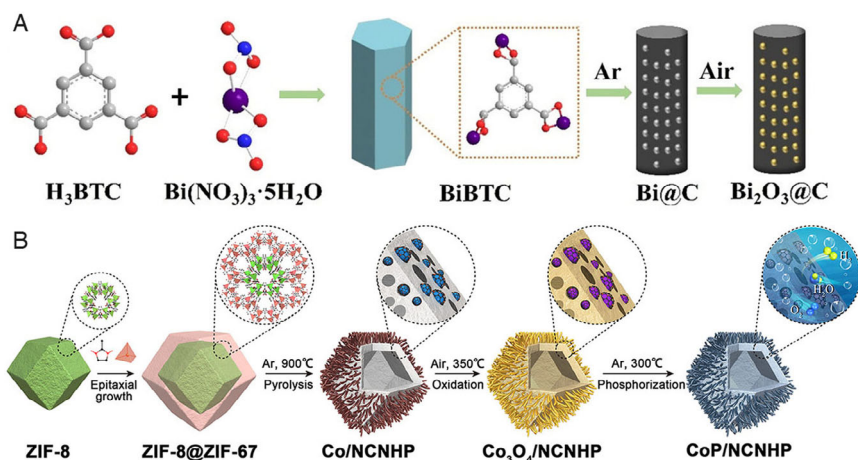


**Figure 35.** A) Schematic illustration for the fabrication of Bi@C and Bi<sub>2</sub>O<sub>3</sub>@C catalysts. Reproduced with permission.<sup>[257]</sup> Copyright 2020, Wiley-VCH GmbH. B) The scheme of procedure for synthesis of CoP/NCNHP. Reproduced with permission.<sup>[258]</sup> Copyright 2018, American Chemical Society.

derivatives encapsulated with other metal compounds. As shown in Figure 35B, Pan et al. proposed a novel pyrolysis–oxidation–phosphating strategy to fabricate hollow polyhedron anchored with CoP NPs in N-doped CNT (NCNHP), which was derived from core–shell ZIF-8@ZIF-67.<sup>[258]</sup> The CoP/NCNHP hybrid exhibited superior electrocatalytic performances for electrocatalytic overall water splitting due to the synergistic effects between NCNHP and CoP NPs.

### 3.8.2. Electrocatalytic Water Splitting

Electrochemical water splitting is one of the most promising large-scale and commercial hydrogen production methods. In recent years, the development of MOF derivatives as electrocatalysts to promoting water splitting has been extensively studied.<sup>[259]</sup> TMPs possess excellent HER performance. Chen et al. presented Co-incorporating FeP nanotubes (Co–Fe–P) derived from MIL-88B MOFs.<sup>[260]</sup> The Co, Fe, and P atoms were uniformly dispersed on Co–Fe–P nanotubes with hollow interior, and the synergistic effect caused by the substitution of Co atoms provides rich active sites and improved HER performance over a wide pH range with the overpotentials of 66, 86, and 138 mV@10 mA cm<sup>−2</sup> in 0.5 M H<sub>2</sub>SO<sub>4</sub>, 1.0 M KOH, and 1.0 M PBS, respectively. Meanwhile, transition metal phosphosulfides also exhibited the potential for HER. Li et al. reported the ternary pyrite-type cobalt phosphosulfide (CoPS-N/C) anchored to nitrogen-doped carbon, which was fabricated by carbonization and phosphosulfurization of ZIF-67.<sup>[261]</sup> The CoPS NPs were anchored on the inherent polyhedron of ZIF-67 and the catalysts exhibited outstanding HER activity in both acidic and alkaline conditions, achieving a small overpotential of −80 and −148 mV@10 mA cm<sup>−2</sup> in 0.5 M H<sub>2</sub>SO<sub>4</sub> and 1.0 M KOH, respectively.

Reducing the energy barrier of OER is also an effective way to promote the electrocatalytic activity.<sup>[262]</sup> MOF derivatives have been considered as promising electrocatalysts to overcome the kinetic barriers of OER to replace precious metal catalysts (RuO<sub>2</sub> and IrO<sub>2</sub>). Recently, 2D MOF derivatives with intriguing physicochemical properties have attracted increasing attention for OER. Lin et al. proposed a topology-guided bottom-up strategy of a novel hexagonal 2D MOF nanoplate.<sup>[263]</sup> The morphology can be modified into nanoplates through substitution suppression under the inhibition and modulation of pyridine. The obtained N-doped Ni@carbon composite after pyrolysis treatment exhibited superior OER performance (a small overpotential of 307 mV@10 mA cm<sup>−2</sup>). Tian et al. presented a novel strategy to convert bulk MOFs into ultrathin metal oxyhydroxide nanosheets for efficient OER through electric-field assisted hydrolysis.<sup>[264]</sup> The MOF-derived ultrathin nanosheets achieve high OER activity (a low overpotential of 231 mV@10 mA cm<sup>−2</sup> and a small Tafel slope of 42 mV dec<sup>−1</sup>). The work provides new ideas for the preparation of novel MOF derivatives for OER. Furthermore, the 3D structure stacked by 2D nanosheets can also effectively improve the OER performance. Li et al. prepared the interconnected nanoarrays embedded with Co–Ni bimetallic metaphosphate NPs (Co<sub>2–x</sub>Ni<sub>x</sub>P<sub>4</sub>O<sub>12</sub>-C) through a mild phosphorylating process of CoNi-ZIF.<sup>[265]</sup> Co<sub>2–x</sub>Ni<sub>x</sub>P<sub>4</sub>O<sub>12</sub>-C exhibited excellent OER activity ( $\eta$  = 230 mV @10 mA cm<sup>−2</sup>) and long-term stability in 1 M KOH, which can be attributed to the absorption sites on the doping Ni site and the morphology integrity of the interconnected metaphosphate nanoarrays.

In view of the cost effect of electrolytic water splitting in practical applications, the catalysts with both HER and OER activity are expected. Liu et al. presented a universal vapor-phase strategy to fabricate echinops-like Co-based MOF (EC-MOF), which was well aligned on conductive carbon cloth (Figure 36).<sup>[266]</sup> Since the electron transfer between active Co<sub>3</sub>S<sub>4</sub> species and EC-MOF

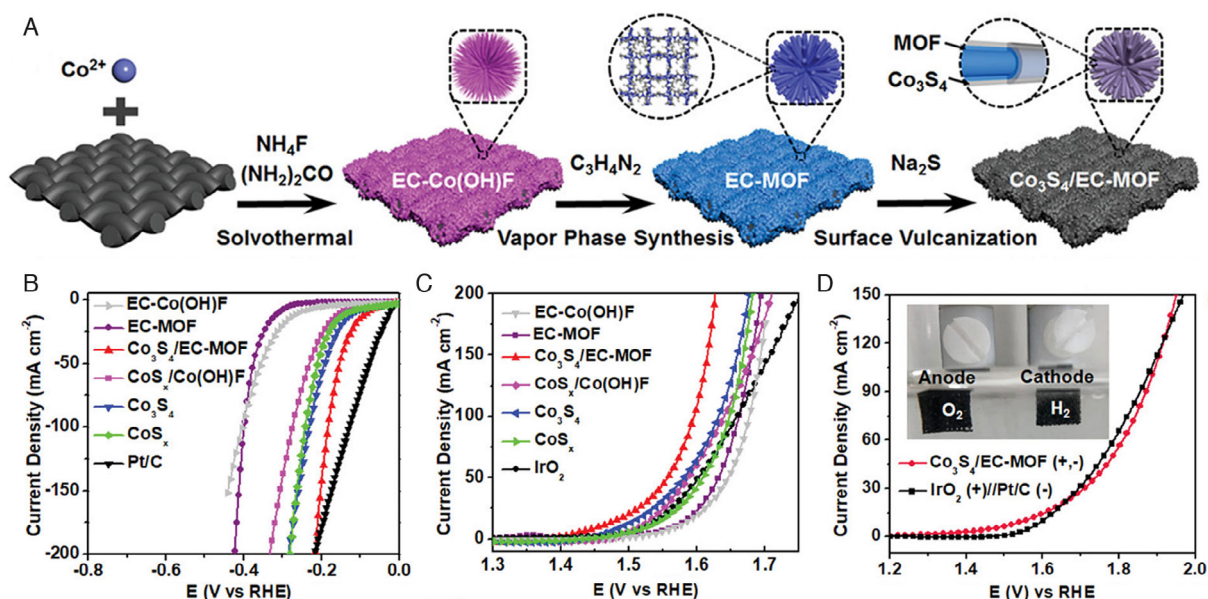


**Figure 36.** A) Schematic illustration of Co<sub>3</sub>S<sub>4</sub>/EC-MOF catalyst. B) LSV plots for HER and C) LSV plots for OER of Co(OH)F, EC-MOF, Co<sub>3</sub>S<sub>4</sub>/EC-MOF, CoS<sub>x</sub>/Co(OH)F, Co<sub>3</sub>S<sub>4</sub>, CoS<sub>x</sub>, and Pt/C. D) LSV plots and photograph of the overall water-splitting reaction. Reproduced with permission.<sup>[266]</sup> Copyright 2019, Wiley-VCH GmbH.

provides a more optimized adsorption performance for Co, the  $\text{Co}_3\text{S}_4/\text{EC-MOF}$  hybrid showed a much enhanced electrocatalytic performance with overpotentials of 84 and 226 mV@10 mA  $\text{cm}^{-2}$  for both HER and OER, resulting in a highly efficient overall water splitting, and the system afforded a cell voltage of 1.55 V@10 mA  $\text{cm}^{-2}$  which is lower than that of commercial Pt/C-IrO<sub>2</sub> (1.61 V) (Figure 36B,D).

### 3.8.3. Electrocatalytic ORR

Pt-based catalysts, despite their excellent ORR properties, hinder the development of large-scale commercialization due to their high cost and poor durability. As cathode catalysts for ORR, MOF derivatives possess hierarchical pores, high active sites density, and excellent conductivity; especially, potential rich N-C or M-N-C (M refers to Co, Fe, etc.) active sites play a vital role in improving ORR performance.<sup>[255c,267]</sup> Niu et al. reported efficient N-doped CNTs (N-CNTs) derived from MOFs with N-doped carbon dots (N-Cdots) for ORR.<sup>[268]</sup> The N-Cdots not only provide hydroxyl and amine groups, which are beneficial to the formation of N-CNTs, but also induce the graphitic structure and extra nitrogen to extend the ORR activity for N-CNTs. Thus, N-CNTs showed a positive onset potential (0.88 V vs RHE) and a low Tafel slope ( $\approx 81 \text{ mV dec}^{-1}$ ). Extensive studies of M-N-C materials have shown that they have outstanding ORR activity and stability, and M-N-C materials are promising substitutes for Pt/C catalysts.<sup>[269]</sup> Ang et al. developed a versatile strategy to prepare hollow N-doped carbon capsules. One or more atomic metals (H-M-N<sub>x</sub>-C and H-M<sub>mix</sub>-N<sub>x</sub>-C, respectively, M = Co, Fe or Ni)

were dispersed to study the relationship between catalyst composition and electrocatalytic activity for ORR.<sup>[270]</sup> The catalyst was fabricated through annealing the core-shell (ZIF core and a metal-tannic acid coordination polymer shell) precursors to obtain N-doped carbon support dispersed with metal NPs uniformly. The optimized catalysts exhibit respectable ORR performance in acid media. In a recent report, Meng et al. fabricated porous Co-Zn-N-C electrocatalysts with a hierarchical structure via soft template method, as shown in Figure 37A.<sup>[271]</sup> The mesoporous structure was formed through the control of the MOF precursors on P123 and the evaporation of Zn species. The HC-5Co95Zn catalysts exhibited an outstanding onset potential (0.88 V vs RHE), a half-wave potential of 0.78 V vs RHE, and diffusion limiting current density of 5.73 mA  $\text{cm}^{-2}$ , which was close to that of commercial Pt/C catalyst in acidic conditions (Figure 37B,C). Moreover, HC-5Co95Zn showed superior long-term stability in acidic medium (Figure 37D).

As Fe-containing catalysts exhibit superior ORR activity, the Fe-containing MOF derivatives have been extensively studied.<sup>[272]</sup> Increasing the density and accessibility of the active sites is the key to improving the ORR performance. Chen et al. proposed a melamine-assisted strategy without a template to fabricate Fe-embedded and N-doped carbon (Fe-N-C) through directly annealing Fe-ZIF-8 covered with melamine layer.<sup>[273]</sup> The strategy afforded high density of atomically dispersed Fe-N<sub>x</sub> active sites in 3D-interconnected mesopores, which improved the ORR activity of Fe@MNC-1. The optimized Fe@MNC-1 exhibited a larger positive half-wave potential of 0.88 V in alkaline media compared with that of 20 wt% commercial Pt/C catalyst (0.85 V). Recently, single-atom M-N-C catalysts have attracted

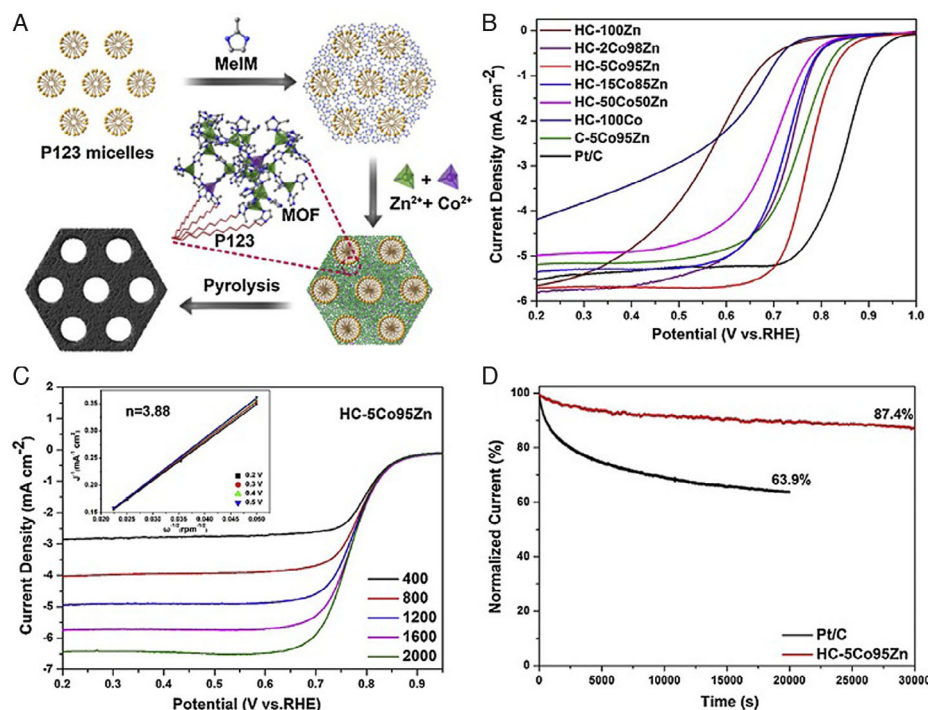


**Figure 37.** A) Illustration of bimetallic MOF self-adjusted synthesis of Co-N-C-x. B) LSV plots of HC-xCo(100-x)Zn, C-5Co95Zn, and Pt/C at 1600 rpm and C) LSV plots of HC-5Co95Zn with different rotation speeds both tested in O<sub>2</sub>-saturated 0.1 M HClO<sub>4</sub>. D) Chronoamperometric response of HC-5Co95Zn and commercial Pt/C. Reproduced with permission.<sup>[271]</sup> Copyright 2019, Elsevier.



widespread attention, and the M–N<sub>4</sub> sites near the N-bonding environment play a key role in the catalytic performance of the ORR. Jiang et al. fabricated a series of Fe–N–C nanoarchitectures with atomically dispersed Fe–N<sub>4</sub> sites through precise atomic-level control method.<sup>[274]</sup> The Fe–N<sub>4</sub> sites possessed well-defined single-atom sites and were dispersed on 3D hierarchically porous carbon. Adjustable grading of micro-mesoporous structures and the exposure of Fe–N<sub>4</sub> single sites make a significant contribution to ORR activity. The catalyst containing 0.2 wt% of transition metal (Fe SAs/N/C-20) exhibited excellent ORR performance ( $E_{1/2} = 0.915$  V vs RHE), which was significantly higher than that of commercial Pt ( $E_{1/2} = 0.85$  V) in 0.1 M KOH. In particular, atomic utilization is enhanced by ten times compared with most previous reports.

### 3.8.4. Electrocatalytic CO<sub>2</sub>RR

Efficient electrocatalytic CO<sub>2</sub>RR not only reduces greenhouse effect, but also converts CO<sub>2</sub> to value-added products.<sup>[275]</sup> However, the high overpotential of electron transfer from electrocatalysts to CO<sub>2</sub> and the competition of side reactions seriously impede the high energy efficiency and scalability for CO<sub>2</sub>RR.<sup>[276]</sup> Over the past decades, MOF derivatives have been considered as potential catalysts for CO<sub>2</sub>RR due to their promising activity sites and adjustable structures. Wang et al. prepared a series of atomically dispersed Co catalysts derived from bimetallic Co/Zn ZIFs, which possessed different nitrogen coordination numbers.<sup>[277]</sup> The obtained catalyst with two coordinate nitrogen atoms exhibited a high FE for CO (94%) and high selectivity. The synergistic interactions based on various molecules and their interfaces of plenary single-atomic structures can significantly promote the CO<sub>2</sub>RR process.

Later, Ren et al. developed an efficient nitrogenated carbon catalyst anchored with isolated diatomic Ni–Fe sites for CO<sub>2</sub>RR.<sup>[278]</sup> Based on the mechanism research, the structural change of bimetal nitrogen sites effectively reduces the reaction energy barrier, resulting in superior CO<sub>2</sub>RR activity. The Ni/Fe–N–C showed an outstanding FE for CO (up to 98%) and robust durability. Gu et al. developed a catalyst dispersed with single-atom Fe sites, which presented ultrahigh activity for CO<sub>2</sub>RR.<sup>[279]</sup> The single-atom Fe catalyst (Fe<sup>3+</sup>–N–C) was fabricated via annealing the Fe-doped ZIF-8 in N<sub>2</sub> at 900 °C. They found that the discrete Fe<sup>3+</sup> ions possessed more activity compare with Fe<sup>2+</sup> sites, resulting in faster adsorption for CO<sub>2</sub> and weaker absorption for CO. Thus, Fe<sup>3+</sup>–N–C exhibited superior CO<sub>2</sub>RR performance that only required an overpotential of 80 mV to produce CO and the current density reached 94 mA cm<sup>−2</sup> at a low overpotential of 340 mV.

### 3.8.5. Other Electrocatalytic Reactions

In addition to the earlier electrocatalytic reactions (ORR, HER, OER, and CO<sub>2</sub>RR), MOF derivatives have also been applied to other catalytic reactions (such as NRR and MOR). Given the promising and environmental-friendly method of electrochemical NRR for sustainable ammonia production, the development of MOF derivatives for efficient NRR has attracted increasing attention.<sup>[280]</sup> Liu et al. successfully synthesized the N-doped

porous carbon (NPC) derived from nitrogen-rich ZIF-8 as the cost-effective NRR catalyst.<sup>[281]</sup> Through adjusting the N content and species, the N<sub>2</sub> chemical adsorption and N≡N cleavage significantly enhanced, resulting in high activity of the optimized NPC for NRR. They found that the contents of pyridinic and pyrrolic N were crucial for promoting ammonia production on NPC by theory and calculation. Geng et al. presented nitrogen-doped carbon distributed with Ru single atoms (Ru SAs/N-C) as N<sub>2</sub> reduction catalysts.<sup>[282]</sup> The obtained Ru SAs/N-C derived from ZIF-8 exhibited a record-high activity for N<sub>2</sub> electrochemical reduction, which achieved an FE of 29.6% for NH<sub>3</sub> production and a high ammonia production rate of 120.9 μg h<sup>−1</sup> mg<sub>cat</sub><sup>−1</sup>. Recently, Luo et al. reported nitrogen-doped carbon/Co<sub>3</sub>O<sub>4</sub> nanocomposites (Co<sub>3</sub>O<sub>4</sub>@NCs) derived from ZIF-67 with core-shell structures, which exhibited an outstanding NRR performance with an FE of 8.5% at −0.2 V vs RHE and a high NH<sub>3</sub> yield of 42.58 μg h<sup>−1</sup> mg<sub>cat</sub><sup>−1</sup>.<sup>[283]</sup>

Due to the simplicity, high energy-conversion efficiency, and renewable fuel, direct methanol fuel cells (DMFCs) are regarded as promising power sources for energy demand in future.<sup>[284]</sup> Recently, Rezaee and Shahrokhian reported the fabrication of 3D ultrathin nanoporous carbon composites embedded with petal-like NiCo/NiO–CoO metal/metal oxides.<sup>[285]</sup> The nanoporous carbon composite is synthesized through direct carbonization of the as-designed bimetallic MOFs. The obtained NiCo/NiO–CoO/NPCC exhibited excellent electrocatalytic MOR performance with a small  $E_{onset}$  of 0.32 V compared with Ni/NiO/NPCC ( $E_{onset} = 0.38$  V) and Co/CoO/NPCC ( $E_{onset} = 0.43$  V), which can be attributed to the fast ion/electron transfer offered by the enlarged specific surface of a unique ultrathin petal-like structure.

## 4. Summary and Perspective

In summary, the recent progress of MOF-based materials, including pristine MOFs, MOF composites, and MOF derivatives for photo/electrocatalysis, is comprehensively reviewed. The novel strategies to improve photo/electrocatalytic activities are discussed and highlighted. The vast developments in the past several years have proven that MOFs are promising photo/electrocatalysts to resolve the energy and environmental problems. Though tremendous achievements have been realized, MOF-based photo/electrocatalysts still face some challenges which have to be addressed.

The main drawbacks of MOFs for photo/electrocatalysis are their low stability and low conductivity, hampering their photo/electrocatalytic activities. Highly stable MOFs with improved conductivity are crucial for high catalytic activity and long-term durability. Also, the low-cost, facile, and large-scale synthesis of MOFs with high catalytic activities is an everlasting target for large-scale industry applications. What's more, the build-up of the structure–property relationship of MOFs for photo/electrocatalysis is highly eager. A deep insight into the catalytic mechanism and reaction pathways can predict and modulate the activity and selectivity, guiding the rational design of highly efficient photo/electrocatalysts of MOFs. Advanced in situ and operando techniques are needed to investigate the real active sites and reaction pathways.



The semiconductor-like behavior is the most important characteristic for MOF photocatalysts. The bandgaps of MOFs can be modulated via metal doping, ligand functionalization, and forming composites with other materials to improve the light-harvesting efficiency. The location of HOMO and LUMO levels to match the redox potential is a prior consideration for some photochemical reactions. The study and understanding of the systematic control of the band structure of MOFs is particularly important but still lacking. Also, most MOF photocatalysts suffer from low conversion efficiency, especially for photocatalytic CO<sub>2</sub> reduction and organic synthesis, so a trade-off between efficiency and selectivity should be considered, and MOF photocatalysts with both high efficiency and selectivity have to be explored.

Noble metal materials are usually utilized to improve the photocatalytic activities of MOFs, such as using noble metal Pt as cocatalyst or using Ru-/Ir-based molecules as light-harvesting component. Yet, the scarcity and high price of noble metal materials limit their practical applications. The replacement of noble metals with Earth-abundant elements as cocatalysts or light-harvesting components without loss of high efficiency is highly important. Also, for most photocatalytic reactions such as HER, OER, and CO<sub>2</sub>RR, only half reduction or oxidation reactions can be utilized and sacrificial agents as electron donors or acceptors are needed. It is highly desirable to integrate the reduction reaction and oxidation reaction together to avoid the usage of sacrificial agents. For practical applications using natural sunlight, the use of sacrificial agents is not feasible. The photocatalytic overall water-splitting process only uses H<sub>2</sub>O as the reactant, and in the natural photosynthesis of plants, the photocatalytic CO<sub>2</sub>RR only involves H<sub>2</sub>O and CO<sub>2</sub> to produce carbohydrates and O<sub>2</sub>. Yet, MOFs for photocatalytic reactions without sacrificial agents were rarely investigated and reported. The artificial photosynthesis that mimics photosynthesis with high efficiency and selectivity for carbohydrates is still a formidable but also promising task.

For large-scale and industrial applications, electrocatalysis should be conducted at a large current density (usually 200–500 mA cm<sup>-2</sup>) with high efficiency and stability. Yet, the electrocatalytic performances of MOFs at large current density are still rare and the stability of MOFs in these conditions needs more research. The electrochemical reactions are conducted in electrolyte, which usually need strong acidic or basic conditions that are harmful to environments and the stability of catalysts. More attention has to be paid to the development of efficient MOF electrocatalysts working at environmentally benign conditions and neutral-pH electrolyte or even solid electrolyte. Electrocatalytic pollution degradation and electro-organic synthesis possess much higher conversion efficiency compared with photocatalytic reactions and are more promising when utilizing electricity generated by clean solar energy. Yet, the studies of electrocatalytic pollution degradation and electro-organic synthesis are quite limited and in the early stage. 2D ultrathin MOFs are very promising electrocatalysts with superior activity and efficiency, due to the high density of CUMSs, superior electron transfer, rapid mass transport, and fast permeation of gas/liquid molecules. Yet, the development of the facile and large-scale synthesis of 2D MOFs in multigram quantities is still lacking.

MOF derivatives have the advantages to surpass the low-stability and low-conductivity issues of pristine MOFs and have demonstrated superior photo/electrocatalytic activities. Yet, the lack of knowledge of the transformation mechanism from MOFs to MOF derivatives hampers the precise control of fine structures. Using in situ and operando techniques to monitor the synthesis process can help establish a better understanding of the formation mechanism of MOF derivatives, guiding the accurate control of the structure and active sites of MOF derivatives toward aimed photo/electrocatalysis. SACs derived from MOFs have caused widespread concern for their superior photo/electrocatalytic performance. Yet, MOF-based SACs are still in the early stages, and more experimental and theoretical studies should be launched for a better understanding of the formation process of SACs and revealing the catalytic mechanism on the active sites at an atomic level. Also, new strategies for the facile and low-cost synthesis of MOF-based SACs should be explored.

By integrating various MOF-based photo/electrocatalysis together, it is possible to build a sustainable system with a low-carbon or even a carbon-neutral energy cycle. H<sub>2</sub>O, CO<sub>2</sub>, and N<sub>2</sub> can be converted to high value-added compounds via electrocatalysis driven by renewable energy or photocatalysis. ORR and OER catalysts-driven metal–air battery can drive the electrocatalytic water splitting process, and the generated H<sub>2</sub> and O<sub>2</sub> are used to generate clean electricity in fuel cells via hydrogen oxidation reaction (HOR) and ORR reactions, forming a self-powered system. All the system parts that involve photo/electrocatalysis can be realized via MOFs with high stability and catalytic efficiency, providing sustainable pathways for the production of high value fuels and chemicals. There is no doubt that MOF-based photo/electrocatalysts will continue to trigger much increasing research in the future. We believe that low-cost, stable, and efficient MOF-based photo/electrocatalysts combined with other emerging applications such as gas storage and separation will present a bright future for creating global-scale sustainable energy system.

## Acknowledgements

This work was supported by the Natural Science Foundation of Zhejiang Province (no. LY19E020007) and the Grant AX-1730 from the Welch Foundation (B.C.).

## Conflict of Interest

The authors declare no conflict of interest.

## Keywords

electrocatalysis, energy, metal–organic frameworks, photocatalysis

Received: January 30, 2021

Revised: February 28, 2021

Published online: May 5, 2021

- [1] a) J. W. Ager, A. A. Lapkin, *Science* **2018**, 360, 707; b) S. J. Davis, N. S. Lewis, M. Shaner, S. Aggarwal, D. Arent, I. L. Azevedo, S. M. Benson, T. Bradley, J. Brouwer, Y.-M. Chiang, *Science* **2018**, 360, eaas9793.
- [2] S. Ren, D. Joulié, D. Salvatore, K. Torbensen, M. Wang, M. Robert, C. P. Berlinguette, *Science* **2019**, 365, 367.
- [3] M. Ding, R. W. Flaig, H.-L. Jiang, O. M. Yaghi, *Chem. Soc. Rev.* **2019**, 48, 2783.
- [4] M. M. Nowaczyk, N. Plumeré, *Nat. Chem. Biol.* **2016**, 12, 990.
- [5] X. Su, J. Ma, X. Wei, P. Cao, D. Zhu, W. Chang, Z. Liu, X. Zhang, M. Li, *Science* **2017**, 357, 815.
- [6] C. Gisriel, I. Sarrou, B. Ferlez, J. H. Golbeck, K. E. Redding, R. Fromme, *Science* **2017**, 357, 1021.
- [7] a) N. S. Lewis, *Science* **2016**, 351, aad1920; b) D. J. Nürnberg, J. Morton, S. Santabarbara, A. Telfer, P. Joliot, L. A. Antonaru, A. V. Ruban, T. Cardona, E. Krausz, A. Boussac, *Science* **2018**, 360, 1210; c) E. Kabir, P. Kumar, S. Kumar, A. A. Adelodun, K.-H. Kim, *Renew. Sustain. Energy Rev.* **2018**, 82, 894; d) H. L. Nguyen, *Adv. Energy Mater.* **2020**, 10, 2002091.
- [8] a) S. Chen, T. Takata, K. Domen, *Nat. Rev. Mater.* **2017**, 2, 17050; b) X. Yang, D. Wang, *ACS Appl. Energy Mater.* **2018**, 1, 6657; c) J. Balajka, M. A. Hines, W. J. DeBenedetti, M. Komora, J. Pavelec, M. Schmid, U. Diebold, *Science* **2018**, 361, 786; d) W.-J. Ong, L.-L. Tan, Y. H. Ng, S.-T. Yong, S.-P. Chai, *Chem. Rev.* **2016**, 116, 7159.
- [9] R. F. Service, *Science* **2019**, 365, 108.
- [10] a) H. Deng, S. Grunder, K. E. Cordova, C. Valente, H. Furukawa, M. Hmadeh, F. Gándara, A. C. Whalley, Z. Liu, S. Asahina, *Science* **2012**, 336, 1018; b) O. K. Farha, I. Eryazici, N. C. Jeong, B. G. Hauser, C. E. Wilmer, A. A. Sarjeant, R. Q. Snurr, S. T. Nguyen, A. Yazaydin, J. T. Hupp, *J. Am. Chem. Soc.* **2012**, 134, 15016.
- [11] a) H. Li, L. Li, R.-B. Lin, W. Zhou, S. Xiang, B. Chen, Z. Zhang, *EnergyChem* **2019**, 1, 100006; b) J. Gao, X. Qian, R. Lin, R. Krishna, H. Wu, W. Zhou, B. Chen, *Angew. Chem. Int. Ed.* **2020**, 59, 4396.
- [12] a) Y. Cui, J. Zhang, H. He, G. Qian, *Chem. Soc. Rev.* **2018**, 47, 5740; b) H. Xu, J. Gao, X. Qian, J. Wang, H. He, Y. Cui, Y. Yang, Z. Wang, G. Qian, *J. Mater. Chem. A* **2016**, 4, 10900.
- [13] G. M. Espallargas, E. Coronado, *Chem. Soc. Rev.* **2018**, 47, 533.
- [14] M. X. Wu, Y. W. Yang, *Adv. Mater.* **2017**, 29, 1606134.
- [15] a) H. Konnerth, B. M. Matsagar, S. S. Chen, M. H. Precht, F.-K. Shieh, K. C.-W. Wu, *Coord. Chem. Rev.* **2020**, 416, 213319; b) Y.-T. Liao, N. Ishiguro, A. P. Young, C.-K. Tsung, K. C.-W. Wu, *Appl. Catal. B: Environ.* **2020**, 270, 118805; c) Y.-T. Liao, B. M. Matsagar, K. C.-W. Wu, *ACS Sustainable Chem. Eng.* **2018**, 6, 13628.
- [16] a) C.-C. Chueh, C.-I. Chen, Y.-A. Su, H. Konnerth, Y.-J. Gu, C.-W. Kung, K. C.-W. Wu, *J. Mater. Chem. A* **2019**, 7, 17079; b) C. C. Lee, C. I. Chen, Y. T. Liao, K. C. W. Wu, C. C. Chueh, *Adv. Sci.* **2019**, 6, 1970030.
- [17] a) L. Wang, H. Xu, J. Gao, J. Yao, Q. Zhang, *Coord. Chem. Rev.* **2019**, 398, 213016; b) J. Li, X. Wang, G. Zhao, C. Chen, Z. Chai, A. Alsaedi, T. Hayat, X. Wang, *Chem. Soc. Rev.* **2018**, 47, 2322; c) W. Ren, J. Gao, C. Lei, Y. Xie, Y. Cai, Q. Ni, J. Yao, *Chem. Eng. J.* **2018**, 349, 766.
- [18] a) D. Li, H.-Q. Xu, L. Jiao, H.-L. Jiang, *EnergyChem* **2019**, 1, 100005; b) X. Wang, H. Xu, Y. Han, Y. Li, C. Sheng, Z. Xu, J. Xu, M. Wang, *Inorg. Chim. Acta* **2017**, 461, 15; c) Y. Li, Y. Su, J. Xu, Z.-I. Xu, H. Xu, *Bull. Chem. Soc. Jpn.* **2017**, 90, 1152.
- [19] F.-Y. Yi, R. Zhang, H. Wang, L.-F. Chen, L. Han, H.-L. Jiang, Q. Xu, *Small Methods* **2017**, 1, 1700187.
- [20] F. Strieth-Kalthoff, M. J. James, M. Teders, L. Pitzer, F. Glorius, *Chem. Soc. Rev.* **2018**, 47, 7190.
- [21] a) C. Zhou, C. Lai, C. Zhang, G. Zeng, D. Huang, M. Cheng, L. Hu, W. Xiong, M. Chen, J. Wang, Y. Yang, L. Jiang, *Appl. Catal. B: Environ.* **2018**, 238, 6; b) A. Dhakshinamoorthy, Z. Li, H. Garcia, *Chem. Soc. Rev.* **2018**, 47, 8134; c) J. Zhu, P.-Z. Li, W. Guo, Y. Zhao, R. Zou, *Coord. Chem. Rev.* **2018**, 359, 80; d) Z. Liang, C. Qu, W. Guo, R. Zou, Q. Xu, *Adv. Mater.* **2018**, 30, 1702891; e) X. Fang, Q. Shang, Y. Wang, L. Jiao, T. Yao, Y. Li, Q. Zhang, Y. Luo, H.-L. Jiang, *Adv. Mater.* **2018**, 30, 1705112; f) X. Ma, L. Wang, Q. Zhang, H.-L. Jiang, *Angew. Chem. Int. Ed.* **2019**, 58, 12175; g) C. Xu, Y. Pan, G. Wan, H. Liu, L. Wang, H. Zhou, S.-H. Yu, H.-L. Jiang, *J. Am. Chem. Soc.* **2019**, 141, 19110.
- [22] a) Z. Pan, G. Zhang, X. Wang, *Angew. Chem. Int. Ed.* **2019**, 58, 7102; b) L. Zhao, X. Chen, X. Wang, Y. Zhang, W. Wei, Y. Sun, M. Antonietti, M.-M. Titirici, *Adv. Mater.* **2010**, 22, 3317; c) B. Yan, L. Zhang, Z. Tang, M. Al-Mamun, H. Zhao, X. Su, *Appl. Catal. B: Environ.* **2017**, 218, 743.
- [23] a) L. Feng, K.-Y. Wang, J. Powell, H.-C. Zhou, *Matter* **2019**, 1, 801; b) Y. Li, H. Xu, S. Ouyang, J. Ye, *Phys. Chem. Chem. Phys.* **2016**, 18, 7563; c) J. Hao, X. Xu, H. Fei, L. Li, B. Yan, *Adv. Mater.* **2018**, 30, 1705634; d) D. Li, M. Kassymova, X. Cai, S.-Q. Zang, H.-L. Jiang, *Coord. Chem. Rev.* **2020**, 412, 213262; e) D. Li, S. H. Yu, H.-L. Jiang, *Adv. Mater.* **2018**, 30, 1707377; f) J.-D. Xiao, H.-L. Jiang, *Acc. Chem. Res.* **2018**, 52, 356; g) C. Xu, H. Liu, D. Li, J.-H. Su, H.-L. Jiang, *Chem. Sci.* **2018**, 9, 3152; h) Y. Yan, C. Li, Y. Wu, J. Gao, Q. Zhang, *J. Mater. Chem. A* **2020**, 8, 15245.
- [24] a) M. Fuentes-Cabrera, D. M. Nicholson, B. G. Sumpter, M. Widom, *J. Chem. Phys.* **2005**, 123, 124713; b) B. Civalieri, F. Napoli, Y. Noël, C. Roetti, R. Dovesi, *CrystEngComm* **2006**, 8, 364.
- [25] S. Wang, X. Wang, *Small* **2015**, 11, 3097.
- [26] a) D. H. Meenakshi, S. Christian, F. Théo, R. Laurence, M. Guillaume, S. Clément, F. Gérard, *J. Am. Chem. Soc.* **2010**, 131, 10857; b) P. L. Feng, S. Nikodemski, B. W. Jacobs, S. T. Meek, M. D. Allendorf, *J. Am. Chem. Soc.* **2010**, 132, 15487.
- [27] C. G. Silva, I. Luz, F. X. Llabres i Xamena, A. Corma, H. Garcia, *Chem. Eur. J.* **2010**, 16, 11133.
- [28] Y. Fu, D. Sun, Y. Chen, R. Huang, Z. Ding, X. Fu, Z. Li, *Angew. Chem. Int. Ed.* **2012**, 51, 3364.
- [29] D. Sun, L. Ye, Z. Li, *Appl. Catal. B: Environ.* **2015**, 164, 428.
- [30] P. Huo, T. Chen, J.-L. Hou, L. Yu, Q.-Y. Zhu, J. Dai, *Inorg. Chem.* **2016**, 55, 6496.
- [31] G. Wang, Q. Sun, Y. Liu, B. Huang, Y. Dai, X. Zhang, X. Qin, *Chem. Eur. J.* **2015**, 21, 2364.
- [32] a) C. H. Fang, Y. L. Chen, C. H. Yang, Y. Chi, Y. S. Yeh, E. Y. Li, Y. M. Cheng, C. J. Hsu, P. T. Chou, C. T. Chen, *Chem. Eur. J.* **2007**, 13, 2686; b) Y. Ding, J.-X. Guo, X.-S. Wang, S.-S. Liu, F.-C. Ma, *Chinese J. Chem. Phys.* **2009**, 22, 269.
- [33] C. A. Kent, D. Liu, L. Ma, J. M. Papanikolas, T. J. Meyer, W. Lin, *J. Am. Chem. Soc.* **2011**, 133, 12940.
- [34] C. Wang, Z. Xie, K. E. deKrafft, W. Lin, *J. Am. Chem. Soc.* **2011**, 133, 13445.
- [35] M. A. Nasalevich, R. Becker, E. V. Ramos-Fernandez, S. Castellanos, S. L. Veber, M. V. Fedin, F. Kapteijn, J. N. H. Reek, J. I. van der Lugt, J. Gascon, *Energy Environ. Sci.* **2015**, 8, 364.
- [36] a) Y. Kataoka, K. Sato, Y. Miyazaki, K. Masuda, H. Tanaka, S. Naito, W. Mori, *Energy Environ. Sci.* **2009**, 2, 397; b) X. Deng, J. Alberio, L. Xu, H. Garcia, Z. Li, *Inorg. Chem.* **2018**, 57, 8276.
- [37] a) M. B. Chambers, X. Wang, L. Ellezam, O. Ersen, M. Fontecave, C. Sanchez, L. Rozes, C. Mellot-Draznieks, *J. Am. Chem. Soc.* **2017**, 139, 8222; b) J.-L. Wang, C. Wang, W. Lin, *ACS Catal.* **2012**, 2, 2630.
- [38] E.-X. Chen, M. Qiu, Y.-F. Zhang, Y.-S. Zhu, L.-Y. Liu, Y.-Y. Sun, X. Bu, J. Zhang, Q. Lin, *Adv. Mater.* **2018**, 30, 1704388.
- [39] H.-Q. Xu, J. Hu, D. Wang, Z. Li, Q. Zhang, Y. Luo, S.-H. Yu, H.-L. Jiang, *J. Am. Chem. Soc.* **2015**, 137, 13440.
- [40] D. Wang, M. Wang, Z. Li, *ACS Catal.* **2015**, 5, 6852.

- [41] a) W. Mei, D. Li, H. Xu, J. Zan, L. Sun, Q. Li, B. Zhang, Y. Wang, D. Xia, *Chem. Phys. Lett.* **2018**, 706, 694; b) R. Li, W. Zhang, K. Zhou, *Adv. Mater.* **2018**, 30, 1705512; c) D. Wang, R. Huang, W. Liu, D. Sun, Z. Li, *ACS Catal.* **2014**, 4, 4254.
- [42] K. G. Laurier, F. Vermoortele, R. Ameloot, D. E. De Vos, J. Hofkens, M. B. Roeflaers, *J. Am. Chem. Soc.* **2013**, 135, 14488.
- [43] L. Shi, T. Wang, H. Zhang, K. Chang, X. Meng, H. Liu, J. Ye, *Adv. Sci.* **2015**, 2, 1500006.
- [44] a) C. Li, H. Xu, J. Gao, W. Du, L. Shangguan, X. Zhang, R.-B. Lin, H. Wu, W. Zhou, X. Liu, J. Yao, B. Chen, *J. Mater. Chem. A* **2019**, 7, 11928; b) J. Gao, J. Miao, P.-Z. Li, W. Y. Teng, L. Yang, Y. Zhao, B. Liu, Q. Zhang, *Chem. Commun.* **2014**, 50, 3786.
- [45] X.-K. Wang, J. Liu, L. Zhang, L.-Z. Dong, S.-L. Li, Y.-H. Kan, D.-S. Li, Y.-Q. Lan, *ACS Catal.* **2019**, 9, 1726.
- [46] D.-C. Liu, T. Ouyang, R. Xiao, W.-J. Liu, D.-C. Zhong, Z. Xu, T.-B. Lu, *ChemSusChem* **2019**, 12, 2166.
- [47] H. Zhang, J. Wei, J. Dong, G. Liu, L. Shi, P. An, G. Zhao, J. Kong, X. Wang, X. Meng, J. Zhang, J. Ye, *Angew. Chem. Int. Ed.* **2016**, 55, 14308.
- [48] B. Pattengale, S. Yang, J. Ludwig, Z. Huang, X. Zhang, J. Huang, *J. Am. Chem. Soc.* **2016**, 138, 8072.
- [49] D. Sun, W. Liu, M. Qiu, Y. Zhang, Z. Li, *Chem. Commun.* **2015**, 51, 2056.
- [50] J.-D. Xiao, L. Han, J. Luo, S.-H. Yu, H.-L. Jiang, *Angew. Chem. Int. Ed.* **2018**, 57, 1103.
- [51] Y. Liang, R. Shang, J. Lu, W. An, J. Hu, L. Liu, W. Cui, *Int. J. Hydrogen Energy* **2019**, 44, 2797.
- [52] Z.-H. Yan, M.-H. Du, J. Liu, S. Jin, C. Wang, G.-L. Zhuang, X.-J. Kong, L.-S. Long, L.-S. Zheng, *Nat. Commun.* **2018**, 9, 3353.
- [53] T. Kajiwara, M. Fujii, M. Tsujimoto, K. Kobayashi, M. Higuchi, K. Tanaka, S. Kitagawa, *Angew. Chem. Int. Ed.* **2016**, 55, 2697.
- [54] a) K. M. Choi, D. Kim, B. Rungtaweivoranit, C. A. Trickett, J. T. D. Barmannbek, A. S. Alshammari, P. Yang, O. M. Yaghi, *J. Am. Chem. Soc.* **2017**, 139, 356; b) Y. Fang, Y. Ma, M. Zheng, P. Yang, A. M. Asiri, X. Wang, *Coord. Chem. Rev.* **2018**, 373, 83; c) P. Liu, Y. Zhao, R. Qin, S. Mo, G. Chen, L. Gu, D. M. Chevrier, P. Zhang, Q. Guo, D. Zang, *Science* **2016**, 352, 797.
- [55] Z. Jiang, X. Xu, Y. Ma, H. S. Cho, D. Ding, C. Wang, J. Wu, P. Oleynikov, M. Jia, J. Cheng, *Nature* **2020**, 586, 549.
- [56] H. Wu, X. Y. Kong, X. Wen, S.-P. Chai, E. C. Lovell, J. Tang, Y. H. Ng, *Angew. Chem. Int. Ed.* **2021**, <https://doi.org/10.1002/anie.202015735>.
- [57] S. Wang, X. Wang, *Appl. Catal. B: Environ.* **2015**, 162, 494.
- [58] H. Liu, J. Zhang, D. Ao, *Appl. Catal. B: Environ.* **2018**, 221, 433.
- [59] L. Shi, T. Wang, H. Zhang, K. Chang, J. Ye, *Adv. Funct. Mater.* **2015**, 25, 5360.
- [60] G. Burgeth, H. Kisch, *Coord. Chem. Rev.* **2002**, 230, 41.
- [61] a) W. Zhang, Z. Chen, M. Al-Naji, P. Guo, S. Cwik, O. Halbherr, Y. Wang, M. Muhler, N. Wilde, R. Gläser, R. A. Fischer, *Dalton Trans.* **2016**, 45, 14883; b) C.-C. Wang, Y.-Q. Zhang, J. Li, P. Wang, *J. Mol. Struct.* **2015**, 1083, 127.
- [62] C. Wang, K. E. deKrafft, W. Lin, *J. Am. Chem. Soc.* **2012**, 134, 7211.
- [63] J. D. Xiao, Q. Shang, Y. Xiong, Q. Zhang, Y. Luo, S. H. Yu, H. L. Jiang, *Angew. Chem. Int. Ed.* **2016**, 55, 9389.
- [64] a) R. Wang, L. Wu, B. Chica, L. Gu, G. Xu, Y. Yuan, *J. Materiomics* **2017**, 3, 58; b) S. Kampouri, T. N. Nguyen, C. P. Ireland, B. Valizadeh, F. M. Ebrahim, G. Capano, D. Ongari, A. Mace, N. Guijarro, K. Sivula, A. Sienkiewicz, L. Forro, B. Smit, K. C. Stylianou, *J. Mater. Chem. A* **2018**, 6, 2476.
- [65] Z. Li, J.-D. Xiao, H.-L. Jiang, *ACS Catal.* **2016**, 6, 5359.
- [66] C. C. Shen, Y. N. Liu, X. Wang, X. X. Fang, Z. W. Zhao, N. Jiang, L. B. Ma, X. Zhou, T. Y. Cheang, A. W. Xu, *Dalton Trans.* **2018**, 47, 11705.
- [67] B. Zhang, J. Zhang, X. Tan, D. Shao, J. Shi, L. Zheng, J. Zhang, G. Yang, B. Han, *ACS Appl. Mater. Interfaces* **2018**, 10, 16418.
- [68] J. He, Z. Yan, J. Wang, J. Xie, L. Jiang, Y. Shi, F. Yuan, F. Yu, Y. Sun, *Chem. Commun.* **2013**, 49, 6761.
- [69] J. J. Zhou, R. Wang, X. L. Liu, F. M. Peng, C. H. Li, F. Teng, Y. P. Yuan, *Appl. Surf. Sci.* **2015**, 346, 278.
- [70] G. Zhou, M.-F. Wu, Q.-J. Xing, F. Li, H. Liu, X.-B. Luo, J.-P. Zou, J.-M. Luo, A.-Q. Zhang, *Appl. Catal. B: Environ.* **2018**, 220, 607.
- [71] S. Yun, Z. Zhe, L. Hong, W. Yong, *Appl. Catal. B: Environ.* **2017**, 200, 448.
- [72] L. Hong, Z. Jiang, A. Dan, *Appl. Catal. B: Environ.* **2017**, 221, 433.
- [73] K. Sun, M. Liu, J. Pei, D. Li, C. Ding, K. Wu, H.-L. Jiang, *Angew. Chem. Int. Ed.* **2020**, 59, 22749.
- [74] a) Y. Zheng, L. Lin, B. Wang, X. Wang, *Angew. Chem. Int. Ed.* **2015**, 54, 12868; b) M. Zhang, X. Wang, *Energy Environ. Sci.* **2014**, 7, 1902.
- [75] P. P. Bag, X.-S. Wang, P. Sahoo, J. Xiong, R. Cao, *Catal. Sci. Technol.* **2017**, 7, 5113.
- [76] J. L. Segura, M. J. Mancheño, F. Zamora, *Chem. Soc. Rev.* **2016**, 45, 5635.
- [77] F.-M. Zhang, J.-L. Sheng, Z.-D. Yang, X.-J. Sun, H.-L. Tang, M. Lu, H. Dong, F.-C. Shen, J. Liu, Y.-Q. Lan, *Angew. Chem. Int. Ed.* **2018**, 57, 12106.
- [78] C. Wang, J. L. Wang, W. Lin, *J. Am. Chem. Soc.* **2012**, 134, 19895.
- [79] B. Nepal, S. Das, *Angew. Chem. Int. Ed.* **2013**, 52, 7224.
- [80] L. Chi, Q. Xu, X. Liang, J. Wang, X. Su, *Small* **2016**, 12, 1351.
- [81] Y. An, Y. Liu, P. An, J. Dong, B. Xu, Y. Dai, X. Qin, X. Zhang, M.-H. Whangbo, B. Huang, *Angew. Chem. Int. Ed.* **2017**, 56, 3036.
- [82] Y. Xiao, Y. Qi, X. Wang, X. Wang, F. Zhang, C. Li, *Adv. Mater.* **2018**, 30, 1803401.
- [83] J. Zhang, T. Bai, H. Huang, M.-H. Yu, X. Fan, Z. Chang, X.-H. Bu, *Adv. Mater.* **2020**, 32, 2004747.
- [84] S. Wang, M. Cabrero-Antonino, S. Navalón, C.-C. Cao, A. Tissot, I. Dovgaliuk, J. Marrot, C. Martineau-Corcós, L. Yu, H. Wang, *Chem* **2020**, 6, 3409.
- [85] X.-M. Cheng, X.-Y. Dao, S.-Q. Wang, J. Zhao, W.-Y. Sun, *ACS Catal.* **2020**, 11, 650.
- [86] P. M. Stanley, C. Thomas, E. Thyrahaug, A. Urstoege, M. Schuster, J. R. Hauer, B. Rieger, J. Warnan, R. A. Fischer, *ACS Catal.*, 11, 871.
- [87] Q. Huang, J. Liu, L. Feng, Q. Wang, W. Guan, L.-Z. Dong, L. Zhang, L.-K. Yan, Y.-Q. Lan, H.-C. Zhou, *Natl. Sci. Rev.* **2020**, 7, 53.
- [88] Y. Wang, N.-Y. Huang, J.-Q. Shen, P.-Q. Liao, X.-M. Chen, J.-P. Zhang, *J. Am. Chem. Soc.* **2018**, 140, 38.
- [89] P. Wu, C. He, J. Wang, X. Peng, X. Li, Y. An, C. Duan, *J. Am. Chem. Soc.* **2012**, 134, 14991.
- [90] Y. Zhang, J. Guo, L. Shi, Y. Zhu, K. Hou, Y. Zheng, Z. Tang, *Sci. Adv.* **2017**, 3, e1701162.
- [91] J. Long, S. Wang, Z. Ding, S. Wang, Y. Zhou, L. Huang, X. Wang, *Chem. Commun.* **2012**, 48, 11656.
- [92] L. Xiao, Q. Zhang, P. Chen, L. Chen, F. Ding, J. Tang, Y.-J. Li, C.-T. Au, S.-F. Yin, *Appl. Catal. B: Environ.* **2019**, 248, 380.
- [93] Y.-Z. Chen, Z.-U. Wang, H. Wang, J. Lu, S.-H. Yu, H.-L. Jiang, *J. Am. Chem. Soc.* **2017**, 139, 2035.
- [94] H. Liu, C. Xu, D. Li, H.-L. Jiang, *Angew. Chem. Int. Ed.* **2018**, 57, 5379.
- [95] J. Shi, J. Zhang, T. Liang, D. Tan, X. Tan, Q. Wan, X. Cheng, B. Zhang, B. Han, L. Liu, F. Zhang, G. Chen, *ACS Appl. Mater. Interfaces* **2019**, 11, 30953.
- [96] C.-C. Wang, J.-R. Li, X.-L. Lv, Y.-Q. Zhang, G. Guo, *Energy Environ. Sci.* **2014**, 7, 2831.
- [97] L. Ai, C. Zhang, L. Li, J. Jiang, *Appl. Catal. B: Environ.* **2014**, 148, 191.
- [98] M. Alvaro, E. Carbonell, B. Ferrer, F. X. Llabres i Xamena, H. Garcia, *Chem. Eur. J.* **2007**, 13, 5106.
- [99] J. Li, J. Yang, Y. Y. Liu, J. F. Ma, *Chem. Eur. J.* **2015**, 21, 4413.
- [100] S. Rengaraj, S. Venkataraj, J.-W. Yeon, Y. Kim, X. Z. Li, G. K. H. Pang, *Appl. Catal. B: Environ.* **2007**, 77, 157.

- [101] R. Liang, L. Shen, F. Jing, W. Wu, N. Qin, R. Lin, L. Wu, *Appl. Catal. B: Environ.* **2015**, 162, 245.
- [102] a) Y.-Z. Chen, R. Zhang, L. Jiao, H.-L. Jiang, *Coord. Chem. Rev.* **2018**, 362, 1; b) T. Zhang, W. Lin, *Chem. Soc. Rev.* **2014**, 43, 5982; c) Y. Pan, Y. Qian, X. Zheng, S.-Q. Chu, Y. Yang, C. Ding, X. Wang, S.-H. Yu, H.-L. Jiang, *Natl. Sci. Rev.* **2021**, 8, nwaa224.
- [103] a) X. Cao, B. Zheng, X. Rui, W. Shi, Q. Yan, H. Zhang, *Angew. Chem. Int. Ed.* **2014**, 53, 1404; b) H. Chen, K. Shen, J. Chen, X. Chen, Y. Li, J. Mater. Chem. A **2017**, 5, 9937; c) Z.-F. Huang, J. Song, K. Li, M. Tahir, Y.-T. Wang, L. Pan, L. Wang, X. Zhang, J.-J. Zou, J. Am. Chem. Soc. **2016**, 138, 1359; d) M. Lan, R.-M. Guo, Y. Dou, J. Zhou, A. Zhou, J.-R. Li, *Nano Energy* **2017**, 33, 238.
- [104] W. Chen, J. Fang, Y. Zhang, G. Chen, S. Zhao, C. Zhang, R. Xu, J. Bao, Y. Zhou, X. Xiang, *Nanoscale* **2018**, 10, 4463.
- [105] a) Y. Su, D. Ao, H. Liu, Y. Wang, J. Mater. Chem. A **2017**, 5, 8680; b) S. Chandrasekaran, L. Yao, L. Deng, C. Bowen, Y. Zhang, S. Chen, Z. Lin, F. Peng, P. Zhang, *Chem. Soc. Rev.* **2019**, 48, 4178.
- [106] X. Zhao, J. Feng, J. Liu, J. Lu, W. Shi, G. Yang, G. Wang, P. Feng, P. Cheng, *Adv. Sci.* **2018**, 5, 1700590.
- [107] W. Chen, B. Han, C. Tian, X. Li, S. Liang, H. Deng, Z. Lin, *Appl. Catal. B: Environ.* **2019**, 244, 996.
- [108] a) T. Sakakura, J.-C. Choi, H. Yasuda, *Chem. Rev.* **2007**, 107, 2365; b) S. Xiao, D. Pan, R. Liang, W. Dai, Q. Zhang, G. Zhang, C. Su, H. Li, W. Chen, *Appl. Catal. B: Environ.* **2018**, 236, 304; c) J.-H. Zhang, W. Yang, M. Zhang, H.-J. Wang, R. Si, D.-C. Zhong, T.-B. Lu, *Nano Energy*, 80, 105542.
- [109] L. Wang, J. Wan, Y. Zhao, N. Yang, D. Wang, *J. Am. Chem. Soc.* **2019**, 141, 2238.
- [110] Y. Su, Z. Song, W. Zhu, Q. Mu, X. Yuan, Y. Lian, H. Cheng, Z. Deng, M. Chen, W. Yin, *ACS Catal.* **2020**, 11, 345.
- [111] a) A. Ahmed, M. Forster, J. Jin, P. Myers, H. Zhang, *ACS Appl. Mater. Interfaces* **2015**, 7, 18054; b) P. Liang, C. Zhang, H. Sun, S. Liu, M. Tade, S. Wang, *Energy Fuels* **2016**, 31, 2138.
- [112] Y. Pi, S. Jin, X. Li, S. Tu, Z. Li, J. Xiao, *Appl. Catal. B: Environ.* **2019**, 256, 117882.
- [113] M. Z. Hussain, A. Schneemann, R. A. Fischer, Y. Zhu, Y. Xia, *ACS Appl. Energy Mater.* **2018**, 1, 4695.
- [114] E. Skúlason, V. Tripkovic, M. E. Björketun, S. Gudmundsdottir, G. Karlberg, J. Rossmeisl, T. Bligaard, H. Jónsson, J. K. Nørskov, *J. Phys. Chem. C* **2010**, 114, 18182.
- [115] J. Wang, H. Zhang, X. Wang, *Small Methods* **2017**, 1, 1700118.
- [116] N. Mahmood, Y. Yao, J.-W. Zhang, L. Pan, X. Zhang, J.-J. Zou, *Adv. Sci.* **2018**, 5, 1700464.
- [117] a) N. B. Halck, V. Petrykin, P. Krtíl, J. Rossmeisl, *Phys. Chem. Chem. Phys.* **2014**, 16, 13682; b) E. Fabbri, T. J. Schmidt, *ACS Catal.* **2018**, 8, 9765.
- [118] N.-T. Suen, S.-F. Hung, Q. Quan, N. Zhang, Y.-J. Xu, H. M. Chen, *Chem. Soc. Rev.* **2017**, 46, 337.
- [119] J. Rossmeisl, A. Logadottir, J. K. Nørskov, *Chem. Phys.* **2005**, 319, 178.
- [120] Y. Wang, W. Qiu, E. Song, F. Gu, Z. Zheng, X. Zhao, Y. Zhao, J. Liu, W. Zhang, *Natl. Sci. Rev.* **2017**, 5, 327.
- [121] Y. Li, X. Du, J. Huang, C. Wu, Y. Sun, G. Zou, C. Yang, J. Xiong, *Small* **2019**, 15, 1901980.
- [122] L. Dai, *Adv. Mater.* **2019**, 31, 1900973.
- [123] X. Wang, Z. Li, Y. Qu, T. Yuan, W. Wang, Y. Wu, Y. Li, *Chem* **2019**, 5, 1486.
- [124] R. Ma, G. Lin, Y. Zhou, Q. Liu, T. Zhang, G. Shan, M. Yang, J. Wang, *npj Comput. Mater.* **2019**, 5, 78.
- [125] J. K. Nørskov, J. Rossmeisl, A. Logadottir, L. Lindqvist, J. R. Kitchin, T. Bligaard, H. Jónsson, *J. Phys. Chem. B* **2004**, 108, 17886.
- [126] L. Yang, J. Shui, L. Du, Y. Shao, J. Liu, L. Dai, Z. Hu, *Adv. Mater.* **2019**, 31, e1804799.
- [127] H. Zhang, J. Li, Q. Tan, L. Lu, Z. Wang, G. Wu, *Chem. Eur. J.* **2018**, 24, 18137.
- [128] Q. Lu, F. Jiao, *Nano Energy* **2016**, 29, 439.
- [129] a) R. Kortlever, J. Shen, K. J. P. Schouten, F. Calle-Vallejo, M. T. M. Koper, *J. Phys. Chem. Lett.* **2015**, 6, 4073; b) M. G. Kibria, J. P. Edwards, C. M. Gabardo, D. Cao-Thang, A. Seifitokaldani, D. Sinton, E. H. Sargent, *Adv. Mater.* **2019**, 31, 1807166.
- [130] C. Shi, H. A. Hansen, A. C. Lausche, J. K. Nørskov, *Phys. Chem. Chem. Phys.* **2014**, 16, 4720.
- [131] M. Li, H. Huang, J. Low, C. Gao, R. Long, Y. Xiong, *Small Methods* **2019**, 3, 1800388.
- [132] G.-F. Chen, S. Ren, L. Zhang, H. Cheng, Y. Luo, K. Zhu, L.-X. Ding, H. Wang, *Small Methods* **2019**, 3, 1800337.
- [133] S.-S. Wang, G.-Y. Yang, *Chem. Rev.* **2015**, 115, 4893.
- [134] D.-Y. Du, J.-S. Qin, S.-L. Li, Z.-M. Su, Y.-Q. Lan, *Chem. Soc. Rev.* **2014**, 43, 4615.
- [135] B. Nohra, H. El Moll, L. M. Rodríguez Albello, P. Mialane, J. Marrot, C. Mellot-Draznieks, M. O'Keeffe, R. Ngo Biboum, J. Lemaire, B. Keita, *J. Am. Chem. Soc.* **2011**, 133, 13363.
- [136] J.-S. Qin, D.-Y. Du, W. Guan, X.-J. Bo, Y.-F. Li, L.-P. Guo, Z.-M. Su, Y.-Y. Wang, Y.-Q. Lan, H.-C. Zhou, *J. Am. Chem. Soc.* **2015**, 137, 7169.
- [137] L. Zhang, S. Li, C. J. Gómez-García, H. Ma, C. Zhang, H. Pang, B. Li, *ACS Appl. Mater. Interfaces* **2018**, 10, 31498.
- [138] W. Salomon, G. Paille, M. Gomez-Mingot, P. Mialane, J. Marrot, C. Roch-Marchal, G. Nocton, C. Mellot-Draznieks, M. Fontecave, A. Dolbecq, *Cryst. Growth Des.* **2017**, 17, 1600.
- [139] a) L. Sun, M. G. Campbell, M. Dincă, *Angew. Chem. Int. Ed.* **2016**, 55, 3566; b) J. Wen, Y. Li, J. Gao, *Chem. Res. Chin. Univ.* **2020**, 36, 662.
- [140] A. J. Clough, J. W. Yoo, M. H. Mecklenburg, S. C. Marinescu, *J. Am. Chem. Soc.* **2015**, 137, 118.
- [141] R. Dong, M. Pfeiffermann, H. Liang, Z. Zheng, X. Zhu, J. Zhang, X. Feng, *Angew. Chem. Int. Ed.* **2015**, 54, 12058.
- [142] R. Dong, Z. Zheng, D. C. Tranca, J. Zhang, N. Chandrasekhar, S. Liu, X. Zhuang, G. Seifert, X. Feng, *Chem. Eur. J.* **2017**, 23, 2255.
- [143] J. Duan, S. Chen, C. Zhao, *Nat. Commun.* **2017**, 8, 15341.
- [144] M. Jahan, Z. Liu, K. P. Loh, *Adv. Funct. Mater.* **2013**, 23, 5363.
- [145] Y. P. Wu, W. Zhou, J. Zhao, W. W. Dong, Y. Q. Lan, D. S. Li, C. Sun, X. Bu, *Angew. Chem. Int. Ed.* **2017**, 56, 13001.
- [146] D. Micheroni, G. Lan, W. Lin, *J. Am. Chem. Soc.* **2018**, 140, 15591.
- [147] I. Hod, P. Deria, W. Bury, J. E. Mondloch, C.-W. Kung, M. So, M. D. Sampson, A. W. Peters, C. P. Kubiak, O. K. Farha, *Nat. Commun.* **2015**, 6, 8304.
- [148] X. Dai, M. Liu, Z. Li, A. Jin, Y. Ma, X. Huang, H. Sun, H. Wang, X. Zhang, *J. Phys. Chem. C* **2016**, 120, 12539.
- [149] C. Wang, Y. Su, X. Zhao, S. Tong, X. Han, *Chem. Eur. J.* **2018**, 24, 1080.
- [150] D. Zhu, J. Liu, Y. Zhao, Y. Zheng, S. Z. Qiao, *Small* **2019**, 15, 1805511.
- [151] T. Liu, P. Li, N. Yao, G. Cheng, S. Chen, W. Luo, Y. Yin, *Angew. Chem. Int. Ed.* **2019**, 58, 4679.
- [152] a) E. Cortés, *Science* **2018**, 362, 28; b) A. Agrawal, S. H. Cho, O. Zandi, S. Ghosh, R. W. Johns, D. J. Milliron, *Chem. Rev.* **2018**, 118, 3121.
- [153] C. Wang, X.-G. Nie, Y. Shi, Y. Zhou, J.-J. Xu, X.-H. Xia, H.-Y. Chen, *ACS Nano* **2017**, 11, 5897.
- [154] S.-S. Wang, L. Jiao, Y. Qian, W.-C. Hu, G.-Y. Xu, C. Wang, H.-L. Jiang, *Angew. Chem. Int. Ed.* **2019**, 58, 10713.
- [155] M. Tahir, L. Pan, F. Idrees, X. Zhang, L. Wang, J.-J. Zou, Z. L. Wang, *Nano Energy* **2017**, 37, 136.
- [156] a) A. Kulkarni, S. Siahrostami, A. Patel, J. K. Nørskov, *Chem. Rev.* **2018**, 118, 2302; b) J. S. Kim, B. Kim, H. Kim, K. Kang, *Adv. Energy Mater.* **2018**, 8, 1702774; c) B. Zhang, X. Zheng,



- O. Voznyy, R. Comin, M. Bajdich, M. García-Melchor, L. Han, J. Xu, M. Liu, L. Zheng, *Science* **2016**, 352, 333.
- [157] a) S. Pintado, S. Goberna-Ferrón, E. C. Escudero-Adán, J. R. N. Galán-Mascaros, *J. Am. Chem. Soc.* **2013**, 135, 13270; b) L. Han, P. Tang, A. I. Reyes-Carmona, B. Rodríguez-García, M. Torrén, J. R. Morante, J. Arbiol, J. R. Galán-Mascaros, *J. Am. Chem. Soc.* **2016**, 138, 16037.
- [158] J. Jiang, L. Huang, X. Liu, L. Ai, *ACS Appl. Mater. Interfaces* **2017**, 9, 7193.
- [159] S. Wang, Y. Hou, S. Lin, X. Wang, *Nanoscale* **2014**, 6, 9930.
- [160] L. Tao, C.-Y. Lin, S. Dou, S. Feng, D. Chen, D. Liu, J. Huo, Z. Xia, S. Wang, *Nano Energy* **2017**, 41, 417.
- [161] a) B. Wurster, D. Grumelli, D. Hötger, R. Gutzler, K. Kern, *J. Am. Chem. Soc.* **2016**, 138, 3623; b) P. Manna, J. Debgupta, S. Bose, S. K. Das, *Angew. Chem. Int. Ed.* **2016**, 55, 2425.
- [162] a) A. Eftekhari, *Mater. Today Energy* **2017**, 5, 37; b) J. Zhang, Q. Zhang, X. Feng, *Adv. Mater.* **2019**, 31, 1808167; c) Z. W. Seh, J. Kibsgaard, C. F. Dickens, I. Chorkendorff, J. K. Nørskov, T. F. Jaramillo, *Science* **2017**, 355, eaad4998.
- [163] X.-F. Lu, P.-Q. Liao, J.-W. Wang, J.-X. Wu, X.-W. Chen, C.-T. He, J.-P. Zhang, G.-R. Li, X.-M. Chen, *J. Am. Chem. Soc.* **2016**, 138, 8336.
- [164] J.-Q. Shen, P.-Q. Liao, D.-D. Zhou, C.-T. He, J.-X. Wu, W.-X. Zhang, J.-P. Zhang, X.-M. Chen, *J. Am. Chem. Soc.* **2017**, 139, 1778.
- [165] N.-Y. Huang, J.-Q. Shen, Z.-M. Ye, W.-X. Zhang, P.-Q. Liao, X.-M. Chen, *Chem. Sci.* **2019**, 10, 9859.
- [166] Y.-T. Xu, Z.-M. Ye, J.-W. Ye, L.-M. Cao, R.-K. Huang, J.-X. Wu, D.-D. Zhou, X.-F. Zhang, C.-T. He, J.-P. Zhang, X.-M. Chen, *Angew. Chem. Int. Ed.* **2019**, 58, 139.
- [167] a) D. Yan, C.-L. Dong, Y.-C. Huang, Y. Zou, C. Xie, Y. Wang, Y. Zhang, D. Liu, S. Shen, S. Wang, *J. Mater. Chem. A* **2018**, 6, 805; b) Y. Guo, T. Wang, J. Chen, J. Zheng, X. Li, K. Ostrikov, *Adv. Energy Mater.* **2018**, 8, 1800085; c) S. Dou, C. L. Dong, Z. Hu, Y. C. Huang, J. I. Chen, L. Tao, D. Yan, D. Chen, S. Shen, S. Chou, *Adv. Funct. Mater.* **2017**, 27, 1702546.
- [168] X.-L. Wang, L.-Z. Dong, M. Qiao, Y.-J. Tang, J. Liu, Y. Li, S.-L. Li, J.-X. Su, Y.-Q. Lan, *Angew. Chem. Int. Ed.* **2018**, 57, 9660.
- [169] a) L. Wang, Y. Wu, R. Cao, L. Ren, M. Chen, X. Feng, J. Zhou, B. Wang, *ACS Appl. Mater. Interfaces* **2016**, 8, 16736; b) W. Zhou, D.-D. Huang, Y.-P. Wu, J. Zhao, T. Wu, J. Zhang, D.-S. Li, C. Sun, P. Feng, X. Bu, *Angew. Chem. Int. Ed.* **2019**, 58, 4227; c) Z. Zou, T. Wang, X. Zhao, W.-J. Jiang, H. Pan, D. Gao, C. Xu, *ACS Catal.* **2019**, 9, 7356; d) J. Gao, J. Cong, Y. Wu, L. Sun, J. Yao, B. Chen, *ACS Appl. Energy Mater.* **2018**, 1, 5140; e) F.-L. Li, Q. Shao, X. Huang, J.-P. Lang, *Angew. Chem. Int. Ed.* **2018**, 57, 1888; f) X.-J. Bai, Y.-N. Li, X.-M. Yang, M.-Y. Zhang, L. Shao, B. Zhang, T.-Q. Wang, X.-M. Zhang, L.-Y. Zhang, Y. Fu, *Chem. Commun.* **2019**, 55, 9343; g) X. Zhao, B. Pattengale, D. Fan, Z. Zou, Y. Zhao, J. Du, J. Huang, C. Xu, *ACS Energy Lett.* **2018**, 3, 2520; h) Z. Xue, Y. Li, Y. Zhang, W. Geng, B. Jia, J. Tang, S. Bao, H.-P. Wang, Y. Fan, Z.-W. Wei, Z. Zhang, Z. Ke, G. Li, C.-Y. Su, *Adv. Energy Mater.* **2018**, 8, 1801564.
- [170] a) W. Liu, R. Yin, X. Xu, L. Zhang, W. Shi, X. Cao, *Adv. Sci.* **2019**, 6, 1802373; b) C. Tan, X. Cao, X.-J. Wu, Q. He, J. Yang, X. Zhang, J. Chen, W. Zhao, S. Han, G.-H. Nam, *Chem. Rev.* **2017**, 117, 6225.
- [171] a) A. Dhakshinamoorthy, A. M. Asiri, H. Garcia, *Adv. Mater.* **2019**, 31, 1900617; b) Y.-Z. Li, Z.-H. Fu, G. Xu, *Coord. Chem. Rev.* **2019**, 388, 79.
- [172] a) S. Zhao, Y. Wang, J. Dong, C.-T. He, H. Yin, P. An, K. Zhao, X. Zhang, C. Gao, L. Zhang, *Nat. Energy* **2016**, 1, 16184; b) F. L. Li, P. Wang, X. Huang, D. J. Young, H. F. Wang, P. Braunstein, J. P. Lang, *Angew. Chem. Int. Ed.* **2019**, 58, 7051; c) J. Huang, Y. Li, R.-K. Huang, C.-T. He, L. Gong, Q. Hu, L. Wang, Y.-T. Xu, X.-Y. Tian, S.-Y. Liu, Z.-M. Ye, F. Wang, D.-D. Zhou, W.-X. Zhang, J.-P. Zhang, *Angew. Chem. Int. Ed.* **2018**, 57, 4632; d) Q. Qian, Y. Li, Y. Liu, L. Yu, G. Zhang, *Adv. Mater.* **2019**, 31, 1901139; e) J. Chen, P. Zhuang, Y. Ge, H. Chu, L. Yao, Y. Cao, Z. Wang, M. O. L. Chee, P. Dong, J. Shen, *Adv. Funct. Mater.* **2019**, 29, 1903875; f) Q. Wang, F. Wei, M. Devaraj, Z. Zhang, J. Xiao, X. Zhao, F. Xiao, H. Wang, S. Wang, *Chem. Commun.* **2019**, 55, 11307.
- [173] W. Cheng, X. Zhao, H. Su, F. Tang, W. Che, H. Zhang, Q. Liu, *Nat. Energy* **2019**, 4, 115.
- [174] a) T. Wen, Y. Zheng, C. Xu, J. Zhang, M. Jaroniec, S.-Z. Qiao, *Mater. Horizons* **2018**, 5, 1151; b) T. Wen, Y. Zheng, J. Zhang, K. Davey, S.-Z. Qiao, *Adv. Sci.* **2019**, 6, 1801920; c) H. Wang, F.-X. Yin, B.-H. Chen, X.-B. He, P.-L. Lv, C.-Y. Ye, D.-J. Liu, *Appl. Catal. B: Environ.* **2017**, 205, 55; d) L. Zhao, B. Dong, S. Li, L. Zhou, L. Lai, Z. Wang, S. Zhao, M. Han, K. Gao, M. Lu, *ACS Nano* **2017**, 11, 5800; e) Y. Fang, X. Li, F. Li, X. Lin, M. Tian, X. Long, X. An, Y. Fu, J. Jin, J. Ma, *J. Power Sources* **2016**, 326, 50; f) D. Zhu, J. Liu, L. Wang, Y. Du, Y. Zheng, K. Davey, S.-Z. Qiao, *Nanoscale* **2019**, 11, 3599; g) J. Wang, H. C. Zeng, *ACS Appl. Mater. Interfaces* **2019**, 11, 23180.
- [175] a) J. Kibsgaard, I. Chorkendorff, *Nat. Energy* **2019**, 4, 430; b) Y. Luo, L. Tang, U. Khan, Q. Yu, H.-M. Cheng, X. Zou, B. Liu, *Nat. Commun.* **2019**, 10, 269.
- [176] H.-W. Lin, D. S. Raja, X.-F. Chuah, C.-T. Hsieh, Y.-A. Chen, S.-Y. Lu, *Appl. Catal. B: Environ.* **2019**, 258, 118023.
- [177] Y. Nie, L. Li, Z. Wei, *Chem. Soc. Rev.* **2015**, 44, 2168.
- [178] Q. Li, R. Cao, J. Cho, G. Wu, *Adv. Energy Mater.* **2014**, 4, 1301415.
- [179] N. Yang, L. Li, J. Li, W. Ding, Z. Wei, *Chem. Sci.* **2018**, 9, 5795.
- [180] L. Li, J. He, Y. Wang, X. Lv, X. Gu, P. Dai, D. Liu, X. Zhao, *J. Mater. Chem. A* **2019**, 7, 1964.
- [181] W. Zhang, W. Lai, R. Cao, *Chem. Rev.* **2017**, 117, 3717.
- [182] W. Li, A. Yu, D. C. Higgins, B. G. Llanos, Z. Chen, *J. Am. Chem. Soc.* **2010**, 132, 17056.
- [183] M. Lions, J. B. Tommasino, R. Chattot, B. Abeykoon, N. Guillou, T. Devic, A. Demessence, L. Cardenas, F. Maillard, A. Fateeva, *Chem. Commun.* **2017**, 53, 6496.
- [184] H. Zhong, K. H. Ly, M. Wang, Y. Krupskaya, X. Han, J. Zhang, J. Zhang, V. Kataev, B. Büchner, I. M. Weidinger, *Angew. Chem. Int. Ed.* **2019**, 58, 10677.
- [185] F. He, L. Mi, Y. Shen, X. Chen, Y. Yang, H. Mei, S. Liu, T. Mori, Y. Zhang, *J. Mater. Chem. A* **2017**, 5, 17413.
- [186] E. M. Miner, L. Wang, M. Dinca, *Chem. Sci.* **2018**, 9, 6286.
- [187] P. Zhang, X. Hou, L. Liu, J. Mi, M. Dong, *J. Phys. Chem. C* **2015**, 119, 28028.
- [188] E. M. Miner, T. Fukushima, D. Sheberla, L. Sun, Y. Surendranath, M. Dincă, *Nat. Commun.* **2016**, 7, 10942.
- [189] a) Y.-L. Li, J.-J. Zhou, M.-K. Wu, C. Chen, K. Tao, F.-Y. Yi, L. Han, *Inorg. Chem.* **2018**, 57, 6202; b) M. K. Smith, K. A. Mirica, *J. Am. Chem. Soc.* **2017**, 139, 16759; c) M. S. Yao, X. J. Lv, Z. H. Fu, W. H. Li, W. H. Deng, G. D. Wu, G. Xu, *Angew. Chem. Int. Ed.* **2017**, 56, 16510; d) M. G. Campbell, S. F. Liu, T. M. Swager, M. Dincă, *J. Am. Chem. Soc.* **2015**, 137, 13780.
- [190] H. Yoon, S. Lee, S. Oh, H. Park, S. Choi, M. Oh, *Small* **2019**, 15, 1805232.
- [191] K. Cho, S.-H. Han, M. P. Suh, *Angew. Chem. Int. Ed.* **2016**, 55, 15301.
- [192] D. Higgins, P. Zamani, A. Yu, Z. Chen, *Energy Environ. Sci.* **2016**, 9, 357.
- [193] M. Jahan, Q. Bao, K. P. Loh, *J. Am. Chem. Soc.* **2012**, 134, 6707.
- [194] a) T. Zheng, K. Jiang, H. Wang, *Adv. Mater.* **2018**, 30, 1802066; b) W. Zhang, Y. Hu, L. Ma, G. Zhu, Y. Wang, X. Xue, R. Chen, S. Yang, Z. Jin, *Adv. Sci.* **2018**, 5, 1700275.
- [195] a) W.-G. Cui, G.-Y. Zhang, T.-L. Hu, X.-H. Bu, *Coord. Chem. Rev.* **2019**, 387, 79; b) A. Sofia Varela, W. Ju, P. Strasser, *Adv. Energy*

- Mater.* **2018**, *8*, 1703614; c) Z. Lei, Y. Xue, W. Chen, W. Qiu, Y. Zhang, S. Horike, L. Tang, *Adv. Energy Mater.* **2018**, *8*, 1801587; d) C. S. Diercks, Y. Liu, K. E. Cordova, O. M. Yaghi, *Nat. Mater.* **2018**, *17*, 301; e) C. A. Trickett, A. Helal, B. A. Al-Maythality, Z. H. Yamani, K. E. Cordova, O. M. Yaghi, *Nat. Rev. Mater.* **2017**, *2*, 17045.
- [196] a) D. Yang, Q. Zhu, C. Chen, H. Liu, Z. Liu, Z. Zhao, X. Zhang, S. Liu, B. Han, *Nat. Commun.* **2019**, *10*, 677; b) G. Iijima, T. Inomata, H. Yamaguchi, M. Ito, H. Masuda, *ACS Catal.* **2019**, *9*, 6305.
- [197] Y. Zheng, A. Vasileff, X. Zhou, Y. Jiao, M. Jaroniec, S.-Z. Qiao, *J. Am. Chem. Soc.* **2019**, *141*, 7646.
- [198] R. Hinogami, S. Yotsuhashi, M. Deguchi, Y. Zenitani, H. Hashiba, Y. Yamada, *ECS Electrochem. Lett.* **2012**, *1*, H17.
- [199] R. S. Kumar, S. S. Kumar, M. A. Kulandainathan, *Electrochem. Commun.* **2012**, *25*, 70.
- [200] J. Albo, D. Vallejo, G. Beobide, O. Castillo, P. Castano, A. Irabien, *ChemSusChem* **2017**, *10*, 1100.
- [201] J.-D. Yi, R. Xie, Z.-L. Xie, G.-L. Chai, T.-F. Liu, R.-P. Chen, Y.-B. Huang, R. Cao, *Angew. Chem. Int. Ed.* **2020**, *132*, 23849.
- [202] Z. Weng, Y. Wu, M. Wang, J. Jiang, K. Yang, S. Huo, X.-F. Wang, Q. Ma, G. W. Brudvig, V. S. Batista, *Nat. Commun.* **2018**, *9*, 415.
- [203] a) R. Francke, B. Schille, M. Roemelt, *Chem. Rev.* **2018**, *118*, 4631; b) J. Han, P. An, S. Liu, X. Zhang, D. Wang, Y. Yuan, J. Guo, X. Qiu, K. Hou, L. Shi, *Angew. Chem. Int. Ed.* **2019**, *58*, 12711; c) X. Qin, S. Zhu, F. Xiao, L. Zhang, M. Shao, *ACS Energy Lett.* **2019**, *4*, 1778; d) Y. Liu, C. C. McCrory, *Nat. Commun.* **2019**, *10*, 1683; e) W. Ju, A. Bagger, X. Wang, Y. Tsai, F. Luo, T. F. Möller, H. Wang, J. Rossmeisl, A. S. Varela, P. Strasser, *ACS Energy Lett.* **2019**, *4*, 1663.
- [204] Y.-R. Wang, Q. Huang, C.-T. He, Y. Chen, J. Liu, F.-C. Shen, Y.-Q. Lan, *Nat. Commun.* **2018**, *9*, 4466.
- [205] N. Kornienko, Y. Zhao, C. S. Kley, C. Zhu, D. Kim, S. Lin, C. J. Chang, O. M. Yaghi, P. Yang, *J. Am. Chem. Soc.* **2015**, *137*, 14129.
- [206] I. Hod, M. D. Sampson, P. Deria, C. P. Kubiak, O. K. Farha, J. T. Hupp, *ACS Catal.* **2015**, *5*, 6302.
- [207] B.-X. Dong, S.-L. Qian, F.-Y. Bu, Y.-C. Wu, L.-G. Feng, Y.-L. Teng, W.-L. Liu, Z.-W. Li, *ACS Appl. Energy Mater.* **2018**, *1*, 4662.
- [208] J.-X. Wu, S.-Z. Hou, X.-D. Zhang, M. Xu, H.-F. Yang, P.-S. Cao, Z.-Y. Gu, *Chem. Sci.* **2019**, *10*, 2199.
- [209] X. Kang, Q. Zhu, X. Sun, J. Hu, J. Zhang, Z. Liu, B. Han, *Chem. Sci.* **2016**, *7*, 266.
- [210] X. Jiang, H. Li, J. Xiao, D. Gao, R. Si, F. Yang, Y. Li, G. Wang, X. Bao, *Nano Energy* **2018**, *52*, 345.
- [211] S. Dou, J. Song, S. Xi, Y. Du, J. Wang, Z. F. Huang, Z. J. Xu, X. Wang, *Angew. Chem. Int. Ed.* **2019**, *58*, 4041.
- [212] Y. Wang, P. Hou, Z. Wang, P. Kang, *ChemPhysChem* **2017**, *18*, 3142.
- [213] Y. Tian, C. Zhu, L.-K. Yan, J.-X. Zhao, Z.-M. Su, *J. Mater. Chem. A* **2019**, *7*, 15341.
- [214] C.-W. Kung, C. O. Audu, A. W. Peters, H. Noh, O. K. Farha, J. T. Hupp, *ACS Energy Lett.* **2017**, *2*, 2394.
- [215] X. Tan, C. Yu, C. Zhao, H. Huang, X. Yao, X. Han, W. Guo, S. Cui, H. Huang, J. Qiu, *ACS Appl. Mater. Interfaces* **2019**, *11*, 9904.
- [216] X. Jiang, H. Wu, S. Chang, R. Si, S. Miao, W. Huang, Y. Li, G. Wang, X. Bao, *J. Mater. Chem. A* **2017**, *5*, 19371.
- [217] Y. T. Guntern, J. R. Pankhurst, J. Vávra, M. Mensi, V. Mantella, P. Schouwink, R. Buonsanti, *Angew. Chem. Int. Ed.* **2019**, *58*, 12632.
- [218] P. De Luna, W. Liang, A. Mallick, O. Shekha, F. P. García de Arquer, A. H. Proppe, P. Todorović, S. O. Kelley, E. H. Sargent, M. Eddaoudi, *ACS Appl. Mater. Interfaces* **2018**, *10*, 31225.
- [219] X. Cui, C. Tang, Q. Zhang, *Adv. Energy Mater.* **2018**, *8*, 1800369.
- [220] a) M. H. Vu, M. Sakar, S. A. Hassanzadeh-Tabrizi, T. O. Do, *Adv. Mater. Interfaces* **2019**, *6*, 1900091; b) C. Tang, S.-Z. Qiao, *Chem. Soc. Rev.* **2019**, *48*, 3166; c) S. Z. Andersen, V. Čolić, S. Yang, J. A. Schwalbe, A. C. Nielander, J. M. McEnaney, K. Enemark-Rasmussen, J. G. Baker, A. R. Singh, B. A. Rohr, M. J. Statt, S. J. Blair, S. Mezzavilla, J. Kibsgaard, P. C. K. Vesborg, M. Carnello, S. F. Bent, T. F. Jaramillo, I. E. L. Stephens, J. K. Nørskov, I. Chorkendorff, *Nature* **2019**, *570*, 504; d) M. M. Rodriguez, E. Bill, W. W. Brennessel, P. L. Holland, *Science* **2011**, *334*, 780.
- [221] a) C. Tang, S.-Z. Qiao, *Joule* **2019**, *3*, 1573; b) L. Li, C. Tang, D. Yao, Y. Zheng, S.-Z. Qiao, *ACS Energy Lett.* **2019**, *4*, 2111.
- [222] H. K. Lee, C. S. L. Koh, Y. H. Lee, C. Liu, I. Y. Phang, X. Han, C.-K. Tsung, X. Y. Ling, *Sci. Adv.* **2018**, *4*, eaar3208.
- [223] a) X. Zhao, F. Yin, N. Liu, G. Li, T. Fan, B. Chen, J. *Mater. Sci.* **2017**, *52*, 10175; b) Y. Yang, S.-Q. Wang, H. Wen, T. Ye, J. Chen, C.-P. Li, M. Du, *Angew. Chem. Int. Ed.* **2019**, *58*, 15362.
- [224] A. R. Singh, B. A. Rohr, J. A. Schwalbe, M. Carnello, K. Chan, T. F. Jaramillo, I. Chorkendorff, J. K. Nørskov, *ACS Catal.* **2017**, *7*, 706.
- [225] a) J. Xiang, M. Shang, Y. Kawamata, H. Lundberg, S. H. Reisberg, M. Chen, P. Mykhailiuk, G. Beutner, M. R. Collins, A. Davies, M. Del Bel, G. M. Gallego, J. E. Spangler, J. Starr, S. Yang, D. G. Blackmond, P. S. Baran, *Nature* **2019**, *573*, 398–; b) K. D. Moeller, *Chem. Rev.* **2018**, *118*, 4817; c) N. Fu, G. S. Sauer, A. Saha, A. Loo, S. Lin, *Science* **2017**, *357*, 575; d) E. J. Horn, B. R. Rosen, Y. Chen, J. Tang, K. Chen, M. D. Eastgate, P. S. Baran, *Nature* **2016**, *533*, 77.
- [226] a) M. Yan, Y. Kawamata, P. S. Baran, *Angew. Chem. Int. Ed.* **2018**, *57*, 4149; b) J.-I. Yoshida, A. Shimizu, R. Hayashi, *Chem. Rev.* **2017**, *118*, 4702.
- [227] L. Yang, F. X. Ma, F. Xu, D. Li, L. Su, H. C. Xu, C. Wang, *Chem. Asian J.* **2019**, *14*, 3557.
- [228] W.-W. Guo, C. Zhang, J.-J. Ye, Z.-K. Liu, K. Chen, C.-D. Wu, *Chem. Asian J.* **2019**, *14*, 3627.
- [229] X. Bu, Y.-P. Wu, J.-W. Tian, S. Liu, B. Li, J. Zhao, L.-F. Ma, D.-S. Li, Y.-Q. Lan, *Angew. Chem. Int. Ed.* **2019**, *58*, 12185.
- [230] L. Yang, L. Cao, R. Huang, Z.-W. Hou, X.-Y. Qian, B. An, H.-C. Xu, W. Lin, C. Wang, *ACS Appl. Mater. Interfaces* **2018**, *10*, 36290.
- [231] C.-W. Kung, Y.-S. Li, M.-H. Lee, S.-Y. Wang, W.-H. Chiang, K.-C. Ho, *J. Mater. Chem. A* **2016**, *4*, 10673.
- [232] Q. Li, Z. Shao, T. Han, M. Zheng, H. Pang, *ACS Sustain. Chem. Eng.* **2019**, *7*, 8986.
- [233] a) B. Liu, H. Shioyama, T. Akita, Q. Xu, *J. Am. Chem. Soc.* **2008**, *130*, 5390; b) K. Shen, X. Chen, J. Chen, Y. Li, *ACS Catal.* **2016**, *6*, 5887; c) K. J. Lee, J. H. Lee, S. Jeoung, H. R. Moon, *Acc. Chem. Res.* **2017**, *50*, 2684; d) S. Dang, Q.-L. Zhu, Q. Xu, *Nat. Rev. Mater.* **2018**, *3*, 17075; e) B. Zhu, D. Xia, R. Zou, *Coord. Chem. Rev.* **2018**, *376*, 430.
- [234] a) W. Xia, A. Mahmood, R. Zou, Q. Xu, *Energy Environ. Sci.* **2015**, *8*, 1837; b) Z. Liang, R. Zhao, T. Qiu, R. Zou, Q. Xu, *EnergyChem* **2019**, *1*, 100001; c) L. Jiao, G. Wan, R. Zhang, H. Zhou, S.-H. Yu, H.-L. Jiang, *Angew. Chem. Int. Ed.* **2018**, *57*, 8525; d) L. Jiao, W. Yang, G. Wan, R. Zhang, X. Zheng, H. Zhou, S.-H. Yu, H.-L. Jiang, *Angew. Chem. Int. Ed.* **2020**, *59*, 20589; e) L. Jiao, R. Zhang, G. Wan, W. Yang, X. Wan, H. Zhou, J. Shui, S.-H. Yu, H.-L. Jiang, *Nat. Commun.* **2020**, *11*, 2831.
- [235] C.-C. Hou, Q. Xu, *Adv. Energy Mater.* **2019**, *9*, 1801307.
- [236] a) J. Guo, J. Huo, Y. Liu, W. Wu, Y. Wang, M. Wu, H. Liu, G. Wang, *Small Methods* **2019**, *3*, 1900159; b) T. Sun, L. Xu, D. Wang, Y. Li, *Nano Res.* **2019**, *12*, 1; c) H. Yang, X. Wang, *Adv. Mater.* **2019**, *31*, 1800743.
- [237] C. Castillo-Blas, N. López-Salas, M. C. Gutiérrez, I. Puente-Orench, E. Gutiérrez-Puebla, M. L. Ferrer, M. Á. Monge, F. Gándara, *J. Am. Chem. Soc.* **2019**, *141*, 1766.
- [238] G. Yilmaz, T. Yang, Y. Du, X. Yu, Y. P. Feng, L. Shen, G. W. Ho, *Adv. Sci.* **2019**, *6*, 1900140.

- [239] a) A. Wang, J. Li, T. Zhang, *Nat. Rev. Chem.* **2018**, 2, 65; b) M. D. Hossain, Z. Liu, M. Zhuang, X. Yan, G. L. Xu, C. A. Gadre, A. Tyagi, I. H. Abidi, C. J. Sun, H. Wong, *Adv. Energy Mater.* **2019**, 9, 1803689; c) Z. Song, L. Zhang, K. Doyle-Davis, X. Fu, J. L. Luo, X. Sun, *Adv. Energy Mater.* **2020**, 10, 2001561; d) L. Jiao, H.-L. Jiang, *Chem* **2019**, 5, 786; e) H. Huang, K. Shen, F. Chen, Y. Li, *ACS Catal.* **2020**, 12, 6579.
- [240] Y. Deng, B. Chi, J. Li, G. Wang, L. Zheng, X. Shi, Z. Cui, L. Du, S. Liao, K. Zang, J. Luo, Y. Hu, X. Sun, *Adv. Energy Mater.* **2019**, 9, 1802856.
- [241] C. C. Hou, L. Zou, L. Sun, K. Zhang, Z. Liu, Y. Li, C. Li, R. Zou, J. Yu, Q. Xu, *Angew. Chem. Int. Ed.* **2020**, 132, 7454.
- [242] a) Z. Xie, W. Xu, X. Cui, Y. Wang, *ChemSusChem* **2017**, 10, 1645; b) X. Wei, X. Wang, X. Tan, Q. An, L. Mai, *Adv. Funct. Mater.* **2018**, 28, 1804458.
- [243] H. Chen, K. Shen, Q. Mao, J. Chen, Y. Li, *ACS Catal.* **2018**, 8, 1417.
- [244] Y. Xiong, Y. Yang, F. J. DiSalvo, H. D. Abruña, *J. Am. Chem. Soc.* **2019**, 141, 10744.
- [245] Z.-X. Cai, Z.-L. Wang, J. Kim, Y. Yamauchi, *Adv. Mater.* **2019**, 31, 1804903.
- [246] Z. Xie, Y. Wang, *Electrochim. Acta* **2019**, 296, 372.
- [247] Y. Xu, P. Deng, G. Chen, J. Chen, Y. Yan, K. Qi, H. Liu, B. Y. Xia, *Adv. Funct. Mater.* **2020**, 30, 1906081.
- [248] a) D.-D. Ma, Q.-L. Zhu, *Coord. Chem. Rev.* **2020**, 422, 213483; b) Z. Li, X. Zhang, H. Cheng, J. Liu, M. Shao, M. Wei, D. G. Evans, H. Zhang, X. Duan, *Adv. Energy Mater.* **2020**, 10, 1900486; c) H. Xu, B. Fei, G. Cai, Y. Ha, J. Liu, H. Jia, J. Zhang, M. Liu, R. Wu, *Adv. Energy Mater.* **2020**, 10, 1902714.
- [249] L. Zheng, S. Yu, X. Lu, W. Fan, B. Chi, Y. Ye, X. Shi, J. Zeng, X. Li, S. Liao, *ACS Appl. Mater. Interfaces* **2020**, 12, 13878.
- [250] H. Zhong, J. Wang, Y. Zhang, W. Xu, W. Xing, D. Xu, Y. Zhang, X. Zhang, *Angew. Chem. Int. Ed.* **2014**, 53, 14235.
- [251] C. Zhu, H. Li, S. Fu, D. Du, Y. Lin, *Chem. Soc. Rev.* **2016**, 45, 517.
- [252] X. Sun, S. Sun, S. Gu, Z. Liang, J. Zhang, Y. Yang, Z. Deng, P. Wei, J. Peng, Y. Xu, *Nano Energy* **2019**, 61, 245.
- [253] J. Zhou, Y. Dou, A. Zhou, L. Shu, Y. Chen, J.-R. Li, *ACS Energy Lett.* **2018**, 3, 1655.
- [254] a) S. Chen, J. Bi, Y. Zhao, L. Yang, C. Zhang, Y. Ma, Q. Wu, X. Wang, Z. Hu, *Adv. Mater.* **2012**, 24, 5593; b) X. Liu, L. Dai, *Nat. Rev. Mater.* **2016**, 1, 16064.
- [255] a) A. Han, B. Wang, A. Kumar, Y. Qin, J. Jin, X. Wang, C. Yang, B. Dong, Y. Jia, J. Liu, X. Sun, *Small Methods* **2019**, 3, 1800471; b) F. Marpaung, M. Kim, J. H. Khan, K. Konstantinov, Y. Yamauchi, M. S. A. Hossain, J. Na, J. Kim, *Chem. Asian J.* **2019**, 14, 1331; c) H.-F. Wang, L. Chen, H. Pang, S. Kaskel, Q. Xu, *Chem. Soc. Rev.* **2020**, 49, 1414; d) L. Wang, Y. Zhu, C. Du, X. Ma, C. Cao, *J. Mater. Chem. A* **2020**, 8, 24895.
- [256] J. Zhang, J. Fang, J. Han, T. Yan, L. Shi, D. Zhang, *J. Mater. Chem. A* **2018**, 6, 15245.
- [257] P. Deng, F. Yang, Z. Wang, S. Chen, Y. Zhou, S. Zaman, B. Y. Xia, *Angew. Chem. Int. Ed.* **2020**, 59, 10807.
- [258] Y. Pan, K. Sun, S. Liu, X. Cao, K. Wu, W.-C. Cheong, Z. Chen, Y. Wang, Y. Li, Y. Liu, *J. Am. Chem. Soc.* **2018**, 140, 2610.
- [259] a) Y. Xu, M. Kraft, R. Xu, *Chem. Soc. Rev.* **2016**, 45, 3039; b) J. Du, F. Li, L. Sun, *Chem. Soc. Rev.* **2021**, 50, 2663; c) Y. Li, M. Lu, Y. Wu, Q. Ji, H. Xu, J. Gao, G. Qian, Q. Zhang, *J. Mater. Chem. A* **2020**, 8, 18215; d) Y. Li, T. Zhao, M. Lu, Y. Wu, Y. Xie, H. Xu, J. Gao, J. Yao, G. Qian, Q. Zhang, *Small* **2019**, 15, 1901940.
- [260] J. Chen, J. Liu, J.-Q. Xie, H. Ye, X.-Z. Fu, R. Sun, C.-P. Wong, *Nano Energy* **2019**, 56, 225.
- [261] Y. Li, S. Niu, D. Rakov, Y. Wang, M. Cabán-Acevedo, S. Zheng, B. Song, P. Xu, *Nanoscale* **2018**, 10, 7291.
- [262] a) B. Y. Xia, Y. Yan, N. Li, H. B. Wu, X. W. D. Lou, X. Wang, *Nat. Energy* **2016**, 1, 15006; b) C. Spoerl, J. T. H. Kwan, A. Bonakdarpour, D. P. Wilkinson, P. Strasser, *Angew. Chem. Int. Ed.* **2017**, 56, 5994; c) Q. Liang, J. Chen, F. Wang, Y. Li, *Coord. Chem. Rev.* **2020**, 424, 213488.
- [263] Y. Lin, H. Wan, D. Wu, G. Chen, N. Zhang, X. Liu, J. Li, Y. Cao, G. Qiu, R. Ma, *J. Am. Chem. Soc.* **2020**, 142, 7317.
- [264] J. Tian, F. Jiang, D. Yuan, L. Zhang, Q. Chen, M. Hong, *Angew. Chem. Int. Ed.* **2020**, 59, 13101.
- [265] Y. Li, Z. Wang, J. Hu, S. Li, Y. Du, X. Han, P. Xu, *Adv. Funct. Mater.* **2020**, 30, 1910498.
- [266] T. Liu, P. Li, N. Yao, T. Kong, G. Cheng, S. Chen, W. Luo, *Adv. Mater.* **2019**, 31, 1806672.
- [267] a) C. Zhu, Q. Shi, B. Z. Xu, S. Fu, G. Wan, C. Yang, S. Yao, J. Song, H. Zhou, D. Du, *Adv. Energy Mater.* **2018**, 8, 1801956; b) X. Duan, S. Ren, N. Pan, M. Zhang, H. Zheng, *J. Mater. Chem. A* **2020**, 8, 9355.
- [268] W.-J. Niu, Y.-P. Wang, J.-Z. He, W.-W. Liu, M.-C. Liu, D. Shan, L. Lee, Y.-L. Chueh, *Nano Energy* **2019**, 63, 103788.
- [269] a) H. Tang, Y. Zeng, D. Liu, D. Qu, J. Luo, K. Binnemans, D. E. De Vos, J. Fransaer, D. Qu, S.-G. Sun, *Nano Energy* **2016**, 26, 131; b) G. A. Ferrero, K. Preuss, A. Marinovic, A. B. Jorge, N. Mansor, D. J. Brett, A. B. Fuertes, M. Sevilla, M.-M. Titirici, *ACS Nano* **2016**, 10, 5922.
- [270] H. Yang, X. Chen, W.-T. Chen, Q. Wang, N. Cantillo Cuello, A. Nafady, A. M. Al-Enizi, G. I. N. Waterhouse, G. A. Goenaga, T. A. Zawodzinski, *ACS Nano* **2019**, 13, 8087.
- [271] Z. Meng, S. Cai, R. Wang, H. Tang, S. Song, P. Tsiakaras, *Appl. Catal. B: Environ.* **2019**, 244, 120.
- [272] a) G. Wu, K. L. More, C. M. Johnston, P. Zelenay, *Science* **2011**, 332, 443; b) Q.-L. Zhu, W. Xia, L.-R. Zheng, R. Zou, Z. Liu, Q. Xu, *ACS Energy Lett.* **2017**, 2, 504.
- [273] X. Chen, N. Wang, K. Shen, Y. Xie, Y. Tan, Y. Li, *ACS Appl. Mater. Interfaces* **2019**, 11, 25976.
- [274] R. Jiang, L. Li, T. Sheng, G. Hu, Y. Chen, L. Wang, *J. Am. Chem. Soc.* **2018**, 140, 11594.
- [275] a) S. Lin, C. S. Diercks, Y.-B. Zhang, N. Kornienko, E. M. Nichols, Y. Zhao, A. R. Paris, D. Kim, P. Yang, O. M. Yaghi, C. J. Chang, *Science* **2015**, 349, 1208; b) T.-T. Zhuang, Z.-Q. Liang, A. Seifitokaldani, Y. Li, P. De Luna, T. Burdyny, F. Che, F. Meng, Y. Min, R. Quintero-Bermudez, *Nat. Catal.* **2018**, 1, 421; c) W. Ju, A. Bagger, G.-P. Hao, A. S. Varela, I. Sinev, V. Bon, B. R. Cuenya, S. Kaskel, J. Rossmeisl, P. Strasser, *Nat. Commun.* **2017**, 8, 944; d) Y. Mun, K. Kim, S. Kim, S. Lee, S. Kim, W. Choi, S. Kim, J. W. Han, J. Lee, *Appl. Catal. B: Environ.* **2018**, 236, 154; e) H. Song, M. Im, J. T. Song, J.-A. Lim, B.-S. Kim, Y. Kwon, S. Ryu, J. Oh, *Appl. Catal. B: Environ.* **2018**, 232, 391.
- [276] D. D. Zhu, J. L. Liu, S. Z. Qiao, *Adv. Mater.* **2016**, 28, 3423.
- [277] X. Wang, Z. Chen, X. Zhao, T. Yao, W. Chen, R. You, C. Zhao, G. Wu, J. Wang, W. Huang, *Angew. Chem. Int. Ed.* **2018**, 57, 1944.
- [278] W. Ren, X. Tan, W. Yang, C. Jia, S. Xu, K. Wang, S. C. Smith, C. Zhao, *Angew. Chem. Int. Ed.* **2019**, 58, 6972.
- [279] J. Gu, C.-S. Hsu, L. Bai, H. M. Chen, X. Hu, *Science* **2019**, 364, 1091.
- [280] a) W. Guo, Z. Liang, J. Zhao, B. Zhu, K. Cai, R. Zou, Q. Xu, *Small Methods* **2018**, 2, 1800204; b) X. Guo, H. Du, F. Qu, J. Li, *J. Mater. Chem. A* **2019**, 7, 3531; c) Q. Wang, Y. Lei, D. Wang, Y. Li, *Energy Environ. Sci.* **2019**, 12, 1730; d) H. Liu, L. Wei, F. Liu, Z. Pei, J. Shi, Z.-J. Wang, D. He, Y. Chen, *ACS Catal.* **2019**, 9, 5245.
- [281] Y. Liu, Y. Su, X. Quan, X. Fan, S. Chen, H. Yu, H. Zhao, Y. Zhang, J. Zhao, *ACS Catal.* **2018**, 8, 1186.
- [282] Z. Geng, Y. Liu, X. Kong, P. Li, K. Li, Z. Liu, J. Du, M. Shu, R. Si, J. Zeng, *Adv. Mater.* **2018**, 30, 1803498.
- [283] S. Luo, X. Li, B. Zhang, Z. Luo, M. Luo, *ACS Appl. Mater. Interfaces* **2019**, 11, 26891.



- [284] J.-B. Raoof, S. R. Hosseini, S. Rezaee, *Electrochim. Acta* **2014**, 141, 340.
- [285] S. Rezaee, S. Shahrokhian, *Appl. Catal. B: Environ.* **2019**, 244, 802.
- [286] H. Wang, X. Yuan, Y. Wu, G. Zeng, X. Chen, L. Leng, H. Li, *Appl. Catal. B: Environ.* **2015**, 174, 445.
- [287] D. Sun, Y. Fu, W. Liu, L. Ye, D. Wang, L. Yang, X. Fu, Z. Li, *Chem. Eur. J.* **2013**, 19, 14279.
- [288] D. Chen, H. Xing, C. Wang, Z. Su, *J. Mater. Chem. A* **2016**, 4, 2657.
- [289] S. Wang, W. Yao, J. Lin, Z. Ding, X. Wang, *Angew. Chem. Int. Ed.* **2014**, 53, 1034.
- [290] Y. Liu, Y. Yang, Q. Sun, Z. Wang, B. Huang, Y. Dai, X. Qin, X. Zhang, *ACS Appl. Mater. Interfaces* **2013**, 5, 7654.
- [291] Y. Lee, S. Kim, H. Fei, J. K. Kang, S. M. Cohen, *Chem. Commun.* **2015**, 51, 16549.
- [292] L. Li, S. Zhang, L. Xu, J. Wang, L.-X. Shi, Z.-N. Chen, M. Hong, J. Luo, *Chem. Sci.* **2014**, 5, 3808.
- [293] S. Zhang, L. Li, S. Zhao, Z. Sun, J. Luo, *Inorg. Chem.* **2015**, 54, 8375.
- [294] M. B. Chambers, X. Wang, N. Elgrishi, C. H. Hendon, A. Walsh, J. Bonnefoy, J. Canivet, E. A. Quadrelli, D. Farrusseng, C. Mellot-Draznieks, M. Fontecave, *ChemSusChem* **2015**, 8, 603.
- [295] D. Sun, Y. Gao, J. Fu, X. Zeng, Z. Chen, Z. Li, *Chem. Commun.* **2015**, 51, 2645.
- [296] D. Sun, W. Liu, Y. Fu, Z. Fang, F. Sun, X. Fu, Y. Zhang, Z. Li, *Chem. Eur. J.* **2014**, 20, 4780.
- [297] L. Rui, J. Hu, M. Deng, H. Wang, X. Wang, Y. Hu, H. L. Jiang, J. Jiang, Q. Zhang, X. Yi, *Adv. Mater.* **2014**, 26, 4783.
- [298] S. Yan, S. Ouyang, H. Xu, M. Zhao, X. Zhang, J. Ye, *J. Mater. Chem. A* **2016**, 4, 15126.
- [299] Q. Liu, Z.-X. Low, L. Li, A. Razmjou, K. Wang, J. Yao, H. Wang, *J. Mater. Chem. A* **2013**, 1, 11563.
- [300] Y. Su, Z. Zhang, H. Liu, Y. Wang, *Appl. Catal. B: Environ.* **2017**, 200, 448.
- [301] S. Wang, J. Lin, X. Wang, *Phys. Chem. Chem. Phys.* **2014**, 16, 14656.
- [302] H. Chen, Z.-G. Gu, S. Mirza, S.-H. Zhang, J. Zhang, *J. Mater. Chem. A* **2018**, 6, 7175.
- [303] M. Li, S. Song, C. Su, L. Li, Z. Yan, X. Cao, *Catal. Sci. Technol.* **2019**, 9, 3828.
- [304] Y.-C. Luo, K.-L. Chu, J.-Y. Shi, D.-J. Wu, X.-D. Wang, M. Mayor, C.-Y. Su, *J. Am. Chem. Soc.* **2019**, 141, 13057.
- [305] S. Kampouri, C. P. Ireland, B. Valizadeh, E. Oveis, P. A. Schouwink, M. Mensi, K. C. Stylianou, *ACS Appl. Energy Mater.* **2018**, 1, 6541.
- [306] J. Liu, X. Zhao, P. Jing, W. Shi, P. Cheng, *Chem. Eur. J.* **2019**, 25, 2330.
- [307] B. Ma, T.-T. Chen, Q.-Y. Li, H.-N. Qin, X.-Y. Dong, S.-Q. Zang, *ACS Appl. Energy Mater.* **2019**, 2, 1134.
- [308] I. Mondal, S. Gonuguntla, U. Pal, *J. Phys. Chem. C* **2019**, 123, 26073.
- [309] Y. Xu, J. Mo, G. Xie, D. Ding, S. Ding, X. Wang, C. Li, *Chem. Commun.* **2019**, 55, 6862.
- [310] K. Zhao, S. Zhao, C. Gao, J. Qi, H. Yin, D. Wei, M. F. Mideksa, X. Wang, Y. Gao, Z. Tang, R. Yu, *Small* **2018**, 14, 1800762.
- [311] W. Xiong, Z. Zeng, G. Zeng, Z. Yang, R. Xiao, X. Li, J. Cao, C. Zhou, H. Chen, M. Jia, Y. Yang, W. Wang, X. Tang, *Chem. Eng. J.* **2019**, 374, 91.
- [312] Z.-X. Li, B.-L. Yang, Y.-F. Jiang, C.-Y. Yu, L. Zhang, *Cryst. Growth Des.* **2018**, 18, 979.
- [313] A. A. Dubale, I. N. Ahmed, X.-H. Chen, C. Ding, G.-H. Hou, R.-F. Guan, X. Meng, X.-L. Yang, M.-H. Xie, *J. Mater. Chem. A* **2019**, 7, 6062.
- [314] S. Roy, Z. Huang, A. Bhunia, A. Castner, A. Kumar Gupta, X. Zou, S. Ott, *J. Am. Chem. Soc.* **2019**, 141, 15942.
- [315] D.-D. Huang, S. Li, Y.-P. Wu, J.-H. Wei, J.-W. Yi, H.-M. Ma, Q.-C. Zhang, Y.-L. Liu, D.-S. Li, *Chem. Commun.* **2019**, 55, 4570.
- [316] H. Jia, Y. Yao, J. Zhao, Y. Gao, Z. Luo, P. Du, *J. Mater. Chem. A* **2018**, 6, 1188.
- [317] W.-H. Li, J. Lv, Q. Li, J. Xie, N. Ogiwara, Y. Huang, H. Jiang, H. Kitagawa, G. Xu, Y. Wang, *J. Mater. Chem. A* **2019**, 7, 10431.
- [318] F. Sun, G. Wang, Y. Ding, C. Wang, B. Yuan, Y. Lin, *Adv. Energy Mater.* **2018**, 8, 1800584.
- [319] D. Senthil Raja, X. F. Chuah, S. Y. Lu, *Adv. Energy Mater.* **2018**, 8, 1801065.
- [320] K. Jayaramulu, J. Masa, D. M. Morales, O. Tomanec, V. Ranc, M. Petr, P. Wilde, Y. T. Chen, R. Zboril, W. Schuhmann, *Adv. Sci.* **2018**, 5, 1801029.
- [321] D. S. Raja, H.-W. Lin, S.-Y. Lu, *Nano Energy* **2019**, 57, 1.
- [322] J. Mao, L. Yang, P. Yu, X. Wei, L. Mao, *Electrochem. Commun.* **2012**, 19, 29.
- [323] X.-H. Liu, W.-L. Hu, W.-J. Jiang, Y.-W. Yang, S. Niu, B. Sun, J. Wu, J.-S. Hu, *ACS Appl. Mater. Interfaces* **2017**, 9, 28473.
- [324] H. Wang, F. Yin, B. Chen, G. Li, *J. Mater. Chem. A* **2015**, 3, 16168.
- [325] S. Sohrabi, S. Dehghanpour, M. Ghalkhani, *ChemCatChem* **2016**, 8, 2356.
- [326] Q. Huang, Q. Li, J. Liu, R. Wang, Y.-Q. Lan, *Matter* **2019**, 1, 1656.
- [327] Y. Chen, P. Li, H. Noh, C. W. Kung, C. T. Buru, X. Wang, X. Zhang, O. K. Farha, *Angew. Chem. Int. Ed.* **2019**, 58, 7682.
- [328] L. Ye, J. Liu, Y. Gao, C. Gong, M. Addicoat, T. Heine, C. Woell, L. Sun, *J. Mater. Chem. A* **2016**, 4, 15320.
- [329] J.-X. Wu, W.-W. Yuan, M. Xu, Z.-Y. Gu, *Chem. Commun.* **2019**, 55, 11634.
- [330] X.-Q. Wu, J. Zhao, Y.-P. Wu, W.-W. Dong, D.-S. Li, J.-R. Li, Q. Zhang, *ACS Appl. Mater. Interfaces* **2018**, 10, 12740.
- [331] R. Mehek, N. Iqbal, T. Noor, H. Nasir, Y. Mehmood, S. Ahmed, *Electrochim. Acta* **2017**, 255, 195.
- [332] A. Vulcu, L. Olenic, G. Blanita, C. Berghian-Grosan, *Electrochim. Acta* **2016**, 219, 630.
- [333] G. Jia, Y. Gao, W. Zhang, H. Wang, Z. Cao, C. Li, J. Liu, *Electrochem. Commun.* **2013**, 34, 211.
- [334] a) T. Ishimoto, T. Ogura, M. Koyama, L. Yang, S. Kinoshita, T. Yamada, M. Tokunaga, H. Kitagawa, *J. Phys. Chem. C* **2013**, 117, 10607; b) L. Yang, S. Kinoshita, T. Yamada, S. Kanda, H. Kitagawa, M. Tokunaga, T. Ishimoto, T. Ogura, R. Nagumo, A. Miyamoto, M. Koyama, *Angew. Chem. Int. Ed.* **2010**, 49, 5348.
- [335] Y. Liu, Y. Zhang, J. Chen, H. Pang, *Nanoscale* **2014**, 6, 10989.
- [336] B. Yuan, J. Zhang, R. Zhang, H. Shi, N. Wang, J. Li, F. Ma, D. Zhang, *Sensor. Actuat. B: Chem.* **2016**, 222, 632.
- [337] S. R. Ahrenholtz, C. C. Epley, A. J. Morris, *J. Am. Chem. Soc.* **2014**, 136, 2464.
- [338] Y. Zhang, X. Bo, A. Nsabimana, C. Han, M. Li, L. Guo, *J. Mater. Chem. A* **2015**, 3, 732.
- [339] L. Wang, Q. Teng, X. Sun, Y. Chen, Y. Wang, H. Wang, Y. Zhang, *J. Colloid Interface Sci.* **2018**, 512, 127.
- [340] D. K. Yadav, V. Ganesan, F. Marken, R. Gupta, P. K. Sonkar, *Electrochim. Acta* **2016**, 219, 482.
- [341] L. Wang, T. Meng, Y. Fan, C. Chen, Z. Guo, H. Wang, Y. Zhang, *J. Colloid Interface Sci.* **2018**, 524, 1.
- [342] H. Hosseini, H. Ahmar, A. Dehghani, A. Bagheri, A. Tadjarodi, A. R. Fakhari, *Biosens. Bioelectron.* **2013**, 42, 426.
- [343] E. Zhou, Y. Zhang, Y. Li, X. He, *Electroanalysis* **2014**, 26, 2526.
- [344] C. Zhang, M. Wang, L. Liu, X. Yang, X. Xu, *Electrochem. Commun.* **2013**, 33, 131.
- [345] R. Wang, X.-Y. Dong, J. Du, J.-Y. Zhao, S.-Q. Zang, *Adv. Mater.* **2018**, 30, 1703711.
- [346] Y. Yu, X. Qiu, X. Zhang, Z. Wu, H. Wang, W. Wang, Z. Wang, H. Tan, Z. Peng, X. Guo, H. Liu, *Electrochim. Acta* **2019**, 299, 423.
- [347] X. Wang, J. He, B. Yu, B. Sun, D. Yang, X. Zhang, Q. Zhang, W. Zhang, L. Gu, Y. Chen, *Appl. Catal. B: Environ.* **2019**, 258, 117996.



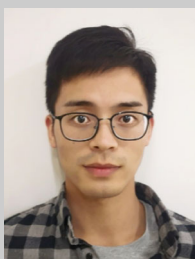
- [348] X. Wang, L. Yu, B. Y. Guan, S. Song, X. W. Lou, *Adv. Mater.* **2018**, *30*, 1801211.
- [349] X. Wang, L. Chai, J. Ding, L. Zhong, Y. Du, T.-T. Li, Y. Hu, J. Qian, S. Huang, *Nano Energy* **2019**, *62*, 745.
- [350] Y. Fu, W. Wang, J. Wang, X. Li, R. Shi, O. Peng, B. N. Chandrashekar, K. Liu, A. Amini, C. Cheng, *J. Mater. Chem. A* **2019**, *7*, 17299.
- [351] H. B. Aiyappa, P. Wilde, T. Quast, J. Masa, C. Andronescu, Y.-T. Chen, M. Muhler, R. A. Fischer, W. Schuhmann, *Angew. Chem. Int. Ed.* **2019**, *58*, 8927.
- [352] H. Zou, B. He, P. Kuang, J. Yu, K. Fan, *ACS Appl. Mater. Interfaces* **2018**, *10*, 22311.
- [353] T. Sun, S. Zhang, L. Xu, D. Wang, Y. Li, *Chem. Commun.* **2018**, *54*, 12101.
- [354] M.-R. Liu, Q.-L. Hong, Q.-H. Li, Y. Du, H.-X. Zhang, S. Chen, T. Zhou, J. Zhang, *Adv. Funct. Mater.* **2018**, *28*, 1801136.
- [355] F. Pan, H. Zhang, K. Liu, D. Cullen, K. More, M. Wang, Z. Feng, G. Wang, G. Wu, Y. Li, *ACS Catal.* **2018**, *8*, 3116.
- [356] P. Song, L. Kang, H. Wang, R. Guo, R. Wang, *ACS Appl. Mater. Interfaces* **2019**, *11*, 12408.
- [357] X. Long, P. Yin, T. Lei, K. Wang, Z. Zhan, *Appl. Catal. B: Environ.* **2020**, *260*, 118187.



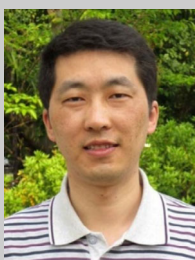
**Junkuo Gao** was born in Henan, China. He received his B.S. (2005) and Ph.D. (2010) from Zhejiang University in China under the supervision of Professor Guodong Qian. He worked with Professor Hans Agren at Royal Institute of Technology (KTH), Sweden, and Professor Qichun Zhang at Nanyang Technological University, Singapore, as a postdoctoral fellow in 2010–2013. He is now a Qianjiang Scholar Distinguished Professor at Zhejiang Sci-Tech University, China. His research interest is related to functional porous materials including metal–organic frameworks and hydrogen-bonded organic frameworks for photo/electrocatalysis and gas separation.



**Qing Huang** received her B.S. from Jiangxi Normal University in 2015 and Ph.D. (2020) from Nanjing Normal University under the supervision of Professor Ya-Qian Lan. Now she works as a postdoctoral in South China Normal University. Her current research is mainly focused on the synthesis of porous crystalline materials (MOFs and POMOFs) and their photo/electrochemical applications, such as photoreduction of CO<sub>2</sub>, photocatalytic water splitting, electroreduction of CO<sub>2</sub>, and oxygen reduction reaction.



**Yuhang Wu** was born in 1993 in Zhejiang, China. He is now a Ph.D. candidate working with Professor Junkuo Gao at Zhejiang Sci-Tech University. His current research interest focuses on metal–organic framework derivatives for energy-conversion applications.



**Ya-Qian Lan** was born in 1978 in Jilin, China. He received his B.S. and Ph.D. (2009) from Faculty of Chemistry, Northeast Normal University, under the supervision of Professor Zhong-Min Su. In 2010, he worked as a JSPS postdoctoral fellow at AIST. Since the fall of 2012, he has been a Professor of Chemistry at Nanjing Normal University. His current research interests focus on synthesis of porous crystalline materials and catalytic research related to clean energy applications.



**Banglin Chen** was born in Zhejiang, China. He received B.S. (1985) and M.S. (1988) in chemistry from Zhejiang University in China and his Ph.D. from National University of Singapore in 2000. He worked with Professors Omar M. Yaghi at University of Michigan, Stephen Lee, at Cornell University, and Andrew W. Maverick at Louisiana State University as a postdoctoral fellow during 2000–2003 before joining the University of Texas-Pan American in 2003. He moved to the University of Texas at San Antonio in August 2009, where he is a professor of chemistry, working on multifunctional metal–organic frameworks and hydrogen-bonded organic framework materials.